Faculty of Science and Engineering
Department of Exploration Geophysics

Study of stress-induced anisotropy and effect of crack infill in oil and gas reservoirs

Olivia Collet

This thesis is presented for the Degree of
Doctor of Philosophy
of
Curtin University

March 2015

Declaration

To the best of my knowledge and belief this thesis contains no material previously published by any other person except where due acknowledgment has been made.

This thesis contains no material which has been accepted for the award of any other degree or diploma in any university.

Date: 2 March 2015

Signature:

Abstract

For most of its history, seismic processing and inversion has been based on an isotropic earth model, despite the recognized fact that many geological formations are anisotropic. Seismic anisotropy is defined as the dependence of seismic velocities upon propagation direction. Analysis of seismic anisotropy is challenging as it requires a number of parameters that are difficult to constrain from measured field data. This thesis aims at deriving new rock physics models in order to gain a better insight on how external stresses and fluid affect seismic anisotropy.

First, we focus on modelling the stress-induced anisotropy of dry rocks. The anisotropy pattern resulting from the application of a small triaxial stress on an initially isotropic medium is expressed in terms of anisotropy parameters, which are a convenient notation to describe the effect of anisotropy on velocities. Interestingly, the medium is found to be ellipsoidal. This result provides a potential way of differentiating between stress-induced and fracture-induced anisotropy by estimating the degree of anellipticity. The model also expresses the ratio of P- to S-wave anisotropy parameters as a function of the compliance ratio of grain contacts and the Poisson's ratio of the unstressed isotropic rock. The model predictions are consistent with laboratory measurements made on a sample of Penrith sandstone, although crack opening in the direction of maximum stress should be taken into account for larger stresses.

Next, we analyse the effect of fluid on anisotropy based on Gassmann theory. In the limit of weak anisotropy, it is possible to derive analytical expressions relating anisotropy parameters in saturated transversely isotropic or orthorhombic media as a function of anisotropy parameters in the dry medium. This approach is only valid at low frequencies, for which pore pressure is equilibrated throughout the pore space.

At higher frequencies, fluid pressure gradients cause local flow between pores of different shapes and orientations. This squirt flow is responsible for velocity dispersion and attenuation. To tackle this issue, a simple model of squirt-flow relaxation in anisotropic media saturated with fluid is developed for two cases: the simple case for which cracks

are parallel and the case for which anisotropy results from the application of uniaxial stress on an initially isotropic medium. For liquid-saturated rocks in the limit of weak anisotropy, simple analytical expressions of elastic moduli and anisotropy parameters are presented. The anisotropy and attenuation patterns are significantly different in the two investigated cases. In particular, we show that the stress-induced anisotropy remains elliptical for all frequency ranges in saturated media, contrary to the anisotropy resulting from the presence of aligned cracks.

Finally, we use some of the results described above to derive a new methodology for estimating stress-induced azimuthal P-wave anisotropy from S-wave anisotropy measured in logs or vertical seismic profiles (VSP). The azimuthal P-wave anisotropy of the dry medium is first calculated from the measured S-wave anisotropy using results of the stress-induced anisotropy model developed for dry rocks. Then, analytical expressions linking the anisotropy parameters in the saturated and dry media are utilized in order to infer the azimuthal P-wave anisotropy parameter in the saturated medium as a function of its counterpart in the dry medium. This workflow is tested using log data acquired in the North West Shelf of Australia, where substantial azimuthal P-wave anisotropy has been inferred from seismic data using orthorhombic tomography. This anisotropy is likely caused by large differences between minimum and maximum horizontal stresses in the area. In the clean sandstone layers, for which the stress-induced anisotropy model is expected to be applicable, the results show a fairly good agreement with the azimuthal P-wave anisotropy estimated by the tomographic analysis. The methodology could be used to provide prior information to constrain an initial velocity model for anisotropic migration or azimuthal amplitude variations with offset (AVO) inversion.

To Lilo and Eliott

Acknowledgements

Firstly, I would like to thank sincerely my supervisor Boris Gurevich for his guidance and his support. It has been a great privilege to work with him and to benefit from his brilliant ideas. I am also grateful to my co-supervisors Marina Pervukhina, Mahyar Madadi and Andrej Bóna for their assistance and enthusiasm. I thank Maxim for his constant good mood and for his patience when teaching me in the lab.

I am grateful to Guy Duncan from BHP Billiton for providing us with results of the orthorhombic tomography performed on the dual-azimuth seismic survey shot in the North-West Shelf of Australia.

For this study, I was under the financial assistance of CGG. For this, I would like to acknowledge Salvador Rodriguez who recognized my potential and who dealt with all the administrative hurdles. I am also grateful to Jean-Paul Grufeille and Thomas Hertweck who took over Salvador and to Jon Downton for his technical advice and encouragements. Additionally, I wish to acknowledge the financial support of Curtin Reservoir Geophysics Consortium (CRGC) sponsors and Curtin University through the CIPRS scholarship.

I thank all present and past members of Curtin Department of Exploration Geophysics for making this work environment so pleasant. I thank Deirdre Hollingsworth and Robert Verstanding for their assistance with administrative and IT related issues.

I am deeply grateful to all the beautiful people I have met during these three years, without whom this PhD experience would not have been so enjoyable. My special thanks go to Sinem and Conny for all the laughs and for making me smile even when I was going through hard times; Eva and Elmar for their help upon my arrival and for fruitful discussions; Lisa and Estelle, my travel companions, for all the good memories we share together and Andrew for the climbing adventures.

Last but not least, I thank my family and friends back in France for supporting me and giving me so much positive energy despite the distance.

Contents

List of Figures

List of Tables

Abbreviations

AVO	**A**mplitude **V**ariation with **O**ffset
HTI	**T**ransversely **I**sotropic with a **H**orizontal symmetry axis
NMO	**N**ormal **M**ove-**O**ut
S$\parallel$	S-wave polarized in the plane parallel to the isotropy plane in HTI media; also known as SH-wave and pure shear wave
S$\perp$	S-wave polarized in the plane perpendicular to the isotropy plane in HTI media; also known as SV-wave and quasi-shear wave
TI	**T**ransversely **I**sotropic
VSP	**V**ertical **S**eismic **P**rofiling
VTI	**T**ransversely **I**sotropic with a **V**ertical symmetry axis
WIFF	**W**ave **I**nduced **F**luid **F**low

Symbols

A	area of the crack or fracture
B	compliance ratio
B_N	displacement discontinuity that is normal to the crack or fracture produced by a unit normal traction
B_T	displacement discontinuity that is parallel to the crack or fracture produced by a unit shear traction
$\boldsymbol{C}$	elastic stiffness tensor
C_{ijkl}	components of the elastic stiffness tensor
C_{ij}	components of the stiffness tensor in two-index (Voigt) notation
D'	see equation 5.17
D_0	see equation 5.83
D'_0	see equation 5.84
J_i	Bessel function of the first kind of order i
K	bulk modulus of the dry medium
K^*	generalized drained bulk modulus
K_f	fluid bulk modulus
K_f^*	modified fluid bulk modulus
K_g	grain (mineral) bulk modulus
L	P-wave modulus
P	confining pressure
P_c	characteristic crack closing pressure
Q	quality factor

$\boldsymbol{Q}$	matrix of quality factors in anisotropic media defined by Carcione [2001]
Q_{ij}	quality factors in anisotropic media defined by Carcione [2001]
S	total area of cracks with a given orientation
$\boldsymbol{S}$	compliance tensor
S_{ijkl}	components of the compliance tensor
S^0_{ijkl}	compliance tensor of the host rock in the unstressed (reference) state
V	representative volume of rock
Z_N	normal crack (or fracture) compliance
Z_{N0}	normal crack compliance in the unstressed (reference) state
Z_T	tangential crack (or fracture) compliance
Z_{T0}	tangential crack compliance in the unstressed (reference) state
a	crack aspect ratio
a_h	ratio of minimum horizontal stress to maximum horizontal stress
a_v	ratio of vertical stress to maximum horizontal stress
b	normalized stress $b = \sigma_{11}/P_c$
h	thickness of the disc-shaped crack
k	wavenumber of the fluid pressure diffusion wave
n_i	i^{th} component of the normal to the cracks or fracture
r	radius of the disc-shaped crack
s	specific area of cracks with a given orientation
s_0	specific area of cracks with a given orientation in the unstressed state
v_P	P-wave velocity
v_ψ	phase velocity
v_S	S-wave velocity
v_{SF}	fast S-wave velocity
v_{SS}	slow S-wave velocity
v_{ij}	velocity of an elastic wave propagating along the x_i-axis and polarized along the x_j-axis

Δ_N	normal weakness of cracks or fractures
Δ_T	tangential weakness of cracks or fractures
$\boldsymbol{\Delta S}$	excess compliance tensor due to the presence of cracks or fractures
ΔS_{ijkl}	components of the excess cracks compliance tensor
α	Biot-Willis effective stress coefficient
α_0	Biot-Willis effective stress coefficient of the hypothetical isotropic rock
α_i	analogues of Biot-Willis effective stress coefficient in anisotropic media
$\boldsymbol{\alpha}$	2^{nd}-rank crack compliance tensor
$\boldsymbol{\beta}$	4^{th}-rank crack compliance tensor
δ	Thomsen [1986] anisotropy parameter in HTI media
$\delta_{(i)}$	orthorhombic anisotropy parameters: Thomsen's δ in the $[x_2,x_3]$-, $[x_1,x_3]$- and $[x_1,x_2]$-planes of symmetry, when $i = 1, 2$ and 3, respectively
δ_{ij}	Kronecker delta; $\delta_{ij} = 1$ when $i = j$ and $\delta_{ij} = 0$ when $i \neq j$
δ_Q	attenuation anisotropy parameter defined by Zhu & Tsvankin [2006]
δ_{Qa}	alternative definition for the attenuation anisotropy parameter δ_Q
ϵ	Thomsen [1986] anisotropy parameter in HTI media
$\epsilon_{(i)}$	orthorhombic anisotropy parameters: Thomsen's ϵ in the $[x_2,x_3]$-, $[x_1,x_3]$- and $[x_1,x_2]$-planes of symmetry, when $i = 1, 2$ and 3, respectively
ϵ_Q	attenuation anisotropy parameter defined by Zhu & Tsvankin [2006]
ϵ_{Qa}	alternative definition for the attenuation anisotropy parameter ϵ_Q
η	anellipticity parameter
η_f	dynamic viscosity of the saturating fluid
θ	angle between the propagation direction and the symmetry axis
γ	Thomsen [1986] anisotropy parameter in HTI media
$\gamma_{(i)}$	orthorhombic anisotropy parameters: Thomsen's γ in the $[x_2,x_3]$-, $[x_1,x_3]$- and $[x_1,x_2]$-planes of symmetry, when $i = 1, 2$ and 3, respectively
γ_Q	attenuation anisotropy parameter defined by Zhu & Tsvankin [2006]
γ_{Qa}	alternative definition for the attenuation anisotropy parameter γ_Q
λ	first Lamé parameter

μ	shear modulus of the dry medium
μ_0	shear modulus of the dry medium in the unstressed (reference) state
ν	Poisson's ratio
ν_0	Poisson's ratio of the dry unstressed medium
ϕ	total porosity
ϕ_c	compliant porosity
ϕ_{c0}	compliant porosity in the unstressed (reference) state
ϕ_C	fracture porosity
ϕ_P	background porosity
ϕ_s	stiff porosity
χ	ratio λ/L
ρ	density
σ_{ij}	components of the stress tensor
σ_n	normal stress traction acting on the crack surface
ω	wave pulsation

Sub- and Superscripts

(r)	r^{th} crack or fracture
b	background rock
h	high-stress limit
mf	modified frame
sat, HF	saturated medium in the high-frequency limit
sat, LF	saturated medium in the low-frequency limit
uf	unrelaxed frame

Chapter 1

Introduction

1.1 Research background

It is a well-known fact that seismic anisotropy is omnipresent in geological formations, and as such, seismic anisotropy has been extensively investigated in the past decades [Helbig, 1994, MacBeth & Lynn, 2000, Rüger, 2001, Tsvankin, 2001]. In isotropic media, seismic wave velocities are independent on the propagation direction and thus such media can be characterized by a few parameters only, typically two for elastic isotropic media. By contrast, in anisotropic rocks, seismic waves propagate at different velocities in different directions. This velocity dependence upon propagation direction implies that knowledge of additional parameters is necessary to describe anisotropic media. Indeed, elastic anisotropic media are characterized by three to twenty-one independent parameters. Since the number of parameters available from field measurements is limited, anisotropy has long been seen as an unwanted complication. The isotropic assumption can however lead to erroneous estimates of rock properties even if the formation anisotropy is weak. In recent years, the development of new geophysical tools and seismic acquisition geometries facilitated the estimation of anisotropy. In order to better assist the interpretation of seismic data acquired for the purpose of detecting

hydrocarbons, more work still needs to be done so as to gain more insight on how anisotropy relates to reservoir characteristics.

Anisotropy may result from various causes. At the field-scale, anisotropy is generally due to large-scale layering, preferred orientation of large-scale fractures or differential stresses acting on the rock. Understanding the rock physics of fractured media and the effect of stress on elastic parameters is therefore of great interest. In addition, subsurface formations are usually saturated with fluid. Hence, studying the impact of fluid on anisotropy is also very important.

1.1.1 Stress-induced anisotropy

The anisotropy of tectonic stresses in the Earth's crust is one of the main causes of seismic anisotropy in sedimentary rocks. Stress causes variations of elastic properties of rocks, which are often attributed to the closure of compliant grain contacts or micro-cracks [Nur & Simmons, 1969, Shapiro, 2003]. Non-hydrostatic stress can cause elastic anisotropy depending on the orientation of these compliant discontinuities with respect to the stress field. Knowledge of the pattern of stress-induced anisotropy can be useful for distinguishing it from other causes of anisotropy, such as the presence of aligned fractures or intrinsic anisotropy due to fine layering or clay particles alignment. Such patterns can also be used to estimate, say, P-wave anisotropy from S-wave anisotropy estimated from S-wave splitting when the cause of anisotropy is known.

A number of authors analysed the stress-induced anisotropy by assuming the rock to contain angular distributions of idealized penny-shaped cracks [Nur, 1971, Sayers, 1988] and by inferring distributions of crack aspect ratios with various orientations when the rock was subjected to a given stress. However, these models, due to the idealized crack geometry, may not give an adequate quantitative description of grain contacts in rocks [Gurevich, Makarynska, & Pervukhina, 2009a]. As an alternative, Rasolofosaon [1998] and Prioul et al. [2004] applied the acousto-elasticity theory [Thurston, 1974], also known as non-linear elasticity or third-order elasticity theory, to describe the stress

dependency of elastic properties and anisotropy. Their works are limited to a stress range where stiffnesses are quasilinear with stress, which is usually suitable for downhole applications since most of the observed stress-induced anisotropy perturbations are often small [Lei et al., 2012]. These models can be calibrated using in-situ downhole measurements (e.g. Donald & Prioul [2015]) provided the in-situ stress state is known. Mavko et al. [1995] and Sayers [2002, 2005, 2006] estimated stress-induced velocity anisotropy from measurements without assuming any particular crack geometry. The model of Mavko et al. [1995] requires numerical calculations to obtain an insight into anisotropy patterns. Sayers [2002] directly inverted velocity measurements made while the rock was subjected to anisotropic stress. Being able to predict stress-induced anisotropy from quantities that are available from hydrostatic (isotropic) stress measurements would be an improvement since anisotropic and especially triaxial stress tests are not always easy to carry out.

Based on several assumptions, Gurevich et al. [2011] modelled the anisotropy caused by the application of a small uniaxial stress on a linearly isotropic elastic medium. They expressed the effective elastic properties of the stressed medium as a function of four physically meaningful parameters, which can be inferred from hydrostatic stress velocity measurements. Their main assumption is that a rock containing an initially isotropic distribution of cracks is subjected to a small uniaxial stress, which results in the closure of cracks perpendicular to the applied stress. This preferential closure of cracks causes a weak anisotropy of the crack orientation distribution and weak elastic anisotropy. The model predicts elliptical anisotropy, which is consistent with results previously obtained from Rasolofosaon [1998] and Prioul et al. [2004]. It also predicts the ratio of Thomsen [1986] anisotropy parameters ϵ/γ as a function of the compliance ratio B and Poisson's ratio of the unstressed rock. Madadi et al. [2013] extended the model of Gurevich et al. [2011] to larger stresses. Both works however assume that the rock is subjected to a uniaxial stress. Extending their approach to a more realistic stress state, where all three principal stresses are different, would thus be valuable.

1.1.2 Effect of crack infill on seismic anisotropy

One of the main issues in reservoir characterization is predicting seismic velocities in fluid-saturated rocks; this is called the fluid substitution problem. To date, most case studies dealing with fluid substitution assume an isotropic Earth model. Indeed, at seismic frequencies, the most commonly used approach for fluid substitution is based on the Gassmann [1951] equations derived for isotropic media. In the same paper, Gassmann [1951] also derived similar equations for anisotropic media. Using both of these solutions, several authors showed that applying the isotropic Gassmann fluid substitution in anisotropic media could lead to considerable errors in the prediction of seismic velocities [Mavko & Bandyopadhyay, 2009, Sava et al., 2000].

The anisotropic Gassmann fluid substitution is however difficult to apply due to the large number of unknown parameters it involves. In the field, logging and VSP tools usually measure the vertical P-wave and two S-wave velocities [MacBeth, 2002, Tang & Cheng, 2004], which is insufficient to recover the complete anisotropic elastic tensor. Besides, the anisotropic Gassmann fluid substitution is usually expressed in terms of stiffness [Gassmann, 1951] or compliance [Brown & Korringa, 1975] coefficients that do not provide an intuitive understanding of how fluid affects the anisotropy. Several authors tried to reduce the number of parameters by applying the anisotropic Gassmann theory to transversely isotropic (TI) media. Gurevich [2003] expressed the saturated stiffness coefficients of a saturated porous medium containing aligned fractures as a function of the porosity, the fluid and grain bulk moduli and four parameters describing the dry medium, i.e. two elastic constants characterizing the isotropic dry porous matrix and two fracture parameters. Similar results were obtained by Thomsen [1995] for the case of aligned penny-shaped fractures, and by Cardona [2002]. These approaches are restricted to the case in which anisotropy is caused by aligned fractures. Mavko & Bandyopadhyay [2009] gave an approximate fluid substitution for weakly anisotropic TI media but their study was limited to velocities of seismic waves propagating along the symmetry axis. To gain an insight on how fluid affects anisotropy, Thomsen [2012] derived expressions of anisotropy parameters in saturated media. His derivation is

based on Brown & Korringa [1975] formulas, which are written in terms of compliance coefficients. As a result, the expressions obtained for anisotropy parameters are complex and hard to solve. In the following, we show that using the original anisotropic Gassmann [1951] equations is more straightforward and yields simple approximations for anisotropy parameters in saturated media in the case for which anisotropy is weak.

At higher frequencies, elastic wave moduli are typically higher than the ones predicted by Gassmann [1951] theory. This velocity dispersion, i.e. the variation of propagation velocity with frequency, is attributed to the fluid flow induced by a passing wave. When an elastic wave propagates through a fluid-saturated medium, it creates pressure gradients within the fluid phase, resulting in fluid flow and corresponding internal friction until the pore pressure is equilibrated. Wave-induced fluid flow (WIFF) mechanisms can be categorized according to the length scale of the pressure gradients [Müller et al., 2010]. The fluid flow resulting from wavelength-scale pressure gradients is called global flow and is theoretically quantified by Biot [1956] theory of poroelasticity. When spatial variations of the pressure gradients occur on a scale larger than the pore size but smaller than the wave-length, the resulting flow is called mesoscopic flow. Mesoscopic flow is significant, especially in fractured media for which flow might occur between fractures and the porous background. In such a case, the frequency dependence of elastic moduli is mainly controlled by the size of the fractures [Maultzsch et al., 2003]. Several studies attempt to model this flow (e.g. Chapman [2003], Galvin & Gurevich [2015]). The third type of flow is the local flow, also known as squirt flow, which occurs at the pore scale between pores of different shape, size and orientation and thus different compliance. This flow is believed to be predominant at ultrasonic frequencies [Jones, 1986, Mavko & Nur, 1975], but may also play a role at seismic and sonic frequency ranges [Mavko et al., 2003, Müller et al., 2010]. Since squirt flow mechanism involves cracks and compliant pores, which are the same features involved in the modelling of stress-induced anisotropy, we mainly focus on this type of WIFF in this work.

Squirt flow has been modelled by several authors in isotropic media (e.g. O'Connell & Budiansky [1977], Mavko & Nur [1975], Endres & Knight [1997]). There are usually

two types of approaches for these models. The first one is based on the analysis of aspect ratio distributions [Mavko & Nur, 1979, Palmer & Traviolia, 1980]. The second one is based on the observation that the pore space has a binary structure [Gurevich et al., 2010, Mavko & Jizba, 1991, Shapiro, 2003]: stiff pores, which form most of the pore space and compliant pores, which are responsible for the pressure dependency of the elastic moduli [Chapman et al., 2002, Dvorkin et al., 1995, Murphy et al., 1986]. Anisotropic squirt flow models have been developed to a lesser extent. Mukerji & Mavko [1994] and Xu [1998] respectively extend the isotropic models of Mavko & Jizba [1991] and Endres & Knight [1997] to anisotropic media. Guéguen & Sarout [2011] also develop an anisotropic squirt flow model by considering the crack-to-crack flow in in two types of anisotropic media; the first one is made of aligned cracks embedded in an isotropic matrix and the second one consists of an isotropic medium permeated by vertical cracks with normals randomly oriented in the horizontal plane. These studies only provide the low- and high-frequency limits of saturated elastic moduli and as such, they only give some information on the velocity dispersion but not on the associated attenuation, which corresponds to the exponential decay of wave amplitude with distance. Gaining some insight on the attenuation occurring in anisotropic media is however essential as attenuation anisotropy might be more significant than velocity anisotropy [Arts et al., 1992, Tao & King, 1990].

1.2 Aim of the research

The overall objective of this project is to derive new rock physics models in order to gain a better understanding on seismic anisotropy. Ultimately, being able to adequately quantify and describe anisotropy can help improving seismic imaging and reservoir characterization. To achieve this goal, the research conducted in this project focuses on the topics listed below.

- The first issue addressed is the stress-induced anisotropy of dry rocks. While anisotropy resulting from the presence of aligned fractures has been an active

field of research in the past years, studies dealing with stress-induced anisotropy are still limited. However, in areas where differences between maximum and minimum horizontal stresses are large, significant azimuthal anisotropy can be observed despite the absence of fractures. To model the effect of in-situ stresses on elastic parameters, we extend the stress-induced anisotropy models derived by Gurevich et al. [2011] and Madadi et al. [2013] to a more realistic stress state where all three principal stresses are different. The resulting anisotropy pattern is further used to estimate P-wave anisotropy from S-wave anisotropy measured in log and VSP data.

- As subsurface formations are typically saturated with fluid, there is a need to take fluid effects into account. We thus rewrite the anisotropic Gassmann [1951] equations in terms of Thomsen [1986] anisotropy parameters. When the anisotropy is assumed to be weak, simple analytical expressions relating anisotropy parameters in the saturated medium to anisotropy parameters in the dry medium can be derived. Using these expressions, we compare the stress- and fracture-induced anisotropy patterns in saturated media.

- The use of the anisotropic Gassmann [1951] equations is based on the underlying assumption that fluid pressure is equilibrated throughout the pore space. This is usually a valid assumption for seismic frequencies. However, at higher frequencies, the pore pressure does not reach equilibrium and local fluid flow, known as squirt flow, may occur between pores of different shapes, sizes and orientations. We develop a new anisotropic squirt flow model, allowing for the study of velocity dispersion and attenuation in isotropic media permeated by aligned compliant pores or subjected to uniaxial stress.

1.3 Thesis layout

The thesis comprises seven chapters. For the benefit of the reader, the chapters contents are briefly described below.

Chapter 2. This chapter explains the basics of the theoretical concepts that will be used throughout the thesis. The chapter covers the following topics: introduction to anisotropy; description of the linear slip deformation theory, which is used to characterize effective elastic properties of cracked or fractured media; presentation of stress sensitivity models that form the basis for the new stress-induced anisotropy model developed in Chapter 3; revision of Gassmann [1951] equations and existing squirt flow models.

Chapter 3. In this chapter, a new rock physics model that accounts for the effect of triaxial stress on elastic properties of an initially dry isotropic medium is developed. The model is first derived for small stresses before being extended to larger stresses. The model predictions are tested against laboratory measurements made by Chaudhry [1995] on a dry sample of sandstone. Contents of this chapter have been published in Geophysics [Collet et al., 2014] and have been reproduced by permission of SEG.

Chapter 4. The aim of this chapter is to study the effect of fluid filling cracks and pores on anisotropy at low frequencies. Explicit expressions of anisotropy parameters in weakly anisotropic media saturated with a given fluid are derived using the anisotropic Gassmann equations. Weak anisotropy approximations of these expressions are used to investigate the anisotropy patterns arising from the presence of aligned fractures and the presence of anisotropic stress acting on a rock in saturated media. This chapter includes the article published by Collet & Gurevich [2013]. Due acknowledgement is made in the text.

Chapter 5. The main focus of this chapter is the study of attenuation and dispersion caused by squirt flow in anisotropic media. Analytical expressions for frequency-dependent elastic properties, anisotropy parameters and inverse quality factors are derived. A new definition for attenuation anisotropy parameters is also proposed. The anisotropic squirt flow model is derived for two anisotropy patterns: the anisotropy pattern resulting from the presence of aligned compliant pores and the stress-induced anisotropy pattern.

Chapter 6. In this chapter, a new methodology is developed to infer azimuthal P-wave anisotropy from S-wave anisotropy calculated from log or VSP data in areas where anisotropy is primarily stress-induced. This workflow utilizes the relationships between anisotropy parameters established in Chapter 3 and expressions of anisotropy parameters in saturated media derived in Chapter 4 to take fluid effects into account. The workflow is applied to data acquired in the North West Shelf of Australia, where seismic anisotropy is likely to be caused by the large difference between horizontal stresses observed in the area.

Chapter 7. In this conclusion chapter, main outcomes and limitations of the models and methodologies developed in this thesis are summarized. Based on the limitations of the models, recommendations for further research are given.

Chapter 2

Theoretical background

2.1 Chapter overview

This chapter explains the basics of various theoretical concepts that will be used throughout the thesis. There is no novelty in the theory presented in this chapter; it has been included to provide a consistent background for the new models and expressions derived in the following chapters. The chapter is organized as follows. First, we give a brief introduction on anisotropy, its causes, the various symmetry systems that exist and how to conveniently characterize it. Second, we describe the linear slip deformation theory, also referred as Sayers & Kachanov [1995] theory, which is used to characterize the effect of fractures or cracks on effective elastic properties of a medium. Then, we introduce the stress sensitivity models that form the basis of the stress-induced anisotropy model developed in the following chapter. Lastly, we give a reminder about Gassmann [1951] equations, which are typically used to account for fluid effects at low frequencies. Frequency dependence of elastic properties in saturated media, and the associated velocity dispersion and attenuation, are also reviewed at the end of the chapter.

2.2 Anisotropy

Anisotropy is defined as the directional dependence of a physical property, as opposed to isotropy, for which the physical property remains the same in all directions [Helbig, 1994]. Seismic anisotropy is omnipresent in subsurface formations [Babuska & Cara, 1991], which implies that seismic wave velocities depend on the direction of propagation. Seismic anisotropy can be due to various causes such as preferred orientation of minerals, layering, presence of aligned fractures or non-hydrostatic stresses acting on a rock [Thomsen, 2002]. Presence of anisotropy can have a distorting effect on seismic data processing, imaging and quantitative interpretation based on isotropic models (e.g. Tsvankin [2001]). On the other hand, it can also give useful information on reservoir properties, such as fracture orientation and density (e.g. Liu & Martinez [2013] and Tsvankin & Grechka [2011]) and orientation of the principal stresses (e.g. Crampin & Lovell [1991]). Being able to adequately characterize and quantify anisotropy is thus an important matter. In this section, we review the causes of anisotropy before describing the various symmetry systems that exist. Anisotropy parameters, which conveniently quantify the degree of anisotropy, are then introduced.

2.2.1 Causes

Seismic anisotropy occurs over a range of length scales and can result from a variety of causes. At the microscopic scale, anisotropy is usually caused by preferred orientation of crystals (lattice preferred orientation, LPO). At the hand-specimen scale, preferred alignment of microcracks and grain boundary contacts, small-scale layering and non-random distribution of mineral phases can create small heterogeneities leading to anisotropy. At the field-scale, anisotropy is generally due to large-scale layering, preferred orientation of large-scale fractures or non-hydtrostatic tectonic stresses [Hall et al., 2008]. Though anisotropy usually results from a certain combination of the above factors, understanding the anisotropic seismic signature that may arise from these factors separately is essential. In this work, we thus focus on stress-induced

anisotropy, i.e. the anisotropy which solely results from the application of a non-hydrostatic (or anisotropic) stress to an initially isotropic medium. We also compare it to the anisotropy caused by the presence of aligned fractures, sometimes referred as fracture-induced anisotropy in the following.

The effect of stress on seismic properties has been brought to evidence by several laboratory experiments (e.g. Nur & Simmons [1969]). When applying a uniaxial stress on isotropic samples, velocities of waves propagating parallel to the applied stress were observed to be higher than the ones of waves propagating perpendicular to the applied stress. This observation is often justified by the closure of grain contacts and microcracks perpendicular to the applied stress (e.g. Gurevich et al. [2011], Shapiro [2003]), which tends to increase the velocities of waves propagating in this direction. Crack opening parallel to the maximum stress direction might also contribute to decrease the velocities perpendicular to the applied stress [Lockner et al., 1977, Sayers, 2002]. Whether or not this crack opening is significant at small stresses is still matter of debate.

Fractures are very common structural features in the Earth's crust. They can be observed on outcrops, core samples or in image logs. Fractures mainly result from brittle failure due to the stress field and usually affect wave velocities. For instance, in media permeated by a set of aligned fractures, waves propagate slower in the direction perpendicular to the fractures. Seismic anisotropy in fractured media has been extensively studied in recent years (e.g. Hudson [1980], Bakulin et al. [2000], Hall & Kendall [2003], Kachanov et al. [2010], Prioul et al. [2007]) . Some of these modelling approaches are reviewed in Liu & Martinez [2013]. This urge to model fracture-induced anisotropy has been partly motivated by the fact that fractures have a profound impact on reservoir management. Indeed, they might provide important pathways for fluid flow in oil and gas reservoirs or on the contrary, act as flow barriers.

Throughout the thesis, we make the assumption of weak anisotropy, which is characterized by low values of anisotropy parameters (see Section 2.2.3). This assumption, often used for seismic data processing, is usually reasonable [Helbig & Thomsen, 2005].

Based on laboratory data, Wang [2002] studied the magnitude of intrinsic anisotropy in various types of sedimentary rocks. His main conclusions are that large intrinsic anisotropy can be encountered in shales, while very little intrinsic anisotropy exist in sands, sandstones and carbonates at reservoir conditions. One has to be careful with these results however, since laboratory samples might be more consolidated than many recent sediments, which might lead to higher values of anisotropy, especially for shales [Helbig & Thomsen, 2005]. The magnitude of extrinsic anisotropy caused by the presence of aligned fractures varies as a function of the fracture density: the higher the fracture density, the higher the anisotropy level. Based on shear-wave splitting observations in crustal rocks, Crampin [1994] showed that unfractured rocks whose anisotropy has been interpreted to be stress-induced, exhibit low degrees of anisotropy. Note that sedimentary rocks such as high-porosity and poorly consolidated sandstones are usually more stress-sensitive than crustal rocks. As such, the stress-induced anisotropy degree in sedimentary rocks might reach higher levels, depending on the anisotropy of the stress field and the type of rock.

2.2.2 Anisotropic symmetry systems

As mentioned earlier, anisotropy can result from different mechanisms : layering, fractures, differential stresses acting on a rock. Those mechanisms often render specific symmetries. For instance, layering is often horizontal, leading to a rotational symmetry around the vertical axis. Naturally occurring fractures can often be divided into sets based on their orientation as shown in Figure 2.1; planes of symmetry can be found depending on the fracture orientations and dips. An anisotropic stress field can be resolved in three orthogonal principal components. As a consequence, when the three principal stresses are different and applied on an isotropic medium, this medium exhibits three mutually orthogonal planes of symmetry. These particular symmetries allow considerable simplifications of the stiffness tensor C_{ijkl}, whose structure determines the velocity and polarization of plane waves for any propagation direction.

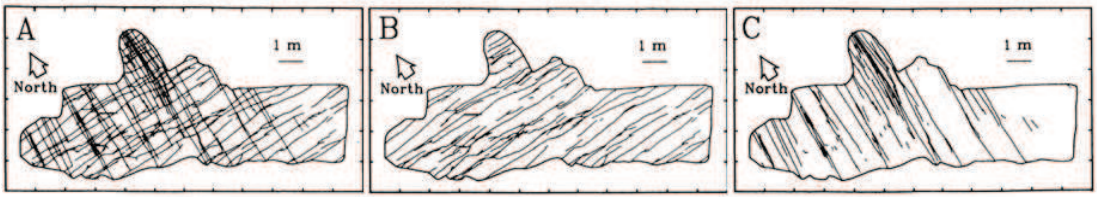

FIGURE 2.1: Maps of joint traces on bedding surface of Rico Formation, Monument upwarp, southeastern Utah. (a) Both sets of fractures. (b) East-west set. (c) North-south set. From Schoenberg & Sayers [1995].

In the elasticity theory, the stiffness tensor $\mathbf{C}$ relates the strain ϵ_{ij} and stress σ_{ij} tensors through the well-known Hooke's law:

$$\sigma_{ij} = C_{ijkl}\epsilon_{kl}. \tag{2.1}$$

Due to the symmetry of the strain and the stress tensors, it is possible to interchange indices i and j, k and l, so that

$$C_{ijkl} = C_{jikl} \text{ and } C_{ijkl} = C_{ijlk} \ . \tag{2.2}$$

Also, from thermodynamics considerations, indices i and k, j and l can be interchanged [Aki & Richards, 2002],

$$C_{ijkl} = C_{klij} \ . \tag{2.3}$$

As a result, the number of independent stiffness coefficients is reduced from $3^4 = 81$ to 21 coefficients. The stiffness tensor $\mathbf{C}$ can thus be represented in the form of a 6x6 matrix using Voigt notation: each pair of indices (ij and kl) is replaced by a single index: $11 \to 1$, $22 \to 2$, $33 \to 3$, $23 \to 4$, $13 \to 5$, $12 \to 6$. The transformation of the index pair ij into the corresponding index p is given by the following formula [Tsvankin, 2001]:

$$p = i\delta_{ij} + (9 - i - j)(1 - \delta_{ij)}, \tag{2.4}$$

where δ_{ij} is the Kronecker delta (see Nomenclature).

Symmetry class	Number of independent elastic constants	Examples
Triclinic	21	Dipping cracks in a horizontally layered medium
Monoclinic	11	Two sets of non-orthogonal fractures
Orthotropic	9	Isotropic medium subjected to triaxial stress Two orthogonal cracks sets
Transversely isotropic	5	Isotropic medium subjected to uniaxial stress One set of vertical or horizontal fractures Fine layering / Shale
Isotropic	2	Isotropic rock subjected to hydrostatic stress Random distribution of cracks

TABLE 2.1: Various anisotropy symmetry classes from the most general triclinic case to the highest symmetry system of isotropy.

Each anisotropic symmetry system is characterized by a particular structure of the stiffness matrix, with the number of independent elements decreasing from lower-symmetry to higher-symmetry systems. The most encountered symmetry classes, alongside with typical examples forming such symmetries, are listed in Table 2.1. In the following, we only describe the symmetries that we use in our study, starting from the simplest case of isotropy to orthotropic (or orthorhombic) symmetry. We refer to Tsvankin [2001] for a more thorough review of anisotropic symmetry systems. In the sections below, we use the right-handed orthonormal coordinate system (x_1,x_2,x_3), where x_3 is the vertical unit vector pointing downwards, as a reference system.

2.2.2.1 Isotropic media

In isotropic media, all directions of wave propagation are equivalent. Note that isotropic media permeated by randomly oriented and distributed fractures remain isotropic. Isotropic media subjected to hydrostatic stress, i.e. three orthogonal equal stresses, also remain isotropic. In isotropic media, only two independent parameters called Lamé's

constants and denoted as λ and μ are required to construct the stiffness matrix:

$$C^{(iso)} = \begin{bmatrix} \lambda+2\mu & \lambda & \lambda & 0 & 0 & 0 \\ \lambda & \lambda+2\mu & \lambda & 0 & 0 & 0 \\ \lambda & \lambda & \lambda+2\mu & 0 & 0 & 0 \\ 0 & 0 & 0 & \mu & 0 & 0 \\ 0 & 0 & 0 & 0 & \mu & 0 \\ 0 & 0 & 0 & 0 & 0 & \mu \end{bmatrix}. \tag{2.5}$$

The P- and S-waves velocities, v_P and v_S, can be expressed as a function of λ, μ and the rock density ρ:

$$v_P = \sqrt{\frac{\lambda+2\mu}{\rho}} \text{ and } v_S = \sqrt{\frac{\mu}{\rho}}\,. \tag{2.6}$$

Equation 2.5 expresses the stiffness matrix of an isotropic medium. Inverting this matrix yields the compliance matrix $S^{(iso)}$ of isotropic media :

$$S^{(iso)} = \begin{bmatrix} \frac{\lambda+\mu}{\mu(3\lambda+2\mu)} & -\frac{\lambda}{2\mu(3\lambda+2\mu)} & -\frac{\lambda}{2\mu(3\lambda+2\mu)} & 0 & 0 & 0 \\ -\frac{\lambda}{2\mu(3\lambda+2\mu)} & \frac{\lambda+\mu}{\mu(3\lambda+2\mu)} & -\frac{\lambda}{2\mu(3\lambda+2\mu)} & 0 & 0 & 0 \\ -\frac{\lambda}{2\mu(3\lambda+2\mu)} & -\frac{\lambda}{2\mu(3\lambda+2\mu)} & \frac{\lambda+\mu}{\mu(3\lambda+2\mu)} & 0 & 0 & 0 \\ 0 & 0 & 0 & \frac{1}{\mu} & 0 & 0 \\ 0 & 0 & 0 & 0 & \frac{1}{\mu} & 0 \\ 0 & 0 & 0 & 0 & 0 & \frac{1}{\mu} \end{bmatrix}. \tag{2.7}$$

2.2.2.2 Transversely isotropic media

Transversely isotropic (TI) media possess a single axis of rotational symmetry. Seismic signatures in TI media only depend on the angle between the propagation direction and the symmetry axis. Any plane containing the symmetry axis represents a plane of mirror symmetry, and any plane orthogonal to the symmetry axis is another plane of symmetry called isotropy plane as shown in Figure 2.2 [Rüger, 2001]. There are

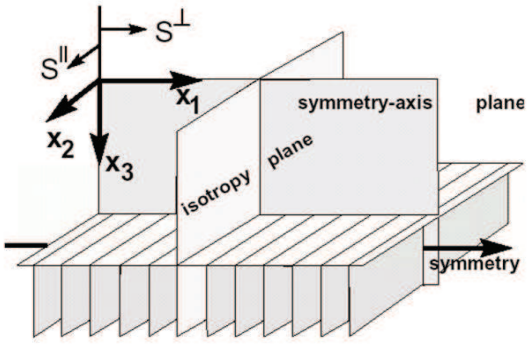

FIGURE 2.2: Example of a HTI medium created by a set of vertical fractures embedded in an isotropic background From Rüger [2001].

several types of TI media depending on the orientation of the symmetry axis: VTI, HTI and TTI media, which respectively refer to transversely isotropic media with a vertical, horizontal and tilted symmetry axis. All TI media are fully characterized by 5 independent stiffness coefficients. In the paragraphs below, we recall expressions of the stiffness matrix for VTI and HTI media only, as we do not deal with TTI media in this thesis.

VTI media: transversely isotropic media with a vertical symmetry axis - Seismic signatures of compressional waves in VTI media have been largely investigated in the past decades. This specific interest can be explained by the fact that most sedimentary basins and most sedimentary rocks were formed by deposition followed by compaction. As such, many formations exhibit a particular symmetry characterized by a vertical symmetry axis. In particular, the VTI assumption provides a good approximation for modelling shales (e.g. Sayers [1994]) and finely layered, horizontally stratified media (e.g. Backus [1962]). In VTI media, the symmetry axis is along the

x_3-axis, and the stiffness matrix is written as

$$C^{(\mathrm{vti})} = \begin{bmatrix} C_{11} & C_{11}-2C_{66} & C_{13} & 0 & 0 & 0 \\ C_{11}-2C_{66} & C_{11} & C_{13} & 0 & 0 & 0 \\ C_{13} & C_{13} & C_{33} & 0 & 0 & 0 \\ 0 & 0 & 0 & C_{55} & 0 & 0 \\ 0 & 0 & 0 & 0 & C_{55} & 0 \\ 0 & 0 & 0 & 0 & 0 & C_{66} \end{bmatrix}. \tag{2.8}$$

Diagonal components of the stiffness matrix are related to the P- and S-wave velocities propagating and polarized along the coordinate axis. Components C_{11} and C_{33} are respectively proportional to the squared velocities of P-waves propagating horizontally and vertically. The velocity of the wave propagating vertically and polarized horizontally (or vice versa) is given by C_{55}, while the wave polarized along the x_1-axis and propagating along the x_2-axis (or vice versa) is given by C_{66}.

HTI media: transversely isotropic media with a horizontal symmetry axis - The HTI symmetry is the most simple first-order model to describe azimuthal anisotropy. HTI symmetry can result from the presence of vertical aligned fractures embedded in an isotropic background or from the application of a uniaxial stress on an initially isotropic medium. In HTI media, the symmetry axis coincides with the x_1-axis (or x_2-axis) and the stiffness matrix has the following form (when the symmetry axis is along x_1):

$$C^{(\mathrm{hti})} = \begin{bmatrix} C_{11} & C_{13} & C_{13} & 0 & 0 & 0 \\ C_{13} & C_{33} & C_{33}-2C_{44} & 0 & 0 & 0 \\ C_{13} & C_{33}-2C_{44} & C_{33} & 0 & 0 & 0 \\ 0 & 0 & 0 & C_{44} & 0 & 0 \\ 0 & 0 & 0 & 0 & C_{55} & 0 \\ 0 & 0 & 0 & 0 & 0 & C_{55} \end{bmatrix}. \tag{2.9}$$

In TI media, velocities of waves propagating in any direction can be expressed as a function of the five independent stiffness coefficients and the angle between the propagation direction and the symmetry axis. In HTI media, the angle dependence of wave velocities is given by (see Tsvankin [2001]):

$$V_P(\theta) = \sqrt{\frac{C_{33}\sin^2\theta + C_{11}\cos^2\theta + C_{55} + \sqrt{D(\theta)}}{2\rho}}, \tag{2.10}$$

$$V_{S\perp}(\theta) = \sqrt{\frac{C_{33}\sin^2\theta + C_{11}\cos^2\theta + C_{55} - \sqrt{D(\theta)}}{2\rho}}, \tag{2.11}$$

$$V_{S\parallel}(\theta) = \sqrt{\frac{C_{44}\sin^2\theta + C_{55}\cos^2\theta}{2\rho}}, \tag{2.12}$$

where

$$D(\theta) = \Big((C_{33} - C_{55})\sin^2\theta - (C_{11} - C_{55})\cos^2\theta\Big)^2 + (C_{13} + C_{55})^2\sin^2 2\theta. \tag{2.13}$$

In equations 2.10 to 2.12, V_P, $V_{S\perp}$ and $V_{S\parallel}$ respectively correspond to the P-wave velocity, the velocity of the S-wave polarized in the plane perpendicular to the isotropy plane and the velocity of the S-wave polarized parallel to the isotropy plane, as shown in Figure 2.2. The S$\parallel$-wave is sometimes referred to as pure-shear wave or SH-wave, while the S$\perp$-wave is also known as quasi-shear wave or SV-wave.

2.2.2.3 Orthorhombic media

Orthorhombic (or orthotropic[1]) anisotropy is often regarded as the simplest realistic symmetry for many geophysical problems [Bakulin et al., 2000]. Orthorhombic media are characterized by three mutually orthogonal planes of symmetry, which reduces the number of independent stiffness coefficients to 9 when choosing the coordinate system associated with the three symmetry planes. The most common orthorhombic media are formations containing one set of vertical fractures embedded in a VTI background. For

[1]Orthotropic is the most appropriate term to use since it refers to the material symmetry, while orthorhombic refers to the crystal symmetry. In the rest of the thesis, we however kept the orthorhombic terminology because it is still the most commonly used term in seismics and rock physics.

instance, a horizontally layered shale containing vertical fractures may be considered as orthorhombic. Orthorhombic media may also be due to two or three sets of mutually orthogonal fractures or two sets of identical fractures [Winterstein, 1990] though such a configuration is seldom encountered in practice. In this work, we mainly focus on orthorhombic media resulting from the application of triaxial stress on initially isotropic media. For orthorhombic media having planes of symmetry corresponding to the $[x_1,x_2]$-, $[x_1,x_3]$- and $[x_2,x_3]$-planes, the stiffness matrix has the form

$$C^{(\mathrm{ort})} = \begin{bmatrix} C_{11} & C_{12} & C_{13} & 0 & 0 & 0 \\ C_{12} & C_{22} & C_{23} & 0 & 0 & 0 \\ C_{13} & C_{23} & C_{33} & 0 & 0 & 0 \\ 0 & 0 & 0 & C_{44} & 0 & 0 \\ 0 & 0 & 0 & 0 & C_{55} & 0 \\ 0 & 0 & 0 & 0 & 0 & C_{66} \end{bmatrix}. \tag{2.14}$$

Again, diagonal components are linked to the squared velocities of P- and S-waves propagating along the coordinate axis.

2.2.3 Anisotropy parameters

As shown in the previous section, specific anisotropy symmetries lead to considerable simplifications of the stiffness tensor. However, the stiffness coefficients do not give a clear insight on the magnitude of anisotropy and how anisotropy affects velocity propagation. To tackle this issue, Thomsen [1986] came up with a convenient parametrization for TI media, in which the medium can be described by two reference velocities and three dimensionless parameters quantifying the degree of anisotropy. An analog parametrization was further defined by Tsvankin [1997] for orthorhombic media.

2.2.3.1 Initial definition for transversely isotropic media

Thomsen [1986] introduced a convenient parametrization for TI media: he suggested that the five elastic coefficients necessary to describe TI media could be replaced by two reference velocities (usually taken as the P- and S-wave velocities along the symmetry axis) and three dimensionless parameters, the so-called anisotropy parameters. He initially defined these parameters for VTI media, i.e. assuming the symmetry axis was along the x_3-direction. However, in the rest of the thesis, we mainly deal with HTI media, so we express these anisotropy parameters assuming that the symmetry axis is along the x_1-direction, which yields:

$$\epsilon = \frac{C_{33} - C_{11}}{2C_{11}}, \tag{2.15}$$

$$\gamma = \frac{C_{44} - C_{55}}{2C_{55}}, \tag{2.16}$$

$$\delta = \frac{(C_{13} + C_{55})^2 - (C_{11} - C_{55})^2}{2C_{11}(C_{11} - C_{55})}. \tag{2.17}$$

The parameters ϵ and γ are sometimes simplistically called the P- and S-wave anisotropies since expressions 2.15 and 2.16 are respectively close to the fractional difference between the horizontal and vertical P- and S$\|$-wave velocities. The parameter δ, which combines the P- and S$\perp$-wave velocities, determines the second derivative of the P-wave velocity with respect to the incidence angle in the vicinity of the symmetry axis. In many subsurface formations, the anisotropy is weak, i.e. $\epsilon, \delta, \gamma \ll 1$, and δ reduces to

$$\delta = \frac{C_{13} + 2C_{55} - C_{11}}{C_{11}}. \tag{2.18}$$

Another useful parameter is the anellipticity parameter introduced by Alkhalifah & Tsvankin [1995], which quantifies the deviation of the P-wave phase velocity surface from an ellipsoid:

$$\eta = \frac{\epsilon - \delta}{1 + 2\epsilon}. \tag{2.19}$$

In case of small anisotropy, expression 2.19 reduces to

$$\eta = \epsilon - \delta. \tag{2.20}$$

When $\epsilon = \delta$ (i.e. $\eta = 0$), the medium is elliptically anisotropic, which means that the P-wavefronts emanating from a point source are elliptical [Helbig, 1983]. This case is of particular interest since several authors [Gurevich et al., 2011, Rasolofosaon, 1998, Sun & Prioul, 2010] showed that anisotropy arising from the application of a small uniaxial stress to an isotropic elastic medium is always elliptical.

2.2.3.2 Equivalent definition for orthorhombic media

Tsvankin [1997] extended Thomsen [1986] notation to more complicated, but also more realistic, orthorhombic models. He defined two reference velocities: the vertical P-wave velocity and the velocity of the vertically traveling S-wave polarized in the x_1-direction. The seven other parameters required to characterize the medium correspond to Thomsen's parameters defined in the three planes of symmetry of the orthorhombic medium:

$$\begin{aligned}
\epsilon_{(1)} &= \frac{C_{22} - C_{33}}{2C_{33}}, \gamma_{(1)} = \frac{C_{66} - C_{55}}{2C_{55}}, \delta_{(1)} = \frac{(C_{23} + C_{44})^2 - (C_{33} - C_{44})^2}{2C_{33}(C_{33} - C_{44})}, \\
\epsilon_{(2)} &= \frac{C_{11} - C_{33}}{2C_{33}}, \gamma_{(2)} = \frac{C_{66} - C_{44}}{2C_{44}}, \delta_{(2)} = \frac{(C_{13} + C_{55})^2 - (C_{33} - C_{55})^2}{2C_{33}(C_{33} - C_{55})}, \\
\delta_{(3)} &= \frac{(C_{12} + C_{66})^2 - (C_{11} - C_{66})^2}{2C_{11}(C_{11} - C_{66})},
\end{aligned} \tag{2.21}$$

with subscripts (1), (2) and (3) respectively referring to anisotropy parameters in the $[x_2, x_3]$, $[x_1, x_3]$ and $[x_1, x_2]$ planes of symmetry. Assuming that the anisotropy is weak, $\delta_{(i)}$ can be written as

$$\delta_{(1)} = \frac{C_{23} + 2C_{44} - C_{33}}{C_{33}}, \ \delta_{(2)} = \frac{C_{13} + 2C_{55} - C_{33}}{C_{33}}, \ \delta_{(3)} = \frac{C_{12} + 2C_{66} - C_{11}}{C_{11}}. \tag{2.22}$$

For the analysis of azimuthal anisotropy, it is convenient to introduce two new parameters:

$$\epsilon_{(3)} = \frac{C_{22} - C_{11}}{2C_{11}}, \gamma_{(3)} = \frac{C_{44} - C_{55}}{2C_{55}}. \tag{2.23}$$

2.3 Effective elastic properties of cracked media

Fractures and cracks are present at various scales in rocks and usually impact seismic wave propagation. In particular, they may have a specific orientation, which might lead to seismic anisotropy. In the following, we use the word "crack" to describe small-scale features such as compliant grain boundaries or microcracks while the word "fractures" refers to larger-scale features, which may form aligned patterns. The effective elastic properties of materials containing traction-free cracks (i.e. using cracks as surfaces of displacement discontinuity) have been analysed since the 1960s. Bristow [1960] derived the effective constants for randomly oriented cracks in the non-interaction approximation and introduced the crack-density parameter. In rock mechanics, similar results were obtained through different means by Walsh [1965a,b,c] with an extension to frictionally sliding cracks. Later, Kachanov [1980] and Schoenberg [1980] generalized the problem by using the respectively so-called excess-compliance or linear-slip approaches, which are conceptually the same, to calculate the effective compliance of fractured and cracked media. These approaches will be mostly referred as "linear slip deformation theory" or "Sayers & Kachanov [1995] theory" in the rest of the thesis.

The linear slip deformation theory assumes that fractures and cracks can be modelled as imperfectly bonded interfaces where traction is continuous across the interfaces but displacement might be discontinuous [Schoenberg, 1980] (see Figure 2.3). The i-th component of this displacement discontinuity can be expressed as

$$[u_i] = B_{ij} t_j, \tag{2.24}$$

where t_j is the j-th component of the traction vector and B_{ij} is the fracture compliance matrix [Kachanov, 1992]. There are no particular assumptions on the crack geometry:

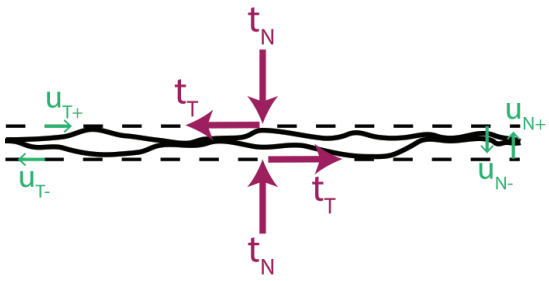

FIGURE 2.3: Model of fractures used in the linear slip deformation theory. Parameters t_N and t_T denote the normal and tangential tractions applied across the interfaces of the fracture. Quantities u_{N+} and u_{T+} are the normal and tangential displacements of the upper interface while u_{N-} and u_{T-} are those of the lower interface.

cracks may be in partial contact along their area and may have arbitrary in-plane shapes. When they are assumed to be rotationally symmetrical around their normal, equation 2.24 can be rewritten as

$$[u_N] = B_N t_N, \tag{2.25}$$

$$[u_T] = B_T t_T, \tag{2.26}$$

where $[u_N] = u_{N+} - u_{N-}$ and $[u_T] = u_{T+} - u_{T-}$ are respectively the normal and tangential displacement discontinuities across the fracture or crack; u_{N+} and u_{T+} are the normal and tangential average displacements of the upper interface while u_{N-} and u_{T-} are the corresponding displacements of the lower interface. The parameters B_N and B_T are the normal and tangential fracture compliances, expressed in m/Pa. Quantities t_N and t_T denote the normal and shear tractions applied on the fracture or crack, as depicted in Figure 2.3. If fractures or cracks are filled with fluid or minerals, they are more resistant to compression, which leads to a lower value of the normal compliance B_N. Note that if the fracture or crack is composed of rough asperities in contact and is not a traction-free crack, the formalism is essentially the same, but the magnitude of the displacement discontinuities will depend on the contact characteristics [Kachanov et al., 2010].

When neglecting interactions and pressure communication between cracks or fractures

(i.e. for moderate crack densities), Sayers & Kachanov [1995] showed that the effective compliance tensor of a cracked solid S_{ijkl} can be written as the sum of the matrix compliance tensor S^b_{ijkl} and an excess compliance tensor due to cracks ΔS_{ijkl}:

$$S_{ijkl} = S^b_{ijkl} + \Delta S_{ijkl}, \tag{2.27}$$

with

$$\Delta S_{ijkl} = \bar{\alpha}_{ijkl} + \beta_{ijkl}, \tag{2.28}$$

and

$$\bar{\alpha}_{ijkl} = \frac{\delta_{ik}\alpha_{jl} + \delta_{il}\alpha_{jk} + \delta_{jk}\alpha_{il} + \delta_{jl}\alpha_{ik}}{4}. \tag{2.29}$$

In equations 2.28 and 2.29, α_{ij} and β_{ijkl} are second- and fourth-rank crack compliance tensors, which quantify the effect of the orientation distribution and the normal and shear compliances of the discontinuities on the elastic properties of the rock. They are defined by

$$\alpha_{ij} = \frac{1}{V}\sum_r B_T^{(r)} n_i^{(r)} n_j^{(r)} A^{(r)}, \tag{2.30}$$

and

$$\beta_{ijkl} = \frac{1}{V}\sum_r (B_N^{(r)} - B_T^{(r)}) n_i^{(r)} n_j^{(r)} n_k^{(r)} n_l^{(r)} A^{(r)}, \tag{2.31}$$

where $B_N^{(r)}$ and $B_T^{(r)}$ are the normal and shear compliances of the r-th crack in an elementary representative volume V, $n_i^{(r)}$ is the i-th component of the normal to the crack, and $A^{(r)}$ is the area of the crack, as shown in Figure 2.4. The parameter $B_N^{(r)}$ characterizes the normal displacement jump across the crack produced by a unit normal traction, while $B_T^{(r)}$ characterizes the shear displacement jump produced by a unit shear traction, as expressed by equations 2.25 and 2.26. We can note from equations 2.29 to 2.31 that elements of $\bar{\alpha}_{ijkl}$ and β_{ijkl} remain the same after any permutation of their indices; for instance $\beta_{ijkl} = \beta_{jikl} = \beta_{lkij}$ ...

Special case of aligned fractures or cracks - The anisotropy pattern resulting from the presence of aligned fractures embedded in an isotropic background will be

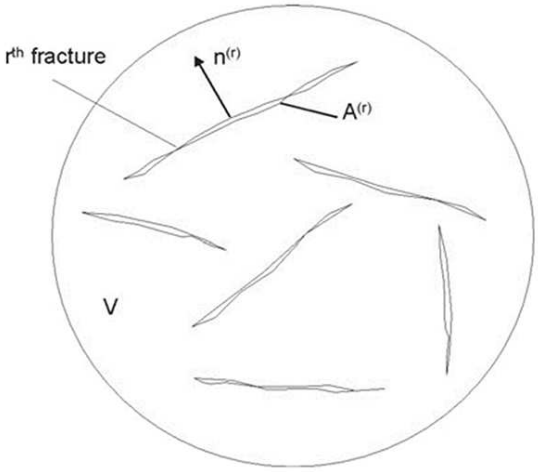

FIGURE 2.4: Elementary representative volume of rock containing several fractures. $n^{(r)}$ and $A^{(r)}$ are respectively the normal and the area of the r^{th} fracture. From Sayers [2009].

studied in Chapters 4 and 5. Below, we recall the main expressions that will be used later on. For a single set of identical cracks with normals along the x_1-axis (vertical cracks), the excess compliance due to cracks is expressed as [Schoenberg & Douma, 1988]

$$\Delta S_{ij} = \begin{bmatrix} Z_N & 0 & 0 & 0 & 0 & 0 \\ 0 & 0 & 0 & 0 & 0 & 0 \\ 0 & 0 & 0 & 0 & 0 & 0 \\ 0 & 0 & 0 & 0 & 0 & 0 \\ 0 & 0 & 0 & 0 & Z_T & 0 \\ 0 & 0 & 0 & 0 & 0 & Z_T \end{bmatrix} \tag{2.32}$$

where $Z_N = sB_N$ and $Z_T = sB_T$, expressed in MPa^{-1} are the effective normal and tangential crack (or fracture) compliances. The specific area of cracks s corresponds to the total area of cracks divided by the volume of rock: $s = NA/V$, N being the number of cracks of area A in the representative volume V. The effective stiffness of

the medium for the particular case of aligned cracks or fractures is given by

$$C = \begin{bmatrix} L_b(1-\Delta_N) & \lambda_b(1-\Delta_N) & \lambda_b(1-\Delta_N) & 0 & 0 & 0 \\ \lambda_b(1-\Delta_N) & L_b(1-\chi_b^2\Delta_N) & \lambda_b(1-\chi_b\Delta_N) & 0 & 0 & 0 \\ \lambda_b(1-\Delta_N) & \lambda_b(1-\chi_b\Delta_N) & L_b(1-\chi_b^2\Delta_N) & 0 & 0 & 0 \\ 0 & 0 & 0 & \mu_b & 0 & 0 \\ 0 & 0 & 0 & 0 & \mu_b(1-\Delta_T) & 0 \\ 0 & 0 & 0 & 0 & 0 & \mu_b(1-\Delta_T) \end{bmatrix}, \tag{2.33}$$

where L_b and μ_b are respectively the P- and S-wave moduli of the background matrix, and the parameter χ_b is written as $\chi_b = \lambda_b/L_b$. Parameters Δ_N and Δ_T, which follow the inequality $0 \leq \Delta_N, \Delta_T < 1$, are two dimensionless parameters called normal and tangential crack weaknesses [Bakulin et al., 2000, Schoenberg & Helbig, 1997]. They are expressed as

$$\Delta_N = \frac{Z_N L_b}{1 + Z_N L_b}, \tag{2.34}$$

$$\Delta_T = \frac{Z_T \mu_b}{1 + Z_T \mu_b}. \tag{2.35}$$

Fracture weakness parameters describe how fractures and cracks weaken the background rock; the higher Δ_N and Δ_T, the more weakened the rock is. In turn, normal and tangential compliances Z_N and Z_T can be written as a function of normal and tangential weaknesses:

$$Z_N = \frac{\Delta_N}{L_b(1-\Delta_N)}, \tag{2.36}$$

$$Z_T = \frac{\Delta_T}{\mu_b(1-\Delta_T)}, \tag{2.37}$$

As indicated in equation 2.33, isotropic media permeated by a set of aligned fractures or cracks are fully described by four parameters: two parameters describing the background rock, L_b and μ_b, and two parameters characterizing the fractures, Δ_N and Δ_T. This noteworthy feature implies that there is a relationship linking the five elastic coefficients usually required to characterize TI media. In terms of anisotropy parameters,

this relationship yields the following expression [Gurevich, 2003]:

$$\delta = 2(1-\nu_b)\epsilon - 2\frac{1-2\nu_b}{1-\nu_b}\gamma, \tag{2.38}$$

where ν_b is the Poisson's ratio of the background rock: $\nu_b = \lambda_b/2(\lambda_b + \mu_b)$. Besides, anisotropy parameters ϵ and γ can be expressed as a function of crack weaknesses (e.g. Gurevich [2003])

$$\epsilon = \frac{2\mu_b(\lambda_b+\mu_b)\Delta_N}{L_b^2(1-\Delta_N)}, \tag{2.39}$$

$$\gamma = \frac{\Delta_T}{2(1-\Delta_T)}, \tag{2.40}$$

or cracks compliances

$$\epsilon = \frac{2\mu_b(\lambda_b+\mu_b)}{\lambda_b+2\mu_b}Z_N, \tag{2.41}$$

$$\gamma = \frac{\mu_b}{2}Z_T. \tag{2.42}$$

From equation 2.40, it is easy to show that the tangential weakness Δ_T of the cracks can be directly inferred from measurements of shear-wave anisotropy.

2.4 Stress sensitivity of elastic properties

Elastic properties in rocks vary as a function of stress. The stress dependency of elastic properties is often attributed to the closure of compliant parts of the pore space, such as grain boundary contacts or microcracks [Nur, 1971, Nur & Simmons, 1969, Shapiro, 2003, Walsh, 1965b,c]. In the following, we always assume the initial unstressed medium is dry, elastic and isotropic, which implies that compliant grain contacts and microcracks are randomly oriented and distributed. When a hydrostatic stress is applied on such a medium, the medium becomes stiffer but remains isotropic. When a uniaxial stress is applied, cracks tend to close preferentially in the direction of the applied stress, which leads to elastic anisotropy characterized by a TI symmetry (see Section 2.2.2.2).

2.4.1 Isotropic rocks subjected to hydrostatic stress

Several authors [Eberhart-Phillips et al., 1989, Zimmerman et al., 1986] showed empirically that the compressional and shear velocity dependence on stress in many dry rocks can be well approximated by the relationship

$$v(P) = A_1 + A_2 P - A_3 \exp(-A_4 D), \tag{2.43}$$

where v and P are respectively the velocity and confining pressure and A_1, A_2, A_3, A_4 are fitting parameters for a given set of measurements. Shapiro [2003] derived a theoretical model based on the dual porosity-concept to account for this dependency of elastic moduli upon pressure. More precisely, he showed that if the total porosity ϕ of an isotropic rock can be divided into a stiff porosity part ϕ_s and a compliant part ϕ_c, as illustrated in Figure 2.5, then the elastic moduli of the rock can be expressed as

$$\frac{1}{K(P)} = \frac{1}{K_h}\Big(1 + \theta_s \Delta\phi_s(P) + \theta_c \phi_c(P)\Big), \tag{2.44}$$

$$\frac{1}{\mu(P)} = \frac{1}{\mu_h}\Big(1 + \theta_{s\mu} \Delta\phi_s(P) + \theta_\mu \phi_c(P)\Big), \tag{2.45}$$

where K and μ are respectively the bulk and shear moduli of the dry rock for a given confining pressure P; K_h and μ_h correspond to the bulk and shear moduli in the high

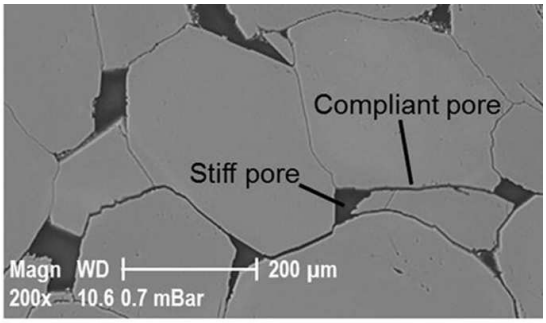

FIGURE 2.5: Scanning electron microscope (SEM) image of Lochaline sandstone illustrating the dual-porosity concept assumed by Shapiro [2003]. Compliant porosity is made of thin pores such as microcracks or grain contacts while stiff porosity mainly consists of pores with higher aspect ratios, which will be less affected by the application of stress.

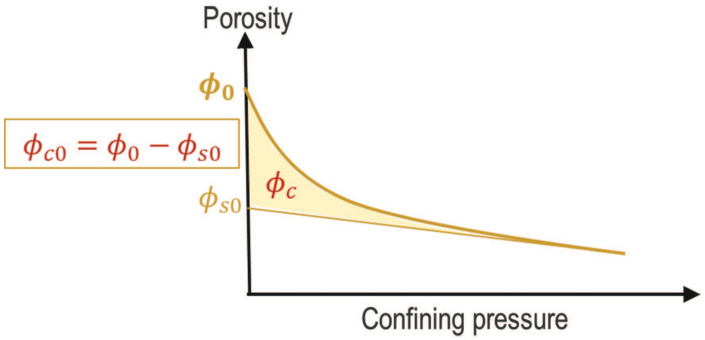

FIGURE 2.6: Cartoon illustrating the dependence of stiff (ϕ_s) and compliant (ϕ_c) porosities upon pressure.

stress limit, for which all compliant pores are assumed to be closed. Quantities θ_c and θ_μ are bulk and shear stress sensitivity parameters relative to compression of the compliant porosity, while θ_s and $\theta_{s\mu}$ are corresponding parameters due to weak compression of stiff porosity. The term $\Delta\phi_s(P) = \phi_s(P) - \phi_{s0}$ is the deviation of the stiff porosity from its zero-pressure value ϕ_{s0}. The stiff porosity $\phi_s(P)$ is a linear function of pressure. The dependence of the compliant porosity $\phi_c(P)$ upon pressure is given by

$$\phi_c(P) = \phi_{c0} \exp\Big(- \frac{\theta_c P}{K_h} \Big), \tag{2.46}$$

where ϕ_{c0} is the compliant porosity in the initial unstressed state. Stress dependency of stiff and compliant porosities are illustrated in Figure 2.6. Note that the ratio $P_c = K_h/\theta_c$ corresponds to the exponential decay constant characterizing the decrease of compliant porosity caused by the closure of compliant grain contacts and microcracks. In the following, we call this characteristic pressure the characteristic crack closing pressure.

As shown in Figure 2.7, elastic moduli are typically strongly affected by changes of the compliant porosity and weakly by those of the stiff porosity. Mathematically, this can be written as: $\theta_s \Delta\phi_s \ll \theta_c \phi_c$ and $\theta_{s\mu} \Delta\phi_s \ll \theta_{s\mu} \phi_c$, so equations 2.44 and 2.45 reduce

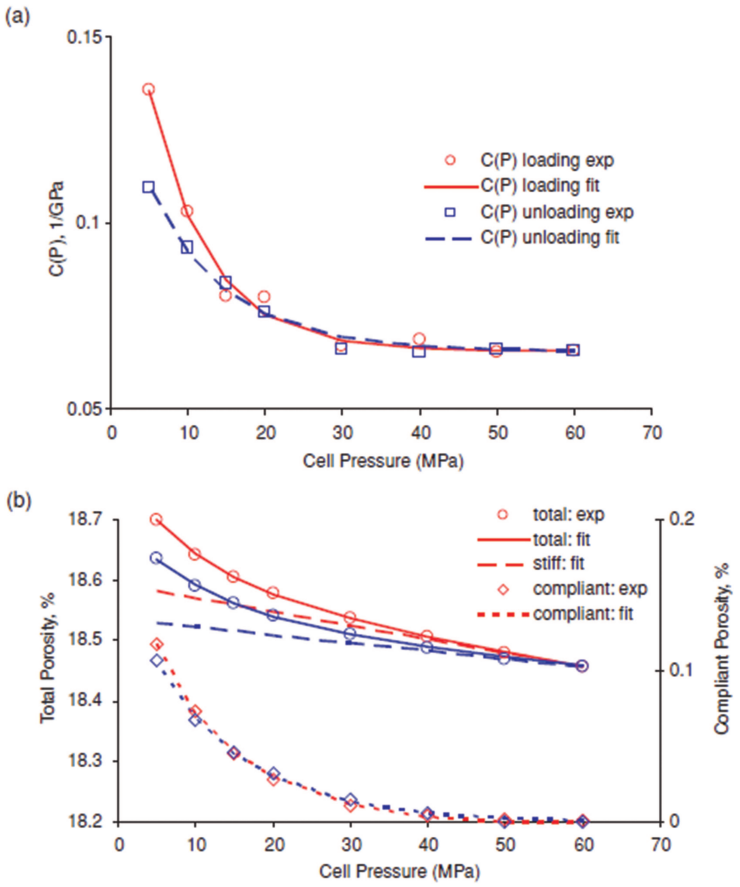

FIGURE 2.7: Experimental measurements and fitting of the stress dependency of the (a) compressibility $C(P) = 1/K(P)$ and (b) porosity of a dry sandstone. (a) Red and blue symbols and curves respectively correspond to measurements and their corresponding fitting using Shapiro [2003] model for the loading and unloading cycles. (b) Solid, dashed and dotted lines show the fit for the total porosity, stiff and compliant porosity, respectively. From Pervukhina et al. [2010].

to:

$$\frac{1}{K(P)} = \frac{1}{K_h}\Big(1 + \theta_c \phi_c(P)\Big), \tag{2.47}$$

$$\frac{1}{\mu(P)} = \frac{1}{\mu_h}\Big(1 + \theta_\mu \phi_c(P)\Big). \tag{2.48}$$

Equations 2.47 and 2.48 are useful to approximate the stress dependency of elastic moduli at low pressures. Assuming that all cracks are identical and characterized by their normal and tangential compliances Z_N and Z_T, Gurevich, Makarynska, &

Pervukhina [2009a] showed that the stress sensitivities θ_c and θ_μ can be linked to crack parameters by the relationships

$$Z_N = \frac{\theta_c}{K_h}\phi_{c0}\exp\Big(-\frac{\theta_c P}{K_h}\Big), \tag{2.49}$$

$$Z_T = \Big(\frac{5}{2}\frac{\theta_\mu}{\mu_h} - \frac{2}{3}\frac{\theta_c}{K_h}\Big)\frac{\theta_c}{K_h}\phi_{c0}\exp\Big(-\frac{\theta_c P}{K_h}\Big). \tag{2.50}$$

The stress dependency of dry elastic isotropic media can thus be described by five physically meaningful parameters, which are

- the bulk and shear moduli K_0 and μ_0 of the unstressed medium,
- the characteristic crack closing pressure P_c,
- the tangential compliance Z_{T0} of cracks in the unstressed state,
- the crack compliance ratio $B = Z_{N0}/Z_{T0}$.

2.4.2 Isotropic rocks subjected to a small uniaxial stress

When a uniaxial compressive stress is applied to a dry elastic isotropic medium with a random distribution and orientation of cracks, cracks with normals parallel (or nearly parallel) to the applied stress are believed to close preferentially. As a result, the medium takes on a transversely isotropic symmetry. Based on the linear slip deformation theory and the non-interactive approximation of Sayers & Kachanov [1995] (Section 2.3), Gurevich et al. [2011] modelled the effect of this preferential closure of cracks on elastic properties and anisotropy of dry elastic media.

Their model is in essence similar to the one derived by Shapiro [2003], which accounts for the effect of hydrostatic stress on elastic properties of isotropic media. The initial unstressed medium is assumed to be the same as the one described in the previous section (Section 2.4.1). It can thus be described by the five parameters listed above, i.e. the bulk and shear moduli K_0 and μ_0 of the unstressed medium, the characteristic crack closing pressure P_c, the tangential compliance Z_{T0} of cracks in the unstressed state

and the crack compliance ratio B. Note that those parameters do not depend on the applied stress. As a consequence, they remain the same whether an isotropic stress or a non-hydrostatic stress is applied, provided they are applied to the same initial medium. In other words, the five parameters that control the relationship between P- and S-wave anisotropies in a hydrostatic stress experiment also control pressure dependencies of P- and S-wave velocities in a uniaxial stress experiment. The only difference is that cracks close equally in all directions under hydrostatic stress, whereas they close preferentially perpendicular to the applied stress when a uniaxial stress is applied. The number of cracks along a particular plane is assumed to decrease exponentially as a function of the normal stress applied on this given plane. Gurevich et al. [2011] further assume that the applied uniaxial stress is small compared to the characteristic crack closing pressure P_c, which allows for the linearization of the exponential decrease of the specific area of cracks along the plane perpendicular to the applied stress. Once the dependence of the specific area of cracks upon pressure is known, one can use Sayers & Kachanov [1995] theory (equations 2.27 to 2.31) to calculate the effective elastic properties of the stressed medium. Gurevich et al. [2011] found that the effective compliance matrix of the dry stressed medium S_{ij} can be written as

$$S_{ij}(b) = S^h_{ij} + (\alpha^{is}_{ij} + b\alpha^{an}_{ij})Z_{T0} + (\beta^{is}_{ij} + b\beta^{an}_{ij})(Z_{N0} - Z_{T0}), \tag{2.51}$$

where S^h_{ij} is the compliance matrix in the high stress limit when all compliant pores are closed. Parameters Z_{N0} and Z_{T0} respectively denote the normal and tangential compliances of the initial cracks. The normalized stress magnitude b is given by $b = \sigma_{11}/P_c$, P_c being the characteristic crack closing pressure. Tensors α^{is} and β^{is} describe the contribution of the initial isotropic distribution of cracks, while tensors α^{an} and β^{an} are relative to cracks closing due to application of anisotropic stress. They are

expressed as

$$\alpha^{is} = \begin{bmatrix} \frac{1}{3} & 0 & 0 & 0 & 0 & 0 \\ 0 & \frac{1}{3} & 0 & 0 & 0 & 0 \\ 0 & 0 & \frac{1}{3} & 0 & 0 & 0 \\ 0 & 0 & 0 & \frac{2}{3} & 0 & 0 \\ 0 & 0 & 0 & 0 & \frac{2}{3} & 0 \\ 0 & 0 & 0 & 0 & 0 & \frac{2}{3} \end{bmatrix}, \beta^{is} = \begin{bmatrix} \frac{1}{5} & \frac{1}{15} & \frac{1}{15} & 0 & 0 & 0 \\ \frac{1}{15} & \frac{1}{5} & \frac{1}{15} & 0 & 0 & 0 \\ \frac{1}{15} & \frac{1}{15} & \frac{1}{5} & 0 & 0 & 0 \\ 0 & 0 & 0 & \frac{4}{15} & 0 & 0 \\ 0 & 0 & 0 & 0 & \frac{4}{15} & 0 \\ 0 & 0 & 0 & 0 & 0 & \frac{4}{15} \end{bmatrix}, \tag{2.52}$$

and

$$\alpha^{an} = \begin{bmatrix} \frac{1}{5} & 0 & 0 & 0 & 0 & 0 \\ 0 & \frac{1}{15} & 0 & 0 & 0 & 0 \\ 0 & 0 & \frac{1}{15} & 0 & 0 & 0 \\ 0 & 0 & 0 & \frac{2}{15} & 0 & 0 \\ 0 & 0 & 0 & 0 & \frac{4}{15} & 0 \\ 0 & 0 & 0 & 0 & 0 & \frac{4}{15} \end{bmatrix}, \beta^{an} = \begin{bmatrix} \frac{1}{7} & \frac{1}{35} & \frac{1}{35} & 0 & 0 & 0 \\ \frac{1}{35} & \frac{1}{35} & \frac{1}{105} & 0 & 0 & 0 \\ \frac{1}{35} & \frac{1}{105} & \frac{1}{35} & 0 & 0 & 0 \\ 0 & 0 & 0 & \frac{4}{105} & 0 & 0 \\ 0 & 0 & 0 & 0 & \frac{4}{35} & 0 \\ 0 & 0 & 0 & 0 & 0 & \frac{4}{35} \end{bmatrix}. \tag{2.53}$$

To test the validity of their model, Gurevich et al. [2011] compared predictions of their model to measurements made by Nur & Simmons [1969] on a dry sample of Barre Granite. Since Nur & Simmons [1969] only provide P- and S-wave velocities measured under uniaxial stress, Gurevich et al. [2011] used the velocities measured by Coyner [1984] under hydrostatic stress on another sample of Barre Granite to extract the five model parameters K_0, μ_0, P_c, Z_{T0} and B. Measured (green squares) and fitted velocities (solid green lines) using Shapiro [2003] stress sensitivity model (equations 2.47 and 2.48) are plotted in Figure 2.8a. Figure 2.8a also shows velocities measured along the direction of applied stress (blue dots) and perpendicular to the applied stress (black triangles). As expected, P- and S-waves propagate faster along the direction of applied stress since cracks are closing perpendicular to the applied stress.

To get a more intuitive knowledge of how anisotropy of stress affects anisotropy of the

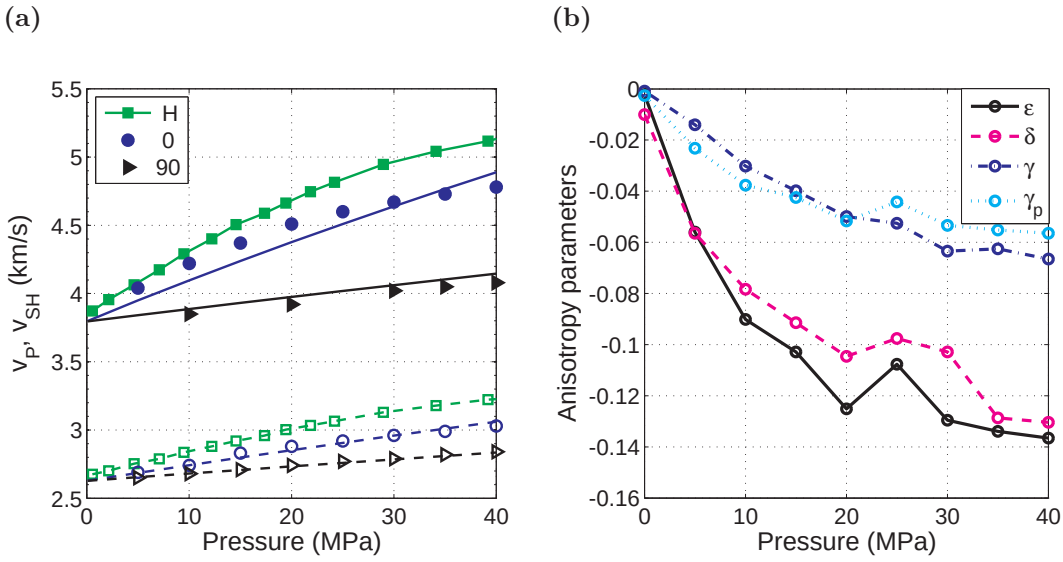

FIGURE 2.8: Comparison of (a) velocities and (b) anisotropy parameters measured by Nur & Simmons [1969] and predicted by the stress-induced model developed for dry isotropic rocks subjected to a small uniaxial stress. Reproduced after Gurevich et al. [2011].

medium, Gurevich et al. [2011] express their results in terms of anisotropy parameters defined by equations 2.15 to 2.16 for TI media:

$$\epsilon = \delta = \frac{2}{105}\frac{(6+2\nu_0)Z_{N0} + (1-2\nu_0)Z_{T0}}{1-\nu_0}\mu_0 b, \tag{2.54}$$

$$\gamma = \frac{1}{105}(4Z_{N0} + 3Z_{T0})\mu_0 b. \tag{2.55}$$

As shown by equation 2.54, the model predicts elliptical anisotropy (i.e. $\epsilon = \delta$) regardless of the value of the compliance ratio B. This ellipticity characteristic of the stress-induced anisotropy is particularly interesting since it provides a way of discriminating stress-induced anisotropy from other causes such as the anisotropy caused by aligned fractures and the intrinsic anisotropy of shales. This result was previously obtained by Rasolofosaon [1998] and Prioul et al. [2004] using the third-order elasticity theory. The model also establishes a relationship between the ratio ϵ/γ and the compliance ratio $B = Z_{N0}/Z_{T0}$ and Poisson's ratio ν_0 of the unstressed rock:

$$\frac{\epsilon}{\gamma} = 2\frac{2\nu_0 B + 6B - 2\nu_0 + 1}{(1-\nu_0)(3+4B)}. \tag{2.56}$$

Those results are consistent with anisotropy parameters ϵ and δ calculated from velocities measured by Nur & Simmons [1969] on the Barre Granite sample. As shown in Figure 2.8b, the parameter γ calculated from measured velocities is also consistent with the anisotropy parameter γ_p calculated from equation 2.56. The relationships linking anisotropy parameters ϵ, δ and γ are interesting in the sense that only three parameters are required to describe the TI medium, provided the compliance ratio B and the Poisson's ratio ν_0 of the unstressed medium are known.

This model is further extended to large uniaxial stress by Madadi et al. [2013] and to triaxial stress in Chapter 3.

2.4.3 Extension to larger uniaxial stress

The model derived by Gurevich et al. [2011] is based on a linear relationship between elastic constants and stress. There is however experimental evidence that elastic constants are non-linear functions of stress (e.g. Scott Jr & Abousleiman [2005]) and linear relationships can only be used to approximate elastic constants for small stress increments. By using a Taylor series expansion instead of linearizing the exponential decrease of the specific area of cracks in a given direction, Madadi et al. [2013] investigated the stress-induced anisotropy of elastic isotropic rocks at larger stresses. One of the main motivations behind this study was to check whether the elliptical result obtained by Gurevich et al. [2011] and the expression of the ϵ/γ ratio were still valid at larger stresses.

The main result of their study is that the stress-induced anisotropy engendered by the application of a uniaxial stress on an elastic isotropic medium can be described by the five independent parameters introduced in Section 2.4.1, which describe the stress dependency of elastic isotropic rocks subjected to isotropic stress. Besides, they showed that in most cases, the ratio ϵ/δ varies between 0.8 and 1.1, which suggests that the stress-induced anisotropy remains close to elliptical. As for the ratio ϵ/γ, they found

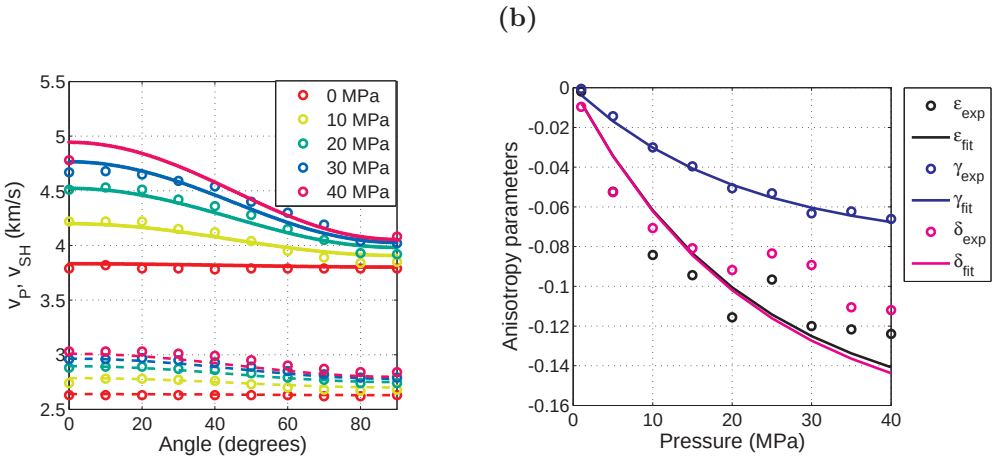

FIGURE 2.9: Comparison of (a) velocities and (b) anisotropy parameters measured by Nur & Simmons [1969] and predicted by the stress-induced model developed for dry isotropic rocks subjected to a large uniaxial stress. Reproduced after Madadi et al. [2013].

out that it still can expressed as a function of the Poisson's ratio of the unstressed rock ν_0 and compliance ratio B but it varies mildly as a function of stress.

The applicability of their model was tested against velocities measured by Nur & Simmons [1969] on the same sample of Barre Granite to test the validity of Gurevich et al. [2011] model. Results are plotted in Figure 2.9.

Note that this model is based on the same assumptions as the one derived by Gurevich et al. [2011]. One of those crucial assumptions is that the model only takes into account the closure of cracks occurring perpendicular to the applied stress and does not handle the opening of cracks that might occur parallel to the applied stress. This effect might be more significant at higher stresses for which cracks might nucleate and propagate along the direction of the applied stress.

2.5 Effective elastic properties of saturated media

Most subsurface formations are saturated with fluid, i.e. pores, cracks and fractures are usually filled by brine, gas and/or oil. The presence of fluid has an effect on

the overall elastic properties of the rock. In the low-frequency limit, for which fluid pressure is supposed to be equilibrated throughout the pore space, the effect of fluid on elastic properties is usually accounted for using Gassmann [1951] equations. At high frequencies however, pore pressure is no longer equilibrated and wave-induced fluid flow might take place.

2.5.1 Effective elastic properties of saturated media at low frequencies

In the low frequency limit, fluid pressure has enough time to equilibrate throughout the pore space. In this case, the effect of fluid mainly consists in a stiffening of the pore space, which leads to an increase of fluid-saturated P-wave moduli compared to dry P-wave moduli. Static models based on theories developed by Gassmann [1951] and Brown & Korringa [1975] can be used to calculate the fluid-saturated elastic constants. In the following, we provide a revision of Gassmann [1951] equations as they are employed in Chapters 4, 5 and 6. In his landmark paper, Gassmann [1951] derived formulas for both isotropic media and anisotropic media.

2.5.1.1 Isotropic Gassmann equations

The most commonly used approach to perform fluid substitution at low frequencies is based on Gassmann [1951] equations derived for fully saturated isotropic media. These equations relate the bulk and shear moduli of a rock to its pore, frame and fluid properties. In fact, Gassmann [1951] showed that the static bulk modulus of an isotropic fluid-saturated porous rock K^{sat} can be expressed as the sum of the bulk modulus K of the dry rock and an additional term responsible for the stiffening effect of the fluid:

$$K^{sat} = K + \alpha^2 M. \tag{2.57}$$

In equation 2.57, α is the Biot-Willis effective stress coefficient, which can be written as

$$\alpha = 1 - K/K_g, \tag{2.58}$$

and M is Gassmann's pore space modulus expressed as

$$M = \frac{K_g}{\left(1 - \frac{K}{K_g}\right) - \phi\left(1 - \frac{K_g}{K_f}\right)}, \tag{2.59}$$

where K_f and K_g are respectively the fluid and grain bulk moduli and ϕ is the porosity. The shear modulus is not affected by the presence of fluid, yielding

$$\mu^{sat} = \mu. \tag{2.60}$$

Gassmann's theory is based on several assumptions as listed below.

- First, the solid grain material is assumed to be homogeneous and isotropic. This assumption might be violated when the rock is composed of multiple minerals with large contrasts in elastic stiffness [Berge, 1998], or anisotropic minerals [Brown & Korringa, 1975]. To overcome this limitation, Brown & Korringa [1975] derived expressions for the compliance tensor in the cases of mixed mineralogy and anisotropic minerals; however, these equations found limited use in practice due to the large number of parameters they require to characterize the rock. A common approach is to use Gassmann [1951] equations with an average modulus for K_g [Knackstedt et al., 2005, Smith et al., 2003], which is usually possible when the bulk moduli of the minerals making up the rock are of the same order of magnitude [Makarynska et al., 2007].

- Second, Gassmann [1951] assumes that all pores are connected and the frequency is sufficiently low so that pore pressure equilibrates throughout the pore space. The assumption regarding pore connectivity might fail at very low porosities. As for the frequency assumption, it may or may not be valid at seismic and well-log frequencies depending on the rock permeability, fluid viscosity and characteristic fracture dimension [Gurevich, Brajanovski, et al., 2009, Maultzsch et al., 2003].

- Finally, Gassmann [1951] assumes that the rock is completely saturated with one fluid. The easiest way to extend Gassmann's theory to partially saturated rocks

at seismic frequencies is to assume an effective fluid modulus that is an isostress average of the moduli of the liquid and gaseous phases:

$$\frac{1}{K_f} = \frac{S_{liq}}{K_{liq}} + \frac{1 - S_{liq}}{K_{gas}}, \tag{2.61}$$

where S_{liq} is the liquid saturation and K_{liq} and K_{gas} are respectively the bulk moduli of the liquid and gas phases. However, this approximation might not be considered optimal, as, when frequencies are not low enough, problems related to patchy saturation might arise (see Section 2.5.2).

2.5.1.2 Anisotropic Gassmann equations

In the same paper, Gassmann [1951] also presented generalizations of equations 2.57 to 2.60 for anisotropic porous media with arbitrary symmetry. The assumptions listed above are maintained; in particular, the grain material is assumed to be isotropic on a microscopic scale. This implies that anisotropy results from preferred alignment of microcracks and grain boundary contacts, small-scale fractures and layering rather than preferred orientation of crystals (lattice preferred orientation, LPO). In this case, Gassmann [1951] expressed the stiffness tensor of the anisotropic saturated rock C^{sat}_{ijkl} as the sum of the dry stiffness tensor C_{ijkl} and a stiffening term due to the action of fluid:

$$C^{sat}_{ijkl} = C_{ijkl} + \frac{\Big(K_g\delta_{ij} - C_{ijaa}/3\Big)\Big(K_g\delta_{kl} - C_{bbkl}/3\Big)}{(K_g/K_f)\phi(K_g - K_f) + \Big(K_g - C_{ccdd}\Big)}. \tag{2.62}$$

In equation 2.62, Einstein summation convention is used and δ_{ij} is the Kronecker delta defined by $\delta_{ij} = 1$ for $i = j$ and $\delta_{ij} = 0$ for $i \neq j$. Using Voigt notation (see Section 2.2.2), tensors C^{sat}_{ijkl} and C_{ijkl} can be rewritten in terms of 6x6 matrices. Besides, if we consider an orthorhombic medium with three orthogonal planes of symmetry oriented perpendicular to the coordinate axes, the anisotropic Gassmann equations (equation 2.62) can be expressed in a similar form as the isotropic Gassmann equations (equations 2.57 and 2.60):

$$C_{ij}^{sat} = C_{ij} + \alpha_i \alpha_j M, \tag{2.63}$$

where

$$\alpha_i = 1 - \frac{\sum_{j=1}^{3} C_{ij}}{3K_g} \text{ for } i = 1, 2, 3 \text{ and } \alpha_4 = \alpha_5 = \alpha_6 = 0, \tag{2.64}$$

and M is the analogue of Gassmann's pore space modulus defined as

$$M = \frac{K_g}{\left(1 - \frac{K^*}{K_g}\right) - \phi\left(1 - \frac{K_g}{K_f}\right)}. \tag{2.65}$$

In Equation 2.65, K^* denotes the so-called generalized drained bulk modulus, which is written as

$$K^* = \frac{1}{9} \sum_{i=1}^{3} \sum_{j=1}^{3} C_{ij}. \tag{2.66}$$

In Chapter 4 we rewrite the anisotropic Gassmann [1951] in terms of anisotropy parameters for weakly anisotropic media exhibiting TI and orthorhombic symmetry. The main purpose of this exercise is to gain a more intuitive knowledge on how fluid affects seismic anisotropy and anisotropy patterns such as stress-induced anisotropy or the anisotropy caused by aligned fractures.

2.5.2 Frequency dependence of elastic properties in saturated media

At higher frequencies, pressure is not fully equilibrated throughout the pore space. When an elastic wave propagates through a fluid-saturated medium, it generates pressure gradients within the fluid phase, resulting in fluid flow accompanied with internal friction until the pore pressure reaches equilibrium. This phenomenon causes frequency-dependent dispersion and attenuation, whose study requires dynamic models. Several models investigating the effect of wave-induced fluid flow (WIFF) on elastic properties of saturated media are available depending on the type of flow. WIFF mechanisms can be categorized according to the length scale of the pressure gradients. The flow

resulting from wavelength-scale pressure gradients is called global or macroscopic flow. The effects of global flow on attenuation and dispersion are quantified by Biot [1956] theory of poroeslaticity.

When the length scale of pressure gradients is smaller than the wavelength, but larger than the pore size, the flow is called mesoscopic. Mesoscopic flow due to patchy saturation and fractured reservoirs has received significant attention as it is believed to be a major cause of attenuation and dispersion in a broad range of frequencies, and especially in the seismic exploration band [Müller et al., 2010]. Patchy saturation occurs when two immiscible fluids with significantly different bulk moduli form pockets (or patches) in the pore space. When the frequency exceeds a certain threshold, which is controlled by the size, shape and spatial distribution of the fluid pockets, the fluid pressure differs from one patch to the other. Mesoscopic flow resulting from patchy saturation has been modelled by e.g. White [1975], Dutta & Odé [1979], Johnson [2001] and Müller & Gurevich [2004]. In this thesis, we assume that rocks are fully saturated with one fluid and thus we do not take into account any patchy saturation effect. Mesoscopic flow is also common in fractured reservoirs in which the pressure might not be equilibrated between fractures and stiff porosity. In such a case, the frequency dependence of elastic moduli is mainly controlled by the size of the fractures [Maultzsch et al., 2003]. This case was modelled by e.g. Chapman [2003], Brajanovski et al. [2005], Galvin & Gurevich [2009].

At the microscopic scale, different compliances between adjacent pores due to their difference in shape, size and orientation can result in fluid flow between these pores. This wave-induced fluid flow, called local flow or squirt flow, is believed to be predominant at ultrasonic frequencies [Jones, 1986, Mavko & Nur, 1975], but it might also play a role at seismic and sonic frequencies [Mavko et al., 2003, Müller et al., 2010]. Squirt flow has been modelled by several authors in isotropic media (e.g. O'Connell & Budiansky [1977], Mavko & Nur [1975], Endres & Knight [1997]). As mentioned in the introduction, there are usually two types of approaches for these models. The first one is based on the analysis of aspect ratio distributions (e.g. Mavko & Nur [1979], Palmer

& Traviolia [1980]). The second approach (e.g. Gurevich et al. [2010], Mavko & Jizba [1991], Shapiro [2003]), that we employ, is based on the dual porosity system described in Section 2.4.1. Anisotropic squirt flow has been investigated to a lesser extent and most models derived so far (e.g. Guéguen & Sarout [2011], Mukerji & Mavko [1994], Xu [1998]) only provide low- and high-frequency limits of elastic moduli. Hence, the main purpose of Chapter 5 is to derive an anisotropic squirt flow model that takes into account the frequency-dependence of elastic moduli, allowing for the computation of attenuation anisotropy along with velocity anisotropy. The model presented in Chapter 5 is essentially an extension of Gurevich et al. [2010] isotropic squirt flow model, which is described in the following subsection. Next, we recall results from Mukerji & Mavko [1994], as they are compared the low- and high-frequency limits of the model derived in Chapter 5.

2.5.2.1 Isotropic squirt flow model from Gurevich et al. [2010]

The isotropic squirt flow model developed by Gurevich et al. [2010] combines the pressure relaxation approach from Murphy et al. [1986] and the linear slip deformation theory from Sayers & Kachanov [1995] described in Section 2.3. The pore space is assumed to have the same binary structure as the one introduced in Section 2.4.1 when explaining Shapiro [2003] stress sensitivity model. The pore space is thus made of stiff pores with porosity ϕ_s and compliant pores with porosity ϕ_c, which form a fully interconnected pore space with porosity ϕ. The dry frame is assumed to be homogeneous, isotropic and made up of a single isotropic grain mineral with bulk modulus K_g. The frame is characterized by bulk and shear moduli K and μ, respectively. The rock is further assumed to be fully saturated by one fluid with bulk modulus K_f and dynamic viscosity η_f.

Low-frequency (relaxed) moduli - In the low-frequency limit, there is enough time for pore pressure to equilibrate throughout the pore space. In this case, the bulk

and shear moduli of the fluid-saturated medium are given by the isotropic Gassmann [1951] equations (equations 2.57 to 2.60).

High-frequency (unrelaxed) moduli - In the high-frequency limit, the fluid pressure does not have enough time to equilibrate between stiff pores and adjacent compliant pores. Compliant pores are effectively isolated from the stiff pores, and become stiffer with respect to normal but not tangential deformation. To model this effect, Mavko & Jizba [1991] introduced the so-called unrelaxed frame in which compliant pores are filled with fluid, while stiff pores are empty. Gurevich, Makarynska, & Pervukhina [2009b] showed that the bulk and shear moduli, K_{uf} and μ_{uf}, of this unrelaxed frame are given by

$$\frac{1}{K_{uf}} = \frac{1}{K_h} + \frac{1}{\dfrac{1}{\dfrac{1}{K} - \dfrac{1}{K_h}} + \dfrac{1}{\left(\dfrac{1}{K_f} - \dfrac{1}{K_g}\right)\phi_c}}, \tag{2.67}$$

$$\frac{1}{\mu_{uf}} = \frac{1}{\mu} - \frac{4}{15}\left(\frac{1}{K} - \frac{1}{K_{uf}}\right), \tag{2.68}$$

where K_h is the bulk modulus of the dry frame in the high-stress limit, i.e. when all compliant pores are closed. When the saturating fluid is liquid, the term $[K^{-1} - K_h^{-1}]^{-1}$ in equation 2.67 is negligible compared with the term $\phi_c[K_f^{-1} - K_h^{-1}]^{-1}$, considering that $K_f \ll K_g$ in general. As a result, equation 2.67 yields

$$\frac{1}{K_{uf}} = \frac{1}{K_h} + \left(\frac{1}{K_f} - \frac{1}{K_g}\right)\phi_c, \tag{2.69}$$

which corresponds to the bulk modulus of the unrelaxed frame obtained by Mavko & Jizba [1991]. This formula however leads to unrealistically high values of the unrelaxed frame bulk modulus when the fluid is saturated with gas, i.e. when the fluid bulk modulus is very low. By contrast, when the saturating fluid is a gas, equation 2.67 yields $K_{uf} = K$.

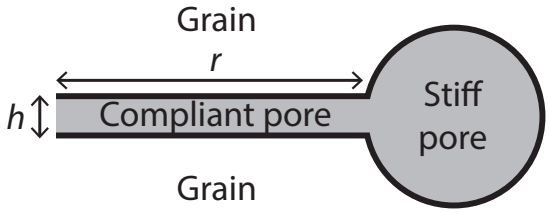

FIGURE 2.10: Sketcth of the pore geometry configuration assumed by Murphy et al. [1986]. The compliant pore, characterized by radius r and thickness h, forms a disc-shaped gap and its edge opens into a toroidal stiff pore.

The high-frequency moduli of the fully saturated rock are then given by replacing the dry (relaxed) bulk and shear moduli, K and μ, by the unrelaxed frame moduli, K^{uf} and μ^{uf}, into the isotropic Gassmann equations (equations 2.57 to 2.60).

Frequency-dependent (partially relaxed) moduli - To determine the frequency-dependent saturated moduli, Gurevich et al. [2010] first considered the so-called modified frame, which is similar to the unrelaxed frame in the sense that compliant pores are filled with fluid but stiff pores are empty. In this modified frame however, there is a fluid pressure relaxation occurring in the area of grain contact. This pressure relaxation is conditioned by the pore geometry, and thus the pore configuration has to be defined. In their study, Gurevich et al. [2010] assumed that the compliant pore geometry is the same as the one described by Murphy et al. [1986]: compliant pores are disc-shaped gaps with radius r, thickness h and aspect ratio $a = h/2r$ and their edges open into toroidal stiff pores, as depicted in Figure 2.10.

By calculating the additional effective stiffness of the gap due to the presence of fluid, Gurevich et al. [2010] showed that the gap stiffness is the same as the one in the unrelaxed frame, but with a modified fluid bulk modulus K_f^* written as

$$K_f^*(\omega) = \left[1 - \frac{2J_1(kr)}{krJ_0(kr)}\right] K_f, \tag{2.70}$$

where $\omega = 2\pi f$ is the pulsation of the passing wave with frequency f and J_i denotes Bessel function of the first kind. The parameter k is the wavenumber of the pressure

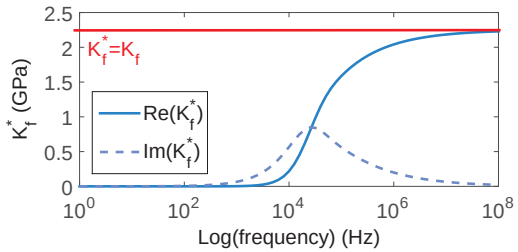

FIGURE 2.11: Frequency dependence of the modified fluid bulk modulus K_f^*. In the low- and high-frequency limits, K_f^* is real and tends to 0 and K_f, respectively.

diffusion expressed as

$$k^2 = -12\frac{i\omega\eta_f}{h^2 K_f} = -\frac{3i\omega\eta_f}{a^2 r^2 K_f}. \tag{2.71}$$

The frequency-dependent bulk and shear moduli $K_{mf}(\omega)$ and $\mu_{mf}(\omega)$ of the modified frame are thus given by

$$\frac{1}{K_{mf}(\omega)} = \frac{1}{K_h} + \frac{1}{\dfrac{1}{\dfrac{1}{K} - \dfrac{1}{K_h}} + \dfrac{1}{\left(\dfrac{1}{K_f^*(\omega)} - \dfrac{1}{K_g}\right)\phi_c}}, \tag{2.72}$$

$$\frac{1}{\mu_{mf}(\omega)} = \frac{1}{\mu} - \frac{4}{15}\left(\frac{1}{K} - \frac{1}{K_{uf}}\right). \tag{2.73}$$

Note that, as illustrated in Figure 2.11, the modified fluid bulk modulus K_f^* tends to 0 and K_f in the low- and high-frequency limits, respectively. As a result, in the low-frequency limit, the modified frame moduli given by equations 2.72 and 2.73 reduce to the dry frame moduli K and μ, while they are equal to the unrelaxed frame moduli given by expressions 2.67 and 2.73 in the high-frequency limit.

The effect of fluid filling the stiff pores is then taken into account by replacing the dry moduli K and μ by the modified frame moduli given by equations 2.72 and 2.73 into the isotropic Gassmann [1951] equations (equations 2.57 to 2.60). Proceeding in this way yields the frequency-dependent elastic moduli of the fully saturated rock.

Asymptotic behavior of attenuation in the liquid-saturated case - As seen in equation 2.70, the frequency dependency of the modified frame moduli is controlled by the

quantity

$$kr = \frac{1}{a}\Big(-\frac{3i\omega\eta_f}{K_f}\Big)^{1/2}. \tag{2.74}$$

To gain a better understanding of attenuation in the liquid-saturated case, Gurevich et al. [2010] considered three limiting cases, referred to in the following as low-, intermediate- and high-frequency cases. Attenuation can be quantified by calculating the inverse quality factor $1/Q_K$ of the modified frame bulk modulus:

$$\frac{1}{Q_K} = \frac{Im(K^{mf})}{Re(K^{mf})}. \tag{2.75}$$

In the low-frequency case, $|kr|^2 \ll 1$ and

$$|kr|^2 \ll \frac{8\phi_c}{\Big(\frac{1}{K} - \frac{1}{K_h}\Big)K_f}. \tag{2.76}$$

In this case, Taylor series expansion of Bessel functions in equation 2.70 yields the following expression for the modified bulk modulus of the liquid:

$$K_f^*(\omega) = -\frac{(kr)^2 K_f}{8} = \frac{3}{8}\frac{i\omega\eta_f}{a^2}. \tag{2.77}$$

By calculating the modified frame bulk modulus and the inverse quality factor defined in equation 2.75, the attenuation is found to be proportional to ω. In the intermediate-frequency case, the quantity kr is such that

$$\frac{8\phi_c}{\Big(\frac{1}{K} - \frac{1}{K_h}\Big)K_f} \ll |kr|^2 \ll 1. \tag{2.78}$$

The modified liquid modulus is again expressed by equation 2.77 and the attenuation is proportional to $\omega^{-1/2}$. In the high-frequency limit, $|kr| \gg 1$, and the modified fluid modulus can be approximated by

$$K_f^*(\omega) = \Big(1 + \frac{2i}{kr}\Big)K_f. \tag{2.79}$$

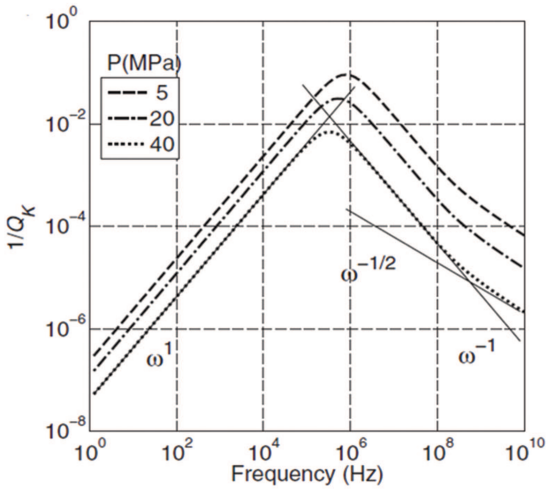

FIGURE 2.12: Asymptotic behavior of squirt flow attenuation in the liquid-saturated case: predictions of inverse quality factors for a water-saturated Berea sandstone subjected to different hydrostatic stress levels. Solid lines show the asymptotic regimes for the low-, intermediate- and high-frequency regimes. From Gurevich et al. [2010]

As an illustration of this asymptotic behavior of the squirt-flow attenuation, the frequency dependence of the inverse quality factor predicted for a water-saturated sample of Berea sandstone for different hydrostatic levels is shown in Figure 2.12. As seen on the figure, the transition between the intermediate and high frequency regimes occurs when the attenuation is negligible. The main conclusion that can be drawn from this observation is that the fluid-saturated moduli can be reasonably approximated by equation 2.77 in the liquid-saturated case.

2.5.2.2 Anisotropic squirt flow model from Mukerji & Mavko [1994]

Mukerji & Mavko [1994] extended Mavko & Jizba [1991] isotropic squirt flow model to anisotropic media. In the low- and high-frequency limits, they found that elastic moduli in anisotropic saturated media depend on five parameters: the frequency, the distribution of compliant porosity, the intrinsic anisotropy, the fluid viscosity and the effective pressure. Here and below, we only show results that will be used in Chapter 5, but the solution derived in their paper is more general as it handles lower-symmetry systems and the presence of intrinsic anisotropy. Their approach is similar to the one

introduced in the isotropic case by Mavko & Jizba [1991] and employed by Gurevich et al. [2010] (Section 2.5.2.1):

- The saturated low-frequency moduli are given by Brown & Korringa [1975] equations, which are the equivalent of the anisotropic Gassmann equations written in terms of compliance.
- To model the high-frequency limit of saturated elastic properties, they first calculate elastic of the unrelaxed frame describe above. The unrelaxed frame properties are then substituted into Brown & Korringa [1975] equations to incorporate the effect of fluid filling stiff pores.

Mukerji & Mavko [1994] demonstrate that the effective compliance of the unrelaxed frame S^{uf}_{ijkl} is written as

$$S^{uf}_{ijkl} = S_{ijkl} - \frac{\Delta S_{\alpha\alpha\beta\beta}}{1 + \phi_c\left(\frac{1}{K_f} - \frac{1}{K_g}\right)\Big/ \Delta S_{\alpha\alpha\beta\beta}} G_{ijkl}, \tag{2.80}$$

where S_{ijkl} is the effective compliance of the dry medium, ΔS_{ijkl} is the excess compliance due to cracks and ϕ_c is the compliant porosity. In equation 2.80, the tensor G_{ijkl} describes the effect of applying an external load on the crack distribution function and is expressed as an integral over all crack orientations:

$$G_{ijkl} = \int f(\Omega) n_i n_j n_k n_l d\Omega, \tag{2.81}$$

where n_i is the unit normal to the cracks and $f(\Omega)$ is the normalized crack orientation distribution function (its integral over all angles equals unity).

For HTI media having their symmetry axis along the x_1-direction, the five independent components of G_{ijkl} are expressed as

$$G_{1111} = \Delta\widetilde{S}_{1111} - \frac{8\widetilde{\alpha}\Delta\widetilde{S}_{1133}}{1-4\widetilde{\alpha}}, \tag{2.82}$$

$$G_{1133} = \Delta\widetilde{S}_{1122}\Big/(1-4\widetilde{\alpha}), \tag{2.83}$$

$$G_{2233} = \Delta\widetilde{S}_{2233}\Big/(1-4\widetilde{\alpha}), \tag{2.84}$$

$$G_{3333} = \Delta\widetilde{S}_{3333} - \frac{4\widetilde{\alpha},}{1-4\widetilde{\alpha}}\Big(\Delta\widetilde{S}_{1133} + \Delta\widetilde{S}_{2233}\Big), \tag{2.85}$$

$$G_{1212} = \frac{\Delta\widetilde{S}_{1212}}{1-4\widetilde{\alpha}} - \frac{\Delta\widetilde{S}_{1111} + \Delta\widetilde{S}_{3333}}{4(1-4\widetilde{\alpha})} + \frac{G_{1111} + G_{3333}}{4}, \tag{2.86}$$

where

$$\Delta\widetilde{S}_{ijkl} = \frac{\Delta\widetilde{S}_{ijkl}}{\Delta\widetilde{S}_{\alpha\alpha\beta\beta}}, \tag{2.87}$$

and

$$\widetilde{\alpha} = \Big(\Delta\widetilde{S}_{\alpha\beta\alpha\beta} - 1\Big)\Big/4. \tag{2.88}$$

For the specific case considered later on in Chapter 5, for which the TI symmetry results in the presence of aligned compliant pores, Mukerji & Mavko [1994] show that equation 2.80 simplifies to

$$S^{uf}_{ijkl} = S_{ijkl} - \frac{\Delta S_{\alpha\alpha ij}\Delta S_{\alpha\alpha kl}}{\Delta S_{\alpha\alpha\beta\beta} + \phi_c\Big(\dfrac{1}{K_f} - \dfrac{1}{K_g}\Big)}. \tag{2.89}$$

The anisotropic squirt flow model developed by Mukerji & Mavko [1994] only provides the low- and high-frequency limits of the saturated elastic properties. In Chapter 5, we combine their approach to the pressure relaxation approach of Murphy et al. [1986] utilized by Gurevich et al. [2010] to derive frequency-dependent elastic properties of saturated media. Insight on velocity anisotropy and attenuation anisotropy is also gained by deriving analytical expressions of velocity and attenuation anisotropy parameters.

Chapter 3

Anisotropy pattern arising from the application of triaxial stress on an isotropic medium

3.1 Chapter overview

In this chapter, we address one of the main objectives of this project, which is to model stress-induced anisotropy. The anisotropy of tectonic stresses in the Earth's crust is one of the main causes of seismic anisotropy in sedimentary rocks. The stress sensitivity of elastic properties of rocks is often attributed to the closure of compliant parts of the pore space [Nur & Simmons, 1969, Shapiro, 2003, Walsh, 1965b,c]. Non-hydrostatic stress can cause elastic anisotropy depending on the orientation of the discontinuities with respect to the stress field. Knowledge of the pattern of stress-induced anisotropy (expressed, for example, by the ratio of anisotropy parameters) can be useful for distinguishing it from other causes of anisotropy, such as the presence of aligned fractures or intrinsic anisotropy due to fine layering or clay particles alignment. Such patterns can also be used to estimate P-wave anisotropy from S-wave anisotropy

estimated from S-wave splitting when the cause of anisotropy is known (see Chapter 6).

Several approaches were used to model stress-induced anisotropy. A number of authors considered angular distributions of idealized penny-shaped cracks [Nur, 1971, Sayers, 1988] and inferred distributions of crack aspect ratios with various orientations when the rock is subjected to a given stress. These models, due to the idealized crack geometry, may not give an adequate quantitative description of grain contacts in rocks [Gurevich, Makarynska, & Pervukhina, 2009a]. As an alternative, Rasolofosaon [1998] and Prioul et al. [2004] applied the third-order elasticity theory, also known as acousto-elasticity theory [Thurston, 1974], to describe the stress dependency of elastic properties and anisotropy. Their works are only suitable for a stress range where stiffnesses are quasilinear with stress, which is usually suitable for downhole applications since most of the observed stress-induced anisotropy perturbations are often small [Lei et al., 2012]. These models can be calibrated using in-situ downhole measurements (e.g. Donald & Prioul [2015]), but it requires the in-situ stress state to be known.

The approach we use in this chapter is essentially similar to the one employed by Mavko et al. [1995] and Sayers [2002, 2005, 2006], who estimated stress-induced velocity anisotropy from measurements without assuming any particular crack geometry. Mavko et al. [1995] studied the pressure dependence of the overall compliance of a stressed medium by considering that the compliant porosity is crack-like and by modelling the effect of the normal traction acting across these cracks. The beauty of their model is that elastic properties of a medium subjected to any stress state are predicted from the pressure dependency of the same medium under hydrostatic stress. This model yet requires numerical calculations to obtain an insight into anisotropy patterns; in this chapter, we derive analytical expressions for anisotropy parameters. Sayers [2002] used the linear-slip deformation formalism, also called excess compliance theory (Chapter 2, Section 2.3), to model the stress dependency of elastic properties. However, he directly fitted velocity measurements made while the rock is subjected to anisotropic stress; in

the following, we try to infer elastic properties of rocks subjected to triaxial stress using parameters that can be obtained from independent hydrostatic measurements.

The model developed in this chapter is an extension of the stress-induced anisotropy model derived by Gurevich et al. [2011] (Chapter 2, Section 2.4.2). In their study, Gurevich et al. [2011] focused on the anisotropy caused by the application of a small uniaxial stress on a linearly isotropic elastic medium; here we extend their approach to a more realistic stress state, where all three principal stresses are different. Based on several assumptions, they expressed the effective elastic properties of the stressed medium as a function of four physically meaningful parameters, which can be inferred from hydrostatic stress velocity measurements. Their main assumption was that a rock containing an initially isotropic distribution of cracks is subjected to a small uniaxial stress, which results in the closure of cracks perpendicular to the applied stress. This preferential closure of cracks causes a weak anisotropy of the discontinuity orientation distribution and weak elastic anisotropy. The model predicts elliptical anisotropy, which is consistent with results previously obtained from Rasolofosaon [1998] and Prioul et al. [2004]. It also predicts the ratio of Thomsen's anisotropy parameters ϵ/γ as a function of the compliance ratio B and Poisson's ratio of the unstressed rock. Madadi et al. [2013] extended the model of Gurevich et al. [2011] to larger uniaxial stress (Chapter 2, Section 2.4.3). Based on their work, we also study the effect of larger stresses in the case of triaxial stress.

The chapter is organized as follows. First, we state the assumptions used in the derivation of the model; most of these assumptions were already made by Gurevich et al. [2011] and Madadi et al. [2013]. Then, we derive the model for small stresses before investigating larger stresses. Finally, the model predictions are tested against laboratory measurements made by Chaudhry [1995]. Contents of this chapter have been published in Geophysics [Collet et al., 2014] and have been reproduced by permission of SEG.

3.2 Assumptions

The derivation of this stress-induced anisotropy model follows a number of assumptions, which are listed and explained below.

- The rock deformation is assumed to be elastic over the entire range of applied stresses.
- The model is designed for anisotropy that is due only to the application of anisotropic stresses. All other causes of anisotropy such as anisotropic grain shapes or anisotropic distribution of cracks are thus ignored. This condition implies that the medium is isotropic in the initial unstressed state.
- The medium is assumed to be dry.
- The effect of grain contacts and microcracks on elastic properties is modelled using Sayers & Kachanov [1995] theory (Chapter 2, Section 2.3). Hence, cracks are assumed to be rotationally symmetrical and adequately represented by linear-slip interfaces. Besides, the crack distribution is assumed to be sufficiently sparse to allow for the use of Sayers & Kachanov [1995] non-interactive approximation.
- The model only takes into account the effect of crack closure occurring perpendicular to applied stresses. In other words, the model does not handle the eventual opening of cracks that might occur in the direction perpendicular to the minimum stress, particularly for large stresses.

3.3 Derivation of the model for small stresses

The initial unstressed medium is the same as the one described in Chapter 2, Section 2.4, when introducing the stress sensitivity models of Shapiro [2003] and Gurevich et al. [2011]. The medium is assumed to be dry, elastic and isotropic. In the initial state, i.e. at ambient stress, this medium is permeated by cracks which are randomly oriented and

randomly distributed in space. Mathematically, the orientation distribution of these cracks is a continuous function of the angular coordinates. Cracks are parametrized in the same way as in the Sayers & Kachanov [1995] theory, i.e. they are defined by their area A and a ratio B of their normal Z_N to tangential Z_T excess crack compliances (Chapter 2, Section 2.3). All cracks are assumed to be identical; thus, A and B are the same for all cracks. When this isotropic rock is subjected to triaxial load, crack closures occur preferentially perpendicular to the stress directions, resulting in orthorhombic anisotropy [Nur, 1971, Rasolofosaon, 1998].

3.3.1 Effect of stress on crack distribution

Let us define the total area $S = \sum_r A^{(r)}$ of cracks with a given orientation and the corresponding specific area $s = S/V$ of cracks with that orientation, V being the volume of rock. When anisotropic stress is applied, the specific area s varies with the direction of the crack normal and the stress acting in this direction. Based on previous models [Gurevich et al., 2011, Mavko et al., 1995, Sayers, 2006, Shapiro, 2003, Vlastos et al., 2006], we approximate this stress dependence by an exponential decay:

$$s = s_0 \exp\left(\frac{\sigma_n}{P_c}\right), \tag{3.1}$$

where s_0 is the specific area of all the cracks before application of anisotropic stress, $\sigma_n = \sigma_{ij} n_i n_j$ is the normal stress traction acting on the crack surface, and P_c is the characteristic crack closing pressure defined in Chapter 2, Section 2.4.1. In equation 3.1, we use the sign convention employed in solid mechanics, i.e. compressive stresses σ_n are negative. Equation 3.1 mathematically describes the fact that the area of cracks oriented perpendicular to the maximum stress is more reduced than the area of cracks oriented perpendicular to the minimum stress. In other words, equation 3.1 reflects the variation of the angular distribution of crack orientation as a function of stress magnitude. If we assume that stresses are small compared to the characteristic crack closing pressure P_c, then the exponential function in equation 3.1 can be linearized so

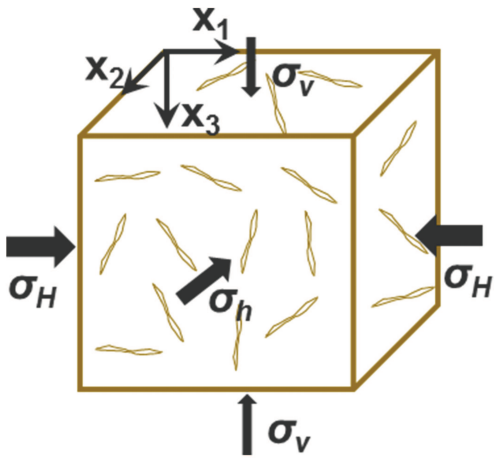

FIGURE 3.1: Cartoon showing the triaxial stress state applied on the medium. The maximum stress corresponds to the maximum horizontal stress σ_H applied along the x_1-axis.

that:

$$s = s_0\Big(1 + \frac{\sigma_n}{P_c}\Big). \tag{3.2}$$

We consider that stresses are applied along three orthogonal directions as illustrated in Figure 3.1. The maximum stress is assumed to be the maximum horizontal stress σ_H, which is the stress acting along the x_1-axis. The normalized stress magnitudes of the minimum horizontal (σ_h) and vertical (σ_v) stresses are given by

$$a_h = \frac{\sigma_{22}}{\sigma_{11}}, \tag{3.3}$$

$$a_v = \frac{\sigma_{33}}{\sigma_{11}}. \tag{3.4}$$

The stress tensor corresponding to this stress regime is expressed as

$$\sigma_{ij} = \sigma_{11}\Big(\delta_{i1}\delta_{j1} + a_h\delta_{i2}\delta_{j2} + a_v\delta_{i3}\delta_{j3}\Big), \tag{3.5}$$

yielding

$$\sigma_n = \sigma_{11}\Big(n_1^2 + a_h n_2^2 + a_v n_3^2\Big). \tag{3.6}$$

3.3.2 Evaluation of crack compliance tensors

After quantifying the effect of applying a triaxial stress on the crack distribution, effective elastic properties of the resulting medium can be calculated using Sayers & Kachanov [1995] theory (Chapter 2, Section 2.3). We assume that, in the initial unstressed state, all cracks are identical, randomly oriented and distributed and that their orientation distribution is a continuous (and smooth) function of angular coordinates. Hence, the sums that account for the contribution of each crack in the definition of the crack compliance tensors $\boldsymbol{\alpha}$ and $\boldsymbol{\beta}$ (equations 2.30 and 2.31) can be replaced by integrals over angular coordinates:

$$\alpha_{ij} = \frac{1}{V}\sum_r B_T^{(r)} n_i^{(r)} n_j^{(r)} A^{(r)} = \frac{1}{4\pi}\int\int s B_T n_i n_j \, d\Omega, \tag{3.7}$$

and

$$\beta_{ijkl} = \frac{1}{V}\sum_r (B_N^{(r)} - B_T^{(r)}) n_i^{(r)} n_j^{(r)} n_k^{(r)} n_l^{(r)} A^{(r)} = \frac{1}{4\pi}\int\int s(B_N - B_T) n_i n_j n_k n_l \, d\Omega, \tag{3.8}$$

where $d\Omega = \sin\theta d\theta d\psi$ is a body angle element. By substituting the variation of the specific area of cracks (equation 3.2) into equations 3.7 and 3.8, we obtain

$$\alpha_{ij} = \frac{Z_{T0}}{4\pi}\int\int \Big(1 + \frac{\sigma_n}{P_c}\Big) n_i n_j \, d\Omega, \tag{3.9}$$

$$\beta_{ijkl} = \frac{(Z_{N0} - Z_{T0})}{4\pi}\int\int \Big(1 + \frac{\sigma_n}{P_c}\Big) n_i n_j n_k n_l \, d\Omega, \tag{3.10}$$

where $Z_{N0} = s_0 B_N$ and $Z_{T0} = s_0 B_T$ are respectively the normal and tangential crack compliances in the unstressed state.

Now the integrals in equations 3.9 and 3.10 can be evaluated analytically to give

$$\alpha_{11} = Z_{T0}\Big[\frac{1}{3} + \Big(\frac{1}{5} + \frac{a_h}{15} + \frac{a_v}{15}\Big)b\Big], \tag{3.11}$$

$$\alpha_{22} = Z_{T0}\Big[\frac{1}{3} + \Big(\frac{1}{15} + \frac{a_h}{5} + \frac{a_v}{15}\Big)b\Big], \tag{3.12}$$

$$\alpha_{33} = Z_{T0}\Big[\frac{1}{3} + \Big(\frac{1}{15} + \frac{a_h}{15} + \frac{a_v}{5}\Big)b\Big], \tag{3.13}$$

$$\alpha_{12} = \alpha_{23} = \alpha_{13} = 0, \tag{3.14}$$

where $b = \sigma_{11}/P_c$ is the normalized stress magnitude. Note that equations 3.11 to 3.14 are consistent with results found previously by Sayers [2005, 2006] who models the effect of a linear change in the effective stress tensor on seismic velocities. The fourth-rank tensor $\bar{\boldsymbol{\alpha}}$, given by a combination of α_{ij} coefficients in equation 2.29, can be expressed as

$$\bar{\alpha}_{iiii} = \alpha_{ii} \text{ for } i = 1,..3, \tag{3.15}$$

$$\bar{\alpha}_{ijij} = \frac{1}{4}\Big(\alpha_{ii} + \alpha_{jj}\Big) \text{ for } i,j = 1,..3,\ i \neq j, \tag{3.16}$$

where no summation over indices is implied. All other components of tensor $\bar{\boldsymbol{\alpha}}$ are zero. The tensor $\bar{\boldsymbol{\alpha}}$ can be rewritten in the form of a 6x6 matrix using Voigt notation (see Chapter 2, Section 2.2.2) and introducing factors 2 and 4 as follows:

$$\bar{\alpha}_{ijkl} \rightarrow \bar{\alpha}_{pq} \text{ when both } p \text{ and } q \text{ are 1, 2, or 3,}$$

$$2\bar{\alpha}_{ijkl} \rightarrow \bar{\alpha}_{pq} \text{ when one of } p \text{ and } q \text{ is 4, 5 or 6,}$$

$$4\bar{\alpha}_{ijkl} \rightarrow \bar{\alpha}_{pq} \text{ when both } p \text{ and } q \text{ are 4, 5 or 6.}$$

The tensor $\bar{\boldsymbol{\alpha}}$ can thus be written as a diagonal matrix with components

$$\bar{\alpha}_{11} = \alpha_{11},\ \bar{\alpha}_{22} = \alpha_{22},\ \bar{\alpha}_{33} = \alpha_{33}, \tag{3.17}$$

$$\bar{\alpha}_{44} = Z_{T0}\Big[\frac{2}{3} + \Big(\frac{2}{15} + \frac{4a_h}{15} + \frac{4a_v}{15}\Big)b\Big], \tag{3.18}$$

$$\bar{\alpha}_{55} = Z_{T0}\Big[\frac{2}{3} + \Big(\frac{4}{15} + \frac{2a_h}{15} + \frac{4a_v}{15}\Big)b\Big], \tag{3.19}$$

$$\bar{\alpha}_{66} = Z_{T0}\Big[\frac{2}{3} + \Big(\frac{4}{15} + \frac{4a_h}{15} + \frac{2a_v}{15}\Big)b\Big]. \tag{3.20}$$

A similar approach can be used to compute the fourth-rank tensor $\boldsymbol{\beta}$. For orthorhombic symmetry, the non-vanishing components of tensor $\boldsymbol{\beta}$ are β_{1111}, β_{2222}, β_{3333}, β_{1122}, β_{1133} and β_{2233} and their symmetrics [Sayers, 2002]. Hence, the remaining components can be written as

$$\beta_{iijj} = \beta_{ij} = \frac{(Z_{N0} - Z_{T0})}{4\pi}\int\int\Big(1 + \frac{\sigma_n}{P_c}\Big)n_i^2 n_j^2\ d\Omega \text{ for } i,j = 1,...3, \tag{3.21}$$

where no summation is implied in the four-index notation β_{iijj} and the two-index version β_{ij} refers to the 6x6 notation. The other non-vanishing coefficients of the 6x6 matrix are $\beta_{44} = 4\beta_{2323}$, $\beta_{55} = 4\beta_{1313}$ and $\beta_{66} = 4\beta_{1212}$. Components of the resulting β_{ij} matrix are given by

$$\beta_{11} = (Z_{N0} - Z_{T0})\Big[\frac{1}{5} + \Big(\frac{1}{7} + \frac{a_h}{35} + \frac{a_v}{35}\Big)b\Big], \tag{3.22}$$

$$\beta_{22} = (Z_{N0} - Z_{T0})\Big[\frac{1}{5} + \Big(\frac{1}{35} + \frac{a_h}{7} + \frac{a_v}{35}\Big)b\Big], \tag{3.23}$$

$$\beta_{33} = (Z_{N0} - Z_{T0})\Big[\frac{1}{5} + \Big(\frac{1}{35} + \frac{a_h}{35} + \frac{a_v}{7}\Big)b\Big], \tag{3.24}$$

$$\beta_{12} = (Z_{N0} - Z_{T0})\Big[\frac{1}{15} + \Big(\frac{1}{35} + \frac{a_h}{35} + \frac{a_v}{105}\Big)b\Big], \tag{3.25}$$

$$\beta_{13} = (Z_{N0} - Z_{T0})\Big[\frac{1}{15} + \Big(\frac{1}{35} + \frac{a_h}{105} + \frac{a_v}{35}\Big)b\Big], \tag{3.26}$$

$$\beta_{23} = (Z_{N0} - Z_{T0})\Big[\frac{1}{15} + \Big(\frac{1}{105} + \frac{a_h}{35} + \frac{a_v}{35}\Big)b\Big], \tag{3.27}$$

$$\beta_{44} = 4\beta_{23},\ \beta_{55} = 4\beta_{13},\ \beta_{66} = 4\beta_{12}. \tag{3.28}$$

By substituting components $\bar{\alpha}_{ij}$ (equations 3.17 to 3.20) and β_{ij} (equations 3.22 of the

crack compliance tensors into the formulas for the effective compliance of a cracked medium (equations 2.27 to 2.29), we compute the overall compliance tensor $\boldsymbol{S}$ of the stressed medium. By inverting this compliance tensor, we obtain the effective stiffness tensor $\boldsymbol{C} = \boldsymbol{S}^{-1}$. Note that, as for all stress sensitivity models presented in Chapter 2, Section 2.4, there are only five parameters required to describe the changes of the compliance and stiffness components as a function of stress. Namely, these parameters are the bulk and shear moduli of the unstressed rock K_0 and μ_0, the tangential compliance Z_{T0}, the ratio of normal to tangential compliance B and the characteristic pressure P_c. In addition, it is straightforward to show that, when a uniaxial stress is applied (i.e. when $a_h = a_v = 0$), the crack tensors $\bar{\boldsymbol{\alpha}}$ and $\boldsymbol{\beta}$ given by equations 3.17 to 3.20 and 3.22 to 3.28 are consistent with the results obtained from Gurevich et al. [2011] (equations 2.52 and 2.53).

3.3.3 Results in terms of anisotropy parameters

To gain a more intuitive insight on how anisotropy is affected by stress, we compute the orthorhombic anisotropy parameters defined by Tsvankin [1997] (see Chapter 2, Section 2.2.3.2). By substituting the effective stiffness components of the stressed medium into the definition of anisotropy parameters (equation 2.21), and retaining only the linear terms in the small parameter $b = \sigma_{11}/P_c$, we obtain

$$\epsilon_{(1)} = \delta_{(1)} = \frac{2}{105}\frac{2\nu_0 B + 6B - 2\nu_0 + 1}{1-\nu_0}\mu_0 Z_{T0}(a_h - a_v)b \tag{3.29}$$

$$\gamma_{(1)} = \frac{1}{105}\Big(3 + 4B\Big)\mu_0 Z_{T0}(a_h - a_v)b \tag{3.30}$$

where ν_0 is the Poisson's ratio of the unstressed rock with an isotropic distribution of cracks and $B = Z_{N0}/Z_{T0}$ is the ratio of normal to tangential compliances of individual cracks. Parameters $\epsilon_{(1)}$, $\delta_{(1)}$ and $\gamma_{(1)}$ quantify the anisotropy in the $[x_2, x_3]$-plane. As a consequence, they are proportional to the difference $(\sigma_{22} - \sigma_{33})$, as expressed in equations 3.29 and 3.30. A similar observation is made for anisotropy parameters in

the other planes of symmetry, which follow the relationships

$$\epsilon_{(1)} = \frac{a_h - a_v}{1 - a_v}\epsilon_{(2)} = \frac{a_h - a_v}{a_h - 1}\epsilon_{(3)}, \tag{3.31}$$

$$\gamma_{(1)} = \frac{a_h - a_v}{1 - a_v}\gamma_{(2)} = \frac{a_h - a_v}{a_h - 1}\gamma_{(3)}, \tag{3.32}$$

$$\delta_{(1)} = \frac{a_h - a_v}{1 - a_v}\delta_{(2)} = \frac{a_h - a_v}{a_h - 1}\delta_{(3)}. \tag{3.33}$$

We notice that for $i = 1, ...3$, $\epsilon_{(i)} = \delta_{(i)}$, which means that crack closure resulting from the application of a small triaxial stress yields ellipsoidal anisotropy, regardless of the value of the compliance ratio B. Note that equations 3.31 and 3.32 agree with the relationship derived by Sun & Prioul [2010] using the third order elasticity theory in the limit of weak anisotropy:

$$\frac{\epsilon_{(1)}}{\epsilon_{(2)}} = \frac{\gamma_{(1)}(1 + 2\gamma_{(2)})}{\gamma_{(2)}(1 + 2\gamma_{(1)})} = \frac{\sigma_{22} - \sigma_{33}}{\sigma_{11} - \sigma_{33}}. \tag{3.34}$$

Further comparison between both of these relationships is discussed in the next section (Section 3.4).

Besides, from equations 3.29 to 3.32, we can express the ratios $\epsilon_{(i)}/\gamma_{(i)}$ as a function of two independent parameters: the Poisson's ratio of the unstressed rock and the compliance ratio,

$$\frac{\epsilon_{(i)}}{\gamma_{(i)}} = 2\frac{2\nu_0 B + 6B - 2\nu_0 + 1}{(1 - \nu_0)(3 + 4B)}. \tag{3.35}$$

These results are consistent with the earlier findings from Gurevich et al. [2011] for a rock subjected to a uniaxial stress (Chapter 2, Section 2.4.2). The above results show that an elastic medium whose anisotropy is caused by the application of stress to an isotropic medium represents a special case of an orthorhombic medium. A general orthorhombic medium is characterized by nine independent elastic constants, while the medium described by our model is characterized by five independent parameters only. This is logical because elasticity of such a medium is completely defined by two moduli of the initial isotropic medium plus three principal stresses (the principal axes are assumed to be known).

3.4 Validity of the results for larger stresses

In the previous section, we assume that stresses are small compared to the characteristic crack closing pressure P_c. In this section, we consider larger stresses by replacing the linear approximation of the exponential function by its Taylor series expansion in equation 3.2. The variation of the specific area of cracks as a function of the applied stress becomes

$$s = s_0 \sum_{n=0}^{\infty} \frac{1}{n!} \left(\frac{\sigma_n}{P_c}\right)^n. \tag{3.36}$$

Mathematical details and expressions of the resulting crack compliance tensors $\boldsymbol{\alpha}$ and $\boldsymbol{\beta}$ are provided in Appendix A. The aim here is twofold:

- First, we want to check if the results concerning the anisotropy parameters ratios $\epsilon_{(i)}/\delta_{(i)}$ and $\epsilon_{(i)}/\gamma_{(i)}$ (equation 3.35) still hold for larger stresses.
- Second, we want to know for which stress ranges the relationships between anisotropy parameters and stress ratios (equations 3.31 to 3.33) are valid.

To investigate the results at larger stresses, we calculate the effective elastic properties using the crack compliance tensors $\bar{\boldsymbol{\alpha}}$ and $\boldsymbol{\beta}$ derived in Appendix A. Input parameters describing the initial medium and the stress states are listed in Table 3.1. Values used for K_0, μ_0, B, P_c and Z_{T0} are values inverted from a hydrostatic stress test made on a Penrith sandstone sample (see Section 3.5.1). We tested two stress states:

- **Stress state 1**, which is characterized by a large difference between the minimum stress σ_{33} and the two other stresses,
- **Stress state 2**, for which there is a relatively small contrast between all stresses.

Figure 3.2a and 3.2b shows the ratios $\epsilon_{(i)}/\delta_{(i)}$ obtained in each plane of symmetry for stress states 1 and 2, respectively. We notice that in the second case, for which the relative differences between stresses are lower, values of $\epsilon_{(i)}/\delta_{(i)}$ lie within 0.95 and

Initial unstressed medium	Stress state 1	Stress state 2
$K_0 = 11.1$ GPa	$b = \frac{\sigma_{11}}{P_c} = 0$ to 10	$b = \frac{\sigma_{11}}{P_c} = 0$ to 10
$\mu_0 = 10.8$ GPa	$a_h = \frac{\sigma_{22}}{\sigma_{11}} = 0.9$	$a_h = \frac{\sigma_{22}}{\sigma_{11}} = 0.9$
$B = 0.48$	$a_v = \frac{\sigma_{33}}{\sigma_{11}} = 0.4$	$a_v = \frac{\sigma_{33}}{\sigma_{11}} = 0.75$
$P_c = 13.4$ MPa		
$Z_{T0} = 0.086$ GPa^{-1}		

TABLE 3.1: Input parameters used to investigate results of the stress-induced anisotropy model at larger stresses.

1.2. Such results indicate that the medium remains close to ellipsoidal even at large stresses. In the first example, the relative error on $\epsilon_{(1)}/\delta_{(1)}$ reaches 15% when the maximum stress equals $3P_c$. This relatively large error suggests that the deviation from the ellipsoidal result becomes significant at large stresses, when the difference between applied stresses is important. Similar conclusions can be drawn from Figure 3.2c and 3.2d about the ratios $\epsilon_{(i)}/\gamma_{(i)}$. Note that typical characteristic pressures P_c range from 10 to 15 MPa [Shapiro, 2003], which suggests that values of the anisotropy parameters ratios $\epsilon_{(i)}/\delta_{(i)}$ and $\epsilon_{(i)}/\gamma_{(i)}$ obtained in the previous section should still be valid for stresses as high as 40 MPa. Nonetheless, this value strongly depends on the characteristic crack closing pressure P_c, which is a function of matrix properties and crack compliance and geometry, and also varies as a function of the stress contrasts quantitatively described by ratios a_h and a_v. As shown by the numerical examples, the model is expected to yield better approximations at high stresses when stress contrasts are small.

Figure 3.3a to 3.3f shows comparisons between the ratios $\epsilon_{(i)}/\epsilon_{(j)}$, $\gamma_{(i)}/\gamma_{(j)}$, $\delta_{(i)}/\delta_{(j)}$ and the stress ratios computed using equations 3.31 to 3.33 (absolute values of the anisotropy parameters ratios and corresponding stress ratios were taken for $(i,j) = (3,1)$ and $(i,j) = (3,2)$). We notice that for both stress states, the ratios $\epsilon_{(1)}/\epsilon_{(2)}$, $\gamma_{(1)}/\gamma_{(2)}$ and $\delta_{(1)}/\delta_{(2)}$ are still within a 15% error margin compared to the stress ratio

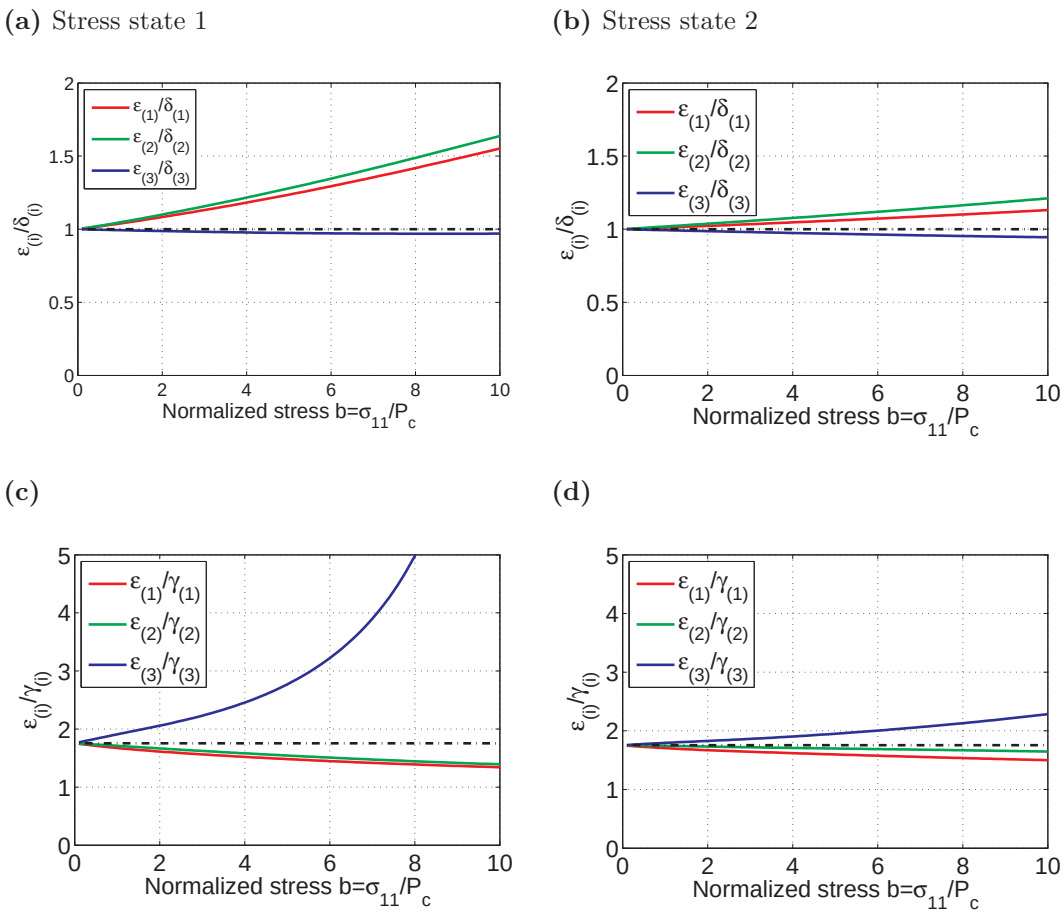

FIGURE 3.2: Ratios $\epsilon_{(i)}/\delta_{(i)}$ and $\epsilon_{(i)}/\gamma_{(i)}$ in each plane of symmetry as a function of normalized stress computed using the model derived for large stresses. Figures on the left show results obtained for Stress state 1 ($a_h = 0.9$ and $a_v = 0.4$), while figures on the right show results for Stress state 2 ($a_h = 0.9$ and $a_v = 0.75$). The black dash-dotted lines show predictions of the model derived for small stresses.

$(a_h - 1)/(a_h - a_v)$, for normalized stresses as high as 4. In Figure 3.3c to 3.3f, the anisotropy parameters ratios computed using the model derived for large stresses deviate significantly from the corresponding stress ratios as a 20% error is obtained for normalized stresses as low as 1.5. In Figure 3.3a and 3.3b, the green dashed curve represents the relationship linking $\gamma_{(1)}$, $\gamma_{(2)}$ and the stress ratio derived by Sun & Prioul [2010] (equation 3.34). We notice that their relationship and the one we derive (equation 3.32) yield very close results; the maximum absolute error between both of these relationships is less than 0.01 for the two examples shown in this study.

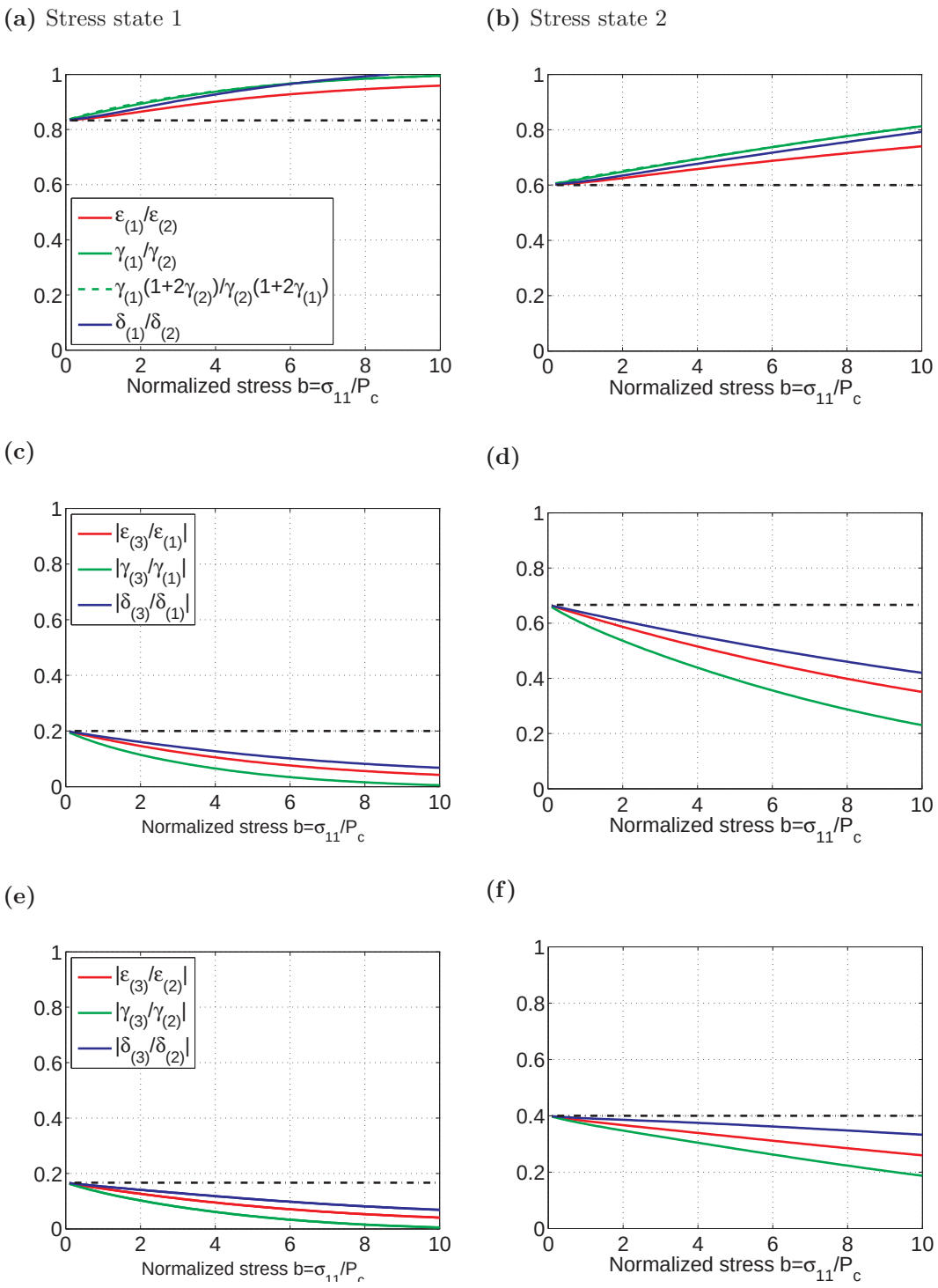

FIGURE 3.3: Ratios $|\epsilon_{(i)}/\epsilon_{(j)}|$, $|\delta_{(i)}/\delta_{(j)}|$ and $|\gamma_{(i)}/\gamma_{(j)}|$ as a function of normalized stress computed using the model derived for large stresses. Figures on the left show results obtained for Stress state 1 ($a_h = 0.9$ and $a_v = 0.4$), while figures on the right show results for Stress state 2 ($a_h = 0.9$ and $a_v = 0.75$). The black dash-dotted lines show the stress ratios estimated from equations 3.31 to 3.33.

3.5 Test against laboratory measurements

We apply the analytical model described above to velocity measurements made by King et al. [1995] and Chaudhry [1995] on a dry sample of Penrith sandstone. This data set was used previously to test the modelling approach of Sayers [2002]. The 51 mm side cubic sandstone specimen was compressed using a true triaxial (polyaxial) loading frame in which the three principal stresses can be varied independently. Transducers mounted on each face of the sample enabled them to measure compressional and shear velocities for propagation parallel to each of the three principal stresses within the frequency range 350-850 kHz. These measurements give access to the elastic stiffness coefficients C_{11}, C_{22}, C_{33}, C_{44}, C_{55} and C_{66} through the relationships

$$C_{11} = \rho v_{11}^2, \tag{3.37}$$

$$C_{22} = \rho v_{22}^2, \tag{3.38}$$

$$C_{33} = \rho v_{33}^2, \tag{3.39}$$

$$C_{44} = \rho v_{23}^2 = \rho v_{32}^2, \tag{3.40}$$

$$C_{55} = \rho v_{13}^2 = \rho v_{31}^2, \tag{3.41}$$

$$C_{66} = \rho v_{12}^2 = \rho v_{21}^2, \tag{3.42}$$

where ρ is the density of the rock sample and v_{ij} is the velocity of an elastic wave propagating along the x_i-axis and polarized along the x_j- axis.

For our study, we are particularly interested in two sets of measurements. The first one consists in a hydrostatic stress experiment (Figure 3.4a) for which the sample is subjected to an isotropic stress $\sigma_{11} = \sigma_{22} = \sigma_{33}$ increasing from 5 MPa to 60 MPa. We use these measurements to determine the model parameters K_0, μ_0, B, P_c and Z_{T0}. In the second experiment, σ_{33} is held constant at 3 MPa and $\sigma_{11} = \sigma_{22}$ is increased from 5 to 100 MPa (Figure 3.4b). Then maintaining σ_{33} at 3 MPa and σ_{22} at 100 MPa, σ_{11} is increased from 100 to 132 MPa (Figure 3.4c). We compare the velocities measured during this experiment to our model predictions. It is worth mentioning that

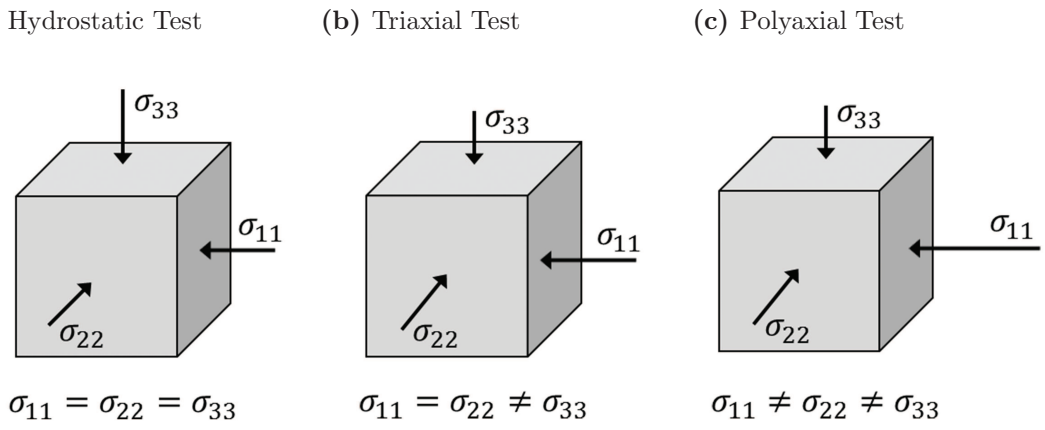

FIGURE 3.4: Various stress tests carried out in laboratories. The hydrostatic stress test is used to infer the model parameters. The triaxial stress test corresponds to the data of Chaudhry [1995] that we model in Section 3.5.2. The polyaxial stress test would be the ideal test to properly validate our model.

this example is not the most suitable example to test our approach. Indeed, for σ_{11} up to 100 MPa, the stresses applied along the x_1- and x_2- axis are equal. At the end of the test, the three stresses are different; however, the stress difference between the vertical stress and both horizontal stresses is so large that velocities measured along the x_1- and x_2-axis remain the same (Figure 3.5b). Testing our model for velocity measured during a polyaxial (or true triaxial) stress test would be more relevant. Due to the complexity of true triaxial cells, we were unable to find such data in the literature.

3.5.1 Determination of model parameters

Figure 3.5a shows the three P-wave velocities (v_{11}, v_{22} and v_{33}) and six S-wave velocities (v_{12}, v_{21}, v_{13}, v_{31}, v_{23} and v_{32}) measured by King et al. [1995] and Chaudhry [1995] on the Penrith sandstone sample subjected to hydrostatic stress increasing from 5 to 60 MPa. We notice that the sample is approximately isotropic suggesting that our model is applicable to this sample.

To determine the bulk and shear moduli of the unstressed rock, the tangential compliance Z_{T0}, the ratio of normal to tangential compliance B and the characteristic

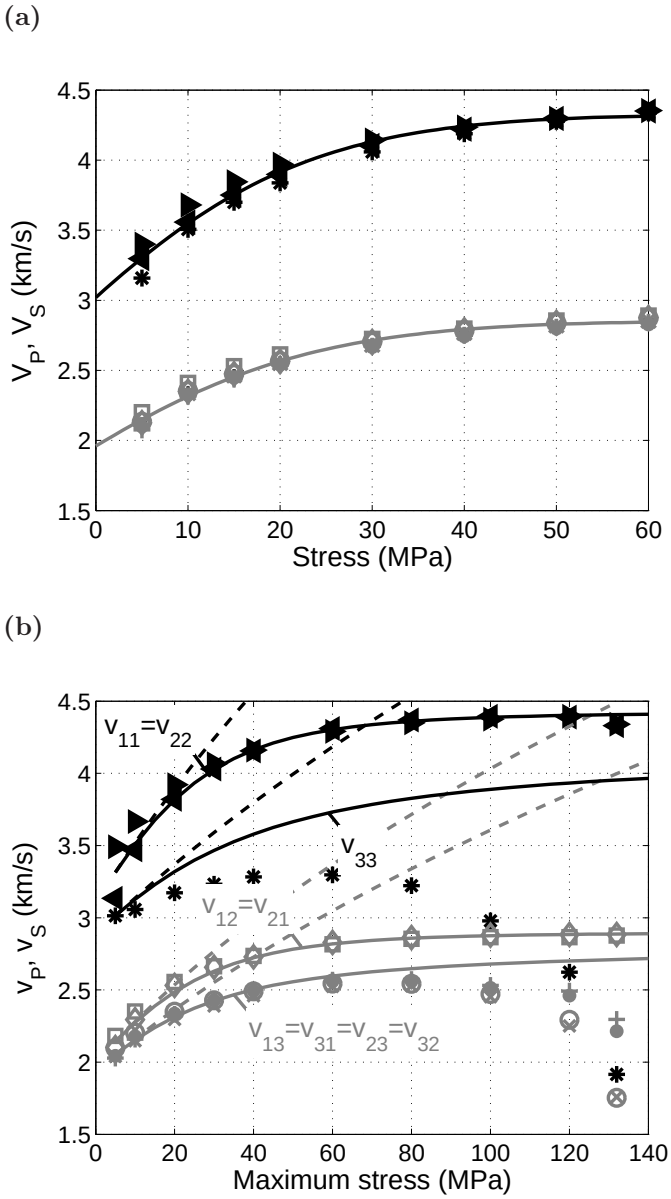

FIGURE 3.5: (a) Measured P-wave velocities $v_{11}(\blacktriangleright)$, $v_{22}(\blacktriangleleft)$, $v_{33}(*)$, and S-wave velocities $v_{13}(\bullet)$, $v_{31}(\circ)$, $v_{23}(+)$, $v_{32}(\times)$, $v_{12}(\square)$, $v_{21}(\diamond)$ as a function of applied hydrostatic stress in a dry Penrith sandstone sample [Chaudhry, 1995]. The curves show the P- and S-wave velocities obtained after the nonlinear fit of Shapiro [2003] to extract the model parameters K_0, μ_0, Z_{T0}, B and P_c. (b) Measured P-wave velocities $v_{11}(\blacktriangleright)$, $v_{22}(\blacktriangleleft)$, $v_{33}(*)$, and S-wave velocities $v_{13}(\bullet)$, $v_{31}(\circ)$, $v_{23}(+)$, $v_{32}(\times)$, $v_{12}(\square)$, $v_{21}(\diamond)$ as a function of the maximum compressive stress during the triaxial stress test [Chaudhry, 1995]. The dashed lines show the predictions of the stress-induced anisotropy model for small stresses, while the solid lines show the predictions of the model for larger stresses.

pressure P_c, we use the fitting procedure described by Gurevich, Makarynska, & Pervukhina [2009a] based on Shapiro [2003] stress sensitivity model (Chapter 2, Section 2.4.1). Hence, we compute the average velocities $\overline{v}_P = (v_{11} + v_{22} + v_{33})/3$ and $\overline{v}_S = (v_{12} + v_{21} + v_{13} + v_{31} + v_{23} + v_{32})/6$ and we invert for the stress sensitivity coefficients θ_c and θ_μ, which minimize the error between the moduli inferred from velocity measurements i.e. $K = \rho(\overline{v}_P^2 - 4\overline{v}_S^2/3)$ and $\mu = \rho\overline{v}_S^2$ and the moduli predicted by Shapiro [2003] (equations 2.47 and 2.48). Values of the bulk and shear moduli in the high-stress limit are taken from Sayers [2002]: $K_h = 20.45$ GPa and $\mu_h = 20.96$ GPa. The bulk and shear moduli of the unstressed rock are the values obtained for the reference pressure P_0 chosen as 3 MPa in this case. The inverted compliant porosity for this reference state is: $\phi_{c0} = 0.069\%$. The other stress-induced anisotropy model parameters are linked to Shapiro [2003] fitting parameters by the following relations [Gurevich, Makarynska, & Pervukhina, 2009a]:

$$B = \Big(\frac{5K_h\theta_\mu}{2\mu_h\theta_c} - \frac{2}{3}\Big)^{-1}, \tag{3.43}$$

$$P_c = \frac{K_h}{\theta_c}, \tag{3.44}$$

$$Z_{T0} = \Big(\frac{5}{2}\frac{\theta_\mu}{\mu_h} - \frac{2}{3}\frac{\theta_c}{K_h}\Big)\phi_{c0}\exp\Big(-\frac{\theta_c P_0}{K_h}\Big). \tag{3.45}$$

Values of the estimated parameters are: $K_0 = 11.1$ GPa, $\mu_0 = 10.8$ GPa, $B = 0.48$, $P_c = 13.4$ MPa and $Z_{T0} = 0.086$ GPa^{-1}. The curves plotted in Figure 3.5a show the P- and S-wave velocities obtained after the fitting procedure.

3.5.2 Predictions of the model

The inverted parameters describing the initial unstressed medium are then used to compute the overall stiffness tensor predicted by the stress-induced anisotropy model. Predictions of the stress-induced anisotropy model are plotted against velocity measurements made under triaxial loading in Figure 3.5b. The dashed lines show velocities predicted by the model when assuming stresses are small i.e. when $\sigma_{11} < P_c$ (Section 3.3). The solid lines show predictions for larger stresses calculated from equations in

Appendix A. As mentioned before, Figure 3.5a shows that the sample is approximately isotropic. However, on Figure 3.5b we notice that for smaller stresses, the difference between the velocities measured along the x_3-axis and the x_1- and x_2- axes is quite large. To overcome this issue, we shifted the model predictions so as to match experimental points measured for the lowest pressure.

We notice that velocities estimated using the linear approximation reasonably fit the data for maximum stresses as high as 20 MPa, even if the predictions should only be valid for stresses smaller than P_c, which equals 13.4 MPa in this case. Besides, there is a good match between velocities predicted using the Taylor series expansion and measured velocities in the direction of maximum stress for the entire range of stresses. On the other hand, we notice that the P-wave and S-wave velocities v_{33}, v_{13}, v_{31}, v_{23} and v_{32} measured along the minimum stress axis are significantly lower than the ones estimated by the model especially for high stresses. This could be partly due to the opening of cracks perpendicular to this direction as explained by Sayers [2002]. Note that the modelling approach of Sayers [2002] better captures the trend of velocity changes at high stresses; his model however requires to invert the triaxial measurements. In contrast, our model uses parameters inverted from the hydrostatic stress experiment, which is an independent measurement more routinely carried out in laboratories, so as to infer the velocity changes when the sample is subjected to triaxial stress.

3.6 Discussion

To derive this stress-induced anisotropy model, a number of assumptions were made. 1) We assumed that the rock is elastic over the entire range of applied stresses. 2) Our model was designed for anisotropy which is due only to the application of anisotropic stresses, meaning that all other causes of anisotropy were ignored. 3) The rock was assumed to be dry and interactions between cracks were neglected. 4) We modelled the effect of stress by assuming that cracks are closing in the direction perpendicular to the

applied stress. This assumption is a significant weakness of the model because cracks might open in the direction of maximum applied stress [Lockner et al., 1977, Sayers, 2002].

The model presented here allows one to predict the anisotropy for all stress levels using only five parameters. Those parameters can be obtained from hydrostatic stress tests using the analytical model of Shapiro [2003], which was tested against experimental data by Pervukhina et al. [2010] (Chapter 2, Section 2.4.1). Predictions of our model show a reasonable agreement with velocity measurements made by Chaudhry [1995] during triaxial loading in the maximum stress direction. In the minimum stress direction however, predictions deviate from measured velocities for stresses larger than 40 MPa. This could be explained by the nucleation, growth and coalescence of microcracks occurring perpendicular to this direction at high stress contrasts [Sayers, 2002]. Note that the linear approximation used for small stresses still yields good results for stresses as high as $2P_c$. The possibility of describing the stress-induced anisotropy with five physically meaningful parameters obtainable from hydrostatic stress measurements is particularly useful. Indeed, true triaxial (or polyaxial) stresses, which are the experiments which most accurately replicate in-situ stress conditions, are hard to conduct due to the complexity of the apparatus it requires and the accuracy of off-angle ultrasonic measurements is limited [Zoback, 2010]. Such measurements would however be valuable to further test our model predictions.

We showed that the anisotropy resulting from the application of a triaxial stress on a linearly elastic isotropic medium is ellipsoidal provided stresses are small enough, which confirms results previously obtained by Rasolofosaon [1998] and Sun & Prioul [2010]. This result opens up the possibility of differentiating stress-induced anisotropy from fracture-induced anisotropy by estimating the degree of anellipticity. Indeed, a fractured medium is ellipsoidal if, and only if, it is composed of two sets of identical scalar fractures or two or three sets of orthogonal scalar fractures, i.e. for each set of fractures, $B = 1$. Such configurations and fracture parameters are not very likely to be

found in reality. One still has to be careful with this result as it was derived assuming the initial rock is isotropic and stresses are small.

In addition to showing that the resulting anisotropy was ellipsoidal, we also expressed the ratios $\epsilon_{(i)}/\gamma_{(i)}$ as a function of the compliance ratio B and the Poisson's ratio of the unstressed rock. Those results allow one to fully describe the orthorhombic medium using four independent parameters instead of nine. Recent developments in sonic logging have made it possible to estimate C_{33}, C_{44}, C_{55} and C_{66} from inverting Stoneley and flexural wave dispersion curves [Pistre et al., 2005]. Knowing these four elastic constants, the model could in theory be used to fully estimate the stiffness tensor. In practice, anisotropy is unlikely to be only due to stress. Hence, great care must be applied when using this model and prior assessment of potential causes of anisotropy and their relative degree is recommended.

In areas where azimuthal anisotropy results from large differential horizontal stresses, this model can prove to be particularly useful in inferring the azimuthal P-wave anisotropy from S-wave anisotropy available from log or VSP data. Indeed, the relationships between the azimuthal anisotropy parameters $\epsilon_{(3)}$, $\delta_{(3)}$ and $\gamma_{(3)}$ (equations 3.29 to 3.33) provide an easy and straightforward way of estimating the azimuthal P-wave anisotropy. The latter is otherwise difficult to estimate as it requires multi-azimuths surveys which are expensive to acquire offshore and thus relatively rare. The development and application of this approach will be the main focus of Chapter 6.

Our model was designed for cracks in an elastic medium (porous or non-porous) and any interactions between cracks were neglected. This assumption is reasonable for dry rocks and fluid-saturated rocks if the fluid-filled cracks are hydraulically isolated. Zatsepin & Crampin [1997] tackled the issue of stress-induced anisotropy in fluid-saturated media. Their model involves a certain number of parameters, which are not easily obtained from laboratory measurements. For interconnected cracks at sufficiently low frequencies, the effect of fluid on anisotropy parameters can be modelled using the anisotropic Gassmann equations [Gassmann, 1951, Gurevich, 2003]. This will be the topic of next chapter (Chapter 4). In particular, we will show that if the dry medium is elliptical, then the

saturated medium is also elliptical, but only if the porosity is sufficiently high. This suggests that an isotropic medium subjected to small triaxial stress remains ellipsoidal even when saturated. This result is also valid at higher frequencies, for which local fluid flow, also known as squirt flow, might occur between compliant pores and adjacent stiff pores (Chapter 6).

3.7 Chapter conclusions

In this chapter, we derived a model to account for the stress dependency of seismic wave velocities in isotropic elastic media subjected to triaxial compression. We showed that this stress dependency is a function of five independent parameters: two elastic moduli of the unstressed rock, the normal and tangential compliances of grain contacts describing the initial crack distribution and the characteristic crack closing pressure. Such parameters can be inverted from hydrostatic stress tests. Comparison of the model predictions with laboratory measurements shows a relatively good agreement, though the model would benefit further testing against other datasets.

For small stresses, the model predicts ellipsoidal anisotropy, i.e. $\epsilon_{(i)} = \delta_{(i)}$ in each plane of symmetry of the resulting orthorhombic medium. The model also expresses the ratios $\epsilon_{(i)}/\gamma_{(i)}$ as a function of the Poisson's ratio of the unstressed rock and the compliance ratio. Besides, we derived relationships between anisotropy parameters ratios and stress ratios. By deriving the model for larger stresses, we showed that those results still hold for stresses as high as approximately 40 MPa depending on the matrix properties, crack geometry and compliance, as well as the stress contrast. The assumption according to which the stress sensitivity is only due to crack closure is a significant weakness of the model as cracks might open in the direction of maximum applied stress.

Such results could be used to differentiate stress-induced anisotropy from fracture-induced anisotropy. Conversely if the anisotropy is known to be due to stresses, one

could use this model to infer P-wave anisotropy from S-wave anisotropy using log or VSP data. Details about this scheme will be provided in Chapter 6.

The model developed in this chapter is only valid for dry rocks or fluid-saturated rocks with hydraulically isolated cracks. The effect of fluid on the stress-induced anisotropy pattern at low and high frequencies will be studied in Chapters 4 and 5, respectively.

Chapter 4

Effect of fluid on anisotropy in weakly anisotropic porous media at low frequencies

4.1 Chapter overview

In Chapter 3, we developed a rock physics model to account for the elastic anisotropy resulting from the application of triaxial stress on dry isotropic rocks. Since most subsurface formations are saturated with a fluid or a mixture of fluids, investigating the effect of fluid on anisotropy is of key importance. At seismic frequencies, the most commonly used approach for fluid substitution is based on the Gassmann [1951] equations derived for isotropic media (Chapter 2, Section 2.5.1.1). Yet, applying the isotropic Gassmann fluid substitution in anisotropic media can lead to considerable errors in the prediction of seismic velocities [Mavko & Bandyopadhyay, 2009, Sava et al., 2000].

In his landmark paper, Gassmann [1951] also presented solutions to account for fluid effect on elastic properties of anisotropic media (Chapter 2, Section 2.5.1.2). However,

these equations are difficult to apply due to the large number of unknown parameters it involves. In the field we usually measure the vertical P-wave and two S-wave velocities, which is insufficient to recover the complete anisotropic elastic tensor. Besides, the anisotropic Gassmann fluid substitution is usually expressed in terms of stiffness [Gassmann, 1951] or compliance [Brown & Korringa, 1975] coefficients that do not provide an intuitive understanding of how fluid influences anisotropy.

Using the anisotropic Gassmann equations, several authors modelled the effect of fluid in TI media made of aligned fractures embedded in an isotropic background [Cardona, 2002, Gurevich, 2003, Thomsen, 1995]. This approach is quite interesting because it allows to reduce the number of parameters required for the use of the anisotropic Gassmann equations. For instance, Gurevich [2003] expressed the saturated stiffness coefficients of a such a fractured TI medium as a function of the porosity, the fluid and grain bulk moduli and four parameters describing the dry medium, i.e. two elastic constants describing the isotropic dry porous matrix and two fracture parameters. These approaches are restricted to the case in which anisotropy is caused by aligned fractures. In the following, we rewrite the anisotropic Gassmann equations in terms of anisotropy parameters in order to gain a direct insight on how fluid affects anisotropy. The derivation is not limited to a specific cause of anisotropy; however, we make the crucial assumption that the anisotropy is weak. Our approach is similar to the work of Thomsen [2012], who also tried to express anisotropy parameters in saturated media as a function of those in the corresponding dry medium. His derivation is based on Brown & Korringa [1975] equations, which are expressed in terms of compliances. As a consequence, the expressions Thomsen [2012] obtained are quite complex and hard to solve.

The chapter is structured as follows. First, we use the anisotropic Gassmann equations to derive explicit expressions of anisotropy parameters in weakly anisotropic TI media saturated with a given fluid. They are expressed in terms of the P- and S-wave velocities along the symmetry axis in the dry and saturated media, the anisotropy parameters in the dry medium, the porosity and the fluid and grain bulk moduli. We also study the

effect of fluid saturation on the anellipticity parameter, which links the anisotropy parameters ϵ and δ. Then, we test the validity of the approximations derived through two different cases; the first one is the case for which anisotropy results from the application of a small uniaxial stress on an initially isotropic rock and in the second case, anisotropy arises from vertically aligned fractures embedded in an isotropic porous background. Finally, we extend this study to weakly anisotropic orthorhombic media. This chapter includes the article published by Collet & Gurevich [2013]. Further reference to this work will not be cited anymore.

4.2 Expression of Gassmann equations as a function of anisotropy parameters in transversely isotropic media

Our aim is to study the fluid dependence of anisotropy parameters. To this end, we express the anisotropy parameters in saturated media as a function of those in dry media.

Taking the P- and S-wave velocities along the x_1-axis as reference velocities, we can define the P- and S-wave moduli, L and μ, of the dry medium as

$$C_{11} = L, \tag{4.1}$$

$$C_{55} = \mu. \tag{4.2}$$

Expressions for C_{33}, C_{44} and C_{13} then follow from the definition of Thomsen [1986] anisotropy parameters in weakly anisotropic HTI media (equations 2.15, 2.16 and 2.18):

$$C_{33} = L(1 + 2\epsilon), \tag{4.3}$$

$$C_{44} = \mu(1 + 2\gamma), \tag{4.4}$$

$$C_{13} = L(1 + \delta) - 2\mu. \tag{4.5}$$

We now rewrite the anisotropic Gassmann [1951] equations given in Chapter 2, Section 2.5.1.2 as a function of the parameters L, μ, ϵ, γ and δ. By substituting equations 4.1 to 4.5 into the analogues of Biot-Willis effective stress coefficients for anisotropic media (equation 2.64), we obtain

$$\alpha_1 = 1 - \frac{C_{11} + 2C_{13}}{3K_g} = \alpha_0 - \frac{2\delta L}{3K_g}, \tag{4.6}$$

$$\alpha_2 = \alpha_3 = 1 - \frac{C_{13} + C_{23} + C_{33}}{3Kg} = \alpha_0 - \frac{(4\epsilon + \delta)L - 4\gamma\mu}{3K_g}, \tag{4.7}$$

$$\alpha_4 = \alpha_5 = \alpha_6 = 0, \tag{4.8}$$

where $\alpha_0 = 1 - \dfrac{K}{K_g}$ and $K = L - \dfrac{4\mu}{3}$ is the bulk modulus of a hypothetical isotropic dry rock with P-wave modulus L and shear modulus μ. Proceeding in the same way, we rewrite the generalized drained bulk modulus K^* (equation 2.66) as

$$K^* = K\Big(1 + 4\frac{(2\epsilon + \delta)L - 2\gamma\mu}{9K}\Big). \tag{4.9}$$

Stiffness coefficients of the saturated medium then follow from the anisotropic Gassmann [1951] equations (equation 2.63). By replacing the dry stiffness coefficients with the saturated coefficients in the definition of anisotropy and anellipticity parameters for weakly anisotropic TI media (equations 2.15, 2.16, 2.18 and 2.20), we obtain

$$\epsilon^{sat} = \frac{L}{L^{sat}}\epsilon + \frac{(\alpha_3^2 - \alpha_1^2)M}{2L^{sat}}, \tag{4.10}$$

$$\gamma^{sat} = \gamma, \tag{4.11}$$

$$\delta^{sat} = \frac{L}{L^{sat}}\delta + \frac{\alpha_1(\alpha_3 - \alpha_1)M}{L^{sat}}, \tag{4.12}$$

$$\eta^{sat} = \frac{L}{L^{sat}}\eta + \frac{(\alpha_3 - \alpha_1)^2 M}{2L^{sat}}. \tag{4.13}$$

Using expressions of α_1 and α_3 given by equations 4.6 and 4.7, we can write η^{sat} as a function of the anisotropy parameters in the dry medium so that

$$\eta^{sat} = \frac{L}{L^{sat}}\eta + \frac{1}{2L^{sat}}\frac{((\delta - 4\epsilon)L + 4\gamma\mu)^2 M}{9K_g^2}. \tag{4.14}$$

Since we assume that the anisotropy is weak, we can linearize α_1^2 and α_3^2 in equation 4.10, which yields

$$\epsilon^{sat} = \frac{L}{L^{sat}}\epsilon + \frac{\alpha_0}{L^{sat}}\frac{((\delta - 4\epsilon)L + 4\gamma\mu)M}{3K_g}. \tag{4.15}$$

In a similar way, δ^{sat} is given by

$$\delta^{sat} = \frac{L}{L^{sat}}\delta + \frac{\alpha_0}{L^{sat}}\frac{((\delta - 4\epsilon)L + 4\gamma\mu)M}{3K_g}. \tag{4.16}$$

Equations 4.11 and 4.14 to 4.16 show how fluid affects the anisotropy parameters. Note that the main assumption used in the derivation (in addition to the assumptions of Gassmann's theory) is the weak anisotropy assumption. Uncertainties resulting from this approximation are discussed in Section 4.4. We can further simplify these equations in order to get a more intuitive insight on the fluid dependence of anisotropy parameters.

Analysis of the derived equations

Analysis of equation 4.14 suggests that the second term in the expression for the anellipticity parameter is quadratic in anisotropy parameters, and thus can be neglected for weak anisotropy. However, this requires Gassmann's pore space modulus M to be of the same order of magnitude as (or smaller than) the other moduli. Hence, let us consider the value of M defined in equation 2.65. From the expression of the generalized drained bulk modulus (equation 4.9), assuming weak anisotropy, we have

$$K^* \approx K. \tag{4.17}$$

Besides, in most cases, $K_f \ll K_g$, so M reduces to

$$M \approx \frac{K_f}{\phi}. \tag{4.18}$$

Mineral	Bulk modulus K_g (GPa)	Poisson ratio ν_g	Characteristic porosity %
Quartz	37.0	0.10	1.24
Feldpsar	37.5	0.35	1.03
Calcite	70.0	0.30	0.99
Dolomite	80.0	0.25	0.78

TABLE 4.1: Characteristic porosities for which the approximation $\eta^{sat} = (L/L^{sat})\eta$ becomes valid for different minerals. To compute these values, we assume that: $K \approx K_g$, $K_f = 2.25$ GPa and $O(\epsilon, \delta, \gamma, \eta) \approx 0.1$.

By replacing the pore space modulus M by this approximation 4.18 in equations 4.10 to 4.13, it is clear that the anisotropy degree is affected to a greater extent when the fluid bulk modulus K_f is high. Also, substituting equation 4.18 into the anellipticity parameter given by equation 4.14 and assuming that the anisotropy parameters ϵ, δ, γ and η in the dry medium have the same order of magnitude, we obtain

$$\eta^{sat} = \frac{L}{L^{sat}}\eta\Big(1 + \frac{1}{6}\frac{1+\nu}{1-\nu}\frac{K}{K_g}\frac{K_f}{K_g}\frac{O(\epsilon,\delta,\gamma,\eta)}{\phi}\Big), \tag{4.19}$$

where $\nu = \dfrac{L-2\mu}{2L-2\mu}$ is the Poisson's ratio of a hypothetical isotropic dry rock with P-wave modulus L and shear modulus μ. To derive the following equations, we assume this Poisson's ratio is close to the Poisson's ratio of the mineral grains ν_g as it is sometimes observed [Krief et al., 1990, Pickett, 1963]. Hence, the second term in the right hand side of equation 4.14 is negligible when

$$\phi \gg \frac{1}{6}\frac{1+\nu_g}{1-\nu_g}\frac{K}{K_g}\frac{K_f}{K_g}O(\epsilon,\delta,\gamma,\eta). \tag{4.20}$$

In this case, η^{sat} can be approximated by

$$\eta^{sat} = \frac{L}{L^{sat}}\eta. \tag{4.21}$$

Table 4.1 shows threshold porosities above which this approximation becomes valid for different minerals. The bulk modulus and the Poisson's ratio of the different minerals are computed using values listed in Mavko et al. [2003]. We assume that

$O(\epsilon, \delta, \gamma, \eta) \approx 0.1$, $K \approx K_g$ and the saturating fluid is water ($K_f = 2.25$ GPa). For the minerals considered here, we notice that the approximation only breaks down at very low porosities (less than 1%). However, pore connectivity can become poor for such cases, which might violate Gassmann's assumption of pore-pressure equilibrium.

As mentioned earlier, the anisotropy resulting from the application of a small uniaxial compressive stress on a dry isotropic medium is elliptical, which yields $\eta = 0$. One of the aims of this work is to check if this statement is still valid for saturated media for which we cannot neglect the interactions between cracks. The expression derived for η^{sat} (equation 4.14) shows analytically that the saturated medium remains elliptical if the second term is negligible, i.e. if the condition given by equation 4.20 is fulfilled. Note that this condition might not be satisfied if the porosity is very low. As discussed previously, for such porosities, the pore space might be poorly connected so Gassmann's theory may not be applicable. However, there are some cases in which Gassmann's fluid substitution is still valid even at low porosities. The first one is the case for which the porosity is low, but the pore space is such that pores are still entirely connected. In this case, frequencies for which Gassmann's theory is applicable are very low. The second case is the case for which the pore space is permeated by identical aligned fractures. Since all fractures have the same shape, the fluid pressure is uniform throughout the pore space despite the lack of hydraulic connectivity [Thomsen, 1995]. This case is discussed in more details in Section 4.3.2.

4.3 Numerical illustrations

We illustrate the effect of fluid on anisotropy parameters and the accuracy of the approximations derived earlier through two different cases. In both of them, we use the anisotropy and anellipticity parameters ϵ^{sat}, δ^{sat} and η^{sat} derived in the previsous section (equations 4.10, 4.12 and 4.13) and compare them to the exact solution given by the anisotropic Gassmann equations. In addition, we check the validity of the linearizations of ϵ^{sat}, δ^{sat} and η^{sat} (equations 4.15, 4.16 and 4.21). In the first example,

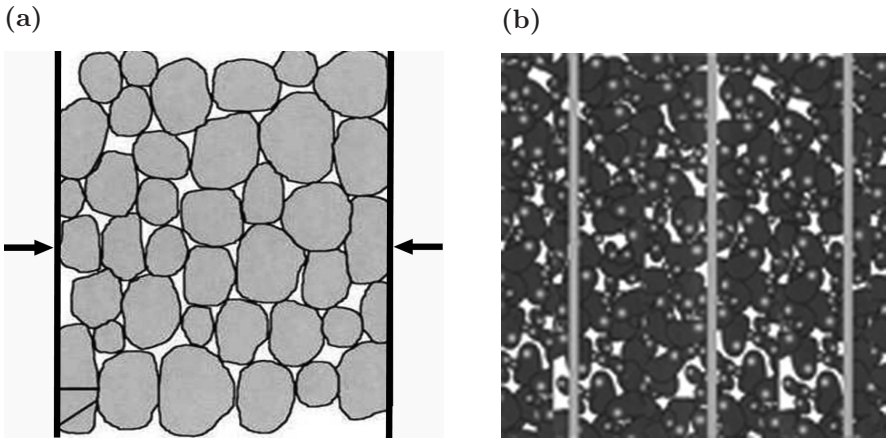

FIGURE 4.1: (a) Cartoon representation of the stress-induced anisotropy model; when stress is applied, grain contacts are closing in the direction perpendicular to the applied stress. (b) Cartoon representation of the model of aligned fractures embedded in an isotropic porous background. From Gurevich, Brajanovski, et al. [2009].

anisotropy results from the application of a small uniaxial stress on an initially isotropic rock. We model this stress-induced anisotropy effect using the theory developed by Gurevich et al. [2011] (Chapter 2, Section 2.4.2). In the second model, anisotropy arises from vertically aligned fractures embedded in an isotropic porous background. For this case, we use the numerical model of Gurevich [2003], which employs the linear-slip deformation theory, also known as excess compliance theory, to model fractures (Chapter 2, Section 2.3).

4.3.1 Stress-induced anisotropy case

In this example, we compute the anisotropy resulting from the application of a small uniaxial stress varying from 0 to 25 MPa on a sample of Barre Granite. This results in the preferential closure of cracks or compliant grain contacts perpendicular to the applied stress, leading to a TI symmetry. Figure 4.1a shows a cartoon representation of this case. Anisotropic dry elastic constants are computed using Gurevich et al. [2011] model (Chapter 2, Section 2.4.2). The input parameters required for this model are the bulk and shear moduli, K_0 and μ_0, and the tangential compliance Z_{T0} of the unstressed rock, the compliance ratio B and the characteristic crack closing pressure

K_0 (GPa)	μ_0 (GPa)	B	P_c (MPa)	Z_{T0} (GPa^{-1})
13.8	18.3	1.76	18.2	0.025

TABLE 4.2: Input parameters used to model the effect of fluid at low frequencies in the stress-induced anisotropy case. These values were previously obtained by Gurevich et al. [2011], who inverted velocities measured by Coyner [1984] on a dry sample of Barre Granite subjected to hydrostatic load

P_c. Values used for this analysis are listed in Table 4.2. They were previously obtained by Gurevich et al. [2011], who inverted velocities measured by Coyner [1984] on a dry sample of Barre Granite subjected to hydrostatic load. The anisotropy parameters predicted by the stress-induced anisotropy model are relatively small ($|\epsilon|, |\delta|, |\gamma| \leq 0.1$) and they are linked by the relationships:

$$\epsilon = \delta, \tag{4.22}$$

$$\frac{\epsilon}{\gamma} = 2\frac{2\nu_0 B + 6B - 2\nu_0 + 1}{(1-\nu_0)(3+4B)}, \tag{4.23}$$

where ν_0 is the Poisson's ratio of the unstressed dry rock.

Figure 4.2 shows the P-wave anisotropy (black lines) and anellipticity (grey lines) parameters in the dry and saturated media as a function of the applied stress. The thick solid lines show the values in the dry medium. The thin solid, dashed and dotted lines respectively refer to the solutions obtained for ϵ^{sat} and η^{sat} using the exact Gassmann equations, the expressions derived in Section 4.2 (equations 4.10 and 4.13) and their linearizations (equations 4.15 and 4.21). We plot the absolute values of ϵ in order to compare them with values of η. However, since cracks are closing in the direction of the applied stress i.e. the x_1-direction, P-waves propagate faster along the x_1-axis, which leads to negative ϵ values. Besides, due to the stress-induced preferential orientation of cracks, the stiffening effect of fluid is more pronounced along the x_2- and x_3-directions, which explains why the P-wave anisotropy is reduced by 20% to 30% when the medium is saturated. We can also observe that there is a reasonable match between the exact solution and the linearization of ϵ^{sat} given by equation 4.15, especially at low stresses for which the anisotropy is weaker.

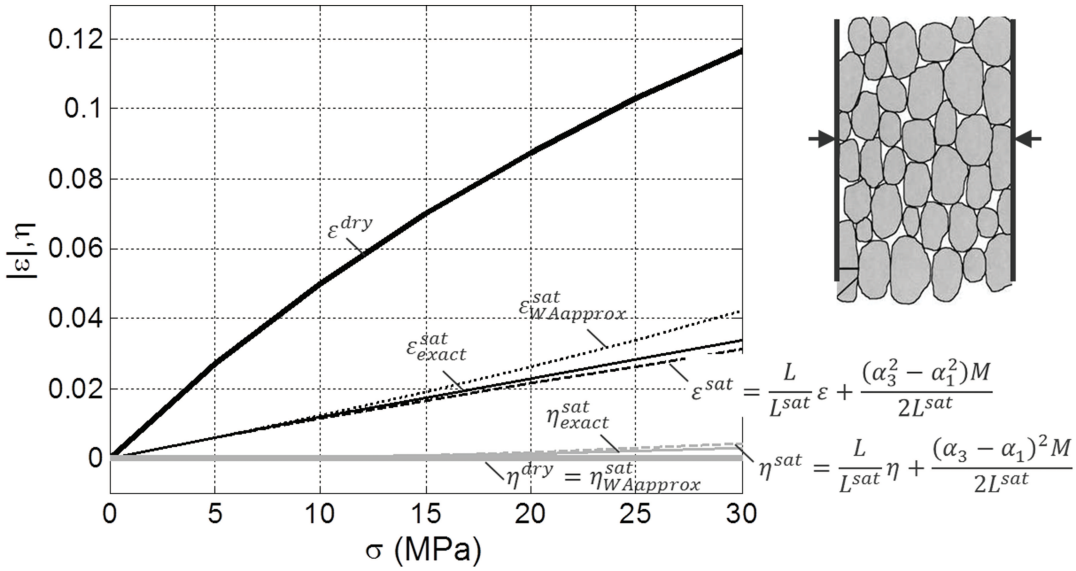

FIGURE 4.2: P-wave anisotropy parameter ϵ (black lines) and anellipticity parameter η (grey lines) versus applied stress in a TI medium resulting from the application of a uniaxial stress on an initially isotropic medium. The solid lines show the values in the dry medium. The thin solid, dashed and dotted lines respectively refer to the solutions using the exact Gassmann equations, the expressions given by equations 4.10 and 4.13 and their linearizations (equations 4.15 and 4.21).

Furthermore, note that even though the porosity for this sample is low, e.g. $\phi = 0.6\%$ [Nur & Simmons, 1969], it still falls into the range of validity of the η^{sat}-approximation given by equation 4.21. Hence, as illustrated by Figure 4.2, the approximated values of the anellipticity parameter match the exact values given by Gassmann's equations reasonably well; thus, because the dry medium is elliptical, the saturated medium is also elliptical.

4.3.2 Anisotropy caused by aligned fractures

We now consider an isotropic porous medium containing a set of parallel vertical fractures as illustrated by Figure 4.1b. As explained in Chapter 2, Section 2.3, this type of TI medium is fully described by four independent parameters: two elastic constants of the isotropic background, say the P- and S-wave moduli L_b and μ_b, and two fracture

parameters Δ_N and Δ_T. These parameters, respectively called normal and tangential weaknesses, describe how fractures weaken the background rock. In such HTI media, the five elastic coefficients are expressed as

$$C_{11} = L_b(1-\Delta_N), \tag{4.24}$$

$$C_{13} = \lambda_b(1-\Delta_N), \tag{4.25}$$

$$C_{33} = L_b(1-\chi_b^2\Delta_N), \tag{4.26}$$

$$C_{44} = \mu_b, \tag{4.27}$$

$$C_{55} = \mu_b(1-\Delta_T), \tag{4.28}$$

where $\lambda_b = L_b + 2\mu_b$ and $\chi_b = \lambda_b/L_b$ (equation 2.33). Normal and tangential weaknesses are linked to normal and shear compliances through the relationships:

$$Z_N = \frac{\Delta_N}{L_b(1-\Delta_N)}, \tag{4.29}$$

$$Z_T = \frac{\Delta_T}{\mu_b(1-\Delta_T)}. \tag{4.30}$$

In this example, we study the effect of background porosity on the anisotropy parameters ϵ and δ and the anellipticity parameter η in the saturated medium. To do so, we use the same approach as Gurevich [2003] to compute the dry-rock elastic coefficients, i.e. we modify the normal fracture weakness Δ_N so that $\epsilon^{dry} = 0.1$ for each porosity. We choose Krief et al. [1990] empirical relations as a convenient model to express the dependence of elastic parameters of the uncracked porous background upon porosity:

$$K_b = (1-\beta)K_g, \tag{4.31}$$

$$\mu_b = (1-\beta)\mu_g, \tag{4.32}$$

where β is Biot's coefficient empirically related to the background porosity ϕ_P by

$$\beta = 1-(1-\phi_P)^{\frac{3}{1-\phi_P}}. \tag{4.33}$$

Background parameters	K_g (GPa)	μ_g (GPa)	ϕ_P
	40	40	0 to 0.4
Fracture parameters	B	ϕ_C	
	0.5 and 1	0.0001	

TABLE 4.3: Input parameters used to model the effect of fluid at low frequencies in the case for which anisotropy results from the presence of aligned fractures embedded in an isotropic porous background.

Table 4.3 specifies parameters that we used for this analysis. The value of the compliance ratio is held constant; we test two values: $B = 0.5$, which is a common value for sandstones [Angus et al., 2009, Sayers & Han, 2002], and $B = 1$, which leads to the particular case of elliptical anisotropy. For each background porosity, we compute the anisotropy parameters ϵ^{sat} and δ^{sat} and the anellipticity parameter η^{sat} in the saturated medium using the exact solution given by the anisotropic Gassmann equations and taking water as the saturating fluid. We then compare it to the expressions derived in Section 4.2 (equations 4.10, 4.12 and 4.13) and their respective linearizations (Equations 4.15, 4.16 and 4.21). Results are plotted in Figure 4.3. The black lines show values of the anisotropy and anellipticity parameters in the dry medium, while the blue, dashed green and dashed brown lines respectively refer to saturated values obtained using the exact solution, the solution derived in the present study and its weak-anisotropy linearization.

Figure 4.3a and 4.3b shows the parameter ϵ in the dry and saturated media as a function of background porosity for compliance ratios respectively equal to 0.5 and 1. Results are similar to those obtained by Gurevich [2003]. At low background porosities, we observe that ϵ^{sat} sharply increases from 0 to a value almost as high as ϵ^{dry}. This is due to the fact that at low background porosities, fractures are hydraulically isolated. Hence, the presence of fluid highly stiffens the fractures as the fluid cannot escape into the pores when compressed. In this case, the normal compliance Z_N tends to zero [Schoenberg & Douma, 1988], which means that P-waves propagating parallel and perpendicular to the fractures almost have the same velocities. This result was also found by Thomsen [1995] who calculated anisotropy parameters in porous rocks permeated by aligned penny-shaped cracks. At higher background porosities, ϵ^{sat} decreases gradually due

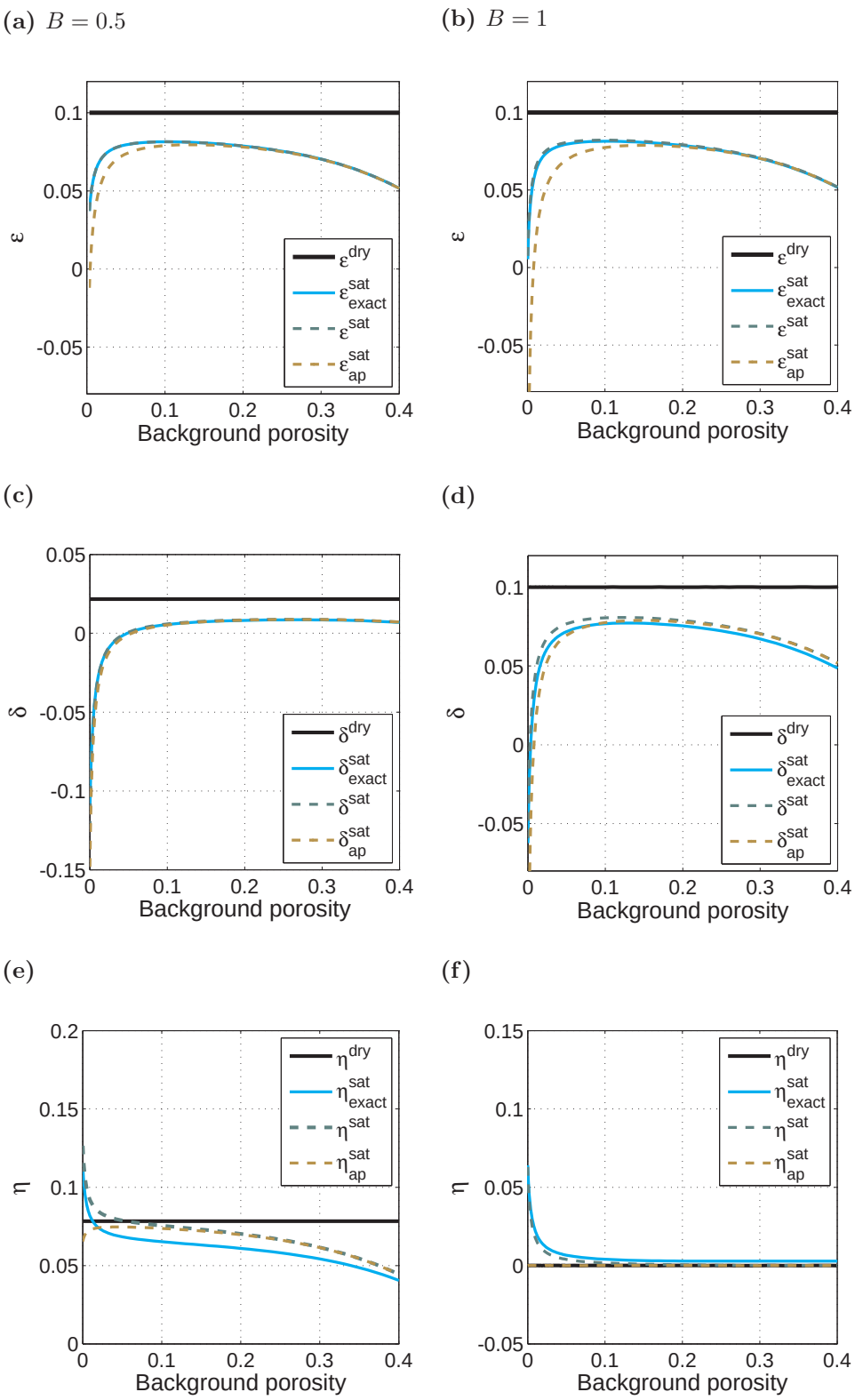

FIGURE 4.3: Anisotropy and anellipticity parameters ϵ, δ and η in the dry and saturated media as a function of background porosity for the case of aligned fractures with compliance ratios $B = 0.5$ (left) and $B = 1$ (right). In Figure 4.3f, $\eta^{dry} = \eta^{sat}_{ap} = 0$.

to fluid saturation. Indeed, the more porous the rock, the greater the effect of the saturating fluid on the overall properties of the rock. The pore fluid being isotropic, it tends to lower the degree of anisotropy. Note that, as shown previously by Gurevich [2003], ϵ only depends on the normal weakness Δ_N, which explains why the exact solution for ϵ^{sat} remains the same regardless of the value of the compliance ratio B. On the other hand, the solutions derived in Section 4.2 (equations 4.10 and 4.15) depend on the compliance ratio B through the anisotropy parameters δ and γ. This dependence is however noticeable only when looking at the approximation (dashed brown lines) at low porosities, i.e. at porosities for which equation 4.15 is not valid.

Figure 4.3c and 4.3d shows the parameter δ in the dry and saturated media as a function of background porosity for compliance ratios respectively equal to 0.5 and 1. Unlike ϵ^{sat}, δ^{sat} does not equal to zero when cracks are isolated, i.e. when $\phi_P = 0$, because δ also depends on the shear component Δ_T. Results obtained with the expression given by equation 4.12 and its linearization (equation 4.16) match the exact solution really well for the case $B = 0.5$. However, increasing the compliance ratio results in an increase of δ in the dry medium. Consequently, the weak anisotropy approximation of δ given by equation 2.18 is not as accurate in the case $B = 1$.

Figure 4.3e and 4.3f shows the parameter η in the dry and saturated media as a function of background porosity, respectively obtained for $B = 0.5$ and $B = 1$. We first see that equation 4.13 slightly deviates from the exact solution, especially for $B = 0.5$. This deviation is due to the lack of accuracy of the weak anisotropy approximation of the anellitpticity parameter η given by equation 2.20. Despite this, we observe that the linearization of η^{sat} given by equation 4.21 reasonably matches the exact solution for porosities as low as 1%. Note that for this case, the threshold porosity given by equation 4.20 below which the approximation breaks down is 1.2%. Again, we notice that if the dry medium is elliptical ($B = 1$), the saturated medium is also elliptical but only if the porosity is sufficiently high. Indeed, in the case of isolated identical fractures for which the background porosity equals zero, the dry medium is elliptical ($\eta^{dry} = 0$)

when $B = 1$, but the anellipticity parameter in the saturated medium is not negligible ($\eta^{dry} = 0.06$), which means that the saturated medium is non-elliptical.

4.4 Discussion on uncertainties

In the previous section, Section 4.2, we presented expressions giving a certain understanding on how fluid affects anisotropy parameters. To derive these equations, we followed the assumptions of monomineralic rocks and low frequency, which are inherent to Gassmann's fluid substitution (Chapter 2, Section 2.5.1). Seismic and log frequencies may or may not fall within the range of validity, depending on the matrix permeability, the fluid viscosity and the characteristic fracture or crack dimension [Gurevich, Brajanovski, et al., 2009, Maultzsch et al., 2003, Mavko et al., 2003]. In addition, we assumed that the anisotropy was sufficiently weak, i.e. $\epsilon, \delta, \gamma \ll 1$. This crucial assumption first yields uncertainties when determining the elastic parameter C_{13} using equation 4.5. These uncertainties are illustrated in Figure 4.4a for the stress-induced anisotropy example, in which we can observe the relative error on C_{13} reaches up to 13% for the highest stresses, with a corresponding error on δ^{dry} of 8.6%. The weak-anisotropy assumption further engenders errors when estimating the anisotropy parameters ϵ^{sat} and δ^{sat} in the saturated medium using equations 4.10 and 4.12. As observed in Figure 4.4b and 4.4c, ϵ^{sat} is better resolved than δ^{sat}. This is due to the fact that no approximation is used to derive equation 4.10; the only error on ϵ^{sat} thus results from the uncertainty on C_{13} (through the parameters α_1 and α_3). In contrast, the error on δ^{sat} not only results from the uncertainty on C_{13} but also stems from the weak anisotropy approximation for δ (equation 2.18) that we use to derive equation 4.12.

Figure 4.5a, 4.5b and 4.5c shows uncertainties on ϵ^{sat}, δ^{sat} and η^{sat} for the case of aligned fractures embedded in an isotropic porous background for which the compliance ratio is $B = 0.5$. In this example, δ^{dry} is low ($\delta^{dry} = 0.02$), yielding a relative uncertainty on C_{13} that does not exceed 0.3%. As mentioned previously, the error on

(a)

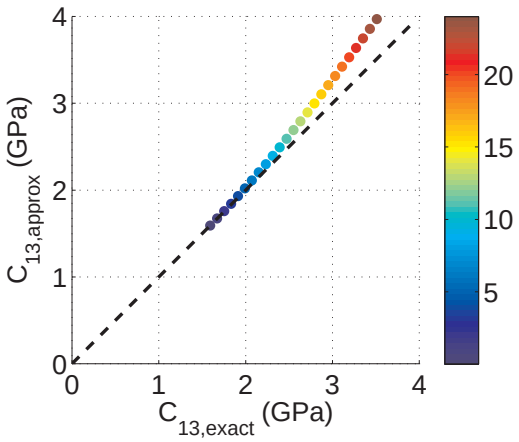

(b)

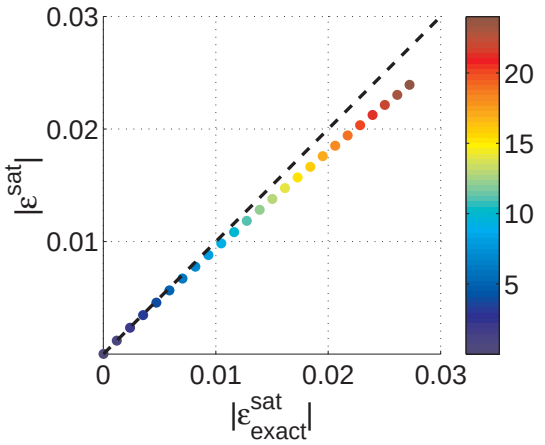

(c)

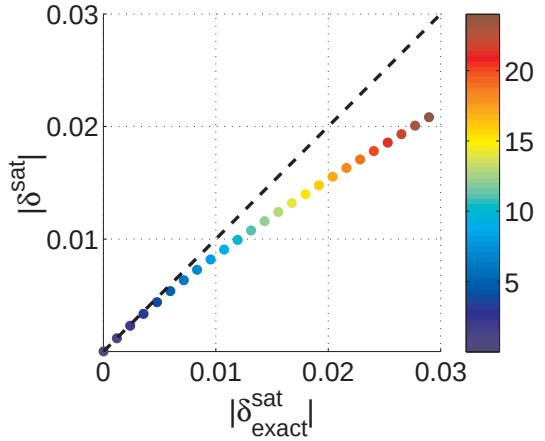

FIGURE 4.4: Illustration of the uncertainties for the stress-induced anisotropy case: comparison of (a) C_{13} given by equations 4.5 and 2.17, (b) ϵ^{sat} given by equation 4.10 and the exact solution given by the anisotropic Gassmann equation, (c) δ^{sat} given by equation 4.12 and the exact solution given by the anisotropic Gassmann equations. The color scale shows the applied stress in MPa.

(a)

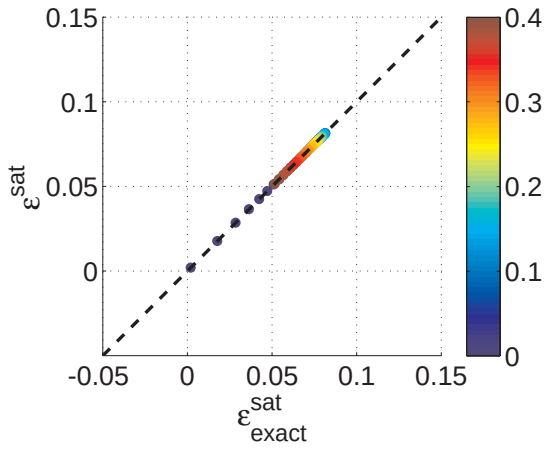

(b)

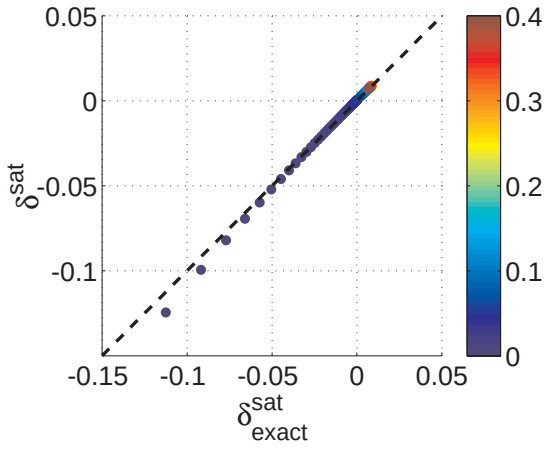

(c)

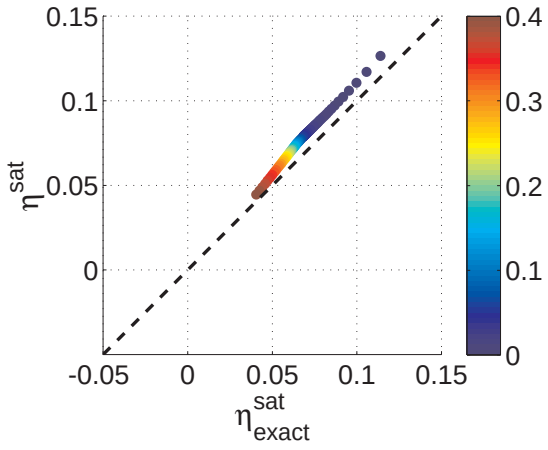

FIGURE 4.5: Illustration of the uncertainties for the case of aligned fractures ($B = 0.5$): comparison of ϵ^{sat} (a), δ^{sat} (b) and η^{sat} (c) respectively given by equations 4.10, 4.12 and 4.13 and the exact solutions given by the anisotropic Gassmann equations. The color scale shows the background porosity.

δ^{sat} is larger than the one on ϵ^{sat}, especially for small porosities. As for η^{sat}, we use the weak anisotropy approximation of the anellipticity parameter given by equation 2.20 to derive equation 4.19. The error on η^{sat} is potentially higher than the ones on ϵ^{sat} and δ^{sat}. However, for the three examples presented in this paper, the largest absolute error on η^{sat} is obtained for the case of aligned fractures embedded in an isotropic background with $B = 0.5$ and this absolute error does not exceed 0.01, which is still reasonable. Besides, it is important to emphasize that equations 4.5 to 4.9 and 4.12 to 4.14 are only valid for weak anisotropy. As for the linearizations of ϵ^{sat}, δ^{sat} and η^{sat} given by equations 4.15, 4.16 and 4.21, they also involve some assumptions on poroelastic coefficients in addition to the weak anisotropy assumption, which yields different validity conditions.

4.5 Extension to orthorhombic media

The aim of this section is to express the anisotropy parameters in saturated orthorhombic media as a function of those in the dry medium. Results presented in this section are a direct extension of those obtained in Section 4.2 for TI symmetry. The derivation follows the same steps as the one described above, one of the main assumptions being that the anisotropy is weak (i.e. $\epsilon_{(i)}$, $\delta_{(i)}$, $\gamma_{(i)} \ll 1$).

As suggested by Tsvankin [1997], we take the vertical P-wave velocity and the velocity of the vertically propagating S-wave polarized in the x_1-direction as reference velocities (Figure 4.6). The reference P- and S-wave moduli are thus defined as

$$C_{33} = L, \tag{4.34}$$

$$C_{55} = \mu. \tag{4.35}$$

Expressions of the seven remaining stiffness constants required to describe the medium follow from the definition of anisotropy parameters in weakly anisotropic orthorhombic

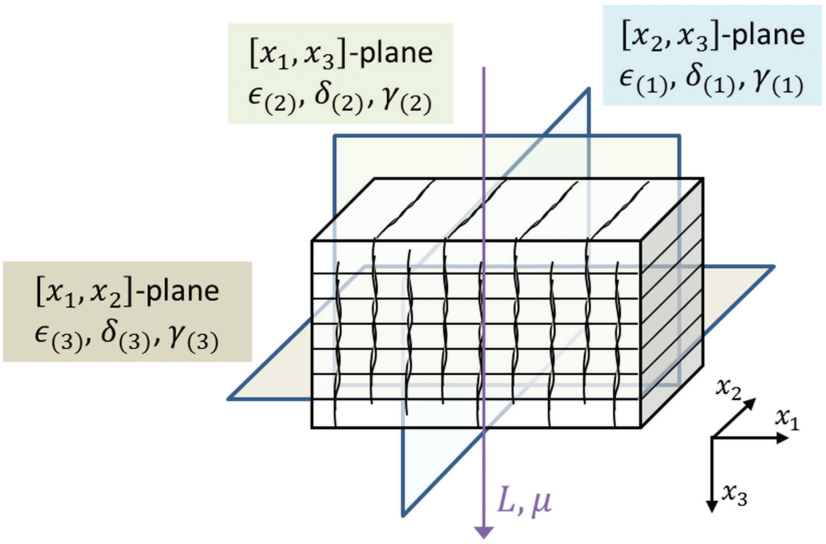

FIGURE 4.6: Sketch of an orthorhombic medium made of aligned vertical fractures embedded in a VTI background. The anisotropic Gassmann equations are rewritten in terms of the reference moduli and anisotropy parameters that are shown here.

media (equations 2.21 and 2.22):

$$C_{11} = L(1 + 2\epsilon_{(2)}), \tag{4.36}$$

$$C_{22} = L(1 + 2\epsilon_{(1)}), \tag{4.37}$$

$$C_{44} = \mu(1 + 2\gamma_{(3)}), \tag{4.38}$$

$$C_{66} = \mu(1 + 2\gamma_{(1)}), \tag{4.39}$$

$$C_{23} = L(1 + \delta_{(1)}) - 2\mu(1 + 2\gamma_{(3)}), \tag{4.40}$$

$$C_{13} = L(1 + \delta_{(2)}) - 2\mu, \tag{4.41}$$

$$C_{12} = L(1 + 2\epsilon_{(2)})(1 + \delta_{(3)}) - 2\mu(1 + 2\gamma_{(1)}). \tag{4.42}$$

Note that because we are assuming that the anisotropy is weak, the product $\epsilon_{(2)}\delta_{(3)}$ is neglected in the following.

Rewriting the Biot-Willis effective stress coefficients for orthorhombic media (equation 2.64) in terms of anisotropy parameters yields

$$\alpha_1 = \alpha_0 - \frac{(4\epsilon_{(2)} + \delta_{(2)} + \delta_{(3)})L - 4\mu\gamma_{(1)}}{3K_g} \tag{4.43}$$

$$\alpha_2 = \alpha_0 - \frac{(2\epsilon_{(1)} + 2\epsilon_{(2)} + \delta_{(1)} + \delta_{(3)})L - 4\mu(\gamma_{(1)} + \gamma_{(3)})}{3K_g} \tag{4.44}$$

$$\alpha_3 = \alpha_0 - \frac{(\delta_{(1)} + \delta_{(2)})L - 4\mu\gamma_{(3)}}{3K_g} \tag{4.45}$$

$$\alpha_4 = \alpha_5 = \alpha_6 = 0 \tag{4.46}$$

where $\alpha_0 = 1 - \dfrac{K}{K_g}$ and $K = L - \dfrac{4G}{3}$ is the reference bulk modulus of the dry medium. The generalized drained bulk modulus K^* given by equation 2.66 can be expressed as

$$K^* = K\Big(1 + 2\frac{(\epsilon_{(1)} + 3\epsilon_{(2)} + \delta_{(1)} + \delta_{(2)} + \delta_{(3)})L - 4(\gamma_{(1)} + \gamma_{(3)})\mu}{9K}\Big). \tag{4.47}$$

We then substitute equations 4.43 to 4.47 into the expression for Gassmann's fluid storage modulus M (equation 2.65) and the expression of the saturated stiffness components given by the anisotropic Gassmann equation (equation 2.63).

Anisotropy parameters in the saturated medium are obtained by replacing the dry stiffness coefficients by the saturated coefficients in the definition of anisotropy parameters in weakly anisotropic, orthorhombic media (equations 2.21 and 2.22). We also calculate the anellipticity parameters given by the following formula when the anisotropy is assumed to be weak:

$$\eta_{(i)} = \epsilon_{(i)} - \delta_{(i)}, \tag{4.48}$$

where $i = 1, 2, 3$ respectively correspond to the $[x_2, x_3]$-, $[x_1, x_3]$-, $[x_1, x_2]$-planes. Below are the results for each plane of symmetry:

- $[x_2, x_3]$-plane,

$$\epsilon_{(1)}^{sat} = \frac{L}{L^{sat}}\epsilon_{(1)} + \frac{(\alpha_2^2 - \alpha_3^2)M}{2L^{sat}}, \tag{4.49}$$

$$\delta_{(1)}^{sat} = \frac{L}{L^{sat}}\delta_{(1)} + \frac{\alpha_3(\alpha_2 - \alpha_3)M}{L^{sat}}, \tag{4.50}$$

$$\gamma_{(1)}^{sat} = \gamma_{(1)}, \tag{4.51}$$

$$\eta_{(1)}^{sat} = \frac{L}{L^{sat}}\eta_{(1)} + \frac{(\alpha_2 - \alpha_3)^2 M}{2L^{sat}}; \tag{4.52}$$

- $[x_1, x_3]$-plane,

$$\epsilon_{(2)}^{sat} = \frac{L}{L^{sat}}\epsilon_{(2)} + \frac{(\alpha_1^2 - \alpha_3^2)M}{2L^{sat}}, \tag{4.53}$$

$$\delta_{(2)}^{sat} = \frac{L}{L^{sat}}\delta_{(2)} + \frac{\alpha_3(\alpha_1 - \alpha_3)M}{L^{sat}}, \tag{4.54}$$

$$\gamma_{(2)}^{sat} = \gamma_{(2)}, \tag{4.55}$$

$$\eta_{(2)}^{sat} = \frac{L}{L^{sat}}\eta_{(2)} + \frac{(\alpha_1 - \alpha_3)^2 M}{2L^{sat}}; \tag{4.56}$$

- $[x_1, x_2]$-plane,

$$\epsilon_{(3)}^{sat} = \frac{L(1+2\epsilon_{(2)})}{L^{sat}(1+2\epsilon_{(2)}^{sat})}\epsilon_{(3)} + \frac{(\alpha_2^2 - \alpha_1^2)M}{2L^{sat}(1+\epsilon_{(2)}^{sat})}, \tag{4.57}$$

$$\delta_{(3)}^{sat} = \frac{L(1+2\epsilon_{(2)})}{L^{sat}(1+2\epsilon_{(2)}^{sat})}\delta_{(3)} + \frac{\alpha_1(\alpha_2 - \alpha_1)M}{L^{sat}(1+2\epsilon_{(2)}^{sat})}, \tag{4.58}$$

$$\gamma_{(3)}^{sat} = \gamma_{(3)}, \tag{4.59}$$

$$\eta_{(3)}^{sat} = \frac{L(1+2\epsilon_{(2)})}{L^{sat}(1+2\epsilon_{(2)}^{sat})}\eta_{(3)} + \frac{(\alpha_2 - \alpha_1)^2 M}{2L^{sat}(1+2\epsilon_{(2)}^{sat})}. \tag{4.60}$$

The anisotropy is assumed to be weak, so equations 4.57 to 4.59 can be written in the same form as equations 4.49 to 4.51 and 4.53 to 4.55. Besides, by linearizing $(\alpha_j - \alpha_k)^2$ in terms of small anisotropy parameters in the expressions for the saturated anellipticity parameters $\eta_{(i)}^{sat}$ (equations 4.52, 4.56, and 4.60), it is easy to demonstrate that $\eta_{(i)}^{sat} = (L/L^{sat})\eta_{(i)}$. As a consequence, if the dry medium is ellipsoidal (i.e. $\eta_{(i)} = 0$ in each plane of symmetry), then the saturated medium is also ellipsoidal. It is also

possible to simplify expressions for parameters $\epsilon_{(i)}^{sat}$ and $\delta_{(i)}^{sat}$ by linearizing the quantities α_j^2 and products $\alpha_j\alpha_k$ in terms of small anisotropy parameters. Analytical results for these approximations are rather cumbersome and thus they will not be shown; however, they will be illustrated in the next section.

4.6 Numerical illustrations for the orthorhombic case

The effect of fluid on orthorhombic anisotropy parameters is illustrated through two numerical examples. The first one simulates the orthorhombic anisotropy resulting from the application of triaxial stress on an isotropic medium. Dry elastic properties for this case are calculated using expressions developed in the previous chapter (Chapter 3, Section 3.3). In the second example, we model the case of aligned fractures embedded in a VTI background using the linear slip deformation theory (Chapter 2, Section 2.3).

4.6.1 Stress-induced anisotropy case

In this example, we examine the influence of fluid on orthorhombic anisotropy parameters in an isotropic medium subjected to triaxial stress. Input parameters for this example are listed in Table 4.4. The medium parameters correspond to values inverted from velocities measured by Chaudhry [1995] on a dry sample of Penrith sandstone (see Chapter 3, Section 3.5.1). The maximum stress is assumed to be applied along the x_1-axis; it varies from 5 to 25 MPa. The other two stresses are defined via the stress ratios $a_h = \sigma_{22}/\sigma_{11}$ and $a_v = \sigma_{33}/\sigma_{11}$. These stress ratios are calculated from

Medium parameters	K_0 (GPa)	μ_0 (GPa)	B	P_c (MPa)	Z_{T0} (GPa^{-1})
	11.1	10.8	0.48	13.4	0.086
Stress state	σ_{11} (MPa)	a_h	a_v		
	5-25	0.32	0.62		

TABLE 4.4: Input parameters used to model the effect of fluid at low frequencies in the case for which anisotropy results from the application of triaxial stress on an isotropic medium.

VTI background parameters	v_{33} (km/s) 4.8	v_{31} (km/s) 3.2	ϵ_v 0.13	δ_v 0.1	γ_v 0.07
Fracture parameters	Δ_N 0-0.2	B 0.5			

TABLE 4.5: Input parameters used to model the effect of fluid at low frequencies in the case for which anisotropy results from the presence of aligned vertical fractures embedded in a VTI background.

the in-situ stress state estimated at the Macedon reservoir depth in Stybarrow field (Chapter 6, Section 6.3.1). Note that these values are just taken as a realistic example; we do not intend to model the anisotropy observed in the Stybarrow field here.

Figure 4.7a, 4.7b and 4.7c shows the P-wave anisotropy and anellipticity parameters calculated in each plane of symmetry of the orthorhombic medium. The trend for these parameters resembles the one of the parameters ϵ and η computed for a sample of Barre granite subjected to uniaxial stress (Figure 4.2). However, we notice that the match between the P-wave anisotropy parameters $\epsilon_{(i)}$ given by the original anisotropic Gassmann equations, the expressions derived in the previous section (equations 4.49, 4.53 and 4.57) and their linearizations is better than the one observed in Figure 4.2 for the Barre granite subjected to uniaxial stress. This better accuracy could be due to the facts that 1) the anisotropy is weaker and 2) the porosity in the Penrith sandstone ($\phi = 13\%$) is higher than the one of the Barre granite ($\phi = 0.6\%$). Again, we notice that the anellipticity parameters in each plane of symmetry remain close to zero in the dry and saturated media. This observation suggests that the anisotropy resulting from the application of small triaxial stress on an initially isotropic medium remains ellipsoidal even when the medium is saturated.

4.6.2 Case of vertical aligned fractures embedded in a VTI background

In this section, we study the effect of fluid in the case for which the orthorhombic anisotropy results from vertical aligned fractures embedded in a VTI background (Figure 4.6). This case is of particular interest as it is the simplest way to model elastic

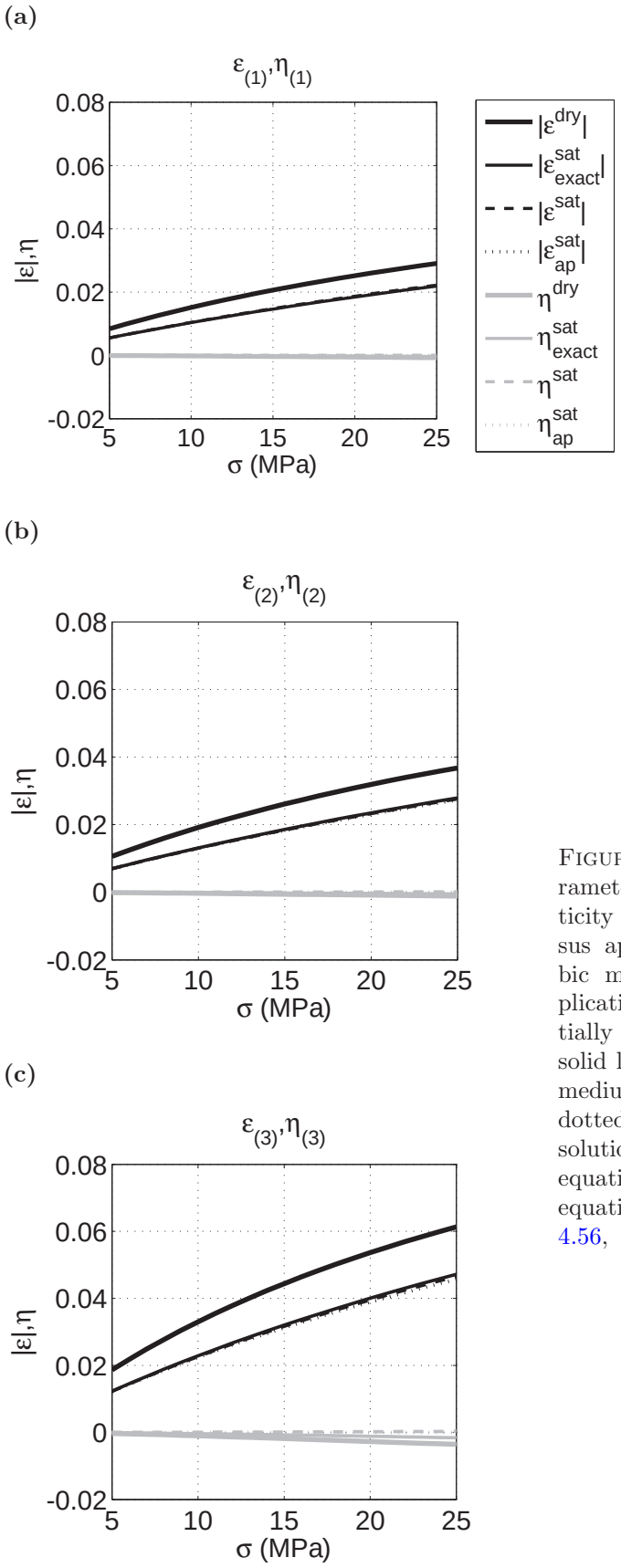

FIGURE 4.7: P-wave anisotropy parameters $\epsilon_{(i)}$ (black lines) and anellipticity parameters $\eta_{(i)}$ (grey lines) versus applied stress in an orthorhombic medium resulting from the application of triaxial stress on an initially isotropic medium. The thick solid lines show the values in the dry medium. The thin solid, dashed and dotted lines respectively refer to the solutions using the exact Gassmann equations, the expressions given by equations 4.49, 4.53, 4.57 and 4.52, 4.56, 4.60 and their linearizations (equations 4.15 and 4.21).

properties of fractured shales or layered media. The approach used hereafter is similar to the one described by Bakulin et al. [2000]. The VTI background is characterized by the vertical P-wave velocity v_{33}, the velocity of the S-wave polarized along the x_1-axis v_{31} and the three anisotropy parameters ϵ_v, γ_v and δ_v originally defined by Thomsen [1986] for VTI media. Expressions for ϵ_v, γ_v and δ_v can be obtained by inverting indices 1 and 3 in the definitions of their equivalent for HTI media (equations 2.15 to 2.18). The effect of fractures on elastic properties is then accounted for using the linear slip deformation theory (see Chapter 2, Section 2.3). The VTI background parameters and fracture parameters that we used for the analysis are listed in Table 4.5.

The anisotropy parameters $\epsilon_{(i)}$ and $\delta_{(i)}$ in the dry and saturated orthorhombic medium are displayed in Figure 4.8. Anisotropy parameters $\epsilon_{(1)}$ and $\delta_{(1)}$ (Figures 4.8a and 4.8b) are relative to the anisotropy parameters in the $[x_2, x_3]$-plane, and as such, they only carry information about the intrinsic anisotropy of the VTI background. Thus, they do not vary with the normal weakness Δ_N of the fractures. We observe that there is a small discrepancy between $\epsilon_{(1)}^{sat}$ and $\delta_{(1)}^{sat}$ calculated from the original anisotropic Gassmann equations (solid blue lines) and from the expressions derived in the previous section and their linearizations (dashed lines). This lack of accuracy could be due to the fact that the anisotropy is significant, and the weak anisotropy assumption used to derive the formulas no longer applies.

The azimuthal anisotropy quantified by parameters $\epsilon_{(3)}$ and $\delta_{(3)}$ (Figures 4.8e and 4.8f) is affected by the presence of fractures, but not by the VTI background anisotropy. Note that, in this case, there is a good match between the exact solution for the anisotropy parameters and the approximations derived in the previous section, even if the P-wave anisotropy parameter $\epsilon_{(3)}$ in the dry medium reaches 0.15 when $\Delta_N = 0.2$.

The overall anisotropy in the $[x_1, x_3]$-plane combines the VTI background anisotropy and the anisotropy caused by the presence of fractures. As a result, the $\epsilon_{(2)}$-parameter (Figure 4.8c) decreases gradually and becomes negative when $\Delta_N = 0.18$, i.e. when the fracture-induced anisotropy becomes as large as the VTI background anisotropy (Figure 4.8e). A small discrepancy between the exact solution for $\delta_{(2)}$ given by Gassmann

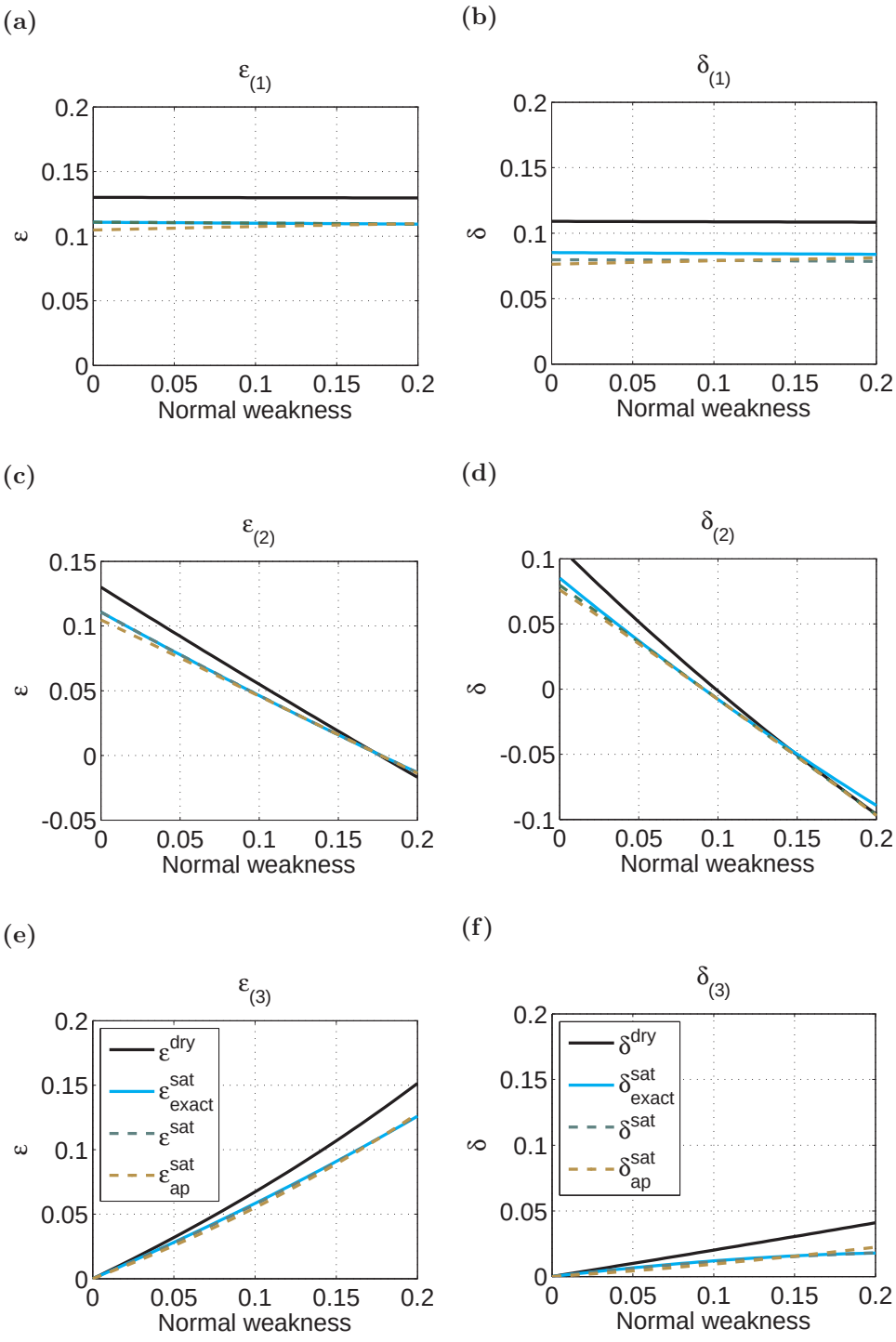

FIGURE 4.8: Effect of fluid on anisotropy in a saturated medium made of vertical fractures embedded in a layered background: anisotropy parameters $\epsilon_{(i)}$, $\delta_{(i)}$ in each plane of symmetry as a function of the normal fracture weakness Δ_N. Black, blue, dashed green and dashed brown lines respectively show results obtained in the dry medium, in the saturated medium using the exact solution given by Gassmann equations, expressions derived in the previous section and their linearizations.

equations and the approximation derived in the previous section is again noticeable for large values of Δ_N (Figure 4.8f). However, the approximations given by equations 4.49 to 4.60 are still adequate in each case.

4.7 Chapter conclusions

Using the anisotropic Gassmann theory, we analytically expressed anisotropy parameters in TI and orthorhombic saturated media as a function of those in dry media. Several other parameters such as the bulk and shear moduli of the dry and saturated media, the grain and fluid bulk moduli and the porosity have to be taken into account. The derived equations are are applicable to any TI or orthorhombic medium, regardless of the cause of anisotropy. This study is however restricted to weak anisotropy.

In general, the presence of fluid tends to reduce the degree of P-wave anisotropy, expressed by the anisotropy parameter ϵ. This is due to the fact that the pore space being isotropic, the stiffening effect of fluid is more pronounced along certain directions depending on the preferential orientation of cracks or fractures. The less compressible the fluid, i.e. the higher the fluid bulk modulus K_f, the more affected the degree of anisotropy. The shear modulus is not affected by the pore fluid so the S-wave anisotropy, described by γ, remains the same in the dry and saturated media.

We studied the value of the anellipticity parameter η, which links the anisotropy parameters ϵ and δ as expressed in equations 2.19 and 2.20. We showed that when the porosity is sufficiently high, the anellipticity parameter in the saturated medium is proportional to the one in the dry medium. The condition on porosity for the approximation to be valid is given by equation 4.20. Note that this is a sufficient condition, meaning that even if it is not fulfilled the approximation of η^{sat} may still be valid. When the approximation applies, it is straightforward to show that if the dry medium is elliptical (or ellipsoidal), then the saturated medium is also elliptical (or ellipsoidal). This opens the possibility of differentiating between stress- and fracture-induced azimuthal anisotropy by estimating the anellipticity parameter. Indeed, anisotropy resulting from

the application of a small uniaxial stress on an isotropic medium is always elliptical. On the other hand, an isotropic medium permeated by a set of aligned identical fractures is elliptical if and only if $B = 1$. However, several experimental studies suggest that typical values of B are between 0.3 and 0.8 [Angus et al., 2009, Baltazar et al., 2002, Biwa et al., 2005]; hence, fracture-induced anisotropy is presumably unlikely to be elliptical.

The main goal in deriving linearized expressions for ϵ^{sat} and η^{sat} was to provide an intuitive understanding of the fluid dependence on the anisotropy parameters. Nonetheless, it is preferable to use the exact anisotropic fluid substitution given by equation 2.63 for computational purposes.

These expressions were derived under several conditions, which have to be fulfilled to allow for the use of Gassmann [1951] theory. In particular, we assume that the fluid pressure is equilibrated throughout the pore space. This is a reasonable assumption for low frequencies; at higher frequencies however, the passing wave might induce pressure gradients within the fluid phase, resulting in local fluid flow between compliant pores and adjacent stiff pores. The effect of this local fluid flow, also known as squirt flow, on anisotropy signatures is investigated in the next chapter (Chapter 5).

Chapter 5

Frequency-dependence of anisotropy in fluid-saturated media: an anisotropic squirt flow model

5.1 Chapter overview

In Chapter 4, we studied the effect of fluid on anisotropy in weakly anisotropic media by rewriting the anisotropic Gassmann [1951] equations in terms of anisotropy parameters. This is a valid approach at low frequencies, when the pore pressure is supposed to be fully equilibrated throughout the pore space. At higher frequencies, wave-induced fluid flow (WIFF) might occur, which may lead to an underestimation of elastic wave moduli using Gassmann theory. When an elastic wave propagates through a fluid-saturated medium, it creates pressure gradients within the fluid phase, resulting in fluid flow and corresponding internal friction until the pore pressure reaches equilibrium. This WIFF usually causes velocity dispersion and attenuation. There are several types of WIFF depending on the length scale of the pressure gradients. The fluid flow resulting from

wavelength-scale pressure gradients, called global flow, is theoretically quantified by Biot [1956] theory of poroelasticity. When spatial variations of the pressure gradients occur on a scale larger than the pore size but smaller than the wave-length, the resulting flow is called mesoscopic flow. Mesoscopic flow is significant, especially in fractured media for which flow might occur between the fractures and the porous background. In such a case, the frequency dependence of elastic moduli is mainly controlled by the size of the fractures [Maultzsch et al., 2003]. Several studies attempt to model this flow (e.g. Chapman [2003], Galvin & Gurevich [2015]). The third type of flow is the local flow, also known as squirt flow, which occurs at the pore scale between pores of different shape, size and orientation and thus different compliance. This flow, which is the main focus of this chapter, is believed to be predominant at ultrasonic frequencies [Jones, 1986, Mavko & Nur, 1975] but may also play a role at seismic and sonic frequency ranges [Mavko et al., 2003, Müller et al., 2010].

Squirt flow in isotropic rocks has been modelled by several authors [Endres & Knight, 1997, Gurevich et al., 2010, Mavko & Jizba, 1991, Mavko & Nur, 1975, O'Connell & Budiansky, 1977]. Mukerji & Mavko [1994] and Xu [1998] respectively extended the isotropic models of Mavko & Jizba [1991] and Endres & Knight [1997] to anisotropic media. Guéguen & Sarout [2011] also developed an anisotropic squirt flow model by considering the crack-to-crack flow in in two types of anisotropic media; the first one is made of aligned cracks embedded in an isotropic matrix and the second one consists of an isotropic medium permeated by vertical cracks with normals randomly oriented in the horizontal plane. These studies only provide the low- and high-frequency limits of saturated elastic moduli and as such, they do not give any information on the attenuation associated with squirt flow. Gaining some insight on the attenuation occurring in anisotropic media is however essential as attenuation anisotropy might be more significant than velocity anisotropy [Arts et al., 1992, Tao & King, 1990].

In this chapter, we derive a new squirt flow model that combines the pressure relaxation approach of Murphy et al. [1986] and the linear slip deformation theory of Sayers & Kachanov [1995]. The model is basically an extension of the isotropic squirt flow model

from Gurevich et al. [2010] (Chapter 2, Section 2.5.2.1) to anisotropic media. In the low-frequency limit, the resulting model is consistent with the anisotropic Gassmann [1951] equations. In the high-frequency limit, the model matches predictions of the anisotropic squirt flow model from Mukerji & Mavko [1994] described in Chapter 2, Section 2.5.2.2. In fact, in the low- and high frequency limits, the model is essentially the same as the one derived by Mukerji & Mavko [1994] rewritten using the linear-slip deformation formalism. The main novelty in this work is the study of intermediate frequencies, which allows us to gain an insight on attenuation as well as velocity dispersion. Studying the frequency dependency of elastic properties in saturated media requires knowledge of the compliant pores orientation distribution. Hereafter we investigate two particular cases: the first one is the case for which anisotropy arises from the presence of aligned compliant pores and the second one is the stress-induced anisotropy case. The case of aligned cracks is modelled using the linear-slip deformation (or excess compliance) theory (Chapter 2, Section 2.3). In the second case, we use Gurevich et al. [2011] stress-induced anisotropy model.

The chapter is divided into two main parts corresponding to the two particular cases studied here. The first part is the derivation of the model for aligned cracks embedded in an isotropic background, while the second part deals with stress-induced anisotropy. In each section, we first give the low- and high-frequency limits of elastic moduli and the frequency dependent elastic properties of the saturated rock. Then, we derive analytical expressions for frequency-dependent anisotropy parameters in order to gain a better insight on how squirt flow affects anisotropy in saturated rocks. Since the squirt flow induced attenuation is also anisotropic, we study the attenuation anisotropy. To quantify this attenuation anisotropy, we compute attenuation anisotropy parameters introduced by Zhu & Tsvankin [2006] and we also propose alternative attenuation anisotropy parameters, which are particularly useful for strong attenuation anisotropy.

Matrix properties	$K_b = 9.72$ GPa
	$\mu_b = 9.32$ GPa
	$\rho = 2.5$ g/cc
	$K_g = 37.5$ GPa
Crack properties	$Z_T = 0.018$ GPa^{-1}
	$Z_N = 0.009$ GPa^{-1}
	$B = Z_N/Z_T = 0.5$
	$a = 10^{-3}$
Porosity	$\phi = 0.13$
	$\phi_c = 0.00069$
Fluid properties	$K_f = 2.25$ GPa
	$\rho_f = 1.0$ g/cc
	$\eta_f = 10^{-3}$ Pa.s

TABLE 5.1: Input parameters used to illustrate the effect of squirt flow in a TI medium for which anisotropy results from the presence of aligned cracks.

5.2 Case of aligned cracks

In this section, we consider the simple case of transversely isotropic rocks with aligned cracks (i.e. aligned compliant pores or microcracks). Though this case might not be realistic, it still provides information on attenuation and velocity dispersion in TI media to some extent. Besides, results obtained in this section for the high-frequency limit will be compared to predictions of Mukerji & Mavko [1994] anisotropic squirt flow model (Chapter 2, Section 2.5.2.2). Thus, in this section, we consider a medium possessing aligned identical cracks embedded in a hypothetical background rock matrix made up of grains and equant pores only. The background rock matrix is assumed to be isotropic and fully characterized by two elastic constants, the Lamé parameters λ_b and μ_b. The cracks are described by their normal and tangential compliances Z_N and Z_T. The overall elastic properties of the dry cracked solid are computed using Sayers & Kachanov [1995] theory (Chapter 2, Section 2.3).

In the following, we first give expressions of the frequency-dependent elastic moduli before deriving expressions for velocity anisotropy parameters and attenuation anisotropy parameters. Each step is illustrated through a numerical example, whose input parameters are listed in Table 5.1.

5.2.1 Frequency-dependence of elastic properties

The aim of this section is to derive expressions for frequency-dependent moduli of our medium when it is fully saturated by a single fluid with bulk modulus K_f and dynamic viscosity η_f. In the following, we first give expressions of the elastic moduli in the low- and high-frequency limits, before deriving expressions for all frequency ranges.

5.2.1.1 Effect of fluid at low frequencies

In the low-frequency limit, there is sufficient time for fluid pressure to reach equilibrium throughout the pore space. The effective stiffness matrix of the saturated medium $\boldsymbol{C^{sat}}$ can thus be expressed as a function of the dry stiffness matrix $\boldsymbol{C}$ following the anisotropic Gassmann [1951] equations (Chapter 2, Section 2.5.1.2). Hence, the stiffness tensor of the saturated TI medium is written as a function of the stiffness tensor of the dry medium $\boldsymbol{C}$ and an additional term due to the stiffening effect of fluid (equations 2.63 to 2.66).

5.2.1.2 Effect of fluid at high frequencies

In the high-frequency limit, the fluid pressure does not have time to equilibrate between stiff pores and adjacent compliant pores; compliant pores effectively become isolated from the stiff pores with regard to fluid flow. To model this effect, Mavko & Jizba [1991] and Mukerji & Mavko [1994] considered the so-called unrelaxed frame, in which compliant pores are filled with fluid while stiff pores are empty. Since the background medium remains the same, the only difference between the effective compliance matrix of the unrelaxed and relaxed (dry) frames is the excess compliance due to cracks. In other words, the effective compliance of the unrelaxed frame $\boldsymbol{S^{uf}}$ can be written in the same way as equation 2.27 for the dry frame:

$$S_{ij}^{uf} = S_{ij}^{b} + \Delta S_{ij}^{uf}, \tag{5.1}$$

but the excess compliance due to cracks given by equation 2.32 is now written as

$$\Delta S_{ij}^{uf} = \begin{bmatrix} Z_N^{uf} & 0 & 0 & 0 & 0 & 0 \\ 0 & 0 & 0 & 0 & 0 & 0 \\ 0 & 0 & 0 & 0 & 0 & 0 \\ 0 & 0 & 0 & 0 & 0 & 0 \\ 0 & 0 & 0 & 0 & Z_T^{uf} & 0 \\ 0 & 0 & 0 & 0 & 0 & Z_T^{uf} \end{bmatrix}. \tag{5.2}$$

In Newtonian fluids, shear stresses are negligible (up to the characteristic frequency of viscous shear relaxation [Mavko & Nur, 1975]), and thus $Z_T^{uf} = Z_T$. The value of the normal compliance of cracks in the unrelaxed frame, Z_N^{uf} can be found by applying Gassmann's equations, considering that only compliant pores are filled with fluid. Note that Gassmann [1951] theory is applicable in this case because we assume that all compliant pores are isolated and identical; hence, the pore pressure is the same in all of them. Using such an approach yields the following expression for Z_N^{uf} (e.g. Gurevich [2003]):

$$Z_N^{uf} = \frac{Z_N}{1 + \dfrac{Z_N}{\phi_c\left(\dfrac{1}{K_f} - \dfrac{1}{K_g}\right)}}, \tag{5.3}$$

where ϕ_c is the compliant porosity of the medium. By substituting equation 5.3 into expressions 5.1 and 5.2, we get the effective compliance tensor of the unrelaxed frame $\boldsymbol{S^{uf}}$. The resulting tensor is consistent with Mukerji & Mavko [1994] model, as demonstrated in Appendix B, Section B.1.

The stiffness tensor of the unrelaxed frame $\boldsymbol{C^{uf}}$ is then obtained either by inverting $\boldsymbol{S^{uf}}$, or by using the expression of the stiffness matrix of isotropic media permeated by

a set of aligned cracks (see Chapter 2, Section 2.3):

$$C_{ij}^{uf} = \begin{bmatrix} L_b(1-\Delta_N^{uf}) & \lambda_b(1-\Delta_N^{uf}) & \lambda_b(1-\Delta_N^{uf}) & 0 & 0 & 0 \\ \lambda_b(1-\Delta_N^{uf}) & L_b(1-\chi_b^2\Delta_N^{uf}) & \lambda_b(1-\chi_b\Delta_N^{uf}) & 0 & 0 & 0 \\ \lambda_b(1-\Delta_N^{uf}) & \lambda_b(1-\chi_b\Delta_N^{uf}) & L_b(1-\chi_b^2\Delta_N^{uf}) & 0 & 0 & 0 \\ 0 & 0 & 0 & \mu_b & 0 & 0 \\ 0 & 0 & 0 & 0 & \mu_b(1-\Delta_T) & 0 \\ 0 & 0 & 0 & 0 & 0 & \mu_b(1-\Delta_T) \end{bmatrix}. \tag{5.4}$$

The normal weakness of cracks in the unrelaxed frame Δ_N^{uf} is written in the same way as the one for the dry frame (equation 2.34):

$$\Delta_N^{uf} = \frac{Z_N^{uf} L_b}{1 + Z_N^{uf} L_b}. \tag{5.5}$$

By substituting the expression of Z_N^{uf} (equation 5.3) into equation 5.5, we obtain

$$\Delta_N^{uf} = \frac{L_b \Delta_N}{L_b + \dfrac{\Delta_N}{\phi_c\left(\dfrac{1}{K_f} - \dfrac{1}{K_g}\right)}} \tag{5.6}$$

Approximation of elastic moduli in the high-frequency limit - A considerable insight can be gained by looking in more detail at expressions 5.3 and 5.6 for the normal crack compliance and weakness. Usually, $K_f \ll K_g$ and $K_f Z_N \gg \phi_c$, so equation 5.3 reduces to

$$Z_N^{uf} = \phi_c / K_f, \tag{5.7}$$

which can be further approximated by

$$Z_N^{uf} \approx 0. \tag{5.8}$$

The approximation 5.8 conveys the fact that in the high-frequency limit fluid-filled cracks become much stiffer with respect to normal (but not tangential) deformation.

In the same way, Δ_N^{uf} reduces to

$$\Delta_N^{uf} = 0. \tag{5.9}$$

When substituting approximation 5.9 into the stiffness matrix $\boldsymbol{C^{uf}}$ (equation 5.4), it becomes clear that, for liquid-filled cracks in the high-frequency limit, P-waves propagate at the same velocity perpendicular and parallel to the cracks (see Figure 5.1a). To check the bias introduced by approximation 5.9, we compute the C_{ij}^{uf} coefficients using the exact and approximated values of the normal weakness Δ_N^{uf} (equations 5.5 and 5.9) for the numerical example whose input parameters are listed in Table 5.1. Results are listed in Table 5.2. The relative error between the exact and approximated values does not exceed 0.6 %, which means that $\Delta_N^{uf} = 0$ is a reasonable assumption for the high-frequency limit.

	Exact C_{ij}^{uf}	Approximated C_{ij}^{uf}	Relative error (%)
C_{11}^{uf}	22.02	22.16	0.62
C_{12}^{uf}	3.48	3.50	0.62
C_{23}^{uf}	3.50	3.50	0.10
C_{33}^{uf}	22.15	22.16	0.02

TABLE 5.2: Exact and approximated values for C_{ij}^{uf} in the case of aligned cracks.

Finally, the effect of fluid filling equant pores is accounted for by replacing the stiffness matrix of the dry medium, $\boldsymbol{C}$, by the one of the unrelaxed frame, $\boldsymbol{C^{uf}}$, in the anisotropic Gassmann equations (equations 2.63 to 2.66). Proceeding in this way yields the moduli of the fully saturated medium in the high-frequency limit.

5.2.1.3 Effect of fluid at intermediate frequencies

Determining the saturated elastic moduli at intermediate frequencies follows the same logic as the one previously explained for high frequencies. First, we calculate the elastic properties of a modified frame, which is similar to the unrelaxed frame in the sense that compliant pores are filled with fluid while stiff pores are empty (Chapter 2, Section 2.5.2.1). In the modified frame however, there is a pressure relaxation occurring in the

cracks. This pressure relaxation is conditioned by the pore geometry; thus, we must define a particular pore configuration to model this phenomenon. Following Murphy et al. [1986] and Gurevich et al. [2010], we assume that compliant pores consist in disc-shaped gaps with radius r, thickness h and corresponding aspect ratio $a = h/2r$, and their edges open into toroidal stiff pores as illustrated in Figure 2.10.

The compliance tensor of the modified frame at intermediate frequencies is expressed in the same way as the ones for the dry and unrelaxed frames (equations 2.27 and 5.1):

$$S_{ij}^{mf}(\omega) = S_{ij}^{b} + \Delta S_{ij}^{mf}(\omega) \tag{5.10}$$

where ω is the pulsation of the wave propagating through the saturated medium and $\boldsymbol{\Delta S^{mf}}$ is given by

$$\Delta S_{ij}^{mf}(\omega) = \begin{bmatrix} Z_N^{mf}(\omega) & 0 & 0 & 0 & 0 & 0 \\ 0 & 0 & 0 & 0 & 0 & 0 \\ 0 & 0 & 0 & 0 & 0 & 0 \\ 0 & 0 & 0 & 0 & 0 & 0 \\ 0 & 0 & 0 & 0 & Z_T & 0 \\ 0 & 0 & 0 & 0 & 0 & Z_T \end{bmatrix}. \tag{5.11}$$

By using the same approach as in the isotropic case [Gurevich et al., 2010], it is possible to calculate the additional stiffness of the gap due to the presence of fluid as a function of fluid pressure. Then, the normal compliance of the cracks in the modified frame can be written as [Gurevich et al., 2010]:

$$Z_N^{mf}(\omega) = \frac{Z_N}{1 + \dfrac{Z_N}{\phi_c\left(1/K_f^*(\omega) - 1/K_g\right)}}, \tag{5.12}$$

which yields in terms of normal weakness:

$$\Delta_N^{mf}(\omega) = \frac{L_b \Delta_N}{L_b + \dfrac{\Delta_N}{\phi_c\Big(\dfrac{1}{K_f^*(\omega)} - \dfrac{1}{K_g}\Big)}}. \tag{5.13}$$

In equations 5.12 and 5.13, K_f^* is the effective bulk modulus of the fluid saturating the compliant pores:

$$K_f^*(\omega) = \Big[1 - \frac{2J_1(kr)}{krJ_0(kr)}\Big] K_f, \tag{5.14}$$

where J_i denotes Bessel function of the first kind of order i and k is the wavenumber of the fluid pressure diffusion wave in the gap.

Particular case of liquid saturation - In order to derive simple analytic expressions for the frequency-dependent elastic moduli, we focus on the most important case of liquid saturation. In this case, Gurevich et al. [2010] showed that the modified fluid bulk modulus can be approximated by equation 2.77 (Chapter 2, Section 2.5.2.1):

$$K_f^*(\omega) = \frac{3}{8}\frac{i\omega\eta_f}{a^2}. \tag{5.15}$$

Substituting this expression into the formula for $\Delta_N^{mf}(\omega)$ (equation 5.13), we obtain

$$\Delta_N^{mf}(\omega) = \frac{L_b^2 \Delta_N}{D'(\omega)} - i\frac{3}{8}\frac{L_b}{D'(\omega)}\frac{\Delta_N \eta_f}{\phi_c a^2}\omega, \tag{5.16}$$

where

$$D'(\omega) = L_b^2 + \Big(\frac{3}{8}\frac{\Delta_N \eta_f}{\phi_c a^2}\omega\Big)^2. \tag{5.17}$$

When combining equations 5.16 and 5.4 for the stiffness tensor of an isotropic medium permeated by aligned cracks, it is straightforward to show that the complex, frequency-dependent stiffness coefficients of the TI medium are written as

$$C_{11}^{mf}(\omega) = L_b\Big(1 - \frac{L_b^2 \Delta_N}{D'(\omega)}\Big) + i\frac{3}{8}\frac{L_b^2}{D'(\omega)}\frac{\Delta_N^2 \eta_f}{\phi_c a^2}\omega, \tag{5.18}$$

$$C_{13}^{mf}(\omega) = \lambda_b\Big(1 - \frac{L_b^2 \Delta_N}{D'(\omega)}\Big) + i\frac{3}{8}\frac{\lambda_b L_b}{D'(\omega)}\frac{\Delta_N^2 \eta_f}{\phi_c a^2}\omega, \tag{5.19}$$

$$C_{33}^{mf}(\omega) = L_b\Big(1 - \frac{\lambda_b^2 \Delta_N}{D'(\omega)}\Big) + i\frac{3}{8}\frac{\lambda_b^2}{D'(\omega)}\frac{\Delta_N^2 \eta_f}{\phi_c a^2}\omega, \tag{5.20}$$

$$C_{44}^{mf}(\omega) = \mu_b, \tag{5.21}$$

$$C_{55}^{mf}(\omega) = \mu_b(1 - \Delta_T). \tag{5.22}$$

After computing the effective compliance tensor of the modified frame $\boldsymbol{C^{mf}(\omega)}$, we calculate the the frequency-dependent saturated moduli $C_{ij}^{sat}(\omega)$ by replacing the dry elastic coefficients C_{ij} by the ones of the modified frame C_{ij}^{mf} into the anisotropic Gassmann equations (equations 2.63 to 2.66). Using the relationship linking stiffness components in TI media to P- and S-wave velocities (equations 2.10 to 2.12), we can then compute the complex seismic velocities as a function of the angle of propagation with the symmetry axis θ. Phase velocities v_ψ and quality factors Q can then be deduced from complex velocities for each type of wave:

$$v_\psi = \Big[Re\Big(\frac{1}{v}\Big)\Big]^{-1}, \tag{5.23}$$

$$Q = \frac{Re(v^2)}{Im(v^2)}, \tag{5.24}$$

where v is either v_P, $v_{S\perp}$ or $v_{S\parallel}$.

5.2.1.4 Summary and numerical illustration

In summary, the fully saturated frequency dependent elastic moduli are given by the anisotropic Gassmann equations:

$$C_{ij}^{sat}(\omega) = C_{ij}^{mf}(\omega) + \alpha_i(\omega)\alpha_j(\omega)M(\omega), \tag{5.25}$$

where

$$\alpha_i(\omega) = 1 - \frac{\sum_{j=1}^{3} C_{ij}^{mf}(\omega)}{3K_g} \text{ for } i = 1,2,3 \text{ and } \alpha_4 = \alpha_5 = \alpha_6 = 0, \tag{5.26}$$

and M is the analogue of Gassmann's pore space modulus defined as

$$M(\omega) = \frac{K_g}{\left(1 - \frac{K^*(\omega)}{K_g}\right) - \phi\left(1 - \frac{K_g}{K_f}\right)}. \tag{5.27}$$

In equation 2.65, $K^*(\omega)$ denotes the so-called generalized drained bulk modulus, which is written as

$$K^*(\omega) = \frac{1}{9}\sum_{i=1}^{3}\sum_{j=1}^{3} C_{ij}^{mf}(\omega). \tag{5.28}$$

In the low-frequency limit, elastic constants of the modified frame $C_{ij}^{mf}(\omega)$ reduce to elastic moduli of the dry frame C_{ij}. In the high-frequency limit, they are equal to the ones of the unrelaxed frame C_{ij}^{uf}. Finding expressions of the elastic moduli in the unrelaxed frame reduces to determining the value of the normal compliance or weakness of the cracks Z_N^{uf} and Δ_N^{uf}, whose expressions are respectively given by 5.3 and 5.6. Since the fluid highly stiffens the cracks in the high-frequency limit, $Z_N^{uf} = \Delta_N^{uf} = 0$ is a reasonable approximation to use. At intermediate frequencies, finding elastic constants of the modified frame also reduces to determining the normal compliance or normal weakness of the cracks $Z_N^{mf}(\omega)$ and $\Delta_N^{mf}(\omega)$. As shown in equations 5.12 and 5.13, they can be expressed in the same way as Z_N^{uf} and Δ_N^{uf}, but the fluid bulk modulus K_f is replaced by a complex, frequency-dependent fluid bulk modulus $K_f^*(\omega)$ (equation 5.14). In the low-frequency limit, $K_f^*(\omega)$ tends to zero, while it tends to K_f in the

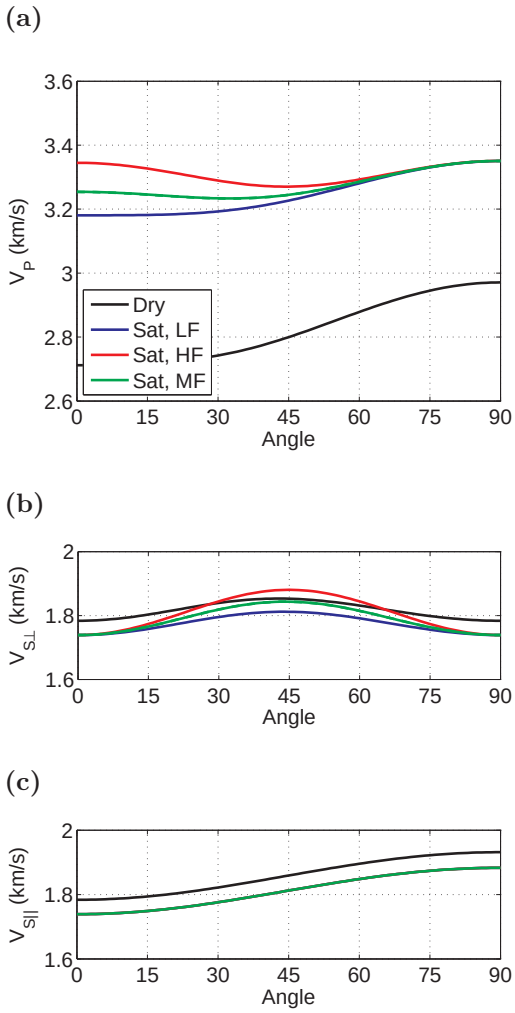

FIGURE 5.1: Variation of velocities as a function of angle with symmetry axis for the dry medium (black curves) and the saturated medium at low (blue curves), high (red curves) and intermediate (green curves) frequencies. Note that the S||-wave velocity does not vary as a function of frequency in the saturated medium, so blue, red and green curves in Figure 5.1c are superimposed.

high-frequency limit. Due to the complexity of expression 5.14 for $K_f^*(\omega)$, it is more convenient to focus on the liquid saturation case, for which $K_f^*(\omega)$ can be approximated by a relatively simple expression (equation 5.15), to derive analytical expressions of elastic properties of the modified frame (equations 5.18 to 5.22).

In order to illustrate the effect of squirt flow on anisotropy, we calculate the velocity dispersion and attenuation in a fully saturated medium containing aligned cracks

connected through equant pores. Input parameters for this numerical simulation are listed in Table 5.1. The normal weakness of the cracks Δ_N was specifically chosen to have a P-wave anisotropy parameter $\epsilon = 0.1$ in the dry medium. Figure 5.1 shows the velocity as a function of the angle from the symmetry axis. Black curves show velocities in the dry medium while blue, green and red curves show velocities in the saturated medium at low, intermediate and high frequencies, respectively. We first notice in Figure 5.1a that P-wave velocities increase when the medium is saturated with fluid. Besides, for the dry and saturated media at low frequencies, the P-wave velocity is minimum in the direction perpendicular to the cracks. However, when the frequency is increased, the velocity in the direction perpendicular to the fractures is increased and approaches the value of the P-wave velocity in the direction parallel to the fractures in the high-frequency limit. As mentioned earlier, this is due to the fact that the presence of fluid highly stiffens the fractures in the high-frequency limit. In Figure 5.1b, the S⊥-velocity variation as a function of the angle shows a different trend. The S⊥-wave velocity is maximum at 45° from the symmetry axis, and is minimum for propagation perpendicular and parallel to the symmetry axis. The velocity dispersion reaches its maximum when velocities reach their maxima, i.e. 45° from the symmetry axis. The S||-wave velocity increases with the angle from the symmetry axis but is not affected by the frequency, as seen in Figure 5.1c. Another way to plot these results is shown in Figure 5.2, in which P- and S⊥- wave velocities are displayed as a function of frequency for different angles of propagation from the symmetry axis. Dashed lines in Figure 5.2 show velocities computed using the liquid-saturated approximation, i.e. the stiffness tensor $\boldsymbol{C^{mf}}$ is calculated from the analytical expressions given in equations 5.18 to 5.22. As seen in the figure, the bias introduced by using the liquid-saturated approximation is negligible.

The frequency dependence of P- and S⊥-wave attenuations is shown in Figure 5.3. The attenuation pattern is similar to the one shown in Figure 2.12 for isotropic rocks: the attenuation is minimum at low frequencies, reaches its peak at the characteristic squirt frequency and decreases again at high frequencies. Dashed lines show the liquid-saturated approximation. Again, we notice that the discrepancy introduced by the use

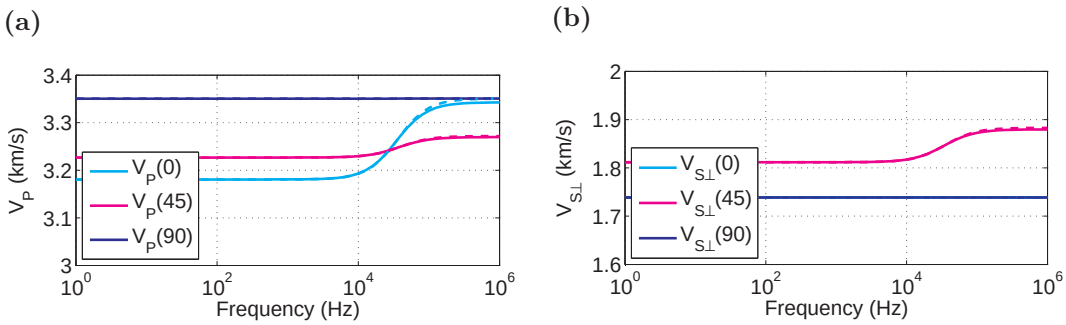

FIGURE 5.2: P- and S⊥-wave velocity dispersion in the case of aligned cracks. The numbers in parenthesis indicate the angle between the direction of propagation and the symmetry axis. Solid lines show the exact solution, while dashed lines show the liquid-saturated approximation for which elastic moduli of the modified frame are computed using equations 5.18 to 5.22.

of the liquid-saturated is negligible. Figure 5.4 shows the P- and S⊥-wave attenuation as a function of the angle between the direction of propagation and the symmetry axis. The P-wave attenuation is greatest perpendicular to the cracks, while the S⊥-wave attenuation reaches its maximum 45° away from the cracks, corresponding to the direction in which the S⊥-wave velocity is maximum.

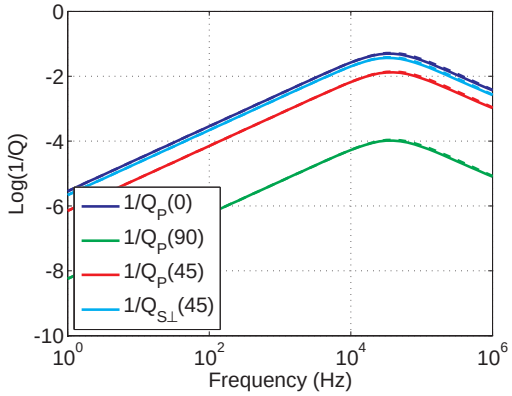

FIGURE 5.3: Frequency dependence of P- and S⊥-wave attenuation for different angles. Solid lines show the exact solution, while dashed lines show the liquid-saturated approximation for which elastic moduli of the modified frame are computed using equations 5.18 to 5.22.

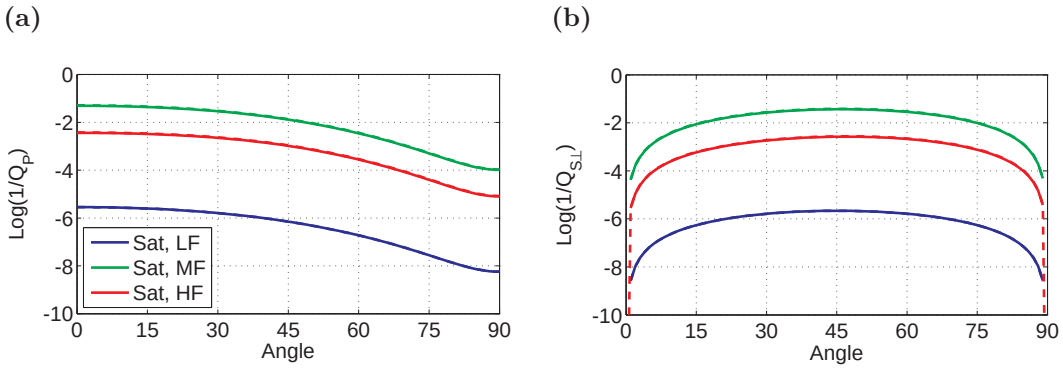

FIGURE 5.4: Attenuation of P- and S⊥-waves as a function of the angle from the symmetry axis in the low-frequency limit (blue), high-frequency limit (red) and at intermediate frequencies (green). Solid lines show the exact solution, while dashed lines show the liquid-saturated approximation for which elastic moduli of the modified frame are computed using equations 5.18 to 5.22.

5.2.2 Results in terms of anisotropy parameters

In order to get a more intuitive insight on how squirt flow affects elastic anisotropy in fully saturated, weakly anisotropic media, we express the anisotropy parameters defined in Chapter 2, Section 2.2.3.1 (equations 2.15, 2.16 and 2.18). These anisotropy parameters allow us to describe the angle dependency in a very concise way: instead of plotting the frequency dependency of velocities for many angles, we just need three curves. In the previous section, we showed that deriving expressions for frequency-dependent elastic parameters in the fully saturated TI medium involves applying the anisotropic Gassmann equations to a modified frame in which compliant pores are filled with fluid while stiff pores are empty. From equations 4.15, 4.11 and 4.16 derived in Chapter 4, Section 4.2, we deduce that frequency-dependent anisotropy parameters in the saturated medium can be approximated by

$$\epsilon^{sat}(\omega) = \frac{L^{mf}}{L^{sat}}\epsilon^{mf} + \frac{\alpha_0^{mf}}{L^{sat}}\frac{((\delta^{mf} - 4\epsilon^{mf})L^{mf} + 4\gamma^{mf}\mu^{mf})M}{3K_g}, \tag{5.29}$$

$$\gamma^{sat}(\omega) = \gamma^{mf}, \tag{5.30}$$

$$\delta^{sat}(\omega) = \frac{L^{mf}}{L^{sat}}\delta^{mf} + \frac{\alpha_0^{mf}}{L^{sat}}\frac{((\delta^{mf} - 4\epsilon^{mf})L^{mf} + 4\gamma^{mf}\mu^{mf})M}{3K_g}. \tag{5.31}$$

In the low-frequency limit, elastic parameters of the modified frame C_{ij}^{mf} are equal to elastic parameters of the relaxed (dry) frame C_{ij}, meaning that anisotropy parameters of the fully saturated medium in the low-frequency limit are given by equations 4.15, 4.11 and 4.16 derived in Chapter 4. In the high-frequency limit, coefficients C_{ij}^{mf} tend to elastic coefficients of the unrelaxed frame. As a consequence, superscripts mf can be replaced by uf in equations 5.29 to 5.31. Since we already studied the effect of Gassmann fluid substitution on anisotropy parameters in Chapter 4, here we concentrate on deriving expressions for the anisotropy parameters of the unrelaxed and modified frames. We first note that the tangential compliance of cracks Z_T is not affected by the effect of fluid. From equation 2.42, it is straightforward to show that the S||-wave anisotropy parameter remains the same in the dry and saturated media for all frequency ranges:

$$\gamma^{mf} = \gamma^{uf} = \gamma. \tag{5.32}$$

Besides, in the modified and unrelaxed frames, only compliant pores are filled with fluid. Thus, the background medium remains the same as the dry background medium and anisotropy parameters in the unrelaxed and modified frames follow the relationships (equations 2.41 and 2.38):

$$\epsilon^{mf,uf} = \frac{2\mu_b(\lambda_b + \mu_b)}{\lambda_b + 2\mu_b} Z_N^{mf,uf}, \tag{5.33}$$

$$\delta^{mf,uf} = 2(1-\nu_b)\epsilon^{mf,uf} - 2\frac{1-2\nu_b}{1-\nu_b}\gamma. \tag{5.34}$$

Based on the approximations derived in the previous section for the normal crack compliances Z_N^{mf} and Z_N^{uf}, we now derive analytical expressions for anisotropy parameters ϵ and δ in the unrelaxed and modified frames separately.

5.2.2.1 Anisotropy parameters of the unrelaxed frame

As mentioned previously, in the high-frequency limit, the fluid cannot escape from the compliant pores into the stiff pores. As a result, cracks are highly stiffened, which is expressed by the fact that the normal compliance of cracks Z_N^{uf} reduces to 0 (equation

5.8). P-waves propagate at the same velocity parallel and perpendicular to the cracks; hence, the P-wave anisotropy parameter in the unrelaxed frame given by equation 5.33 can be approximated by

$$\epsilon^{uf} = 0. \tag{5.35}$$

From equation 5.34, it follows that

$$\delta^{uf} = -2\frac{1-2\nu^b}{1-\nu^b}\gamma^{uf}. \tag{5.36}$$

Note that the expression for δ^{uf} relies on two approximations: the first one is the approximation for ϵ^{uf}, and the second one is the weak anisotropy approximation of the δ-parameter given by equation 5.34. As seen in Figure 5.5a, the combination of both approximations can lead to significant errors if the anisotropy is not very weak.

5.2.2.2 Frequency-dependent anisotropy parameters of the modified frame

The P-wave anisotropy parameter of the modified frame is obtained by substituting expression 5.12 for $Z_N^{mf}(\omega)$ into equation 5.33 :

$$\epsilon^{mf}(\omega) = \frac{\epsilon}{1+\dfrac{D\epsilon}{\phi_c\left(\dfrac{1}{K_f^*(\omega)}-\dfrac{1}{K_g}\right)}}, \tag{5.37}$$

knowing that $Z_N = D\epsilon$ (equation 2.41), where $D = \dfrac{\lambda_b+2\mu_b}{2\mu_b(\lambda_b+\mu_b)}$. When $K_f \ll K_g$, equation 5.37 reduces to

$$\epsilon^{mf}(\omega) = \frac{\epsilon}{1+\dfrac{D\epsilon K_f^*(\omega)}{\phi_c}}. \tag{5.38}$$

In the liquid-saturated case, $K_f^*(\omega)$ can be approximated by equation 5.15, so equation 5.38 becomes

$$\epsilon^{mf}(\omega) = \frac{\epsilon}{1+i\dfrac{3}{8}\dfrac{\eta_f}{a^2\phi_c}D\epsilon\omega}. \tag{5.39}$$

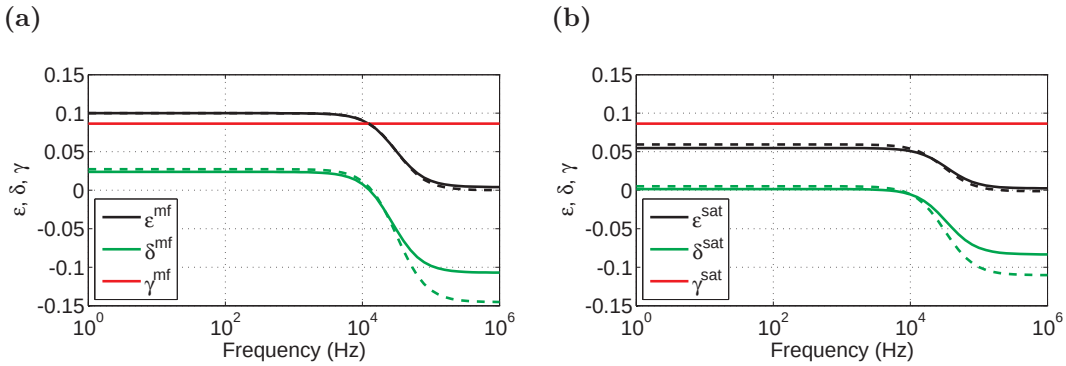

FIGURE 5.5: Frequency dependence of anisotropy parameters (a) in the modified frame and (b) in the saturated medium. Solid lines show the exact solution, while dashed lines show the liquid-saturated approximation.

The parameter δ^{mf} can be expressed via the relationship linking the anisotropy parameters in the special case of aligned fractures (equation 5.34).

We illustrate the frequency dependence of anisotropy parameters of the modified frame in Figure 5.5a. As mentioned earlier, the S||-wave anisotropy parameter γ (red curve) remains the same for all frequency ranges. The P-wave anisotropy parameter ϵ (black curve) is reduced to zero because the normal compliance of the cracks tends to zero in the high-frequency limit; hence, velocities parallel and perpendicular to the cracks are equal. At oblique angles from the symmetry axis however, the P-wave velocity is affected by the tangential compliance Z_T of the cracks and decreases to a minimum value at 45° (Figure 5.1a). As a result, the δ-parameter (green curve), which is affected by the P/S wave conversion at oblique angles, does not vanish and serves as the only indicator of P-wave anisotropy. Figure 5.5b displays the frequency-dependent anisotropy parameters in the fully saturated medium (i.e. after applying Gassmann theory). We notice that the same trends are observed; the only effect of applying Gassmann equations is to reduce the degree of anisotropy. On Figure 5.5, the dashed lines show the approximations of ϵ^{mf} and δ^{mf} (equations 5.39 and 5.34). We note that the approximation for ϵ^{mf} is reasonable, while the one for δ^{mf} introduces more error, which might result from the combined error of the weak-anisotropy approximation of δ given by equation 5.34 and the approximation of ϵ^{mf}.

5.2.3 Attenuation anisotropy parameters

Since attenuation anisotropy might be as significant as the velocity anisotropy analysed in the previous section, it is important to define appropriate quantities to characterize it. Quality factors were initially defined for isotropic media. To extend this concept to anisotropic media, Carcione [2001] introduced the $\boldsymbol{Q}$ matrix, in which components Q_{ij} are expressed as the ratios of the real and imaginary parts of the corresponding complex stiffness coefficients:

$$Q_{ij}(\omega) = \frac{Re(C_{ij}^{sat}(\omega))}{Im(C_{ij}^{sat}(\omega))}. \tag{5.40}$$

As mentioned by Zhu & Tsvankin [2006], the Q-matrix inherits the structure of the stiffness matrix. Particularly, when both real and imaginary parts are isotropic, then the attenuation in the medium is described by two independent coefficients:

$$Q = \begin{bmatrix} Q_{33} & Q_{13} & Q_{13} & 0 & 0 & 0 \\ Q_{13} & Q_{33} & Q_{13} & 0 & 0 & 0 \\ Q_{13} & Q_{13} & Q_{33} & 0 & 0 & 0 \\ 0 & 0 & 0 & Q_{55} & 0 & 0 \\ 0 & 0 & 0 & 0 & Q_{55} & 0 \\ 0 & 0 & 0 & 0 & 0 & Q_{55} \end{bmatrix}, \tag{5.41}$$

where

$$Q_{13} = Q_{33}\frac{C_{33} - 2C_{55}}{C_{33} - 2C_{55}\dfrac{Q_{33}}{Q_{55}}}. \tag{5.42}$$

For HTI media with HTI attenuation, five coefficients are required:

$$Q = \begin{bmatrix} Q_{11} & Q_{13} & Q_{13} & 0 & 0 & 0 \\ Q_{13} & Q_{33} & Q_{23} & 0 & 0 & 0 \\ Q_{13} & Q_{23} & Q_{33} & 0 & 0 & 0 \\ 0 & 0 & 0 & Q_{44} & 0 & 0 \\ 0 & 0 & 0 & 0 & Q_{55} & 0 \\ 0 & 0 & 0 & 0 & 0 & Q_{55} \end{bmatrix}, \tag{5.43}$$

where

$$Q_{23} = Q_{33}\frac{C_{33} - 2C_{55}}{C_{33} - 2C_{55}\dfrac{Q_{33}}{Q_{55}}}. \tag{5.44}$$

Similarly to the approach we employed for the velocity anisotropy, in the following we only derive analytical expressions for the attenuation engendered by fluid filling the compliant pores. In other words, we calculate

$$Q_{ij}^{mf}(\omega) = \frac{Re(C_{ij}^{mf}(\omega))}{Im(C_{ij}^{mf}(\omega))}. \tag{5.45}$$

From the analytical expressions derived for C_{ij}^{mf} in the case of liquid-filled pores (equations 5.18 to 5.22), we have in the limit of small crack density ($\Delta_N \ll 1$):

$$Q_{11}^{mf}(\omega) = \Big(1 - \frac{L_b^2 \Delta_N}{D'(\omega)}\Big) \Big/ \Big(\frac{3}{8}\frac{L_b}{D'(\omega)}\frac{\Delta_N^2 \eta_f}{\phi_c a^2}\omega\Big), \tag{5.46}$$

$$Q_{13}^{mf}(\omega) = Q_{11}^{mf}(\omega), \tag{5.47}$$

$$Q_{33}^{mf}(\omega) = Q_{11}^{mf}(\omega)/\chi_b^2, \tag{5.48}$$

$$Q_{44}^{mf}(\omega) \to \infty, \tag{5.49}$$

$$Q_{55}^{mf}(\omega) \to \infty. \tag{5.50}$$

These Q_{ij} coefficients give information on the attenuation in a particular direction. To gain more insight on attenuation anisotropy, it is useful to define attenuation anisotropy parameters.

5.2.3.1 Attenuation anisotropy parameters defined by Zhu and Tsvankin (2006)

Following the idea of Thomsen [1986] notation to describe velocity anisotropy in elastic media, Zhu & Tsvankin [2006] derived formulas for attenuation anisotropy parameters in order to characterize attenuation in TI media. In HTI media, components of the $\boldsymbol{Q}$ matrix are thus replaced by two reference components Q_{11} and Q_{55} and three so-called attenuation anisotropy parameters ϵ_Q, γ_Q and δ_Q defined as follows:

$$\epsilon_Q = \frac{Q_{11} - Q_{33}}{Q_{33}}, \tag{5.51}$$

$$\gamma_Q = \frac{Q_{55} - Q_{44}}{Q_{44}}, \tag{5.52}$$

$$\delta_Q = \frac{\frac{Q_{11} - Q_{55}}{Q_{55}} Re(C_{55}) \frac{(Re(C_{13}) + Re(C_{11}))^2}{Re(C_{11} - C_{55})} + 2\frac{Q_{11} - Q_{13}}{Q_{13}} Re(C_{13}) Re(C_{13} + C_{55})}{Re(C_{11}) Re(C_{11} - C_{55})}. \tag{5.53}$$

The parameters ϵ_Q and γ_Q respectively quantify the difference between the horizontal and vertical attenuation coefficients of P- and S$\|$-waves. The parameter δ_Q is defined through the second derivative of the P-wave attenuation coefficient in the symmetry direction and reflects the coupling between the attenuation and the velocity anisotropy. Despite the fact that these parameters are physically meaningful, there are several pitfalls with such a definition, as pointed out by Galvin & Gurevich [2015]. First, these expressions are derived assuming weak anisotropy, weak attenuation and weak attenuation anisotropy. Due to the order of magnitude of Q factors, the last assumption regarding weak attenuation anisotropy is quite restrictive and might break down in various cases even if the weak anisotropy and weak attenuation conditions are fulfilled. Besides, in the low- and high-frequency limits, imaginary parts of the stiffness tensor tend to zero, which implies that coefficients of the $\boldsymbol{Q}$ matrix tend to infinity. Hence, there is a potential of having undetermined forms or very large values for the attenuation anisotropy parameters using Zhu & Tsvankin [2006] definition.

In the case that we study here, for which anisotropy results from the presence of aligned cracks, the attenuation anisotropy parameters defined by Zhu & Tsvankin [2006] fail at quantifying attenuation anisotropy in a meaningful way. Indeed, the parameter ϵ_Q^{mf} remains close to -1 for all frequency ranges. This is due to the fact that attenuation is much stronger perpendicular to the cracks and consequently the quality factor Q_{11}^{mf} in this direction is negligible compared to the quality factor Q_{33}^{mf} parallel to the cracks. This is mathematically described by the expressions of Q_{11}^{mf} and Q_{33}^{mf} given in equations 5.46 and 5.48. Besides, the shear wave moduli C_{44} and C_{55} are real since they are only affected by the crack tangential compliance Z_T, which remains real. As a result, quality factors Q_{44}^{mf} and Q_{55}^{mf} tend to infinity (equations 5.49 and 5.50) and the attenuation anisotropy parameters δ_Q^{mf} and γ_Q^{mf} are undetermined values.

5.2.3.2 Alternative definition for attenuation anisotropy parameters

As an alternative way to quantify attenuation anisotropy, we propose to define the attenuation anisotropy parameters as the imaginary parts of Thomsen [1986] parameters, which yields

$$\epsilon_{Qa} = \frac{1+2\epsilon}{2}\Big(\frac{1}{Q_{33}} - \frac{1}{Q_{11}}\Big), \tag{5.54}$$

$$\gamma_{Qa} = \frac{1+2\gamma}{2}\Big(\frac{1}{Q_{44}} - \frac{1}{Q_{55}}\Big), \tag{5.55}$$

$$\delta_{Qa} = (1+\delta)\Big(\frac{1}{Q_{13}} - \frac{1}{Q_{11}}\Big) + 2\frac{Re(C_{55})}{Re(C_{11})}\Big(\frac{1}{Q_{55}} - \frac{1}{Q_{13}}\Big). \tag{5.56}$$

Since anisotropy and attenuation are assumed to be weak, equations 5.54 to 5.56 can be further simplified to give

$$\epsilon_{Qa} = \frac{1}{2}\Big(\frac{1}{Q_{33}} - \frac{1}{Q_{11}}\Big) \tag{5.57}$$

$$\gamma_{Qa} = \frac{1}{2}\Big(\frac{1}{Q_{44}} - \frac{1}{Q_{55}}\Big) \tag{5.58}$$

$$\delta_{Qa} = \Big(\frac{1}{Q_{13}} - \frac{1}{Q_{11}}\Big) + 2\frac{Re(C_{55})}{Re(C_{11})}\Big(\frac{1}{Q_{55}} - \frac{1}{Q_{13}}\Big). \tag{5.59}$$

The definition for ϵ_{Qa} in the case of small anisotropy is similar to the one proposed by Galvin & Gurevich [2015]. It is important to note that ϵ_{Qa}, γ_{Qa} and δ_{Qa} reduce to zero if the attenuation is isotropic or if there is no attenuation (i.e. when Q_{ij} coefficients tend to infinity). In the same way as the δ_Q-parameter defined by Zhu & Tsvankin [2006], the parameter δ_{Qa} reflects the coupling between the attenuation and the velocity anisotropy.

Calculating the anisotropy parameters for the modified frame in the case of liquid saturation yields

$$\epsilon_{Qa}^{mf} = \frac{1}{2Q_{11}^{mf}}(\chi_b^2 - 1), \tag{5.60}$$

$$\gamma_{Qa}^{mf} = 0, \tag{5.61}$$

$$\delta_{Qa}^{mf} = -2\frac{Re(C_{55}^{mf})}{Re(C_{11}^{mf})}\frac{1}{Q_{11}^{mf}}, \tag{5.62}$$

where C_{11}^{mf}, C_{55}^{mf} and Q_{11}^{mf} are given by equations 5.18, 5.22 and 5.46, respectively.

The alternative attenuation anisotropy parameters proposed in equations 5.57 to 5.59 are plotted in Figure 5.6. Figure 5.6a shows the parameters ϵ_{Qa}^{mf} and δ_{Qa}^{mf}. The variation of these parameters follows the same trend as attenuation i.e. they are minimum in the low- and high-frequency limits and reach their maxima at the characteristic frequency. The liquid-saturated approximation (dashed lines) match the exact solution really well. In Figure 5.6b, we display the alternative anisotropy parameters computed from the fully saturated stiffness coefficients C_{ij}^{sat}. The trend observed for ϵ_{Qa} and δ_{Qa} is the same as for ϵ_{Qa}^{mf} and δ_{Qa}^{mf}, but the attenuation is slightly lower. Note that in both cases, the attenuation anisotropy parameter γ_{Qa} equals to zero since there is no S$\|$-wave attenuation.

5.2.4 Discussion on the aligned cracks case

In this section, we have developed a squirt flow model to account for elastic waves attenuation and dispersion in anisotropic media made of aligned compliant pores embedded

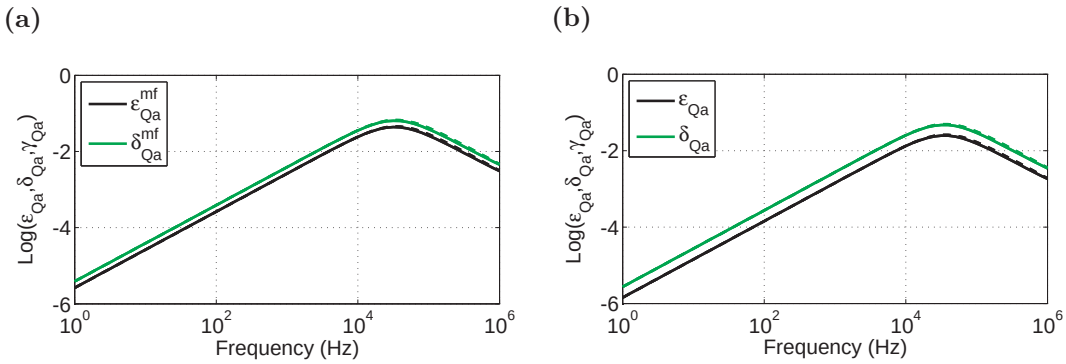

FIGURE 5.6: Frequency dependence of attenuation anisotropy parameters (a) in the modified frame and (b) in the saturated medium. Solid lines show the exact solution, while dashed lines show the liquid-saturated approximation.

in an isotropic matrix. All cracks (i.e. compliant pores) are assumed to be identical and the crack normal and tangential weaknesses are assumed to be sufficiently low so that the anisotropy remains weak. The medium is further assumed to be made of a single isotropic grain material and assumed to be fully saturated with one fluid to allow for the use of Gassmann [1951] theory. The model is in essence similar to the one derived by Mukerji & Mavko [1994]; the low- and high-frequency limits of the elastic properties presented in this work are therefore consistent with predictions from Mukerji & Mavko [1994]. In this chapter, we extend the isotropic squirt flow model derived by Gurevich et al. [2010] to account for the frequency-dependence of elastic parameters and gain in this way some insight on the wave attenuation due to squirt flow in anisotropic media.

The case of aligned compliant pores is the simplest case that can be studied. The dry medium is a simplified TI medium whose symmetry axis is aligned with the normal to the cracks. Instead of five parameters, the dry medium is described by four independent parameters: two parameters describing the elastic properties of the isotropic background matrix and two crack parameters: the normal and tangential crack compliances Z_N and Z_T. In the low-frequency limit, additional information about the porosity, fluid and grain properties are required. At higher frequencies, the compliant porosity has to be known. To study the frequency dependence of elastic parameters, it is necessary to define a pore geometry. In this study, we use the pore configuration

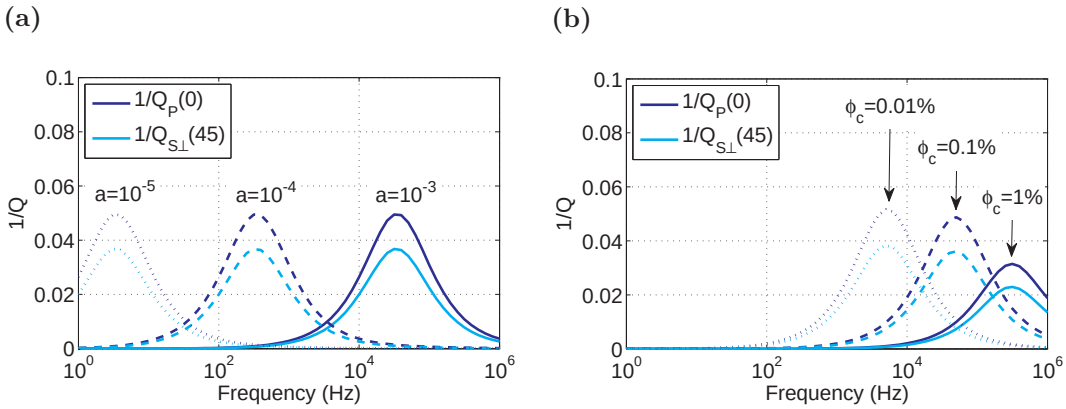

FIGURE 5.7: Influence of aspect ratio (a) and compliance porosity (b) values on the characteristic frequency and attenuation magnitude.

proposed by Murphy et al. [1986]: compliant pores are characterized by their radius and width and the resulting aspect ratio is particularly important as it influences the characteristic frequency at which squirt flow is occurring. As shown in Figure 5.7a, the lower the aspect ratio, the lower the characteristic frequency is. It can also be seen in Figure 5.7b that the value of the compliant porosity affects the value of the characteristic frequency and, to a lower extent, the magnitude of attenuation.

Several interesting points can be drawn from the numerical results presented in the previous sections. First, there is no dispersion observed for S‖-waves because the S‖-wave velocity is only affected by the tangential compliance of the cracks, which remains the same in the dry and saturated media for all frequency ranges. The same observation was made by Xu [1998], who modelled the velocity dispersion in isotropic media containing perfectly aligned compliant pores. Galvin & Gurevich [2015] also noted this absence of S‖- wave attenuation and velocity dispersion when modelling mesoscopic flow in isotropic media permeated by aligned fractures. Second, we notice that the P-wave velocity is minimum in the direction perpendicular to the cracks in the low-frequency limit, but it gradually increases with frequency and it becomes as high as the velocity of waves propagating parallel to the cracks in the high-frequency limit. This frequency-dependent behavior is due to the fact that at low frequencies, the pore pressure is equilibrated throughout the pore space. At higher frequencies however, the

fluid pressure in compliant pores is higher than the fluid pressure in the neighboring stiff pores. In this case, the normal compliance of the compliant pores becomes negligible and thus the P-wave velocity is the same for waves propagating perpendicular and parallel to the cracks. It is also worth mentioning that the non-vanishing tangential crack compliance Z_T affects the P-wave velocity at oblique angles. Hence, the P-wave velocity at oblique angles is lower and reaches its minimum at 45° corresponding to the direction in which the S⊥-wave is faster. These observations translate into having a P-wave velocity anisotropy parameter ϵ decreasing to zero at high-frequencies, while the δ-parameter remains the only indicator of P-S⊥ anisotropy. Such a pattern was also obtained by Galvin & Gurevich [2015] when modelling mesoscopic flow between aligned fractures and the porous background. We can also point out that theses results significantly differ from the ones obtained by Guéguen & Sarout [2011], who do not predict any velocity dispersion when modelling squirt flow between cracks in a medium containing aligned cracks. This is due to the fact that in their model, only compliant pores are considered. Hence, in the high-frequency limit, the fluid pressure is the same in all pores, but it is also the same as in the low-frequency limit.

The attenuation pattern arising from this simple case exhibits some specific characteristics. The P-wave attenuation is maximum in the direction perpendicular to the cracks, while it is negligible parallel to the cracks. Besides, there is no S||-wave attenuation as the tangential compliance of cracks remains the same in the saturated medium for all frequency ranges. This last observation causes some problems when calculating the attenuation anisotropy parameters δ_Q and γ_Q defined by Zhu & Tsvankin [2006]. Indeed, infinite values of quality factors Q_{44} and Q_{55} cause δ_Q and γ_Q to be undetermined. To overcome this issue, we proposed a new definition for attenuation anisotropy parameters (equations 5.57 to 5.59). This new definition presents several advantages. Similarly to Zhu & Tsvankin [2006] attenuation anisotropy parameters, they tend to zero in isotropic media and the parameter δ_{Qa} reflects the coupling between velocity and attenuation. By contrast with Zhu & Tsvankin [2006] parameters, the assumption of weak attenuation anisotropy is not required; the difference in order of magnitude of Q_{ij} factors is thus not an issue. The new parameters ϵ_{Qa}, δ_{Qa} and γ_{Qa} tend to zero in

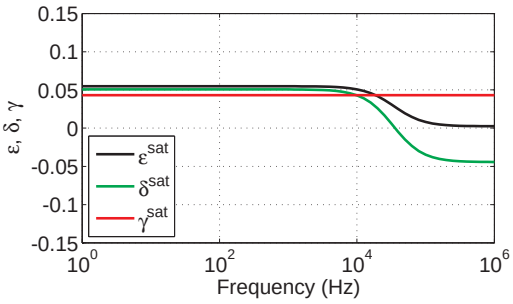

FIGURE 5.8: Frequency dependence of anisotropy parameters when $B = 1$. As seen in the figure, ϵ and δ are equal for low frequencies, which means that the medium is elliptical. In the high-frequency-limit, ϵ tends to zero, while δ becomes negative.

the low- and high-frequency limits, for which there is no attenuation, and they reach their maxima at the squirt flow characteristic frequency.

Another important aspect related to the second part of this chapter is the study of the behavior of the medium when the compliance ratio B of the cracks is equal to 1. In such a case, the dry medium is elliptical, i.e. the velocity anisotropy parameters ϵ and δ are equal. Isotropic media subjected to uniaxial stress were found to be elliptical, regardless of the compliance ratio B (e.g. Rasolofosaon [1998], Gurevich et al. [2011], Sun & Prioul [2010]). Figure 5.8 shows velocity anisotropy parameters calculated for the same input parameters as listed in Table 5.1, but using a compliance ratio $B = 1$ instead of $B = 0.5$. We notice that in the low-frequency limit, ϵ and δ are very close, meaning that the medium is almost elliptical. In the high-frequency limit however, ϵ tends to zero while δ goes from positive to negative, which yields a non-elliptical anisotropy pattern. Studying the frequency dependence of the anellipticity degree could therefore help distinguishing between the anisotropy resulting from the presence of aligned cracks and stress-induced anisotropy.

5.3 Stress-induced anisotropy case

Now, we study the effect of squirt flow on stress-induced anisotropy. Most of the stress-induced anisotropy models derived so far do not explicitly account for the effect of fluid

and squirt flow [Gurevich et al., 2011, Mavko et al., 1995, Sayers, 1988, 2002]. This is however a topic of significant importance since combining the effect of stress and squirt flow could help modelling laboratory experiments carried out on saturated samples under non-hydrostatic stress. Besides, as mentioned earlier, the anisotropy resulting from the application of a uniaxial stress on an isotropic dry medium is elliptical [Gurevich et al., 2011, Rasolofosaon, 1998, Sun & Prioul, 2010]. In Chapter 4, we showed that this ellipticity result was preserved in fully saturated media at low frequencies. Deriving an anisotropic squirt flow model for isotropic rocks subjected to uniaxial stress will allow us to check whether or not this ellipticity result still holds at higher frequencies.

In this section, we try to integrate the attenuation and dispersion caused by wave-induced local (squirt) flow into the rock physics model derived by Gurevich et al. [2011] to account for the stress dependency of elastic properties of isotropic rocks subjected to uniaxial stress (Chapter 2, Section 2.4.2). Note that we restrict ourselves to the case of uniaxial stress for simplicity's sake; the scheme presented below is however easily extendable to triaxial stress using the stress-induced anisotropy model derived in Chapter 3. The dry medium is described by five parameters: the bulk and shear moduli K_h and μ_h of the rock in the hydrostatic high-stress limit, the normal and tangential compliance of cracks Z_{N0} and Z_{T0} in the unstressed state and the characteristic crack closing pressure P_c. These five parameters can be inverted from hydrostatic stress measurements using Shapiro [2003] stress sensitivity model (Chapter 2, Section 2.4.1).

Hereafter, we follow the same steps as the ones described in the previous section for the case of aligned cracks embedded in an isotropic background matrix. We first calculate the frequency-dependent elastic properties of the fully saturated medium, before deriving expressions for velocity and attenuation anisotropy parameters. Each step is again illustrated through a numerical example, whose input parameters are listed in Table 5.3.

Matrix properties	$K_h = 19.2$ GPa
	$\mu_h = 20.0$ GPa
	$\rho = 2.5$ g/cc
	$K_g = 37.5$ GPa
Crack properties	$Z_{T0} = 0.109$ GPa^{-1}
	$Z_{N0} = 0.051$ GPa^{-1}
	$B = Z_{N0}/Z_{T0} = 0.46$
	$P_c = 11.5$ MPa
	$a = 6.10^{-4}$
Porosity	$\phi = 0.13$
	$\phi_{c0} = 0.00059$
Fluid properties	$K_f = 2.25$ GPa
	$\rho_f = 1.0$ g/cc
	$\eta_f = 10^{-3}$ Pa.s

TABLE 5.3: Input parameters used to illustrate the effect of squirt flow in a TI medium for which anisotropy results from the application of a uniaxial stress on an initially isotropic medium.

5.3.1 Frequency dependence of elastic properties

As with the case of aligned fractures, we need to determine frequency dependent elastic properties of the modified frame in order to determine elastic properties of the fully saturated rock. In the modified frame, stiff pores are empty and compliant pores are filled with fluid. The frequency dependence of elastic properties of the modified frame is related to the pressure relaxation occurring in the area of grain contacts. In the low-frequency limit, the modified frame is equivalent to the relaxed (dry) frame. In the high-frequency limit, the fluid cannot escape from the compliant pores into the stiff pores and the modified frame becomes the so-called unrelaxed frame. Once elastic properties of the modified frame are known, we use the anisotropic Gassmann [1951] equations (equations 5.25 to 5.28) to account for the remaining effect of fluid filling the stiff pores.

Before deriving expressions for elastic parameters of the modified frame, let us first analyse the stress sensitivity of elastic properties of the dry frame (equation 2.51) and

how fluid filling compliant pores might affect this stress sensitivity:

$$S_{ij}(b) = S^h_{ij} + (\alpha^{is}_{ij} + b\alpha^{an}_{ij})Z_{T0} + (\beta^{is}_{ij} + b\beta^{an}_{ij})(Z_{N0} - Z_{T0}).$$

In the expression above, the tensor $\boldsymbol{S^h}$ gives elastic properties of the dry frame in the high-stress limit, i.e. when all compliant pores are closed; hence, this tensor remains unaffected by the presence of fluid filling the compliant pores. Tensors $\boldsymbol{\alpha^{is}}$, $\boldsymbol{\beta^{is}}$ and $\boldsymbol{\alpha^{an}}$, $\boldsymbol{\beta^{an}}$, respectively given by equations 2.52 and 2.53, describe the orientation distribution of cracks; they only depend on the relative orientation of cracks with respect to the stress field. The normalized stress magnitude $b = \sigma_{11}/P_c$ does not depend on the presence of fluid either. In fact, in our model the fluid does not have an impact on the characteristic crack closing pressure P_c because the uniaxial pressure σ_{11} is applied very slowly, so the fluid filling the compliant pores has ample time to squeeze out into stiff pores. When the frequency of the wave passing through the medium is high enough, then the presence of fluid stiffens the compliant pores with respect to normal but not tangential deformation; as such, the tangential compliance Z_{T0} of the cracks remains the same in the dry and saturated media, while the normal compliance Z_{N0} is the only parameter affected by the presence of fluid. Hence, the stress sensitivity of the modified frame is written as

$$S^{mf}_{ij}(b,\omega) = S^h_{ij} + (\alpha^{is}_{ij} + b\alpha^{an}_{ij})Z_{T0} + (\beta^{is}_{ij} + b\beta^{an}_{ij})(Z^{mf}_{N0}(\omega) - Z_{T0}). \tag{5.63}$$

In the following, we first derive expressions of elastic properties of the unrelaxed frame, before investigating the frequency-dependence of elastic properties of the modified frame.

5.3.1.1 Elastic properties of the unrelaxed frame (high-frequency limit)

At high frequencies, the fluid pressure does not have time to equilibrate between stiff pores and adjacent compliant pores. Compliant pores are effectively isolated from the stiff pores and hence become stiffer with respect to normal (but not tangential)

deformation. To quantify this effect, we consider the so-called unrelaxed frame, in which compliant pores are filled with fluid while stiff pores are empty [Mavko & Jizba, 1991]. As explained above, the stress-sensitivity of the effective compliance $\boldsymbol{S^{uf}}$ of this unrelaxed frame is written in the same way as for dry rocks (equation 2.51). The only difference is that the normal compliance of the initial cracks Z_{N0} is reduced due to the presence of fluid filling the cracks:

$$S_{ij}^{uf} = S_{ij}^{h} + (\alpha_{ij}^{is} + b\alpha_{ij}^{an})Z_{T0} + (\beta_{ij}^{is} + b\beta_{ij}^{an})(Z_{N0}^{uf} - Z_{T0}). \tag{5.64}$$

The new value Z_{N0}^{uf} of the cracks normal compliance can be determined by applying Gassmann's equations to the initial unstressed state, considering that only compliant pores are filled with fluid. Using such an approach yields the following expression for Z_{N0}^{uf} (e.g. Gurevich, Makarynska, & Pervukhina [2009b]):

$$Z_{N0}^{uf} = \frac{Z_{N0}}{1 + \dfrac{Z_{N0}}{\phi_{c0}\left(\dfrac{1}{K_f} - \dfrac{1}{K_g}\right)}}, \tag{5.65}$$

where ϕ_{c0} is the compliant porosity of the initial unstressed medium. In general, $K_f \ll K_g$ and the compliant porosity is small ($\phi_{c0} < 10^{-3}$), so for liquid-saturated rocks, equation 5.65 can be reasonably approximated by

$$Z_{N0}^{uf} \approx 0. \tag{5.66}$$

Subtracting equation 2.51 to 5.64 yields

$$S_{ij}^{uf} - S_{ij} = (\beta_{ij}^{is} + b\beta_{ij}^{an})(Z_{N0}^{uf} - Z_{N0}). \tag{5.67}$$

As demonstrated in Appendix B, Section B.2.1, this expression is consistent with the isotropic version of Mukerji & Mavko [1994] squirt flow model and with the isotropic squirt flow model derived by Gurevich, Makarynska, & Pervukhina [2009b].

If we rearrange the expression of the compliance tensor $\boldsymbol{S^{uf}}$ (equation 5.64) in order to separate the contribution of the initial isotropic distribution of cracks and the effect of crack closure due to the application of stress, we obtain

$$S_{ij}^{uf} = S_{ij}^{0,uf} + b\Delta S_{ij}^{an,uf}, \tag{5.68}$$

where

$$S_{ij}^{0,uf} = S_{ij}^{h} + \alpha_{ij}^{is} Z_{T0} + \beta_{ij}^{is}(Z_{N0}^{uf} - Z_{T0}), \tag{5.69}$$

and

$$\Delta S_{ij}^{an,uf} = \alpha_{ij}^{an} Z_{T0} + \beta_{ij}^{an}(Z_{N0}^{uf} - Z_{T0}). \tag{5.70}$$

The compliance tensor $\boldsymbol{S^{o,uf}}$ describing the unrelaxed frame when no stress is applied is isotropic. Hence, it is expressed as a function of two elastic parameters L_0^{uf} and μ_0^{uf}, which are related to the dry properties of the unstressed medium L_0 and μ_0 through the isotropic squirt flow model derived by Gurevich, Makarynska, & Pervukhina [2009b] (see Appendix B, Section B.2.1). When the applied stress is small compared to P_c, then the compliance tensor of the unrelaxed frame can be obtained by the following linearization:

$$C_{ij}^{uf} = C_{ij}^{0,uf} - bC_{ij}^{0,uf}\Delta S_{ij}^{an,uf} C_{ij}^{0,uf}, \tag{5.71}$$

which yields

$$C_{11}^{uf}(b) = L_0^{uf} - \frac{8}{35}(\mu_0^{uf})^2 Z_{T0} b, \tag{5.72}$$

$$C_{33}^{uf}(b) = L_0^{uf} - \frac{16}{105}(\mu_0^{uf})^2 Z_{T0} b, \tag{5.73}$$

$$C_{13}^{uf}(b) = \lambda_0^{uf} - \frac{4}{35}(\mu_0^{uf})^2 Z_{T0} b, \tag{5.74}$$

$$C_{44}^{uf}(b) = \mu_0^{uf} - \frac{1}{21} Z_{T0}(\mu_0^{uf})^2 b, \tag{5.75}$$

$$C_{55}^{uf}(b) = \mu_0^{uf} - \frac{16}{105} Z_{T0}(\mu_0^{uf})^2 b, \tag{5.76}$$

when using the approximation $Z_{N0}^{uf} = 0$.

5.3.1.2 Frequency-dependent elastic parameters of the modified frame

As mentioned previously, the stress sensitivity of the modified frame (equation 5.63) is written in the same way as the one for the dry frame; the only parameter affected by the presence of fluid filling the compliant pores is the crack normal compliance Z_{N0}. Hence, determining elastic properties of the modified frame reduces to finding the expression of the normal crack compliance of the modified frame Z_{N0}^{mf} in the unstressed isotropic state. The frequency-dependence of Z_{N0}^{mf} is influenced by the pore geometry and thus, we need to define a particular pore configuration. By using the same pore geometry and the same approach as for the aligned cracks, we obtain

$$Z_{N0}^{mf}(\omega) = Z_{N0}\Big[1 + \frac{Z_{N0}}{\phi_{c0}\Big(1/K_f^*(\omega) - 1/K_g\Big)}\Big]^{-1}, \tag{5.77}$$

where K_f^* is given by 5.14. Due to the complexity of the expression for $K_f^*(\omega)$, it is convenient to limit this study to the case of liquid saturation, for which K_f^* can be approximated by equation 5.15. In this case, the normal compliance of cracks in the modified frame (equation 5.77) can be expressed as

$$Z_{N0}^{mf}(\omega) = \frac{Z_{N0}}{1 + i\frac{3}{8}\frac{Z_{N0}}{\phi_{c0}}\frac{\omega\eta_f}{a^2}}. \tag{5.78}$$

In the same way as for the stiffness tensor of the unrelaxed frame (equation 5.71), the stiffness tensor of the modified frame can be approximated by

$$C_{ij}^{mf}(\omega) = C_{ij}^{0,mf}(\omega) - bC_{ij}^{0,mf}(\omega)\Delta S_{ij}^{an,mf}(\omega)C_{ij}^{0,mf}(\omega), \tag{5.79}$$

where

$$\Delta S_{ij}^{an,mf}(\omega) = \alpha_{ij}^{an} Z_{T0} + \beta_{ij}^{an}(Z_{N0}^{mf} - Z_{T0}). \tag{5.80}$$

The tensor $\boldsymbol{C^{o,mf}}$ corresponds to the stiffness tensor of the modified frame in the unstressed isotropic medium. As such, it is characterized by the P- and S-wave moduli L_0^{mf} and μ_0^{mf}, which can be derived from Gurevich et al. [2010] isotropic squirt flow

model (see Appendix B, Section B.2.2). If we assume that K_f^* is adequately approximated by equation 5.15, then

$$\mu_0^{mf}(\omega) = \mu_0\Big(1 + \frac{4}{15}\frac{(D_0(\omega))^2 Z_{N0}}{1+(D_0(\omega))^2}\mu_0\Big) + i\frac{4}{15}\frac{D_0(\omega)Z_{N0}}{1+(D_0(\omega))^2}\mu_0^2, \tag{5.81}$$

$$L_0^{mf}(\omega) = \Big[L_0 + D_0'\frac{(D_0(\omega))^2 Z_{N0}}{1+(D_0(\omega))^2}\Big] + iD_0'\frac{D_0(\omega)Z_{N0}}{1+(D_0(\omega))^2}, \tag{5.82}$$

where

$$D_0(\omega) = \frac{3}{8}\frac{Z_{N0}}{\phi_{c0}}\frac{\omega\eta_f}{a^2}, \tag{5.83}$$

$$D_0' = L_0^2 - \frac{8}{3}L_0\mu_0 + \frac{29}{45}\mu_0^2 \tag{5.84}$$

Components of the tensor $\boldsymbol{C^{mf}}$ can then be written as

$$C_{11}^{mf} = L_0^{mf} - \frac{1}{3}\Big[\Big(\frac{32}{35}(\mu_0^{mf})^2 - \frac{8}{5}L_0^{mf}\mu_0^{mf} + (L_0^{mf})^2\Big)Z_{N0}^{mf} + \frac{24}{35}(\mu_0^{mf})^2 Z_{T0})\Big]b, \tag{5.85}$$

$$C_{33}^{mf} = L_0^{mf} - \frac{1}{3}\Big[\Big(\frac{96}{35}(\mu_0^{mf})^2 - \frac{16}{5}L_0^{mf}\mu_0^{mf} + (L_0^{mf})^2\Big)Z_{N0}^{mf} + \frac{16}{35}(\mu_0^{mf})^2 Z_{T0})\Big]b, \tag{5.86}$$

$$C_{13}^{mf} = \lambda_0^{mf} - \frac{1}{3}\Big[\Big(\frac{8}{7}(\mu_0^{mf})^2 - \frac{12}{5}L_0^{mf}\mu_0^{mf} + (L_0^{mf})^2\Big)Z_{N0}^{mf} - \frac{12}{35}(\mu_0^{mf})^2 Z_{T0})\Big]b, \tag{5.87}$$

$$C_{44}^{mf} = \mu_0^{mf} - \frac{2}{105}(2Z_{N0}^{mf} + 5Z_{T0})(\mu_0^{mf})^2 b, \tag{5.88}$$

$$C_{55}^{mf} = \mu_0^{mf} - \frac{4}{105}(3Z_{N0}^{mf} + 4Z_{T0})(\mu_0^{mf})^2 b. \tag{5.89}$$

5.3.1.3 Numerical illustration

In order to get some insight on how fluid and squirt flow affect stress-induced anisotropy, we calculate numerical illustrations for an isotropic fluid-saturated rock subjected to a uniaxial stress σ_{11} varying from 0 to 15 MPa. Input parameters for this numerical example are listed in Table 5.3. The parameters K_h, μ_h, Z_{T0}, Z_{N0} and P_c describing the stress sensitivity of dry rocks were obtained by inverting hydrostatic stress measurements made by Chaudhry [1995] on a dry sample of Penrith sandstone. The inversion, based on Shapiro [2003] stress sensitivity model, is described for this particular sample in Chapter 3, Section 3.5.1.

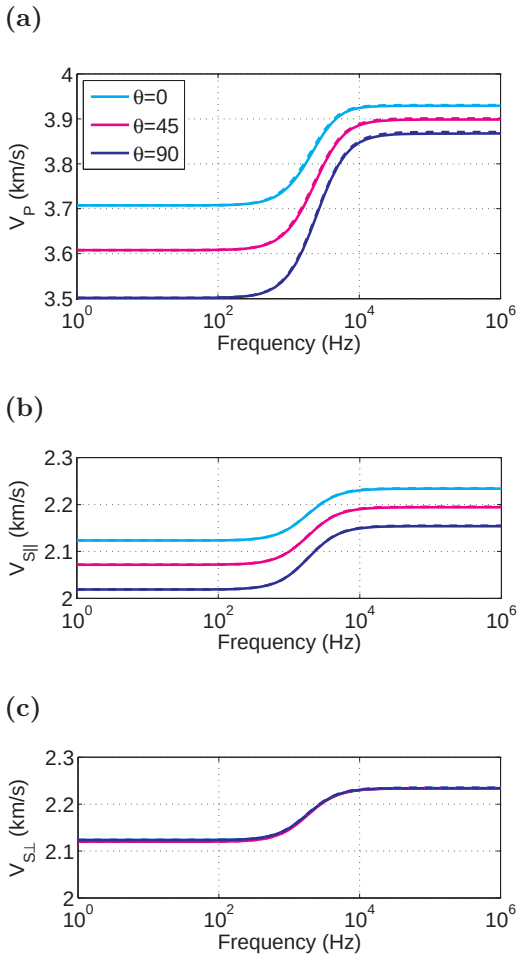

FIGURE 5.9: (a) P-, (b) S⊥- and (c) S||-wave velocity dispersion in the stress-induced anisotropy case.

The velocity dispersion and attenuation computed for $\sigma_{11} = 15$ MPa are shown in Figures 5.9 and 5.10, respectively. The angle θ denotes the angle between the direction of wave propagation and the direction of the applied stress. Cracks are closing preferentially in the direction of the applied stress ($\theta = 0°$), which leads to having P- and S||-waves propagating faster along this direction, especially at low frequencies. At higher frequencies, the stiffening effect of squirt flow induces a velocity increase in all directions. The P- and S||-wave velocity dispersion and the associated attenuation is however less pronounced in the direction of the applied stress due to the crack closure

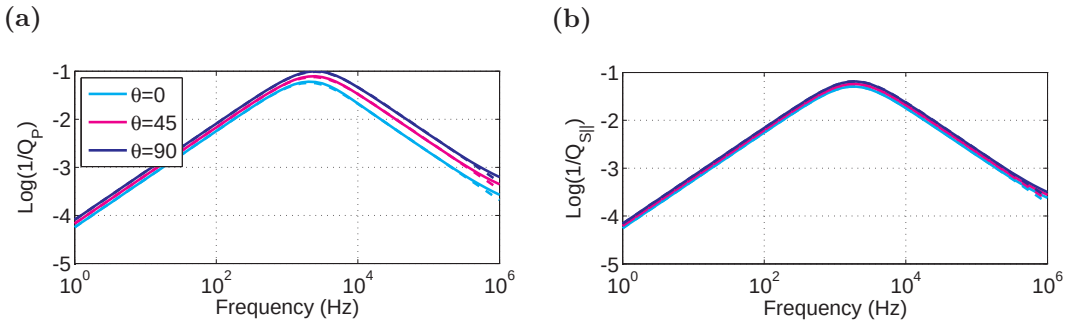

FIGURE 5.10: (a) P- and (b) S||-wave attenuation in the stress-induced anisotropy case.

taking place in this direction. By contrast, the S⊥-wave velocity does not vary significantly as a function of the angle θ, which is a sign that stress-induced anisotropy remains elliptical (i.e. Thomsen [1986] parameters ϵ and δ are equal) for saturated media, regardless of the frequency. The dashed lines show velocities computed from the approximation of stiffness coefficients in the liquid-saturated case, i.e. using equations 5.85 to 5.89. This approximation yields good velocity and attenuation estimations.

In Figure 5.11, we plot the variation of P-wave attenuation as a function of frequency in the direction of the applied stress ($\theta = 0°$) and perpendicular to the applied stress

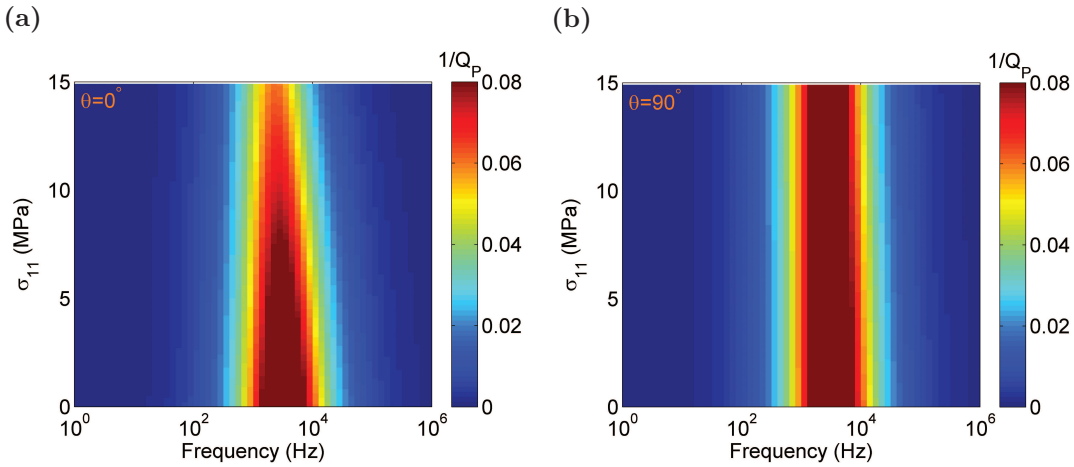

FIGURE 5.11: P-wave attenuation as a function of stress and frequency in the direction of the applied stress (a) and perpendicular to the applied stress (b).

($\theta = 90°$) for uniaxial stress increasing from 0 to 15 MPa. In the direction perpendicular to the stress, the attenuation almost remains the same for each stress level, while it decreases significantly parallel to the applied stress. This observation can be explained by the fact that the squirt flow effect is less important in the direction of the applied stress at high stress levels since cracks are closing preferentially perpendicular to this direction. A similar pattern is observed for attenuation of S$\parallel$-waves, though the attenuation is lower. For S$\perp$-waves, the dispersion remains the same parallel and perpendicular to the applied stress.

5.3.2 Results in terms of anisotropy parameters

In order to better understand the effect of squirt flow on stress-induced anisotropy, we calculate the anisotropy and anellipticity parameters defined for HTI media in Chapter 2, Section 2.2.3.1 (equations 2.15, 2.16, 2.18 and 2.20). Note that we use the weak anisotropy approximation for parameters δ and η since we assume that the applied stress is small, which results in a weak anisotropy. Figure 5.12 shows variation of anisotropy parameters ϵ and γ in the fully saturated medium as a function of frequency and stress. Since the application of stress results in crack closure in the direction perpendicular to the stress, it leads to an increase of P- and S$\parallel$-wave velocities in the direction parallel to the stress ($\theta = 0°$), which is the reason why the anisotropy is seen to increase with stress. On the other hand, the squirt flow tends to stiffen compliant pores, which are predominantly opened along the direction of the applied stress. Hence, when both stress and squirt flow effects are combined, the degree of anisotropy is reduced, which explains the decrease of ϵ^{sat} and γ^{sat} with frequency.

Figure 5.12 shows the exact solution for anisotropy parameters, which cannot be expressed so easily analytically. In order to derive analytical expressions, we first have to consider anisotropy parameters in the modified frame. Approximations for the fully saturated anisotropy parameters can then be obtained using expressions for ϵ^{sat}, γ^{sat}, δ^{sat} and η^{sat} derived in Chapter 4 in the limit of weak anisotropy (equations 4.15, 4.11, 4.16 and 4.21). Here and below, we thus concentrate on finding analytical expressions

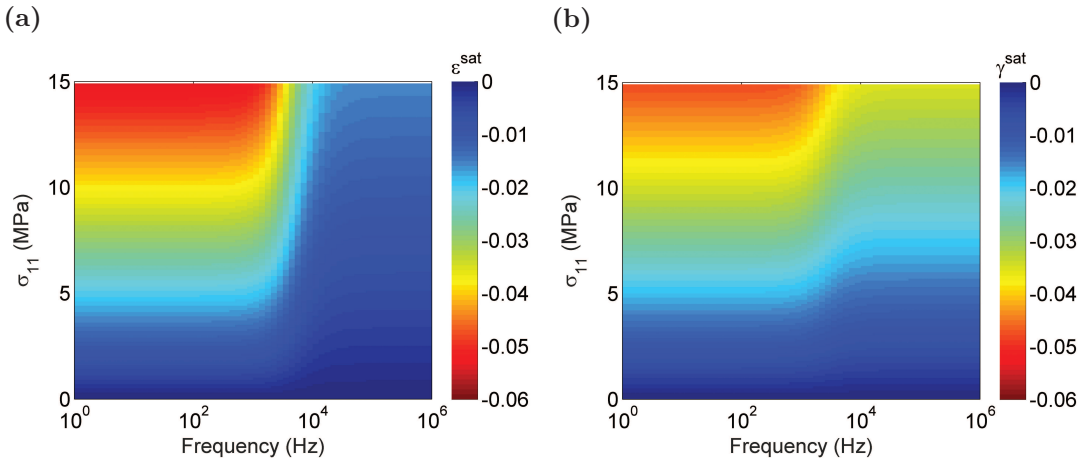

FIGURE 5.12: Variation of anisotropy parameters ϵ^{sat} (a) and γ^{sat} (b) as a function of frequency and stress.

of anisotropy parameters in the modified frame. As explained previously, the stress sensitivity of the modified frame (equation 5.63) is written in the same way as the one of the dry frame (equation 2.51). Hence, anisotropy parameters in the modified frame ϵ^{mf}, δ^{mf} and γ^{mf} can be expressed in a similar way to the ones for the dry medium under stress (equations 2.54 and 2.55). The only difference is that the the Poisson's ratio, shear modulus and normal compliance of the dry unstressed medium, respectively ν_0, μ_0 and Z_{N0} have to be replaced by the corresponding values of the unstressed modified frame, i.e. ν_0^{mf}, μ_0^{mf} and Z_{N0}^{mf}:

$$\epsilon^{mf}(b,\omega) = \delta_{ap}^{mf}(b,\omega) = \frac{2}{105}\frac{(6+2\nu_0^{mf}(\omega))Z_{N0}^{mf}(\omega) + (1-2\nu_0^{mf}(\omega))Z_{T0}}{1-\nu_0^{mf}(\omega)}\mu_0^{mf}(\omega)b, \tag{5.90}$$

$$\gamma^{mf}(b,\omega) = \frac{1}{105}(4Z_{N0}^{mf}(\omega) + 3Z_{T0})\mu_0^{mf}(\omega)b. \tag{5.91}$$

If we assume that the crack density is small, then the Poisson's ratio and shear modulus of the modified frame of the unstressed medium, ν_0^{mf} and μ_0^{mf}, can be replaced by corresponding parameters of the dry medium ν_0 and μ_0 in equations 5.90 and 5.91. Under these conditions, values of the anisotropy parameters of the modified frame can

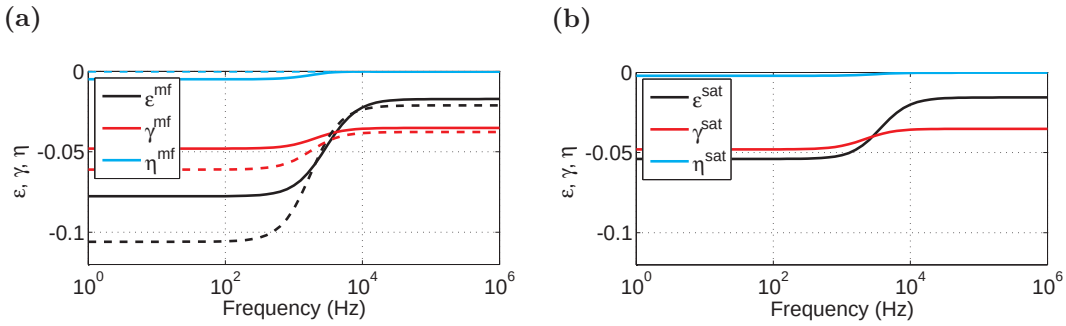

FIGURE 5.13: Frequency dependence of velocity anisotropy parameters in the modified frame (a) and in the saturated medium (b). Solid lines show the exact solution, while dashed lines show the liquid-saturated approximation.

be approximated by

$$\epsilon^{mf}(b,\omega) = \delta^{mf}_{ap}(b,\omega) = \frac{2}{105}\frac{(6+2\nu_0)Z^{mf}_{N0}(\omega) + (1-2\nu_0)Z_{T0}}{1-\nu_0}\mu_0 b, \tag{5.92}$$

$$\gamma^{mf}(b,\omega) = \frac{1}{105}(4Z^{mf}_{N0}(\omega) + 3Z_{T0})\mu_0 b. \tag{5.93}$$

Equations 5.92 and 5.93 convey the fact that the anisotropy degree is reduced with frequency, as the normal compliance of the cracks Z^{mf}_{N0} decreases with frequency. Besides, equation 5.90 shows that the medium remains elliptical at all frequencies, even in the presence of squirt flow. Figure 5.13a shows the exact (solid lines) and approximated (dashed lines) values for the anisotropy and anellipticity parameters ϵ^{mf}, γ^{mf} and η^{mf}. As seen on the figure, the anellipticity parameter remains close to 0, which confirms that the anisotropy caused by the application of a uniaxial stress on an isotropic medium remains elliptical in saturated media, even at high frequencies. Figure 5.13b illustrates the frequency dependence of anisotropy parameters in the fully saturated medium, i.e. after applying the anisotropic Gassmann equations. We can see that the main effect of taking into account the fluid filling the stiff pores is to reduce the degree of P-wave anisotropy. The anisotropy pattern remains the same, in particular, the fully saturated medium remains elliptical.

In the high-frequency limit, the normal compliance of cracks in the unrelaxed frame Z^{uf}_{N0} is close to 0 (equation 5.66), so anisotropy parameters ϵ^{uf} and γ^{uf} in the unrelaxed

frame reduce to

$$\epsilon^{uf}(b) = \delta^{uf}(b) = \frac{2}{105}\frac{1-2\nu_0}{1-\nu_0} Z_{T0}\mu_0 b, \tag{5.94}$$

$$\gamma^{uf}(b) = \frac{3}{105} Z_{T0}\mu_0 b. \tag{5.95}$$

5.3.3 Attenuation anisotropy parameters

The attenuation anisotropy parameters as defined by Zhu & Tsvankin [2006] (equations 5.51 to 5.53) along with the alternative definition proposed in this chapter (equations 5.57 to 5.59) are plotted as a function of frequency in Figure 5.14a. The variation of parameters ϵ_Q, δ_Q and γ_Q follows the same trend as the variation of Thomsen anisotropy parameters, i.e. they vary from a minimum value corresponding to their low-frequency limit to a maximum value corresponding to their high-frequency limit. Note that these parameters are of order unity, which contradicts the weak attenuation anisotropy approximation assumed by Zhu & Tsvankin [2006]. Besides, these parameters are still finite for low and high frequencies, for which attenuation tends to zero. In contrast, parameters ϵ_{Qa}, γ_{Qa} and δ_{Qa}, which provide another way of quantifying attenuation anisotropy, tend to zero in the low- and high-frequency limits and reach their maximum at the characteristic frequency (Figure 5.14b). In addition, $\epsilon_{Qa}, \gamma_{Qa}, \delta_{Qa} \ll 1$ as they are linear functions of coefficients $1/Q_{ij}$, which remain small when considering that the attenuation is weak.

Figure 5.15 illustrates the variation of the attenuation anisotropy as a function of frequency and stress. The attenuation anisotropy is almost null for low stresses, which is consistent with the fact that for low stresses, the anisotropy is very weak (see Figure 5.13). For higher stresses, the attenuation anisotropy becomes more significant.

5.3.4 Discussion on the stress-induced anisotropy case

In this part of the chapter, we have developed a model to account for the combined effect of stress and local fluid flow on elastic properties of an initially elastic and isotropic

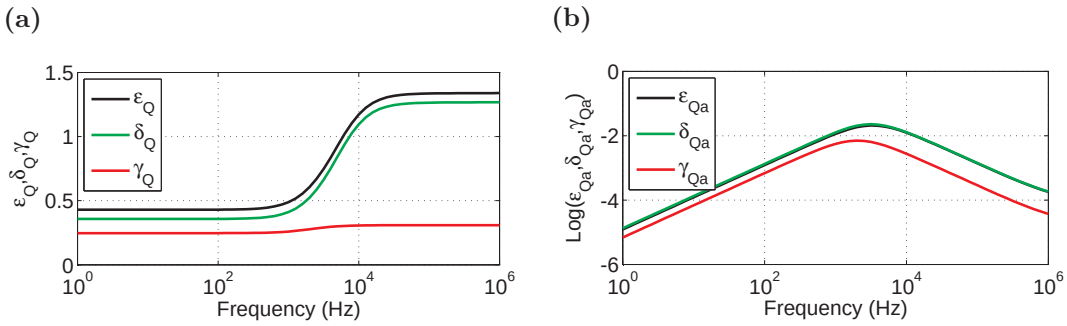

FIGURE 5.14: Frequency dependence of attenuation anisotropy parameters defined by Zhu & Tsvankin [2006] (a) and attenuation anisotropy parameters proposed in equations 5.57 to 5.59 (b) in the saturated medium for $\sigma_{11} = 15$ MPa.

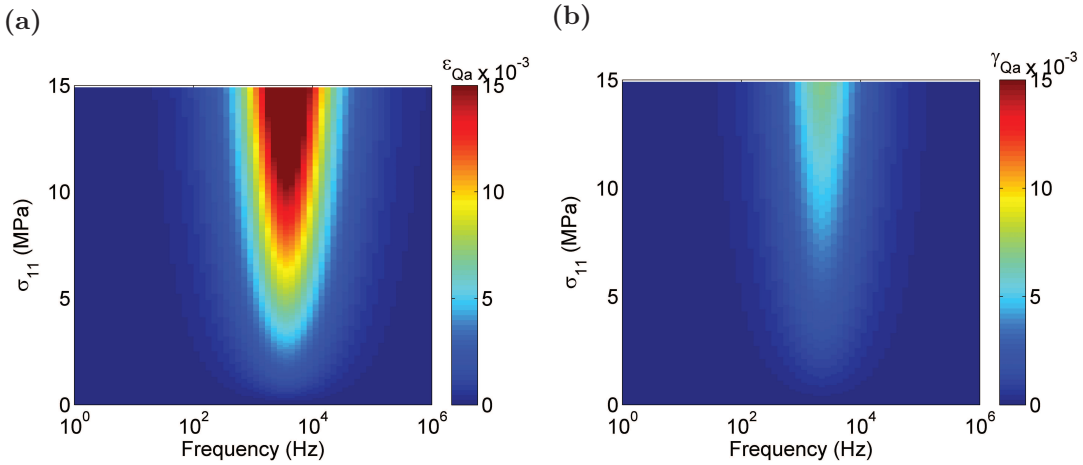

FIGURE 5.15: Variation of attenuation anisotropy parameters ϵ_{Qa} (a) and γ_{Qa} (b) as a function of frequency and stress.

medium. The stress-induced anisotropy of the dry medium is modelled using the approach of Gurevich et al. [2011] (Chapter 2, Section 2.4.2). Squirt flow effects are incorporated to this model by extending the isotropic squirt flow model of Gurevich et al. [2010] to this particular case of anisotropy. By construction, the model is consistent with the anisotropic Gassmann [1951] equations in the low-frequency limit and the Mukerji & Mavko [1994] model in the high-frequency limit. The model developed in this section presents several advantages. In addition to giving the low- and high-frequency limits [Guéguen & Sarout, 2011, Mukerji & Mavko, 1994, Xu, 1998], this model gives the frequency dependency of the stiffness tensor. Thus, it is possible to

gain some insight on attenuation as well as velocity dispersion. Second, it is possible to get closed-form expressions for velocity and attenuation from this model.

The model involves several parameters, most of which can be inferred from hydrostatic stress measurements performed on dry rocks. Indeed, the stress sensitivity of the dry medium varies as a function of five parameters: the bulk and shear moduli K_h and μ_h of the medium in the high-stress limit, the normal and tangential compliance of the cracks Z_{N0} and Z_{T0} and the characteristic crack closing pressure P_c. As discussed previously, these five parameters can be inverted from velocities measured under hydrostatic stress using Shapiro [2003] stress sensitivity model (Chapter 2, Section 2.4.1). At low frequencies, the effect of fluid is accounted for by using the anisotropic Gassmann [1951] equations. Additional parameters required for the application of the anisotropic Gassmann [1951] are the fluid and grain bulk moduli and the total porosity of the medium. In the high-frequency limit, additional knowledge of the compliant porosity ϕ_{c0} in the unstressed state is necessary. This parameter can also be estimated by inverting hydrostatic stress measurements. Finally, the frequency-dependence of elastic parameters is conditioned by the geometry of compliant pores. In our model, we used the pore configuration introduced by Murphy et al. [1986], in which compliant pores are disc-shape gaps whose edges open into toroidal stiff pores. Initially, these gaps are described by their radius and width, but the variable that really matters is the aspect ratio of these pores. Note that this parameter is the only adjustable parameter in our model.

The main conclusions regarding attenuation and velocity dispersion that can be drawn from this model are as follows. 1) The crack closure occurring preferentially perpendicular to the applied stress leads to an increase of seismic velocities as a function of stress in the direction of applied stress. It also causes a decrease of squirt flow induced dispersion and attenuation in this direction. 2) The anisotropy of squirt flow dispersion engenders a decrease in the degree of anisotropy with frequency. 3) The stress-induced anisotropy remains elliptical, even in saturated media, for all frequency ranges. This result is particularly interesting since it provides a way of distinguishing

stress-induced anisotropy from the anisotropy caused by the presence of aligned cracks. Indeed, as mentioned in the first part, in the case of aligned cracks embedded in an isotropic background, the dry medium is elliptical if and only if the compliance ratio B of the cracks equals 1. At low-frequencies, the ellipticity result is preserved provided the background porosity is high enough (Chapter 4). At higher frequencies however, the P-wave anisotropy parameter ϵ vanishes, while the δ-parameter remains the only measure of P-S$\perp$ wave anisotropy (Figure 5.8); the anellipticity parameter thus goes from zero to $-\delta$.

For simplicity's sake, we focused on the anisotropy resulting from the application of a uniaxial stress on an isotropic medium. By using predictions of the stress-induced anisotropy model derived in Chapter 3, it is easy to extend this work to triaxial stress. In fact, expressions of the stress sensitivity of the dry, modified and unrelaxed frames (equations 2.51, 5.63 and 5.64) remain the same, but tensors $\boldsymbol{\alpha}^{\boldsymbol{an}}$ and $\boldsymbol{\beta}^{\boldsymbol{an}}$ describing the effect of crack closure on the elastic properties of the medium under stress are different. Their expressions for triaxial stress can be deduced from expressions for crack tensors $\bar{\boldsymbol{\alpha}}$ and $\boldsymbol{\beta}$ given in Chapter 3 (equations 3.17 to 3.20 and 3.22 to 3.28).

To derive this model, we assume that the uniaxial stress is applied slowly. Hence, the only parameter that is affected by the presence of fluid in the equation describing the stress sensitivity of the modified frame is the normal crack compliance Z_{N0}^{mf}. If the uniaxial stress is applied too fast, then the pore pressure may not have time to equilibrate between stiff pores and compliant pores and the characteristic crack closing pressure P_c might be affected by this overpressure in compliant pores. This overpressure is accounted for by Zatsepin & Crampin [1997].

5.4 Conclusions

In this chapter, we have developed a simple model of squirt-flow relaxation in anisotropic media saturated with fluid. By construction, the model is consistent with the anisotropic Gassmann [1951] equations in the low-frequency limit and the

anisotropic squirt flow model of Mukerji & Mavko [1994] in the high-frequency limit. Studying the effect of squirt flow on elastic properties requires knowledge of the crack distribution. Hence, in this work, we focused on two cases: the simple case for which cracks are parallel and the case for which anisotropy results from the application of uniaxial stress on an initially isotropic medium. Besides, the frequency-dependence of elastic properties in saturated media is governed by the pore geometry. In this study, we chose the pore configuration proposed by Murphy et al. [1986] in which compliant pores form disc-shaped gaps between stiff pores. For liquid-saturated rocks, it is possible to derive analytical expressions of elastic moduli in the limit of weak anisotropy.

The anisotropy and attenuation patterns are significantly different in the two cases studied in this chapter. In the case of aligned cracks, the S$\parallel$-wave only depends on the tangential weakness Z_T, which does not vary as a function of frequency. As a consequence, no S$\parallel$-wave velocity dispersion is observed and the S-wave anisotropy parameter γ is not affected by the presence of fluid for all frequency ranges. Since the presence of fluid highly stiffens cracks in the high-frequency limit, the velocity of P-waves propagating perpendicular and parallel to the cracks are almost equal. Hence, the P-wave anisotropy parameter ϵ vanishes in the high-frequency limit, and the anisotropy parameter δ remains the only indicator of P-S$\perp$ wave anisotropy. This feature also implies that even if the medium is elliptical in the dry state or saturated state in the low-frequency limit, it is no longer the case in the high-frequency limit. In the stress-induced anisotropy case, the crack closure occurring perpendicular to the applied stress leads to an increase of seismic velocities perpendicular to the applied stress, but also causes a decrease of attenuation and velocity dispersion in this direction. The anisotropy of squirt flow dispersion results in a decrease of the anisotropy degree as a function of frequency. Finally, the stress-induced anisotropy remains elliptical for all frequencies in saturated media. This feature could help differentiating between stress- and crack-induced anisotropy by estimating the degree of anellipticity.

Chapter 6

Estimation of azimuthal stress-induced P-wave anisotropy from S-wave anisotropy measured in log or VSP data

6.1 Chapter overview

Based on the relationships between anisotropy parameters established by the stress-induced anisotropy model derived in Chapter 3, we develop a methodology to infer azimuthal P-wave anisotropy from S-wave anisotropy calculated from log or VSP data. The aim of this work is to facilitate the estimation of azimuthal P-wave anisotropy in areas where anisotropy is primarily stress-induced. Estimation of azimuthal P-wave anisotropy usually requires multi-azimuth seismic surveys, which are expensive to acquire offshore and thus are relatively rare. In contrast, shear wave azimuthal anisotropy is nowadays routinely measured in multipole sonic logging [Esmersoy et al., 1994, Tang & Chunduru, 1999] and vertical seismic profiling (VSP) [Pevzner et al., 2011, Winterstein & Meadows, 1991] data through analysis of shear wave birefringence. Hence,

being able to estimate azimuthal P-wave anisotropy from S-wave anisotropy would be very valuable.

There is no general relationship linking P- and S-wave anisotropies; however such a relationship may exist for a particular mechanism of anisotropy. For instance, when anisotropy is caused by the presence of parallel penny-shaped cracks embedded in an isotropic elastic background, both P-wave and S-wave anisotropies are controlled by the same parameter - the crack density [Hudson, 1980, Schoenberg & Douma, 1988], and thus P-wave anisotropy can be estimated from measurements of S-wave anisotropy. The objective of this study is to develop such an approach for stress-induced anisotropy by utilizing the stress-induced anisotropy model presented in Chapter 3. Application of a non-hydrostatic stress to an elastic medium leads to preferential closure of discontinuities depending on the orientation of discontinuities with respect to the stress field. This phenomenon results in P- and S-wave anisotropies, both of which are controlled by the same set of parameters describing the properties of individual discontinuities and their orientation pattern (as well as properties of the embedding matrix) [Mavko et al., 1995, Sayers, 1988, 2006]. Several studies showed that the anisotropy resulting from the application of uniaxial stress on a dry initially elastic isotropic medium is elliptical [Prioul et al., 2004, Schwartz et al., 1994], i.e. Thomsen's (1986) anisotropy parameters ϵ and δ are equal. Using the third order elasticity theory, Rasolofosaon [1998] further demonstrated that initially isotropic media subjected to triaxial stress exhibit ellipsoidal anisotropy. Stress-induced anisotropy models recently derived by Gurevich et al. [2011] and in Chapter 3 are consistent with these results. In addition, they established a direct analytical relationship between Thomsen's anisotropy parameters ϵ and γ, which respectively quantify the degrees of P-wave anisotropy and S-wave anisotropy.

In this chapter, we develop a methodology to infer azimuthal P-wave anisotropy from S-wave anisotropy in areas where the anisotropy is known to be stress-induced. This implies that one has to qualify the azimuthal anisotropy as stress-induced prior to using this workflow. Such a task might be cumbersome; however, absence of fractures

in the image logs, large differences between minimum and maximum horizontal stresses, the presence of loose high porosity sandstone formations and crossover in the dipole dispersion curves measured in the fast and slow directions [Winkler et al., 1998] might indicate that the dominant mechanism of anisotropy is stress-induced. In the following, we assume that the medium has an orthorhombic symmetry and that the azimuthal anisotropy is due only to the presence of differential stress acting on the rock. The workflow presented here only requires knowledge of two parameters: the Poisson's ratio of the dry unstressed isotropic medium and the crack compliance ratio. To include fluid effects into the model, we use expressions of the anisotropic Gassmann [1951] equations in terms of orthorhombic anisotropy parameters derived in Chapter 4, in order to relate the anisotropy parameters in the saturated medium to those of the dry medium. Using the anisotropic Gassmann equations restricts the validity of the study to low frequencies and relatively high permeability reservoirs, for which all pores and cracks can be assumed to be hydraulically connected. For higher frequencies or low permeability rocks, dynamic models such as the one derived by Zatsepin & Crampin [1997] must be used. Such models involve more parameters and, as a result, their implementation is not as straightforward as the methodology presented here.

The chapter outline is as follows. First, we describe the methodology we developed to infer azimuthal P-wave anisotropy from S-wave anisotropy using these models. Then, we apply this workflow to data acquired in the North West Shelf of Australia, where seismic anisotropy has been assessed to be stress-induced, and compare the estimated azimuthal P-wave anisotropy to the one obtained from orthorhombic tomography performed on dual azimuth 3D seismic data.

6.2 Workflow

In this section, we describe the workflow used in order to estimate the azimuthal P-wave anisotropy parameter $\epsilon^{sat}_{(3)}$ from the azimuthal S-wave anisotropy parameter $\gamma_{(3)}$ obtained from log or VSP data measured along a vertical well. The methodology utilizes

the relationship derived in Chapter 3 linking the anisotropy parameters $\epsilon_{(3)}$ and $\gamma_{(3)}$ in dry isotropic media subjected to triaxial stress. The effect of fluid is then taken into account by using the approximation of $\epsilon_{(3)}^{sat}$ as a function of $\epsilon_{(3)}^{dry}$ derived in Chapter 4 from the anisotropic Gassmann equations. Detailed steps of the workflow along with input parameters are explained below.

6.2.1 Input parameters

The input log data consists in the P-wave velocity V_P, the fast and slow shear wave velocities, respectively V_{SF} and V_{SS}, and the density log, which connects the velocities to the stiffness coefficients. The P- and S-wave velocities can alternatively be obtained using VSP data. The porosity log is also necessary to perform Gassmann fluid substitution as well as the fluid and grain bulk moduli K_f and K_g.

In order to apply the stress-induced anisotropy model, values of the compliance ratio B and the Poisson's ratio of the unstressed rock ν_0 are required. As discussed in Chapter 2, Section 2.4.1, those parameters can be determined by fitting Shapiro [2003] stress sensitivity model to hydrostatic stress measurements made on dry core samples. If no core data is available, one can use typical values of the compliance ratio obtained for different lithologies [Angus et al., 2009, Sayers & Han, 2002], and the Poisson's ratio of the unstressed rock ν_0 can be approximated by:

$$\nu_0 = \frac{C_{33} - (C_{44} + C_{55})}{2C_{33} - (C_{44} + C_{55})}. \tag{6.1}$$

6.2.2 Step 1: Computation of the S-wave anisotropy in the dry medium

Taking the x_1-axis along the maximum horizontal stress direction, we compute the shear wave moduli C_{44} and C_{55} by multiplying respectively the squared slow and fast shear-wave velocity logs by the density log. Logs are measured in the saturated medium but since we assume Gassmann [1951] theory is applicable, it follows that $C_{44}^{sat} = C_{44}$

and $C_{55}^{sat} = C_{55}$, which yields

$$C_{44} = \rho V_{SS}^2 \text{ and } C_{55} = \rho V_{SF}^2. \tag{6.2}$$

The azimuthal S-wave anisotropy parameter in the dry medium, which corresponds to the γ-parameter in the $[x_1, x_2]$-plane (Chapter 2, Section 2.2.3.2), is given by

$$\gamma_{(3)} = \frac{C_{44} - C_{55}}{2C_{55}}. \tag{6.3}$$

6.2.3 Step 2: Inversion for C_{33}

The P-wave velocity measured in-situ using logging or VSP is the P-wave velocity in the saturated medium which, combined with the density log, yields C_{33}^{sat}. Using the isotropic Gassmann equations (Chapter 2, Section 2.5.1.1), we express C_{33}^{sat} as a function of the reference P-wave modulus in the dry medium C_{33}:

$$C_{33}^{sat} = C_{33} + \alpha^2 M. \tag{6.4}$$

The quantities α and M are respectively the Biot-Willis coefficient and Gassmann pore space modulus given by equations 2.58 and 2.59 with K being the reference bulk modulus suggested by Tsvankin [1997]:

$$K = C_{33} - \frac{4}{3}C_{55}. \tag{6.5}$$

Using a least square inversion, we fit C_{33} so as to minimize the error between C_{33}^{sat} obtained from the log (or VSP) and C_{33}^{sat} computed from Gassmann fluid substitution (equation 6.4).

6.2.4 Step 3: Computation of the azimuthal P-wave anisotropy in the dry medium

From the relationship established by the stress-induced anisotropy model between the anisotropy parameters $\epsilon_{(3)}$ and $\gamma_{(3)}$ (equation 3.35), we calculate the P-wave anisotropy parameter in the dry medium:

$$\epsilon_{(3)} = 2\frac{2\nu_0 B + 6B - 2\nu_0 + 1}{(1-\nu_0)(3+4B)}\gamma_{(3)}. \tag{6.6}$$

The Poisson's ratio of the unstressed isotropic rock ν_0 is either inferred from core measurements as mentioned previously, or approximated by equation 6.1.

6.2.5 Step 4: Computation of the azimuthal P-wave anisotropy in the saturated medium

Once the P-wave anisotropy parameter $\epsilon_{(3)}$ is known in the dry medium, we can calculate the P-wave anisotropy parameter $\epsilon_{(3)}^{sat}$ in the saturated medium using the approximation derived from the anisotropic Gassmann equations, equation 4.57. Assuming that the anisotropy is weak and that we are dealing with stress-induced anisotropy, equation 4.57 can be further simplified by linearizing α_1^2 and α_2^2 and by taking into account that $\epsilon_{(3)} = \delta_{(3)}$:

$$\epsilon_{(3)}^{sat} = \frac{L}{L^{sat}}\epsilon_{(3)} + \frac{(-3L\epsilon_{(3)} + 4\mu\gamma_{(3)})\alpha_0 M}{3K_g L^{sat}}, \tag{6.7}$$

where $L = C_{33}$ and $L^{sat} = C_{33}^{sat}$. Parameters α_0 and M are given by equations 2.64 and 2.65, respectively, using $K^* = K = C_{33} - 4C_{55}/3$.

6.3 Application to log data from the North West Shelf of Australia

In this section, we test the methodology described above by applying it to log data acquired in the Stybarrow field, located on the North West Shelf of Australia. This area was chosen on purpose as it exhibits significant shear wave anisotropy, which is likely to be due to large differences between the minimum and maximum horizontal stresses acting in the area. Besides, the azimuthal P-wave anisotropy was already estimated in this field via orthorhombic tomography performed on dual azimuth seismic data, which provides a means of checking the validity of our results. In the following, we first give an introduction on the anisotropy, stress field and lithology in the study area. The orthorhombic tomography performed in the area is then briefly described. Finally, we show results obtained when applying the methodology developed above to log data acquired in the area.

6.3.1 Study area

The Stybarrow field is located off the North West Australia coast, in the Exmouth sub-basin, approximately 65 km from Exmouth. Azimuthal shear wave anisotropy was observed in cross-dipole shear sonic logs recorded in several wells in the area (Figures 6.3a, 6.4a, 6.5a) and was further confirmed by shear wave splitting estimated from VSP data (Figure 6.1a) [Pevzner et al., 2011]. Azimuthal P-wave anisotropy was also evoked to account for azimuthal variations of NMO velocities [Bishop et al., 2010, Hung et al., 2006].

The field lies within the Carnarvon basin, which is known for large differences between maximum and minimum horizontal stresses. The stress state in the area corresponds to a strike-slip regime. At the reservoir layer, i.e. in the Macedon sandstone formation, maximum horizontal, minimum horizontal and vertical effective stresses are approximately: $\sigma_{Hmax} = 18.5$ MPa, $\sigma_{hmin} = 6.0$ MPa and $\sigma_V = 11.5$ MPa [Napalowski et

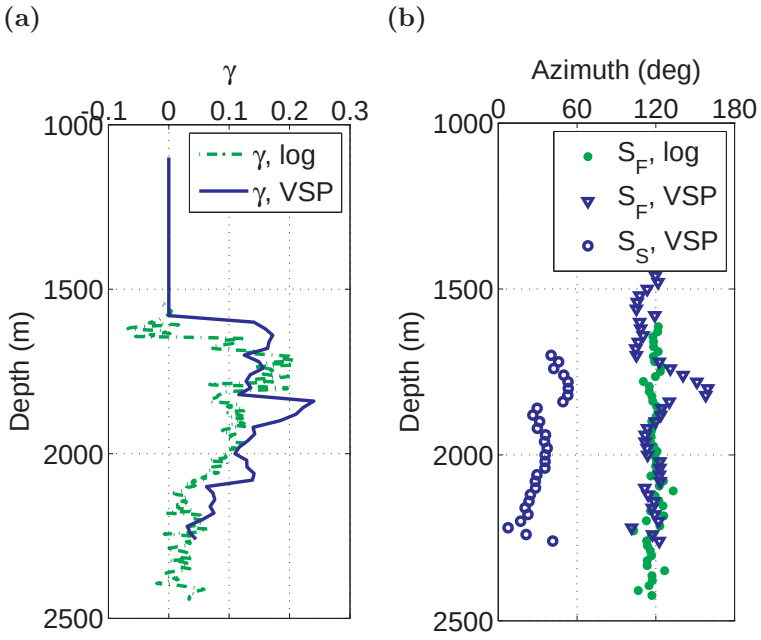

FIGURE 6.1: S-wave anisotropy parameter γ (a) and direction of the fast shear wave velocity (b) estimated from log and VSP data. Reproduced after Pevzner et al. [2011].

al., 2008, Underschultz et al., 2008]. The fast velocity direction observed in log and VSP data (Figure 6.1b) approximately matches the maximum regional stress direction indicated by borehole breakouts (Figure 6.2). The lithology comprises an alternation of sand and shale layers. The sandstone layers are poorly consolidated and soft, with porosity up to 33 % [Ementon et al., 2004]. Since no noticeable fractures are observed in the image logs, it is reasonable to assume that azimuthal anisotropy in this area is due to stress rather than fractures.

6.3.2 Orthorhombic tomography ran in the area

Azimuthal anisotropy parameters were estimated directly from the seismic data. At Stybarrow, two 3D seismic surveys were shot with different acquisition orientations as part of a 4D monitoring project. One survey was shot east-west, which is approximately 30° from the maximum stress direction. The second survey was shot approximately

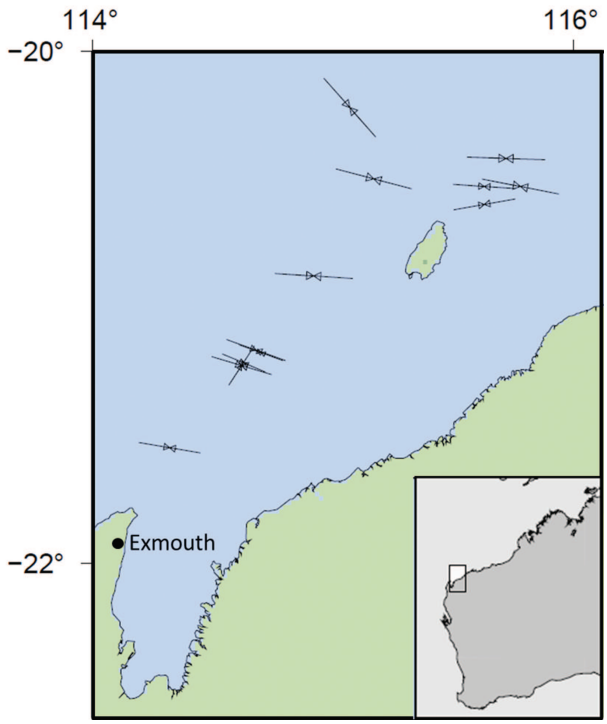

FIGURE 6.2: Maximum horizontal stress orientations obtained from borehole breakouts in the North West Shelf of Australia [Denham, 1983, Hillis et al., 1997]. Modified from Heidbach et al. [2008].

30° east of north, corresponding to the minimum stress direction. Strong azimuthal anisotropy was observed on the seismic data, which was manifested as large timing delays increasing in magnitude with offset, between the two surveys.

The velocity model building process consisted of an iterative approach, using a previously derived VTI velocity model as the initial model. Iterations of VTI tomography were used to update the velocity and anisotropy models in the overburden, where azimuthal anisotropy is weak to absent. In the deeper section below the Barrow Group unconformity, the strength of azimuthal anisotropy is strong. For this section, an initial orthorhombic model was created by updating anisotropy parameters for each individual survey with fixed velocity model. In this initial orthorhombic model, the azimuth of the fast velocity direction was fixed at 120° to match the fast velocity direction indicated by log data. Then, iterations of joint tomography using orthorhombic ray tracing were

used to simultaneously update the parameters V_0, $\delta_{(1)}$, $\delta_{(2)}$, $\epsilon_{(1)}$ and $\epsilon_{(2)}$ using both seismic datasets. The final derived orthorhombic models were used to prestack depth migrate both seismic datasets.

6.3.3 Results

We apply the workflow described in the previous section to three wells located in the Stybarrow oil field. Figures 6.3, 6.4 and 6.5 show the fast and slow S-wave velocities measured from logs, the $\gamma-$ray log, the inverted Poisson's ratio of the unstressed hypothetical rock and the anisotropy parameters estimated for each of these wells. Note that the methodology is applied to the entire log, but the model is expected to work only in the sandstone units of the Barrow, Pyrenees and Macedon members. These units, respectively denoted A, B and C in the following, are highlighted in grey in Figures 6.3, 6.4 and 6.5 using information from Ementon et al. [2004], Underschultz et al. [2008]. Since hydrostatic core sample measurements are not available for these wells, we use $B = 0.6$, which is a typical value for the compliance ratio in dry sandstones [Angus et al., 2009, Sayers & Han, 2002] and we infer the Poisson's ratio of the unstressed rock using equation 6.1. The grain bulk modulus is taken as $K_g = 35$ GPa. We assume that all layers apart from the Macedon reservoir are fully saturated with brine, for which the fluid bulk modulus was estimated to be $K_f = 2.6$ GPa from hydraulic data presented in Underschultz et al. [2008]. In the Macedon reservoir, K_f is fixed at 1.55 GPa, corresponding to oil saturation.

Figures 6.3c, 6.4c and 6.5c show an approximation of the Poisson's ratio in the hypothetical dry unstressed isotropic rock calculated from equation 6.1 after deducing the dry P-wave modulus C_{33} from Gassmann equations. The obtained values lie between 0.05 and 0.25, which is consistent with typical values calculated from core measurements made on dry isotropic sandstone samples [Grochau & Gurevich, 2008, Han, 1986, King, 1966, Mann & Fatt, 1960].

Results obtained for the anisotropy parameters are presented in Figures 6.3d, 6.4d and 6.5d. The solid green lines show the S-wave anisotropy parameter $\gamma_{(3)}$. Since we assume that Gassmann equations are applicable, this parameter is not affected by the presence of fluid, yielding $\gamma_{(3)}^{dry} = \gamma_{(3)}^{sat}$. The red dash-dotted and solid lines respectively show the P-wave anisotropy parameter $\epsilon_{(3)}$ in the dry and saturated media. Note that according to the stress-induced anisotropy model developed in Chapter 3, the anisotropy parameters $\epsilon_{(3)}$ and $\delta_{(3)}$ are equal in the dry medium. As shown in Chapter 4, this result is still valid for saturated media assuming that the anisotropy is weak enough; hence, $\epsilon_{(3)}^{sat} = \delta_{(3)}^{sat}$.

The values obtained for $\epsilon_{(3)}^{sat}$ and $\delta_{(3)}^{sat}$ are compared to the ones obtained at the well locations from orthorhombic tomography conducted on the dual azimuth 3D seismic data acquired in the area (solid and dashed black lines in Figures 6.3d, 6.4d and 6.5d). There is a reasonable agreement between both estimations in the sandstone layers, which can be classified as 'clean' (i.e. sandstone layers having a low γ-ray) (Zones A and C in Figures 6.3d, 6.4d and 6.5d). In the shale and shaly sandstones units (Zone B), there is a discrepancy between our results and the ones obtained via orthorhombic tomography. This discrepancy can be explained by the fact that our model is derived to characterize the stress-induced anisotropy of initially isotropic rocks and thus, it does not handle the anisotropy caused by differential stresses acting on an intrinsically anisotropic rock.

6.4 Applicability of the methodology and uncertainties

In this study, we have developed a methodology to infer azimuthal P-wave anisotropy from S-wave anisotropy using log or VSP data. Note that this methodology is based on the stress-induced anisotropy model derived in Chapter 3. The main assumption of this model is that the unstressed initial medium is isotropic and the anisotropy results from preferential closure of compliant pores. Hence, this workflow only applies in areas where the anisotropy is due to differential stresses acting on the rock, i.e. this methodology is

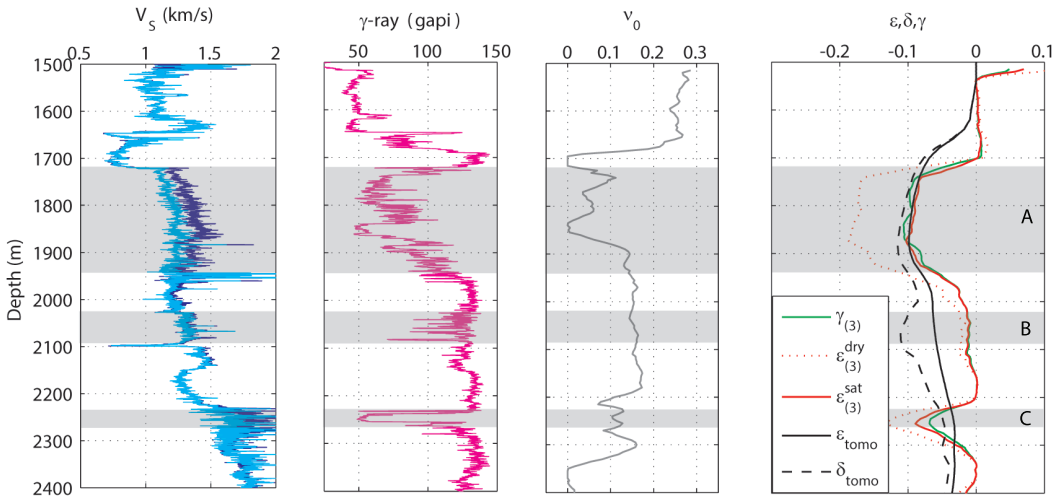

FIGURE 6.3: Log measurements and results for Stybarrow-1 well: (a) S-wave velocity log showing the fast (dark blue) and slow (light blue) wave velocities; (b) γ-ray log; (c) inverted Poisson's ratio of the dry unstressed rock; (d) azimuthal anisotropy parameters obtained using the methodology developed in the present work (green and red curves) compared to those estimated by orthorhombic tomography (black curves). Zones A, B, C respectively indicate the Barrow, Pyrenees and Macedon members.

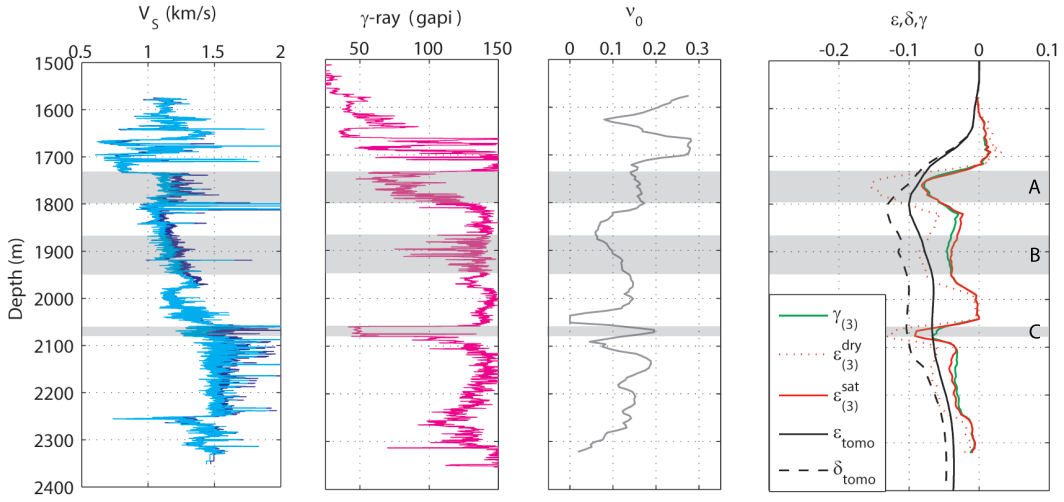

FIGURE 6.4: Log measurements and results for Stybarrow-2 well: (a) S-wave velocity log showing the fast (dark blue) and slow (light blue) wave velocities; (b) γ-ray log; (c) inverted Poisson's ratio of the dry unstressed rock; (d) azimuthal anisotropy parameters obtained using the methodology developed in the present work (green and red curves) compared to those estimated by orthorhombic tomography (black curves).

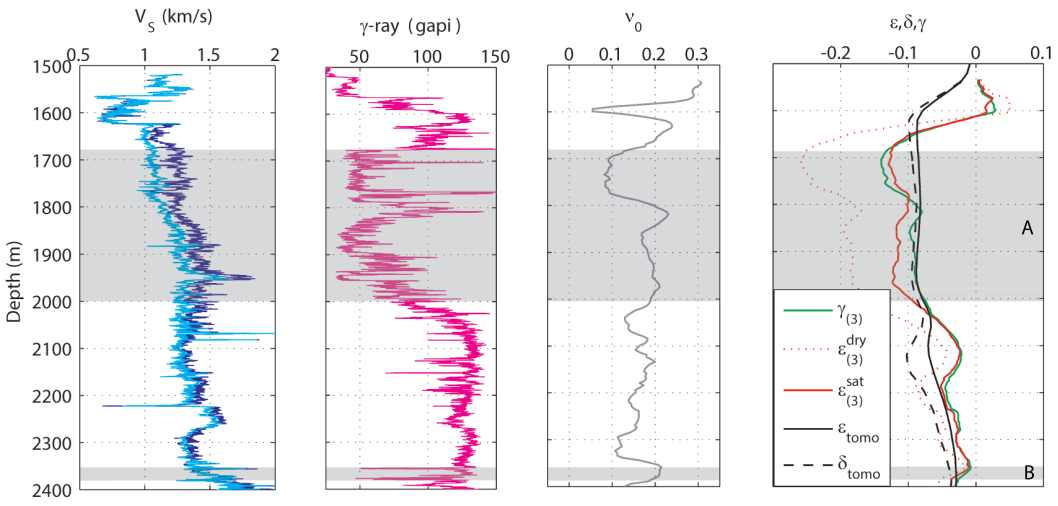

FIGURE 6.5: Log measurements and results for Stybarrow-3 well: (a) S-wave velocity log showing the fast (dark blue) and slow (light blue) wave velocities; (b) γ-ray log; (c) inverted Poisson's ratio of the dry unstressed rock; (d) azimuthal anisotropy parameters obtained using the methodology developed in the present work (green and red curves) compared to those estimated by orthorhombic tomography (black curves).

not suitable for intrinsically anisotropic formations or when anisotropy is partly due to networks of aligned fractures. We acknowledge that assessing the cause of anisotropy is not an easy task, all the more since anisotropy often results from a combination of several factors such as presence of fractures, layering, non-hydrostatic stresses or preferred orientation of crystals. In some specific regions however, absence of fractures in the image logs, large differences between minimum and maximum horizontal stresses and the presence of loose high porosity sandstone formations can suggest that the azimuthal anisotropy is mostly stress-induced.

The study case presented in this chapter is attractive for two reasons. First, the stress field in the Stybarrow area is such that the large difference between the maximum and minimum horizontal stresses can create significant anisotropy in the loose sandstone formations, especially in sandstones of the Barrow and Macedon members, for which we believe that our model is applicable. Second, we were able to compare our predictions with anisotropy parameters previously estimated via orthorhombic tomography performed on the 3D dual azimuth seismic data. Such a comparison however has some

shortcomings. Indeed, our model is only applicable to initially isotropic rocks subjected to differential stresses. Hence, we do not expect the model predictions to be correct in the shale layers or in the shaly sandstone layers. These layers are characterized by a high γ-ray in Figures 6.3, 6.4 and 6.5. Modelling the anisotropy of this type of formations is cumbersome and it requires assumptions about the crack distribution (e.g. Ciz & Shapiro [2008], Pervukhina et al. [2011]). It is also worth emphasizing that the vertical resolution of the orthorhombic tomography is much lower than the resolution of the predictions derived from the log data using our model. This difference in vertical resolution might contribute to the discrepancies observed between anisotropy parameters estimated using our model and those obtained via orthorhombic tomography, in particular in thin reservoir layers.

Absence of knowledge about the compliance ratio B and Poisson's ratio ν_0 of the hypothetical unstressed rock might also engender uncertainties. To illustrate those uncertainties, we display the P-wave anisotropy parameters computed in the dry and saturated medium for $B = 0.4$ (green curves) and $B = 0.8$ (blue curves) in Figure 6.6a. Typical compliance ratios estimated from core sample measurements of dry sandstones lie between these limits [Angus et al., 2009, Sayers & Han, 2002]. The maximum relative error for $\epsilon_{(3)}^{sat}$ is 15 % obtained at 2255 meters depth. To investigate the sensitivity of the results to the Poisson's ratio value, we compute the anisotropy parameters assuming a constant Poisson's ratio of 0.05 and 0.25. Results are presented in Figure 6.6b. The maximum relative error is 22 %.

Other uncertainties stem from the use of the isotropic Gassmann equations to invert for the P-wave modulus in the dry medium C_{33}. Figure 6.6c shows the results for $\epsilon_{(3)}$ in the dry and saturated media when introducing an error of 10 % to the inverted dry P-wave modulus. This range of errors on C_{33} was found by Sava et al. [2000] and Mavko & Bandyopadhyay [2009] when modelling uncertainties resulting from the use of the isotropic Gassmann equations in three types of anisotropic media: a layered medium, a medium permeated by aligned fractures and a medium with a stress-induced anisotropy. Such uncertainties lead to a maximum relative error of 18 % for $\epsilon_{(3)}^{sat}$. Besides, equation

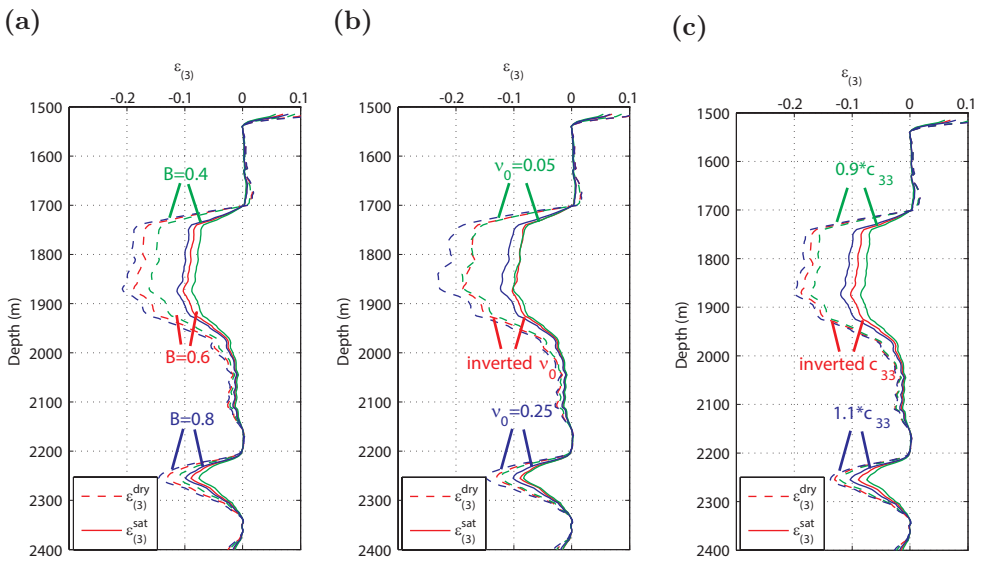

FIGURE 6.6: Sensitivity of results to (a) compliance ratio values B , (b) Poisson's ratio values ν_0 and (c) errors made on the dry P-wave modulus C_{33}.

4.57 used to calculate the P-wave anisotropy parameter in the saturated medium was derived assuming weak anisotropy. In Chapter 4, we estimated that such an assumption yields a relative error on the P-wave anisotropy parameter in the saturated medium of approximately 10 %. Similar error values are expected for this study. In addition, one can argue that the assumption inherent to Gassmann equations, according to which pore pressure equilibrates throughout the pore space, might be violated at logging frequencies. Indeed, when frequencies are high, anisotropic squirt flow has to be taken into account (see e.g. Mukerji & Mavko [1994]). However, logging frequencies might still fall within the range of validity of Gassmann equations, especially when dealing with loose, high porosity formations and fluids with low viscosity [Gurevich et al., 2010]. For the data example presented in this paper, previous work in the area [Pevzner et al., 2011] shows no significant differences between log and VSP velocities, suggesting that Gassmann equations are applicable.

6.5 Conclusions

In this chapter, we presented a methodology for estimating azimuthal P-wave anisotropy from S-wave anisotropy using log and VSP data in areas where the anisotropy is known to be caused by differential stresses. First, we estimated the P-wave anisotropy in the dry medium from the S-wave anisotropy calculated from log or VSP data. This was done based on the relationships between anisotropy parameters established by the stress-induced anisotropy rock physics model, which accounts for the dependency of seismic wave velocities in isotropic elastic media subjected to triaxial compression (Chapter 3). To calculate the P-wave anisotropy parameter in the saturated medium from the one estimated in the dry medium, we used the anisotropic Gassmann equations expressed in terms of orthorhombic anisotropy parameters (Chapter 4).

To test this methodology, we used log data acquired on the North West Shelf of Australia, in an area where anisotropy is likely to be stress-induced. We estimated the azimuthal P-wave anisotropy parameter in three wells. The results agree to first order with values obtained at the well locations via orthorhombic tomography performed on 3D dual azimuth seismic data. In the shale and shaly sandstone layers, there is however a discrepancy between these results, which is mainly due to the fact that the stress-induced anisotropy model we used is only applicable to initially isotropic rocks. Therefore, the model does not handle the stress sensitivity of rocks exhibiting intrinsic anisotropy such as shales.

This methodology provides a quick way to estimate the azimuthal P-wave anisotropy. Such information could be used for example to constrain an initial velocity model for orthorhombic migration or azimuthal amplitude-variations-with-offset (AVO) inversion.

Chapter 7

Thesis Conclusions

In this conclusion chapter, we first review the main outcomes of this project before pointing out the limitations of the work that was done and how it can be improved.

7.1 Main outcomes

The overall objective of this project was to derive new rock physics models to gain a better understanding on seismic anisotropy. Since this is a very broad task, we focused on a few topics: first, we attempted to model stress-induced anisotropy of dry rocks (Chapter 3), then we analysed the effect of fluid on seismic anisotropy at low frequencies (Chapter 4) and finally we developed an anisotropic squirt flow model to account for the effect of fluid at high frequencies (Chapter 5).

While anisotropy resulting from the presence of aligned fractures has been an active field of research in the past years, studies dealing with stress-induced anisotropy are still limited. However, in areas where differences between maximum and minimum horizontal stresses are large, significant azimuthal anisotropy, which may affect seismic data [Bishop et al., 2010, Hung et al., 2006], can be observed despite the absence of fractures. In Chapter 3, we thus address this issue of stress-induced anisotropy and try to develop a new rock physics model to account for the stress sensitivity of dry

isotropic rocks subjected to triaxial stress. To develop this model, we made a number of assumptions. In particular, the initial unstressed medium is assumed to be isotropic and permeated by cracks (i.e. grain contacts and microcracks) that are randomly oriented and distributed. Another crucial assumption of the model is that the stress sensitivity of elastic properties is only due to crack closure occurring perpendicular to the stress directions; in other words the eventual opening of cracks, which might occur along the maximum stress direction, is not accounted for. Following these assumptions, we showed that the stress dependency of isotropic media subjected to triaxial stress is a function of five independent parameters: two elastic moduli of the unstressed rock, the normal and tangential crack compliances describing the initial crack distribution and the characteristic crack closing pressure. Such parameters can be inverted from velocities measured during hydrostatic stress tests. Comparison of the model predictions with laboratory measurements showed a relatively good agreement. For small stresses, the model predicts ellipsoidal anisotropy, i.e. $\epsilon = \delta$ in each plane of symmetry of the resulting orthorhombic medium. The model also expresses the ratios ϵ/γ as a function of the Poisson's ratio of the unstressed rock and the compliance ratio. Besides, we derived relationships between anisotropy parameters ratios and stress ratios. By extending the model to larger stresses, we found that those results still hold for stresses as high as approximately 40 MPa depending on the matrix properties, crack geometry and compliance as well as the stress contrast. These results are interesting as they provide a way of differentiating stress-induced anisotropy from fracture-induced anisotropy by estimating the degree of anellipticity of the medium; besides, the resulting anisotropy pattern could be used to infer azimuthal P-wave anisotropy from S-wave anisotropy as it is suggested in Chapter 6.

The stress-induced anisotropy model developed in Chapter 3 is only valid for dry rocks. Since subsurface formations are usually filled with fluid, we analysed the effect of fluid filling the pore space on anisotropy. Using the anisotropic Gassmann theory, we analytically expressed anisotropy parameters in TI and orthorhombic saturated media as a function of those in dry media. Several other parameters such as the bulk and shear moduli of the dry and saturated media, the grain and fluid bulk moduli and the

porosity have to be taken into account. The derived equations are applicable to any TI or orthorhombic medium, regardless of the cause of anisotropy. This study was however restricted to weak anisotropy. The main conclusions that can be drawn from this analysis are as follows. 1) In general, the presence fluid tends to reduce the degree of P-wave anisotropy, expressed by the anisotropy parameter ϵ. This is due to the fact the stiffening effect of fluid is more pronounced along certain directions depending on the orientation of cracks, fractures or bedding. The less compressible the fluid, i.e. the higher the fluid bulk modulus K_f, the more affected the degree of anisotropy. 2) The shear modulus is not affected by the pore fluid so the S-wave anisotropy, described by the γ-parameter, remains the same in the dry and saturated media. 3) By deriving analytical expressions for the anellipticity parameter η, which links the anisotropy parameters ϵ and δ, we showed that when the porosity is sufficiently high, the anellipticity parameter in the saturated medium is proportional to the one in the dry medium. Consequently, if the dry medium is elliptical (or ellipsoidal), then the saturated medium is also elliptical (or ellipsoidal). As mentioned above, this opens the possibility of differentiating between stress- and fracture-induced anisotropy by estimating the anellipticity parameter. Though the original anisotropic Gassmann equations should still be used for computational purposes, the analytical expressions derived in Chapter 4 still yield reasonable approximations of anisotropy parameters in saturated media, which is useful to gain an insight on how fluid affects anisotropy.

The use of the anisotropic Gassmann [1951] equations is based on the underlying assumption that fluid pressure is equilibrated throughout the pore space. This is usually a valid assumption for seismic frequencies. However, at higher frequencies, the pore pressure does not reach equilibrium and local fluid flow, known as squirt flow, may occur between pores of different shapes, sizes and orientations. To tackle this issue, we developed in Chapter 5 a simple model of squirt-flow relaxation in anisotropic media saturated with fluid. By construction, the model is consistent with the anisotropic Gassmann equations in the low-frequency limit and the anisotropic squirt flow model of Mukerji & Mavko [1994] in the high-frequency limit. Studying the effect of squirt flow on elastic properties requires knowledge of the crack distribution. Hence, in this

work, we focused on two cases: the simple case for which cracks are parallel and the case for which anisotropy results from the application of uniaxial stress on an initially isotropic medium. By modelling compliant pores as disc-shaped gaps between stiff pores, we were able to derive analytical expressions of elastic moduli and anisotropy parameters in the limit of weak anisotropy for liquid-saturated rocks. The anisotropy and attenuation patterns are significantly different in the two investigated cases. In the case of aligned cracks, no S||-wave velocity dispersion is observed and the S-wave anisotropy parameter γ is not affected by the presence of fluid for all frequency ranges. Since the presence of fluid highly stiffens cracks in the high-frequency limit, the velocity of P-waves propagating perpendicular and parallel to the cracks is almost the same. Hence, the P-wave anisotropy parameter ϵ vanishes in the high-frequency limit, and the anisotropy parameter δ remains the only indicator of P-S$\perp$ wave anisotropy. This feature also implies that even if the dry medium is elliptical the saturated medium will no longer be elliptical in the high-frequency limit. In the stress-induced anisotropy case, the crack closure occurring perpendicular to the applied stress leads to an increase of seismic velocities perpendicular to the applied stress, but also causes a decrease of attenuation and velocity dispersion in this direction. The anisotropy of squirt flow dispersion results in a decrease of all anisotropy parameters as a function of frequency. Besides, the stress-induced anisotropy remains elliptical for all frequency ranges in saturated media.

In the last chapter of the thesis, Chapter 6, we applied the concepts developed in Chapters 3 and 4 in order to infer azimuthal P-wave anisotropy from S-wave anisotropy using log or VSP data in areas where the anisotropy is known to be caused by differential stresses. First, we estimated the P-wave anisotropy in the dry medium from the S-wave anisotropy calculated from log or VSP data. This was achieved based on the relationships between anisotropy parameters established by the stress-induced anisotropy rock physics model developed in Chapter 3, which accounts for the dependency of seismic wave velocities in isotropic elastic media subjected to triaxial compression. Then, we used the analytical expressions of anisotropy parameters derived in Chapter 4 in order to calculate the P-wave anisotropy parameter in the saturated medium from the one

estimated in the dry medium. To test this methodology, we used log data acquired on the North West Shelf of Australia, in an area where anisotropy is likely to be stress-induced. We estimated the azimuthal P-wave anisotropy parameter in three wells. The results agreed to first order with values obtained at the well locations via orthorhombic tomography performed on 3D dual azimuth seismic data. In the shale and shaly sandstone layers, there was however a discrepancy between these results, which is mainly due to the fact that the stress-induced anisotropy model we use is only applicable to initially isotropic rocks and therefore does not handle the stress sensitivity of rocks exhibiting intrinsic anisotropy such as shales. This methodology provides a quick way of estimating the azimuthal P-wave anisotropy. Such information could be used for example to constrain an initial velocity model for orthorhombic migration or azimuthal amplitude-variations-with-offset (AVO) inversion.

7.2 Limitations and recommendations for further research

The models developed in this project are based on several assumptions, which restrict their validity. First, to derive the stress-induced anisotropy model in Chapter 3, we assumed that the initial unstressed medium was isotropic. This is a significant weakness of the model since intrinsically anisotropic formations are often encountered in the subsurface. Hence, it would be worth trying to extend this model to initially anisotropic formations. This could be done for instance by defining an initial distribution of cracks in the unstressed state (see e.g. Ciz & Shapiro [2008], Pervukhina et al. [2011].

The stress-induced anisotropy model developed in Chapter 3 also relies on the assumption that the anisotropy is only due to the preferential crack closure occurring perpendicular to the applied stresses. However, cracks might also open along the maximum stress direction. Thus, the model might fail at adequately quantifying the anisotropy degree; indeed, if cracks were to open parallel to the maximum applied stress, then

the model would underestimate the anisotropy degree. Overcoming this issue is however cumbersome. In fact, crack closure is relatively easy to model because we have prior information on the existing cracks that are closing; in other words, we can infer their characteristics from hydrostatic stress measurements for instance. To find such characteristics for opening cracks requires uniaxial or triaxial stress tests. Based on experimental data, one could first invert parameters of closing cracks from hydrostatic stress measurements. Characteristics of opening cracks could then be estimated from the difference between velocities measured during uniaxial or triaxial stress tests and predictions of the model derived in Chapter 3.

An advantage of the stress-induced anisotropy model developed in Chapter 3 is the fact that elastic properties of the medium subjected to anisotropic stresses are expressed as a function of five parameters, which can be inferred from velocity measurements made under isotropic stress. Namely, these parameters are the bulk and shear moduli in the unstressed state, the normal and tangential crack compliances in the unstressed medium and the characteristic crack closing pressure. So far, these parameters are not well-known and well constrained. For instance, there is still some debate on whether or not the compliance ratio B is equal to 1 for dry cracks. Hence, it would be interesting to invert series of velocity measurements made on various types of rocks so as to give order of magnitudes of these parameters in different lithologies. Such data would also prove to be useful to better constrain the input parameters required to estimate azimuthal P-wave anisotropy from S-wave anisotropy employing the methodology described in Chapter 6.

Finally, this thesis is focused on the derivation of theoretical models, which would gain considerable value if they were validated against experimental data. The model derived for stress-induced anisotropy of dry rocks was tested against laboratory measurements. However, the predictions of the model were not matching the velocity measurements so well in the minimum stress direction; hence, the model would benefit further validation. Besides, the measurements that were used to test the model were triaxial tests, i.e. $\sigma_{11} = \sigma_{22}$. The ideal stress test to check the validity of the model would

be a true triaxial (polyaxial) test. Such tests are still seldom in the literature due to the complexity of the true triaxial cell. Besides, recovering the full stiffness tensor of orthorhombic media requires either off-axis measurements, which might lack accuracy, or measurements of the three types of waves in three different directions. Such measurements could be done using the laser-doppler interferometer. In addition, carrying out these measurements on a dry and saturated sample would be useful to verify the relationships derived in Chapters 4 and 5.

Appendix A

Derivation of the stress-induced anisotropy model for large triaxial stress

To derive the model for large stresses, we follow the same steps as the derivation for small stresses but we replace the linear approximation of the exponential function (equation 3.2) by its Taylor series expansion (equation 3.36).

When substituting equation 3.36 into equation 2.30, we obtain for the second-rank tensor α_{ij} [Madadi et al., 2013]

$$\alpha_{ij} = Z_{T0} \sum_{t=0}^{\infty} \frac{1}{t!} (\frac{\sigma_{kl}}{P_c})^t \mathcal{I}(t), \tag{A.1}$$

where

$$\mathcal{I}(t) = \frac{1}{4\pi} \int \int (n_k n_l)^t n_i n_j \, d\Omega. \tag{A.2}$$

The evaluation of all integrals in equation (A.1) gives:

$$\alpha_{ij} = Z_{T0}\Big[\frac{1}{3}\delta_{ij} + (\frac{\sigma_{kl}}{P_c}) \times \frac{1}{5\times 3}\mathcal{P}(\delta_{ij}\delta_{kl}) + \frac{1}{2!}(\frac{\sigma_{kl}}{P_c})(\frac{\sigma_{k'l'}}{P_c}) \times \frac{1}{7\times 5\times 3}\mathcal{P}(\delta_{ij}\delta_{kl}\delta_{k'l'})\cdots + \frac{1}{t!}(\frac{\sigma_{k^1l^1}}{P_c})\cdots(\frac{\sigma_{k^tl^t}}{P_c}) \times \frac{1}{(2t+3)!!}\mathcal{P}(\delta_{ij}\delta_{k^1l^1}\delta_{k^2l^2}...\delta_{k^tl^t}) + \cdots\Big]. \tag{A.3}$$

where $\mathcal{P}(\delta_{ij}\delta_{k^1l^1}\delta_{k^2l^2}...\delta_{k^tl^t})$ is defined as the summation of all permutations of t multiplication of δ-Kronecker function. We can then express the $\overline{\alpha}_{ij}$ tensor as a function of $q-$order series:

$$\overline{\alpha}_{11} = 2Z_{T0}\sum_{t=0}^{q}\sum_{n=0}^{t}\sum_{m=0}^{t-n}\frac{(t+1)!}{(2t+3)!}\frac{(2(t-m-n)+1)!(2m)!(2n)!}{(n!m!(t-m-n)!)^2}a_h^m a_v^n(-a)^t, \tag{A.4}$$

$$\overline{\alpha}_{22} = 2Z_{T0}\sum_{t=0}^{q}\sum_{n=0}^{t}\sum_{m=0}^{t-n}\frac{(t+1)!}{(2t+3)!}\frac{(2(t-m-n))!(2m+1)!(2n)!}{(n!m!(t-m-n)!)^2}a_h^m a_v^n(-a)^t, \tag{A.5}$$

$$\overline{\alpha}_{33} = 2Z_{T0}\sum_{t=0}^{q}\sum_{n=0}^{t}\sum_{m=0}^{t-n}\frac{(t+1)!}{(2t+3)!}\frac{(2(t-m-n))!(2m)!(2n+1)!}{(n!m!(t-m-n)!)^2}a_h^m a_v^n(-a)^t, \tag{A.6}$$

$$\overline{\alpha}_{44} = \overline{\alpha}_{22} + \overline{\alpha}_{33}, \tag{A.7}$$

$$\overline{\alpha}_{55} = \overline{\alpha}_{11} + \overline{\alpha}_{33}, \tag{A.8}$$

$$\overline{\alpha}_{66} = \overline{\alpha}_{11} + \overline{\alpha}_{22}. \tag{A.9}$$

Proceeding in a similar way, we obtain for tensor β:

$$\beta_{iji'j'} = (Z_{N0} - Z_{T0})\sum_{t=0}^{\infty}\frac{1}{t!}(\frac{\sigma_{kl}}{P_c})^t\mathcal{J}(t), \tag{A.10}$$

with

$$\mathcal{J}(t) = \frac{1}{4\pi}\int\int(n_k n_l)^t n_i n_j n_{i'} n_{j'}\, d\Omega. \tag{A.11}$$

Evaluating the integrals yields:

$$\begin{aligned}\beta_{iji'j'} = (Z_{N0} - Z_{T0})\Big[&\frac{1}{5\times 3}\mathcal{P}(\delta_{ij}\delta_{i'j'}) + (\frac{\sigma_{kl}}{P_c}) \times \frac{1}{7\times 5\times 3}\mathcal{P}(\delta_{ij}\delta_{i'j'}\delta_{kl}) \\ &+ \frac{1}{2!}(\frac{\sigma_{kl}}{P_c})(\frac{\sigma_{k'l'}}{P_c}) \times \frac{1}{9\times 7\times 5\times 3}\mathcal{P}(\delta_{ij}\delta_{i'j'}\delta_{kl}\delta_{k'l'})\cdots \\ &+ \frac{1}{t!}(\frac{\sigma_{k^1l^1}}{P_c})\cdots(\frac{\sigma_{k^tl^t}}{P_c}) \times \frac{1}{(2t+5)!!}\mathcal{P}(\delta_{ij}\delta_{i'j'}\delta_{k^1l^1}\delta_{k^2l^2}...\delta_{k^tl^t}) + \cdots\Big] \end{aligned} \tag{A.12}$$

The matrix components of β can then be written as:

$$\beta_{11} = 2(Z_{N0} - Z_{T0})\sum_{t=0}^{q}\sum_{n=0}^{t}\sum_{m=0}^{t-n}\frac{(t+2)!}{(2t+5)!}\frac{(2(t-m-n)+3)!(2m)!(2n)!}{(t-m-n+1)(n!m!(t-m-n)!)^2}a_h^m a_v^n(-a)^t, \tag{A.13}$$

$$\beta_{22} = 2(Z_{N0} - Z_{T0})\sum_{t=0}^{q}\sum_{n=0}^{t}\sum_{m=0}^{t-n}\frac{(t+2)!}{(2t+5)!}\frac{(2(t-m-n))!(2m+3)!(2n)!}{(m+1)(n!m!(t-m-n)!)^2}a_h^m a_v^n(-a)^t, \tag{A.14}$$

$$\beta_{33} = 2(Z_{N0} - Z_{T0})\sum_{t=0}^{q}\sum_{n=0}^{t}\sum_{m=0}^{t-n}\frac{(t+2)!}{(2t+5)!}\frac{(2(t-m-n))!(2m)!(2n+3)!}{(n+1)(n!m!(t-m-n)!)^2}a_h^m a_v^n(-a)^t, \tag{A.15}$$

$$\beta_{12} = 4(Z_{N0} - Z_{T0})\sum_{t=0}^{q}\sum_{n=0}^{t}\sum_{m=0}^{t-n}\frac{(t+2)!}{(2t+5)!}\frac{(2(t-m-n)+1)!(2m+1)!(2n)!}{(n!m!(t-m-n)!)^2}a_h^m a_v^n(-a)^t, \tag{A.16}$$

$$\beta_{13} = 4(Z_{N0} - Z_{T0})\sum_{t=0}^{q}\sum_{n=0}^{t}\sum_{m=0}^{t-n}\frac{(t+2)!}{(2t+5)!}\frac{(2(t-m-n)+1)!(2m)!(2n+1)!}{(n!m!(t-m-n)!)^2}a_h^m a_v^n(-a)^t, \tag{A.17}$$

$$\beta_{23} = 4(Z_{N0} - Z_{T0})\sum_{t=0}^{q}\sum_{n=0}^{t}\sum_{m=0}^{t-n}\frac{(t+2)!}{(2t+5)!}\frac{(2(t-m-n))!(2m+1)!(2n+1)!}{(n!m!(t-m-n)!)^2}a_h^m a_v^n(-a)^t, \tag{A.18}$$

$$\beta_{44} = 4\beta_{23}, \tag{A.19}$$

$$\beta_{55} = 4\beta_{13}, \tag{A.20}$$

$$\beta_{66} = 4\beta_{12}. \tag{A.21}$$

Finally, we can compute the overall compliance tensor by substituting equations A.4 to A.9 and A.13 and A.21 into equation 2.27.

Appendix B

Consistency of the developed anisotropic squirt flow model with previous squirt flow models

In this appendix, we demonstrate the consistency of the anisotropic squirt flow model derived in Chapter 5 with the anisotropic squirt flow model derived by Mukerji & Mavko [1994] in the high-stress limit for the simple case of aligned cracks. We also show how the elastic moduli predicted by the model derived in Chapter 5 reduce to the bulk and shear moduli predicted by Gurevich et al. [2010].

B.1 Consistency with the anisotropic squirt flow model from Mukerji and Mavko (1994) in the case of aligned cracks

In the high-frequency limit, expressions of the elastic moduli predicted by the anisotropic squirt flow model derived in Chapter 5 are essentially the same as the ones predicted by Mukerji & Mavko [1994]. In the following, we show how these two

models relate to each other in the case of aligned cracks. In their paper, Mukerji & Mavko [1994] analysed elastic properties of TI media for which all the compliant, cracks-like pores are parallel. This case is essentially the same as the one presented in Chapter 5, Section 5.2. Main results of Mukerji & Mavko [1994] are recalled in Chapter 2, Section 2.5.2.2. Here and below, we check the consistency of the compliance tensor of the unrelaxed frame derived using both approaches. In the case of aligned cracks, Mukerji & Mavko [1994] showed that the compliance tensor of the unrelaxed frame can be written as (see equation 2.89):

$$S^{uf}_{ijkl} = S^{dry}_{ijkl} - \frac{\Delta S^{dry}_{\alpha\alpha ij}\Delta S^{dry}_{\alpha\alpha kl}}{\Delta S^{dry}_{\alpha\alpha\beta\beta} + \left(\frac{1}{K_f} - \frac{1}{K_g}\right)\phi_c}, \tag{B.1}$$

where ΔS_{ijkl} is defined as

$$\Delta S_{ijkl} = \phi_c \bar{W}_{ijkl}, \tag{B.2}$$

$\bar{W}_{ijkl}$ being the average compliance of the crack set. When the fracture distribution is sparse, Mukerji & Mavko [1994] argue that the largest components of the compliance tensor are the normal compliance $\bar{W}_{1111}$ and tangential compliances $\bar{W}_{1212}$ and $\bar{W}_{1313}$. If we assume that the cracks are rotationnally symmetrical, then both of the tangential compliances are equal. In the Sayers & Kachanov [1995] formalism, the average compliance tensor defined by Mukerji & Mavko [1994] can be written as

$$\bar{W}_{1111} = Z_N, \tag{B.3}$$

$$\bar{W}_{1212} = \bar{W}_{1313} = Z_T, \tag{B.4}$$

which implies that

$$\bar{W}_{\alpha\alpha\beta\beta} \approx \bar{W}_{1111} = Z_N, \tag{B.5}$$

$$\bar{W}_{ij\alpha\alpha} \approx \bar{W}_{1111}\delta_{i1}\delta_{j1} = Z_N\delta_{i1}\delta_{j1}. \tag{B.6}$$

Hence, the compliance tensor of the unrelaxed frame given by equation B.1 can be rewritten as

$$S^{uf}_{ijkl} = S^{dry}_{ijkl} - \frac{Z_N^2 \delta_{i1}\delta_{j1}\delta_{k1}\delta_{l1}}{Z_N + \left(\frac{1}{K_f} - \frac{1}{K_g}\right)\phi_c}. \tag{B.7}$$

Subtracting the compliance tensors of the dry frame (equation 2.27) to the compliance tensor of the unrelaxed frame (equation 5.1) given by the model derived in Chapter 5 leads to

$$S^{dry}_{ijkl} - S^{uf}_{ijkl} = \Delta S_{ijkl} - \Delta S^{uf}_{ijkl}. \tag{B.8}$$

From expressions of the excess crack compliance tensors $\boldsymbol{\Delta S}$ in the dry and unrelaxed frames (equations 2.32 and 5.2), and the normal crack compliance Z_N^{uf} in the unrelaxed frame (equation 5.3), we have

$$\Delta S_{ijkl} - \Delta S^{uf}_{ijkl} = \frac{Z_N^2 \delta_{i1}\delta_{j1}\delta_{k1}\delta_{l1}}{Z_N + \left(\frac{1}{K_f} - \frac{1}{K_g}\right)\phi_c}, \tag{B.9}$$

which matches equation B.7 obtained from Mukerji & Mavko [1994].

B.2 Consistency with previous isotropic squirt flow models in the stress-induced anisotropy case

In this section, we check the consistency of the squirt flow model derived in Chapter 5, Section 5.3 for the stress-induced anisotropy case with the isotropic squirt flow models derived by Gurevich, Makarynska, & Pervukhina [2009b] and Gurevich et al. [2010]. The aim is twofold: first, we want to check the consistency of the model with the isotropic case; second, we derive expressions of the elastic constants of the unrelaxed and modified frames in the unstressed state.

B.2.1 Consistency with the isotropic squirt flow model derived by Gurevich et al. (2009) in the high-frequency limit

The compliance tensor of the unrelaxed frame $\boldsymbol{S^{o,uf}}$ of the unstressed isotropic medium can be obtained by taking only the contribution of the isotropic distribution of cracks in equation 5.67:

$$S_{ij}^{0,uf} - S_{ij}^{0} = \beta_{ij}^{is}(Z_{N0}^{uf} - Z_{N0}). \tag{B.10}$$

The tensor $\boldsymbol{\beta^{is}}$ is the fourth-rank crack tensor given in equation 2.52. From equation 5.65, we deduce that the difference between the normal crack compliances Z_{N0}^{uf} and Z_{N0} in the unrelaxed and dry frames is expressed as

$$Z_{N0}^{uf} - Z_{N0} = \frac{Z_{N0}}{1 + \phi_{c0}\Big(\dfrac{1}{K_f} - \dfrac{1}{K_g}\Big)\Big/ Z_{N0}}. \tag{B.11}$$

In their study, Mukerji & Mavko [1994] showed that in the isotropic case, the compliance tensor of the unrelaxed frame reduces to

$$S_{ijkl}^{uf} = S_{ijkl} - \frac{\Delta S_{\alpha\alpha\beta\beta}}{1 + \phi_{c}\Big(\dfrac{1}{K_f} - \dfrac{1}{K_g}\Big)\Big/ \Delta S_{\alpha\alpha\beta\beta}} G_{ijkl}, \tag{B.12}$$

where $\boldsymbol{G} = \boldsymbol{\beta^{is}}$. Besides, by calculating $\Delta S_{\alpha\alpha\beta\beta} = S_{\alpha\alpha\beta\beta} - S^{h}_{\alpha\alpha\beta\beta}$ retaining only the isotropic terms of the compliance tensor given by equation 2.51, it is straightforward to show that $\Delta S_{\alpha\alpha\beta\beta} = Z_{N0}$. By comparing equations B.10 and B.11 with equation B.12, we note that the isotropic versions of the models derived in Chapter 5 and by Mukerji & Mavko [1994] in the high-stress limit are consistent with each other.

From the expression of the compliance tensor given in equation B.10, we rederive the final expressions given by the isotropic squirt flow model of Gurevich, Makarynska, & Pervukhina [2009b]. These expressions are given in terms of the bulk and shear moduli of the isotropic medium. In order to relate the compliance coefficients of isotropic

media to the bulk and shear moduli, we use the following the formulas:

$$S_{11} = \frac{1}{3\mu} + \frac{1}{9K}, \tag{B.13}$$

$$S_{44} = \frac{1}{\mu}. \tag{B.14}$$

Components $S_{11}^{0,uf}$ and $S_{44}^{0,uf}$ of the unstressed isotropic medium are given by equation 2.51, assuming that the normalized stress $b = \sigma_{11}/P_c$ is zero:

$$S_{11}^{0,uf} = S_{11}^{h} + \frac{2}{15}Z_{T0} + \frac{1}{5}Z_{N0}, \tag{B.15}$$

$$S_{44}^{0,uf} = S_{44}^{h} + \frac{2}{5}Z_{T0} + \frac{4}{15}Z_{N0}. \tag{B.16}$$

By combining equations B.11 and B.13 to B.16, it is easy to show that the cracks normal compliance in the unstressed state can be expressed as a function of the bulk moduli K_0 and K_h of the medium in the unstressed state and in the high-stress limit:

$$Z_{N0} = \frac{1}{K_0} - \frac{1}{K_h}. \tag{B.17}$$

In the same way, the cracks normal compliance in the unrelaxed frame is written as

$$Z_{N0}^{uf} = \frac{1}{K_0^{uf}} - \frac{1}{K_h}. \tag{B.18}$$

By substituting expressions B.17 and B.18 into equation B.11 in order to express the bulk modulus of the unrelaxed frame in the unstressed state, we obtain

$$\frac{1}{K_0^{uf}} = \frac{1}{K_h} + \frac{1}{\dfrac{1}{\left(\dfrac{1}{K_0} - \dfrac{1}{K_h}\right)} + \dfrac{1}{\phi_{c0}\left(\dfrac{1}{K_f} - \dfrac{1}{K_g}\right)}}. \tag{B.19}$$

The expression of the shear modulus can be derived from equations B.10 and B.14:

$$\frac{1}{\mu_0^{uf}} = \frac{1}{\mu_h} + \frac{4}{15}\left(\frac{1}{K_0^{uf}} - \frac{1}{K_h}\right). \tag{B.20}$$

The expressions of K_0^{uf} and μ_0^{uf} given by equations B.19 and B.20 agree with formulas previously derived by Gurevich, Makarynska, & Pervukhina [2009b].

Elastic properties of the unrelaxed frame in the unstressed state - From equations B.10, B.13 and B.14, we get

$$K_0^{uf} = \frac{K_0}{1 + K_0\Big(Z_{N0}^{uf} - Z_{N0}\Big)}, \tag{B.21}$$

$$\mu_0^{uf} = \frac{\mu_0}{1 + \frac{4}{15}\mu_0\Big(Z_{N0}^{uf} - Z_{N0}\Big)}. \tag{B.22}$$

When the crack distribution is sparse, expressions B.21 and B.22 for K_0^{uf} and μ_0^{uf} can be linearized so that:

$$K_0^{uf} = K_0\Big(1 - K_0\Big(Z_{N0}^{uf} - Z_{N0}\Big)\Big), \tag{B.23}$$

$$\mu_0^{uf} = \mu_0\Big(1 - \frac{4}{15}\mu_0\Big(Z_{N0}^{uf} - Z_{N0}\Big)\Big). \tag{B.24}$$

The P-wave modulus in the unrelaxed frame given by $L_0^{uf} = K_0^{uf} + \frac{4}{3}\mu_0^{uf}$ can be expressed as

$$L_0^{uf} = L_0 - \Big(L_0^2 - \frac{8}{3}L_0\mu_0 + \frac{29}{45}\mu_0^2\Big)\Big(Z_{N0}^{uf} - Z_{N0}\Big). \tag{B.25}$$

B.2.2 Consistency with the isotropic squirt flow model derived by Gurevich et al. (2011) for all frequency ranges

Checking the agreement between the model derived for stress-induced anisotropy in Chapter 5 and the isotropic squirt flow model derived by Gurevich et al. [2010] follows the same steps as the ones described for the unrelaxed frame. Substracting the stress sensitivity of the dry and modified frames, respcetively given by equations 2.51 and 5.63, yields

$$S_{ij}^{0,mf} - S_{ij}^{0} = \beta_{ij}^{is}(Z_{N0}^{mf} - Z_{N0}), \tag{B.26}$$

where the difference $Z_{N0}^{mf} - Z_{N0}$ can be calculated from equation 5.77:

$$Z_{N0}^{mf} - Z_{N0} = \frac{Z_{N0}}{1 + \phi_{c0}\Big(\frac{1}{K_f^*} - \frac{1}{K_g}\Big)\Big/ Z_{N0}}. \tag{B.27}$$

Substituting equation B.27 into B.26 and using the relationships between compliance coefficients and bulk and shear moduli (equations B.13 and B.14), we can show that:

$$\frac{1}{K_0^{mf}} = \frac{1}{K_h} + \frac{1}{\dfrac{1}{\Big(\frac{1}{K_0} - \frac{1}{K_h}\Big)} + \dfrac{1}{\phi_{c0}\Big(\frac{1}{K_f^*} - \frac{1}{K_g}\Big)}}, \tag{B.28}$$

$$\frac{1}{\mu_0^{mf}} = \frac{1}{\mu_h} + \frac{4}{15}\Big(\frac{1}{K_0^{mf}} - \frac{1}{K_h}\Big). \tag{B.29}$$

Equations B.28 and B.29 are consistent with predictions of the isotropic squirt flow model derived by Gurevich et al. [2010] (equations 2.72 and 2.73).

Elastic properties of the modified frame in the unstressed state are expressed in the same way their counterparts in the unrelaxed frames by replacing subscripts uf by subscripts mf (equations B.21 to B.25).

Appendix C

Copyright permissions

Permissions

SEG publishes journals, books, and digital works with the primary aim of disseminating research in and theory and applications of applied geophysics. Consistent with this objective, the Society provides mechanisms for those who seek to reuse or republish material from SEG publications while protecting the viability of the SEG publications program. Any further questions about permissions can be sent via email to the SEG publications department at permissions@seg.org.

Fair use
Authors and publishers may present or republish up to two figures or tables per SEG article or per SEG book without seeking written permission from SEG, provided that full acknowledgment of the source is provided in the new work. If SEG has cited a publication for which it is not the publisher, rights should be obtained from that publisher. SEG considers this fair use. There are no fees associated with this permission. Authors who need documentation that SEG is extending this permission are encouraged to print this message and present it to their publishers. Those who require further documentation should contact the SEG publications director. Requests to use any portion of "Seismic Data Analysis: Processing, Inversion, and Interpretation of Seismic Data" should be directed to the SEG publications director.

Permission granting
Those seeking permission to republish more material than described above should contact the SEG publications director. Such requests should include complete citations of works for which permission to republish is sought. If permission for specific figures or tables is sought, please provide figure and table numbers. Requests should include a description of the work in which the SEG material would be republished. Information about the audience and the intended distribution also should be included. The requests should be prepared on institutional letterhead if the requesting party is representing an institution. License fees are assessed only when the request is for a large amount of material or when the proposed usage is commercial in nature or would limit SEG's market. If a license fee is assessed, it must be paid prior to use or the permission is void.

Purchase redistribution rights online
Those seeking to redistribute SEG publications or portions thereof in print, by fax, or online may purchase permission to do so online. SEG publications are registered with the Copyright Clearance Center, and licenses to redistribute SEG articles and portions of books are obtained through this nonprofit agency. Special pricing is available for university professors, including license to distribute SEG material through electronic course packs. Licenses also are available for distribution of journal articles and expanded abstracts via email or posting on Intranets and Extranets for limited time periods.

Authors' right to redistribute
Authors of articles in Geophysics, Interpretation, The Leading Edge, and the Technical Program *Expanded Abstracts* may post their own articles on their personal Web sites or the Web sites of their institutions without obtaining further permission from SEG. Authors of journal articles and *Expanded Abstracts* retain similar rights for print redistribution. If an author or an author's institution redistributes an author's article online or in print, the original publication venue encompassed in a complete citation and including SEG's status as publisher must be identified. Authors of SEG books, or portions of SEG books, must seek permission from the SEG publications director to redistribute these works in any form. Such permission will not be withheld if SEG's investment in the original publication of the works is not threatened. Questions should be directed to the publications director.

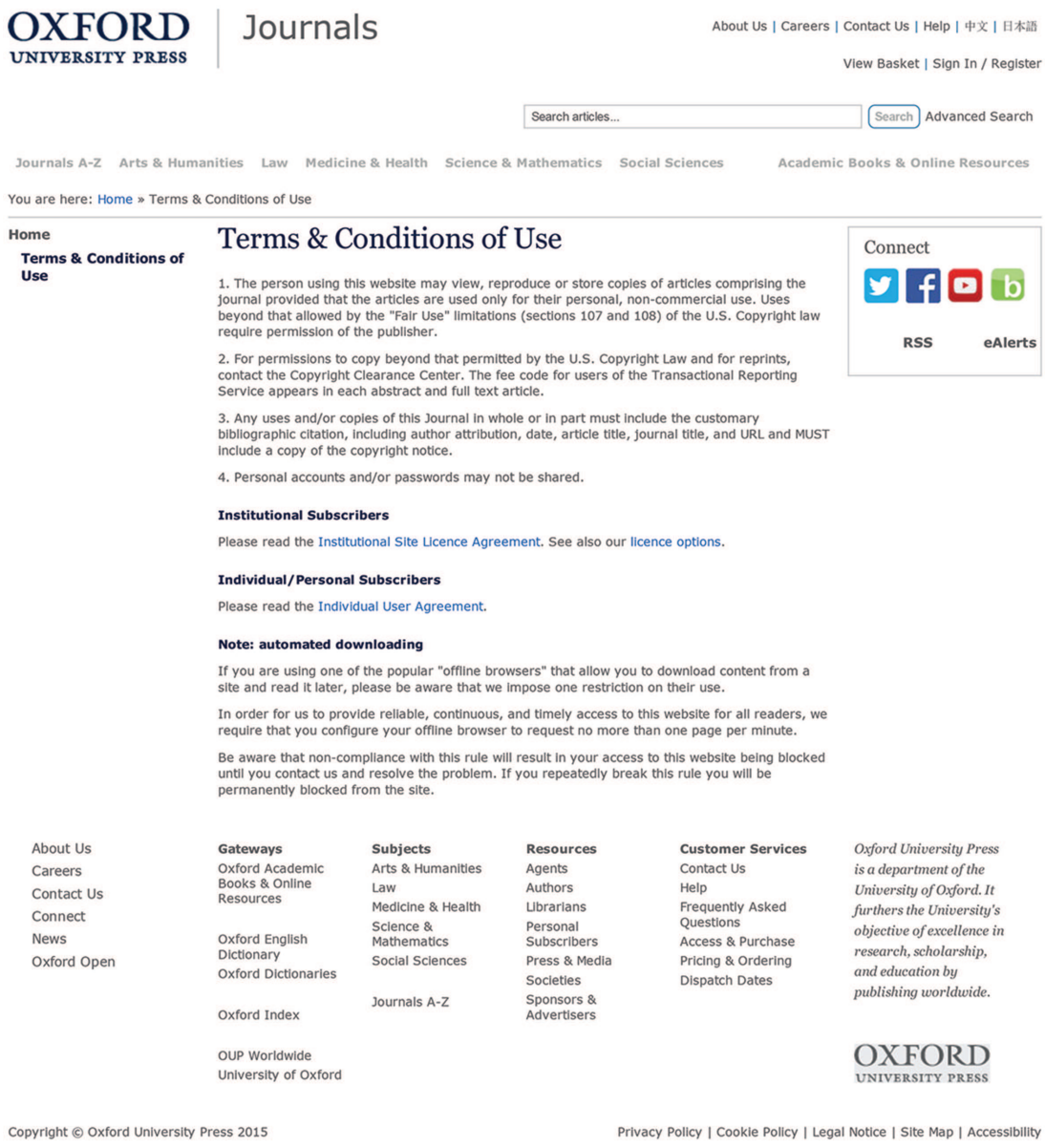

OXFORD UNIVERSITY PRESS | Journals

About Us | Careers | Contact Us | Help | 中文 | 日本語

View Basket | Sign In / Register

Search articles... Search Advanced Search

Journals A-Z Arts & Humanities Law Medicine & Health Science & Mathematics Social Sciences Academic Books & Online Resources

You are here: Home » Terms & Conditions of Use

Home

Terms & Conditions of Use

Terms & Conditions of Use

1. The person using this website may view, reproduce or store copies of articles comprising the journal provided that the articles are used only for their personal, non-commercial use. Uses beyond that allowed by the "Fair Use" limitations (sections 107 and 108) of the U.S. Copyright law require permission of the publisher.

2. For permissions to copy beyond that permitted by the U.S. Copyright Law and for reprints, contact the Copyright Clearance Center. The fee code for users of the Transactional Reporting Service appears in each abstract and full text article.

3. Any uses and/or copies of this Journal in whole or in part must include the customary bibliographic citation, including author attribution, date, article title, journal title, and URL and MUST include a copy of the copyright notice.

4. Personal accounts and/or passwords may not be shared.

Institutional Subscribers

Please read the Institutional Site Licence Agreement. See also our licence options.

Individual/Personal Subscribers

Please read the Individual User Agreement.

Note: automated downloading

If you are using one of the popular "offline browsers" that allow you to download content from a site and read it later, please be aware that we impose one restriction on their use.

In order for us to provide reliable, continuous, and timely access to this website for all readers, we require that you configure your offline browser to request no more than one page per minute.

Be aware that non-compliance with this rule will result in your access to this website being blocked until you contact us and resolve the problem. If you repeatedly break this rule you will be permanently blocked from the site.

Connect

RSS eAlerts

About Us
Careers
Contact Us
Connect
News
Oxford Open

Gateways
Oxford Academic Books & Online Resources
Oxford English Dictionary
Oxford Dictionaries
Oxford Index
OUP Worldwide
University of Oxford

Subjects
Arts & Humanities
Law
Medicine & Health
Science & Mathematics
Social Sciences
Journals A-Z

Resources
Agents
Authors
Librarians
Personal Subscribers
Press & Media
Societies
Sponsors & Advertisers

Customer Services
Contact Us
Help
Frequently Asked Questions
Access & Purchase
Pricing & Ordering
Dispatch Dates

Oxford University Press is a department of the University of Oxford. It furthers the University's objective of excellence in research, scholarship, and education by publishing worldwide.

OXFORD UNIVERSITY PRESS

Privacy Policy | Cookie Policy | Legal Notice | Site Map | Accessibility

One of the rights accorded to the owner of copyright is the right to reproduce or to authorize others to reproduce the work in copies or phonorecords. This right is subject to certain limitations found in sections 107 through 118 of the copyright law (title 17, U. S. Code). One of the more important limitations is the doctrine of "fair use." The doctrine of fair use has developed through a substantial number of court decisions over the years and has been codified in section 107 of the copyright law.

Section 107 contains a list of the various purposes for which the reproduction of a particular work may be considered fair, such as criticism, comment, news reporting, teaching, scholarship, and research. Section 107 also sets out four factors to be considered in determining whether or not a particular use is fair.

1. The purpose and character of the use, including whether such use is of commercial nature or is for nonprofit educational purposes
2. The nature of the copyrighted work
3. The amount and substantiality of the portion used in relation to the copyrighted work as a whole
4. The effect of the use upon the potential market for, or value of, the copyrighted work

The distinction between what is fair use and what is infringement in a particular case will not always be clear or easily defined. There is no specific number of words, lines, or notes that may safely be taken without permission. Acknowledging the source of the copyrighted material does not substitute for obtaining permission.

The 1961 *Report of the Register of Copyrights on the General Revision of the U.S. Copyright Law* cites examples of activities that courts have regarded as fair use: "quotation of excerpts in a review or criticism for purposes of illustration or comment; quotation of short passages in a scholarly or technical work, for illustration or clarification of the author's observations; use in a parody of some of the content of the work parodied; summary of an address or article, with brief quotations, in a news report; reproduction by a library of a portion of a work to replace part of a damaged copy; reproduction by a teacher or student of a small part of a work to illustrate a lesson; reproduction of a work in legislative or judicial proceedings or reports; incidental and fortuitous reproduction, in a newsreel or broadcast, of a work located in the scene of an event being reported."

Copyright protects the particular way authors have expressed themselves. It does not extend to any ideas, systems, or factual information conveyed in a work.

The safest course is to get permission from the copyright owner before using copyrighted material. The Copyright Office cannot give this permission.

When it is impracticable to obtain permission, you should consider avoiding the use of copyrighted material unless you are confident that the doctrine of fair use would apply to the situation. The Copyright Office can neither determine whether a particular use may be considered fair nor advise on possible copyright violations. If there is any doubt, it is advisable to consult an attorney.

FL-102, Reviewed June 2012

U.S. Copyright Office
101 Independence Avenue SE
Washington, DC 20559-6000
(202) 707-3000

References

Aki, K., & Richards, P. G. (2002). *Quantitative seismology* (2nd ed.). University Science Books.

Alkhalifah, T., & Tsvankin, I. (1995). Velocity analysis for transversely isotropic media. *Geophysics*, *60*(5), 1550–1566.

Angus, D., Verdon, J., Fisher, Q., & Kendall, J. (2009). Exploring trends in microcrack properties of sedimentary rocks: An audit of dry-core velocity-stress measurements. *Geophysics*, *74*(5), E193–E203.

Arts, R. J., Rasolofosaon, P. N., et al. (1992). Approximation of velocity and attenuation in general anisotropic rocks. In *1992 SEG Annual Meeting.*

Babuska, V., & Cara, M. (1991). *Seismic anisotropy in the earth* (Vol. 10). Springer Science & Business Media.

Backus, G. E. (1962). Long-wave elastic anisotropy produced by horizontal layering. *Journal of Geophysical Research*, *67*(11), 4427–4440.

Bakulin, A., Grechka, V., & Tsvankin, I. (2000). Estimation of fracture parameters from reflection seismic data-part II: Fractured models with orthorhombic symmetry. *Geophysics*, *65*(6), 1803–1817.

Baltazar, A., Rokhlin, S., & Pecorari, C. (2002). On the relationship between ultrasonic and micromechanical properties of contacting rough surfaces. *Journal of the Mechanics and Physics of Solids*, *50*(7), 1397–1416.

Berge, P. (1998). Pore compressibility in rocks. In *1st Biot Conference on Poromechanics.*

Biot, M. A. (1956). Theory of propagation of elastic waves in a fluid-saturated porous solid. I. Low-frequency range. *The Journal of the Acoustical Society of America*, *28*(2), 168–178.

Bishop, K., Osadchuk, A., & Stanley, M. (2010). Analysis methodology for azimuthal anisotropy. In *72nd EAGE conference & exhibition.*

Biwa, S., Suzuki, A., & Ohno, N. (2005). Evaluation of interface wave velocity, reflection coefficients and interfacial stiffnesses of contacting surfaces. *Ultrasonics*, *43*(6), 495–502.

Brajanovski, M., Gurevich, B., & Schoenberg, M. (2005). A model for P-wave attenuation and dispersion in a porous medium permeated by aligned fractures. *Geophysical Journal International*, *163*(1), 372–384.

Bristow, J. (1960). Microcracks, and the static and dynamic elastic constants of annealed and heavily cold-worked metals. *British Journal of Applied Physics*, *11*(2), 81.

Brown, R., & Korringa, J. (1975). On the dependence of the elastic properties of a porous rock on the compressibility of the pore fluid. *Geophysics*, *40*(4), 608-616.

Carcione, J. M. (2001). *Wave fields in real media: Wave propagation in anisotropic, anelastic, and porous media.* Pergamon Press.

Cardona, R. (2002). Two theories for fluid substitution in porous rocks with aligned cracks. In *2002 SEG Annual Meeting.*

Chapman, M. (2003). Frequency-dependent anisotropy due to meso-scale fractures in the presence of equant porosity. *Geophysical Prospecting*, *51*(5), 369–379.

Chapman, M., Zatsepin, S. V., & Crampin, S. (2002). Derivation of a microstructural poroelastic model. *Geophysical Journal International*, *151*(2), 427–451.

Chaudhry, N. (1995). *Effects of aligned discontinuities on the elastic and transport properties of reservoir rocks* (Unpublished doctoral dissertation). Royal School of Mines.

Ciz, R., & Shapiro, S. A. (2008). Stress-dependent anisotropy in transversely isotropic rocks: Comparison between theory and laboratory experiment on shale. *Geophysics*, *74*(1), D7–D12.

Collet, O., & Gurevich, B. (2013). Fluid dependence of anisotropy parameters in weakly anisotropic porous media. *Geophysics*, *78*(4), 1–9.

Collet, O., Gurevich, B., Madadi, M., & Pervukhina, M. (2014). Modeling elastic anisotropy resulting from the application of triaxial stress. *Geophysics*, *79*(5), C135–C145.

Coyner, K. (1984). *Effects of stress, pore pressure, and pore fluids on bulk strain, velocity, and permeability in rocks* (Unpublished doctoral dissertation). M. I. T., Dept. of Earth, Atmospheric and Planetary Sciences.

Crampin, S. (1994). The fracture criticality of crustal rocks. *Geophysical Journal International*, *118*(2), 428–438.

Crampin, S., & Lovell, J. H. (1991). A decade of shear-wave splitting in the Earth's crust: what does it mean? what use can we make of it? and what should we do next? *Geophysical Journal International*, *107*(3), 387–407.

Denham, D. (1983). Analysis of well logs to determine the stress field in the crust. In *Australian Society of Exploration Geophysicists, 3rd Biennial Conference.*

Donald, J., & Prioul, R. (2015). In situ calibrated velocity-to-stress transforms using shear sonic radial profiles for time-lapse production analysis. *The Leading Edge*, *34*(3), 286–294.

Dutta, N., & Odé, H. (1979). Attenuation and dispersion of compressional waves in fluid-filled porous rocks with partial gas saturation (White model) - Part I: Biot theory. *Geophysics*, *44*(11), 1777–1788.

Dvorkin, J., Mavko, G., & Nur, A. (1995). Squirt flow in fully saturated rocks. *Geophysics*, *60*(1), 97–107.

Eberhart-Phillips, D., Han, D.-H., & Zoback, M. D. (1989). Empirical relationships among seismic velocity, effective pressure, porosity, and clay content in sandstone. *Geophysics*, *54*(1), 82–89.

Ementon, N., Hill, R., Flynn, M., Motta, B., & Sinclair, S. (2004). Stybarrow Oil Field - From Seismic to Production, the Integrated Story So Far. *SPE paper*, *88574*.

Endres, A. L., & Knight, R. J. (1997). Incorporating pore geometry and fluid pressure communication into modeling the elastic behavior of porous rocks. *Geophysics*, *62*(1), 106–117.

Esmersoy, C., Koster, K., Williams, M., Boyd, A., & Kane, M. (1994). Dipole shear anisotropy logging. In *1994 SEG Annual Meeting.*

Galvin, R. J., & Gurevich, B. (2009). Effective properties of a poroelastic medium containing a distribution of aligned cracks. *Journal of Geophysical Research: Solid Earth (1978–2012)*, *114*(B7).

Galvin, R. J., & Gurevich, B. (2015). Frequency-dependent anisotropy of porous rocks with aligned fractures. *Geophysical Prospecting*, *63*(1), 141–150.

Gassmann, F. (1951). Elasticity of porous media. *Vierteljahrsschrder Naturforschenden Gesselschaft*, *96*, 1-23.

Grochau, M. H., & Gurevich, B. (2008). Investigation of core data reliability to support time-lapse interpretation in Campos Basin, Brazil. *Geophysics*, *73*(2), E59–E65.

Guéguen, Y., & Sarout, J. (2011). Characteristics of anisotropy and dispersion in cracked medium. *Tectonophysics*, *503*(1), 165–172.

Gurevich, B. (2003). Elastic properties of saturated porous rocks with aligned fractures. *Journal of Applied Geophysics*, *54*(3), 203-218.

Gurevich, B., Brajanovski, M., Galvin, R. J., Müller, T., & Toms-Stewart, J. (2009). P-wave dispersion and attenuation in fractured and porous reservoirs–poroelasticity approach. *Geophysical Prospecting*, *57*(2), 225–237.

Gurevich, B., Makarynska, D., de Paula, O. B., & Pervukhina, M. (2010). A simple model for squirt-flow dispersion and attenuation in fluid-saturated granular rocks. *Geophysics*, *75*(6), N109–N120.

Gurevich, B., Makarynska, D., & Pervukhina, M. (2009a). Are penny-shaped cracks a good model for compliant porosity? In *2009 SEG Annual Meeting.*

Gurevich, B., Makarynska, D., & Pervukhina, M. (2009b). Ultrasonic moduli for fluid-saturated rocks: Mavko-Jizba relations rederived and generalized. *Geophysics*, *74*(4), N25–N30.

Gurevich, B., Pervukhina, M., & Makarynska, D. (2011). An analytic model for the stress-induced anisotropy of dry rocks. *Geophysics*, *76*(3), WA125–WA133.

Hall, S. A., & Kendall, J.-M. (2003). Fracture characterization at Valhall: Application of P-wave amplitude variation with offset and azimuth (AVOA) analysis to a 3D ocean-bottom data set. *Geophysics*, *68*(4), 1150–1160.

Hall, S. A., Kendall, J.-M., Maddock, J., & Fisher, Q. (2008). Crack density tensor inversion for analysis of changes in rock frame architecture. *Geophysical Journal International*, *173*(2), 577–592.

Han, D.-h. (1986). *Effects of porosity and clay content on acoustic properties of sandstones and unconsolidated sediments* (Unpublished doctoral dissertation). Stanford University.

Heidbach, O., Tingay, M., Barth, A., Reinecker, J., Kurfeß, D., & Müller, B. (2008). The world stress map database release 2008.
doi: 10.1594/GFZ.WSM.Rel2008

Helbig, K. (1983). Elliptical anisotropy - its significance and meaning. *Geophysics*, *48*(7), 825–832.

Helbig, K. (1994). *Foundations of anisotropy for exploration seismics: Handbook of geophysical exploration, I: Seismic exploration* (Vol. 22). Oxford: Pergamon Press.

Helbig, K., & Thomsen, L. (2005). 75-plus years of anisotropy in exploration and reservoir seismics: A historical review of concepts and methods. *Geophysics*, *70*(6), 9ND–23ND.

Hillis, R. R., Mildren, S. D., Pigram, C. J., & Willoughby, D. R. (1997). Rotation of horizontal stresses in the Australian North West continental shelf due to the collision of the Indo-Australian and Eurasian plates. *Tectonics*, *16*(2), 323–335.

Hudson, J. (1980). Overall properties of a cracked solid. In *Mathematical Proceedings of the Cambridge Philosophical Society* (Vol. 88, pp. 371–384).

Hung, B., Zhang, F., Sun, J., Stanley, M., & Osadchuck, A. (2006). An automated 3D method for azimuthal anisotropy analysis in marine seismic data. In *68th EAGE Conference & Exhibition.*

Johnson, D. L. (2001). Theory of frequency dependent acoustics in patchy-saturated porous media. *Journal of the Acoustical Society of America*, *110*(2), 682–694.

Jones, T. D. (1986). Pore fluids and frequency-dependent wave propagation in rocks. *Geophysics*, *51*(10), 1939–1953.

Kachanov, M. (1980). Continuum model of medium with cracks. *Journal of the engineering mechanics division*, *106*(5), 1039–1051.

Kachanov, M. (1992). Effective elastic properties of cracked solids: critical review of some basic concepts. *Applied Mechanics Reviews*, *45*(8), 304–335.

Kachanov, M., Prioul, R., & Jocker, J. (2010). Incremental linear-elastic response of rocks containing multiple rough fractures: Similarities and differences with traction-free cracks. *Geophysics*, *75*(1), D1–D11.

King, M. (1966). Wave velocities in rocks as a function of changes in overburden pressure and pore fluid saturants. *Geophysics*, *31*(1), 50–73.

King, M., Chaudhry, N., & Shakeel, A. (1995). Experimental ultrasonic velocities and permeability for sandstones with aligned cracks. In *International Journal of Rock Mechanics and Mining Sciences and Geomechanics Abstracts* (Vol. 32, pp. 376A–377A).

Knackstedt, M. A., Arns, C. H., & Val Pinczewski, W. (2005). Velocity–porosity relationships: Predictive velocity model for cemented sands composed of multiple mineral phases. *Geophysical Prospecting*, *53*(3), 349–372.

Krief, M., Garat, J., Stellingwerff, J., & Ventre, J. (1990). A petrophysical interpretation using the velocities of P- and S-waves (full waveform sonic). *Log Analyst*, *31*, 355–369.

Lei, T., Sinha, B. K., & Sanders, M. (2012). Estimation of horizontal stress magnitudes and stress coefficients of velocities using borehole sonic data. *Geophysics*, *77*(3), WA181–WA196.

Liu, E., & Martinez, A. (2013). *Seismic fracture characterization: Concepts and practical applications*. EAGE Publications bv.

Lockner, D., Walsh, J., & Byerlee, J. (1977). Changes in seismic velocity and attenuation during deformation of granite. *Journal of Geophysical Research*, *82*(33), 5374–5378.

MacBeth, C. (2002). *Multi-component VSP analysis for applied seismic anisotropy* (Vol. 26; K. Helbig & S. Treitel, Eds.). Elsevier.

MacBeth, C., & Lynn, H. B. (2000). *Applied seismic anisotropy: Theory, background, and field studies* (No. 20). Society of Exploration Geophysicists.

Madadi, M., Pervukhina, M., & Gurevich, B. (2013). Modelling elastic anisotropy of dry rocks as a function of applied stress. *Geophysical Prospecting*, *61*(2), 391–403.

Makarynska, D., Gurevich, B., & Ciz, R. (2007). Finite element modelling of Gassmann fluid substitution of heterogeneous rocks. In *EAGE 69th Conference & Exhibition.*

Mann, R. L., & Fatt, I. (1960). Effect of pore fluids on the elastic properties of sandstone. *Geophysics*, *25*(2), 433–444.

Maultzsch, S., Chapman, M., Liu, E., & Li, X. (2003). Modelling frequency-dependent seismic anisotropy in fluid-saturated rock with aligned fractures: implication of fracture size estimation from anisotropic measurements. *Geophysical Prospecting*, *51*(5), 381–392.

Mavko, G., & Bandyopadhyay, K. (2009). Approximate fluid substitution for vertical velocities in weakly anisotropic VTI rocks. *Geophysics*, *74*(1), D1-D6.

Mavko, G., & Jizba, D. (1991). Estimating grain-scale fluid effects on velocity dispersion in rocks. *Geophysics*, *56*(12), 1940–1949.

Mavko, G., Mukerji, T., & Dvorkin, J. (2003). *The rock physics handbook: Tools for seismic analysis of porous media*. Cambridge University Press.

Mavko, G., Mukerji, T., & Godfrey, N. (1995). Predicting stress-induced velocity anisotropy in rocks. *Geophysics*, *60*(4), 1081–1087.

Mavko, G., & Nur, A. (1975). Melt squirt in the asthenosphere. *Journal of Geophysical Research*, *80*(11), 1444–1448.

Mavko, G., & Nur, A. (1979). Wave attenuation in partially saturated rocks. *Geophysics*, *44*(2), 161–178.

Mukerji, T., & Mavko, G. (1994). Pore fluid effects on seismic velocity in anisotropic rocks. *Geophysics*, *59*(2), 233–244.

Müller, T. M., & Gurevich, B. (2004). One-dimensional random patchy saturation model for velocity and attenuation in porous rocks. *Geophysics*, *69*(5), 1166–1172.

Müller, T. M., Gurevich, B., & Lebedev, M. (2010). Seismic wave attenuation and dispersion resulting from wave-induced flow in porous rocks - A review. *Geophysics*, *75*(5), 75A147–75A164.

Murphy, W. F., Winkler, K. W., & Kleinberg, R. L. (1986). Acoustic relaxation in sedimentary rocks: Dependence on grain contacts and fluid saturation. *Geophysics*, *51*(3), 757–766.

Napalowski, R., Hill, R. A., Stomp, R. J., Derkach, E., Fagervik, E. N., Manning, D. K., et al. (2008). Successful Implementation of Horizontal Open-Hole Gravel Packing in the Stybarrow Field Development Offshore Western Australia. In *SPE Asia Pacific Oil and Gas Conference and Exhibition.*

Nur, A. (1971). Effects of stress on velocity anisotropy in rocks with cracks. *Journal of Geophysical Research*, *76*(8), 2022–2034.

Nur, A., & Simmons, G. (1969). Stress-induced velocity anisotropy in rock: an experimental study. *Journal of Geophysical Research*, *74*(27), 6667–6674.

O'Connell, R. J., & Budiansky, B. (1977). Viscoelastic properties of fluid-saturated cracked solids. *Journal of Geophysical Research*, *82*(36), 5719–5735.

Palmer, I., & Traviolia, M. (1980). Attenuation by squirt flow in undersaturated gas sands. *Geophysics*, *45*(12), 1780–1792.

Pervukhina, M., Gurevich, B., Dewhurst, D. N., & Siggins, A. F. (2010). Applicability of velocity-stress relationships based on the dual porosity concept to isotropic porous rocks. *Geophysical Journal International*, *181*(3), 1473–1479.

Pervukhina, M., Gurevich, B., Golodoniuc, P., & Dewhurst, D. N. (2011). Parameterization of elastic stress sensitivity in shales. *Geophysics*, *76*(3), WA147–WA155.

Pevzner, R., Gurevich, B., & Urosevic, M. (2011). Estimation of azimuthal anisotropy from VSP data using multicomponent S-wave velocity analysis. *Geophysics*, *76*(5), D1–D9.

Pickett, G. (1963). Acoustic character logs and their applications in formation evaluation. *Journal of Petroleum technology*, *15*(6), 659–667.

Pistre, V., Plona, T., Sinha, B., Kinoshita, T., Tashiro, H., Ikegami, T., ... Schilling, K. (2005). A new modular sonic tool provides complete acoustic formation characterization. In *2005 SEG Annual Meeting.*

Prioul, R., Bakulin, A., & Bakulin, V. (2004). Nonlinear rock physics model for estimation of 3D subsurface stress in anisotropic formations: Theory and laboratory verification. *Geophysics*, *69*(2), 415–425.

Prioul, R., Donald, A., Koepsell, R., Marzouki, Z. E., & Bratton, T. (2007). Forward modeling of fracture-induced sonic anisotropy using a combination of borehole image and sonic logs. *Geophysics*, *72*(4), E135–E147.

Rasolofosaon, P. (1998). Stress-induced seismic anisotropy revisited. *Revue de l'Institut Français du Pétrole*, *53*(5), 679–692.

Rüger, A. (2001). *Reflection coefficients and azimuthal AVO analysis in anisotropic media* (Vol. 10; K. Larner, I. Tsvankin, & D. V. Fitterman, Eds.). Society of Exploration Geophysicists.

Sava, D., Mukerji, T., Diaz, M., & Mavko, G. (2000). Seismic detection of pore fluids: Pitfalls of ignoring anisotropy. In *2000 SEG Annual Meeting.*

Sayers, C. M. (1988). Stress-induced ultrasonic wave velocity anisotropy in fractured rock. *Ultrasonics*, *26*(6), 311–317.

Sayers, C. M. (1994). The elastic anisotrophy of shales. *Journal of Geophysical Research: Solid Earth (1978–2012)*, *99*(B1), 767–774.

Sayers, C. M. (2002). Stress-dependent elastic anisotropy of sandstones. *Geophysical prospecting*, *50*(1), 85–95.

Sayers, C. M. (2005). Sensitivity of elastic-wave velocities to stress changes in sandstones. *The Leading Edge*, *24*(12), 1262–1266.

Sayers, C. M. (2006). Sensitivity of time-lapse seismic to reservoir stress path. *Geophysical Prospecting*, *54*(3), 369–380.

Sayers, C. M. (2009). Seismic characterization of reservoirs containing multiple fracture sets. *Geophysical Prospecting*, *57*(2), 187–192.

Sayers, C. M., & Han, D. (2002). The effect of pore fluid on the stress-dependent elastic wave velocities in sandstones. In *2002 SEG Annual Meeting.*

Sayers, C. M., & Kachanov, M. (1995). Microcrack-induced elastic wave anisotropy of brittle rocks. *Journal of Geophysical Research*, *100*(B3), 4149–4156.

Schoenberg, M. (1980). Elastic wave behavior across linear slip interfaces. *The Journal of the Acoustical Society of America*, *68*, 1516.

Schoenberg, M., & Douma, J. (1988). Elastic wave propagation in media with parallel fractures and aligned cracks. *Geophysical Prospecting*, *36*(6), 571–590.

Schoenberg, M., & Helbig, K. (1997). Orthorhombic media: Modeling elastic wave behavior in a vertically fractured earth. *Geophysics*, *62*(6), 1954–1974.

Schoenberg, M., & Sayers, C. M. (1995). Seismic anisotropy of fractured rock. *Geophysics*, *60*(1), 204–211.

Schwartz, L. M., Murphy, W. F., & Berryman, J. G. (1994). Stress-induced transverse isotropy in rocks. In *1994 SEG Annual Meeting.*

Scott Jr, T. E., & Abousleiman, Y. (2005). Acoustic measurements of the anisotropy of dynamic elastic and poromechanics moduli under three stress/strain pathways. *Journal of Engineering Mechanics*, *131*(9), 937–946.

Shapiro, S. (2003). Elastic piezosensitivity of porous and fractured rocks. *Geophysics*, *68*(2), 482–486.

Smith, T., Sondergeld, C., & Rai, C. (2003). Gassmann fluid substitutions: A tutorial. *Geophysics*, *68*(2), 430–440.

Sun, H., & Prioul, R. (2010). Relating shear sonic anisotropy directions to stress in deviated wells. *Geophysics*, *75*(5), D57–D67.

Tang, X., & Cheng, C. H. A. (2004). *Quantitative borehole acoustic methods* (Vol. 24; K. Helbig & S. Treitel, Eds.). Elsevier.

Tang, X., & Chunduru, R. K. (1999). Simultaneous inversion of formation shear-wave anisotropy parameters from cross-dipole acoustic-array waveform data. *Geophysics*, *64*(5), 1502–1511.

Tao, G., & King, M. (1990). Shear-wave velocity and Q anisotropy in rocks: A laboratory study. In *International Journal of Rock Mechanics and Mining Sciences & Geomechanics Abstracts* (Vol. 27, pp. 353–361).

Thomsen, L. (1986). Weak elastic anisotropy. *Geophysics*, *51*(10), 1954–1966.

Thomsen, L. (1995). Elastic anisotropy due to aligned cracks in porous rock. *Geophysical Prospecting*, *43*(6), 805–829.

Thomsen, L. (2002). *Understanding seismic anisotropy in exploration and exploitation* (Vol. 5). Society of Exploration Geophysicist.

Thomsen, L. (2012). On the fluid dependence of the parameters of anisotropy. In *2012 SEG Annual Meeting.*

Thurston, R. (1974). Waves in solids. In C. Truesdell (Ed.), *Encyclopedia of physics* (Vols. VIa/4: Mechanics of solids, IV: Waves in elastic and viscoelastic solids (theory and experiment) Springer-Verlag, p. 109–308).

Tsvankin, I. (1997). Anisotropic parameters and P-wave velocity for orthorhombic media. *Geophysics*, *62*(4), 1292–1309.

Tsvankin, I. (2001). *Seismic signatures and analysis of reflection data in anisotropic media* (Vol. 29; K. Helbig & S. Treitel, Eds.). Elsevier Science.

Tsvankin, I., & Grechka, V. (2011). *Seismology of azimuthally anisotropic media and seismic fracture characterization* (Vol. 17; K. Larner, M. Slawinski, & S. Fomel, Eds.). Society of Exploration Geophysicists.

Underschultz, J., Hill, R., & Easton, S. (2008). The hydrodynamics of fields in the Macedon, Pyrenees, and Barrow Sands, Exmouth Sub-basin, Northwest Shelf Australia: identifying seals and compartments. *Exploration Geophysics*, *39*(2), 85–93.

Vlastos, S., Liu, E., Main, I., Schoenberg, M., Narteau, C., Li, X., & Maillot, B. (2006). Dual simulations of fluid flow and seismic wave propagation in a fractured network: effects of pore pressure on seismic signature. *Geophysical Journal International*, *166*(2), 825–838.

Walsh, J. (1965a). The effect of cracks in rocks on Poisson's ratio. *Journal of Geophysical Research*, *70*(20), 5249–5257.

Walsh, J. (1965b). The effect of cracks on the compressibility of rock. *Journal of Geophysical Research*, *70*(2), 381–389.

Walsh, J. (1965c). The effect of cracks on the uniaxial elastic compression of rocks. *Journal of Geophysical Research*, *70*(2), 399–411.

Wang, Z. (2002). Seismic anisotropy in sedimentary rocks, part 2: Laboratory data. *Geophysics*, *67*(5), 1423–1440.

White, J. (1975). Computed seismic speeds and attenuation in rocks with partial gas saturation. *Geophysics*, *40*(2), 224–232.

Winkler, K. W., Sinha, B. K., & Plona, T. J. (1998). Effects of borehole stress concentrations on dipole anisotropy measurements. *Geophysics*, *63*(1), 11–17.

Winterstein, D. (1990). Velocity anisotropy terminology for geophysicists. *Geophysics*, *55*(8), 1070–1088.

Winterstein, D., & Meadows, M. A. (1991). Changes in shear-wave polarization azimuth with depth in cymric and railroad gap oil fields. *Geophysics*, *56*(9), 1349–1364.

Xu, S. (1998). Modelling the effect of fluid communication on velocities in anisotropic porous rocks. *International Journal of Solids and Structures*, *35*(34), 4685–4707.

Zatsepin, S. V., & Crampin, S. (1997). Modelling the compliance of crustal rock - I. Response of shear-wave splitting to differential stress. *Geophysical Journal International*, *129*(3), 477–494.

Zhu, Y., & Tsvankin, I. (2006). Plane-wave propagation in attenuative transversely isotropic media. *Geophysics*, *71*(2), T17–T30.

Zimmerman, R. W., Somerton, W. H., & King, M. S. (1986). Compressibility of porous rocks. *Journal of Geophysical Research: Solid Earth (1978–2012)*, *91*(B12), 12765–12777.

Zoback, M. D. (2010). *Reservoir geomechanics*. Cambridge University Press.